Dissertation

submitted to the
Combined Faculties for
the Natural Sciences and for Mathematics of the
Ruperto-Carola University of Heidelberg, Germany
for the degree of
Doctor of Natural Sciences

Put forward by
Dipl. Phys. Lukas M. Raffelt
born in Iserlohn

Oral examination: 19th October 2016

Measurement of the Proton Asymmetry (C) in free neutron β-decay with PERKEO III

Lukas Raffelt

8th August 2016

Referees: apl. Prof. Dr. U. Schmidt
Prof. Dr. A. Schöning

This thesis has been compiled using KOMA-Script and XeTeX.

Measurement of the Proton Asymmetry (C) in free neutron β-decay with PERKEO III

The decay of polarized neutrons can be used to search for Physics Beyond the Standard Model. The non-isotropic angular distributions of the decay particles are parity violating and reveal the true nature of the weak interaction. Many observables are available in the decay of polarized neutrons, but the decay itself is only described by three parameters, which allows searches for new physics in a combined analysis. Measurements of the electron angular correlation coefficient (A) can be used to precisely determine the ratio of the axial to the vector coupling constant. The proton angular correlation coefficient (C) has only been measured once by a predecessor of this experiment.

We measured the proton asymmetry with a similar proton detector, but employed a new measuring scheme allowing the collection of the worlds first data on the proton energy dependence of the proton asymmetry. At the current state of the analysis, a statistical uncertainty on the value of C of 0.8 % in each of the two detectors can be reached. For a final value, studies of systematic effects based on field simulations and tracking are still missing.

For this measurement I designed and constructed a new detector. For the first time the scintillator was coated with a transparent conductive coating and together with the new CAD milled light-guides in a four-side readout configuration the low energy performance of the detector could be increased. Several systematic effects have been studied, especially the Point Spread Function of the magnetic transport system.

Messung der Protonenasymmetrie (C) im Zerfall des freien Neutrons mit PERKEO III

Der Zerfall polarisierter Neutronen kann zur Suche nach Physik, die über das Standard Modell der Teilchenphysik hinausgeht, eingesetzt werden. Die nicht isotrope Winkelverteilung der Zerfallsprodukte ist eine Folge der V-A Struktur der schwachen Wechselwirkung. Nur drei Parameter bestimmen die theoretische Beschreibung des Zerfalls. Dem gegenüber stehen viele verschiedene messbare Größen und Verteilungen. Die Elektronen Asymmetrie (A) wird zur besonders präzisen Bestimmung der relativen Stärke von Axialer- und Vektor-Kopplungskonstante benutzt.

Die Protonen Asymmetrie (C) wurde erstmalig von einem Vorgänger dieses Experiments gemessen. Mit einem neuen verbesserten, aber ähnlichen, Detektor haben wir eine Messung der Protonen Asymmetrie durchgeführt. Durch den Einsatz eines Systems von Retardierungselektroden konnte zum ersten Mal die Abhängigkeit der Protonenasymmetrie von der Protonenenergie bestimmt werden. Nach einer vorläufgen Analyse können wir eine Genauigkeit von etwa 0.8 % in jedem der zwei Detektoren erreichen. Für einen endgültigen Wert fehlen noch Untersuchungen einiger systematischer Effekte durch Simulation von Teilchenbahnen.

Für diese Messung habe ich einen neuen Detektor entworfen und konstruiert. Dieser ist mit einer transparenten, elektrisch leitfähigen Beschichtung versehen, die ein Auslesen des Szintillators von der Seite ermöglicht. Zusammen mit den neuen Lichtleitern, die erstmals von einer Fünf-Achs Fräse gefertigt wurden, zeigt der Detektor ein gutes Niederenergieverhalten. Mehrere systematische Korrekturen wurden berechnet, besonders solche die durch die kleine Größe des Detektors hervorgerufenen werden. Dazu wurde die Punktabbildungsfunktion des magnetischen Systems untersucht.

Contents

1. Introduction and Motivation

The study of the elementary particles and their interactions is a field of physics with a very rich and long history. Starting from the discovery of the building blocks of the atoms (neutrons, protons and electrons), nuclear decays and studies at accelerators advanced our understanding of the physics governing the particles that make up the objects of daily life. The current knowledge is summarized in the so called Standard Model of particle physics (SM). Even though we know that the SM cannot explain several astronomic observations (like dark matter) and neutrino oscillations, the SM remains one of the best tested and confirmed theories.

In recent years the first runs of the LHC at CERN have been in the focus of the public attention. The remarkable discovery of the Higgs-Boson completed the SM since it was the last missing but predicted particle whose existence was confirmed. The search for new Physics Beyond the Standard Model (BSM) continues at the LHC and other accelerators around the world. This new physics could manifest itself in the generation of new particles at the energy frontier (as studied by experiments like ATLAS and CMS) or in rare decays of known particles (studied in LHCb, BELLE-II and several other experiments).

However, there is another kind of experiments that is also suited to find physics beyond the SM. Precision experiments at low energies cannot study the generation of new particles, but are sensitive to the very small effects of new physics. Low energy processes usually have very clean theoretical descriptions and can often be measured with a low background.

The subject of this thesis is one of those low energy precision experiments. We measured the proton angular correlation coefficient (**C**) in the decay of free polarized neutrons. This parameter describes the non-isotropic emission of the proton with respect to the spin of the decaying neutron. This is only one of several such correlation coefficients that can and have been measured in neutron decay. **C** itself has only been measured once, whereas there are several measurements for the other coefficients. Combined with other experimental data and precise calculations of theoretical corrections, these parameters can be used to study the fundamental properties of the weak interaction. Possible extensions of the SM might cause deviations of the parameters from their SM predictions.

Our experiment is conducted in a collaboration of the physics institute in Heidelberg, the TU Vienna, the ILL in Grenoble and the TU Munich. We used the spectrometer PERKEO III, the current iteration of a series of spectrometers dedicated to the study of the neutron's decay products. This spectrometer has been build in Heidelberg and was recently used in the currently most precise measurement of the beta-asymmetry, the correlation coefficient of the electron. The spectrometer is designed as a mobile experiment that can be set up at different neutron sources. Until now it has been set up three times at the neutron research facility ILL (Institute Laue-Langevin) in Grenoble, France. Between those measurements the instrument was transported back to Heidelberg and Vienna in order to improve it and use parts of it for test measurements.

The ILL is a research center for neutron science, that mainly utilities the neutrons for structural research in material science or biology and chemistry. These experiments are similar to those at synchrotron facilities like the ESRF or XFEL. In addition to that the ILL offers a few beam sites for fundamental physics. Those are used by different experiments, for example like the one described in this thesis.

To measure the proton asymmetry we utilized a proton detector that uses a thin carbon foil

at high voltage to convert the protons into secondary electrons that then can be detected with a scintillator. Both, the conversion system and the electron detector, are based on an earlier measurement of the proton asymmetry but have been completely redesigned in order to improve the performance of the detector. In order to differentiate between those secondary electrons and the primary electrons from the neutron decay, we used a variable electrostatic barrier to block the protons from reaching the conversion foil. This allows to measure and characterize possible background from the conversion system, which was a major source of the final uncertainty in the previous measurement of **C**. Additionally it was possible to measure the proton asymmetry as a function of the proton energy for the first time.

This thesis is split in four parts. In Part I the theory of neutron decay within the SM is presented. Important quantities are introduced and the theoretical spectra of the decay particles are presented. Additonally it is shown how to use the data from the neutron decay to study physics beyond the SM in the framework of an effective field theory.

The major parts of the experimental setup are introduced in Part II and some of the design decisions are explained. Within this part a large chapter covers the design and construction of the new detector that was a major part of this thesis. For the first time we build a detector with machine milled lightguides and with a transparent conductive coating that is read out from all sides. Also considerations about the detector size are presented especially as the detector is not big enough to intercept all incoming particles. Therefore the so called point spread function (PSF) of the magnetic transport is calculated.

The measurement of the proton asymmetry and the first preliminary results are then subject of Part III. This includes the data analysis and studies of some systematic effects.

The results are compiled in Part IV which also gives an outlook on further improvements for future measurements.

Part I.

Theory

2. Neutron Decay as Probe for Physics Beyond the Standard Model

2.1. History of the Weak Interaction

Studies of nuclear decays have played a major role in the development of the current Standard Model of particle physics.

The famous paper by Lee and Yang [LY56] questioned the conservation of parity in the weak interaction and suggested to search for asymmetric distributions of the decay particles from spin polarized sources. The maximal parity violating nature of the weak interaction was then discovered in the decay of ^{60}Co by Wu et al. [WAH$^+$57]. This unexpected violation of a (assumed) fundamental symmetry of the universe started a whole branch of physics looking for other violations of symmetries and their combinations (C, P, T, CP and even CPT[1]). To explain and describe this behaviour the current-current interactions of Fermi's theory of nuclear decays were expanded to the V-A theory of beta decay (see [SM58] and [FG58]).

In the following years, Glashow [Gla61], Salam [Sal68] and Weinberg [Wei67] managed to unite the electromagnetic interaction with the weak interaction with the proposed $SU(2) \times U(1)$ structure and the corresponding spontaneous symmetry breaking. This combined theory is called electro-weak theory. It predicted the existence of charged and uncharged heavy vector bosons that act as force carriers.

This theory has since then been proven numerous times. Neutral current interactions, a prediction of the electro-weak theory, were first observed in the Gargamelle detector at the CERN's SP accelerator in 1973 [HKK$^+$73]. The $W^\pm$ and Z^0 bosons were then observed at the SPS in 1983 [AAA$^+$83; BBB$^+$83]. As a next step the electron positron collider LEP was constructed. At LEP precision measurements of the decay-width of the Z^0-boson further confirmed the theory and showed that there are exactly three neutrino generations [Sch$^+$06].

Together with Quantum Chromo Dynamic (QCD), used to describe the strong interaction of the hadrons, both theories combined are called the Standard Model.

For many years predictions from the Standard Model have been very successful. The discovery of the top-quark at the predicted energy completed the experimental confirmation of the three families of quarks [CDF95; D095]. The predictive power of the SM culminated in the discovery of the Higgs particle, the last missing predicted SM-particle [ATL12; CMS12].

Since the discovery of the Higgs the SM is considered complete, but this does not mean that it is the final theory for particle physics. Several clearly observed phenomena like neutrino oscillations or the unknown particles of the dark matter cannot be described within the Standard Model. Additionally the high number of parameters and their fine tuning are considered a problem of the theory. Also the SM cannot provide a sufficient answer to the puzzling question why there is so much more matter than antimatter in the universe.

Interesting in the scope of this thesis are precision measurements of SM parameters at low energies. Studies of the neutron decay coefficients can provide precise values of the relative

[1] here C denotes the change of all charges, P the symmetry of an inversion of all space coordinates and T the symmetry under time reversal. The combined symmetry of CPT cannot be violated as long as Lorentz invariance holds.

strength of the V and A parts of the weak interaction.

This chapter will first briefly introduce the SM and its formalism before deriving the formulas of the neutron decay in the SM. Then possible extensions of the SM and their influences on the neutron decay parameters are discussed. After that, the spectra and angular distributions of the decay parameters in the PERKEO configuration are presented. Lastely the behaviour of charged particles in magnetic fields of varying strength is calculated.

2.2. The Standard-Model of Particle Physics

The SM describes the fundamental particles and their interactions. The fundamental particles leptons and quarks are found in three generations. Their interactions are formalized using a current-field description. Leptons interact only via the electro-weak interaction, whereas the quarks can also interact using the strong force described by QCD. The interactions are mediated via force carrying bosons. In the case of the electro-weak interaction these are the $W^{\pm}$, Z^0 and the photon (γ). The strong force uses 8 gluons to interact with the quarks.

Within the electroweak theory all masses are generated by a spontaneously broken scalar higgs field. This gives rise to the additional spin-0 Higgs particle.

The experimental observation of maximum parity violation in the weak interaction is introduced in the SM by allowing only couplings to left handed fermions and right-handed anti-fermions. The there lepton doublets are (excluding their anti-particle partners)

$$\begin{pmatrix} \nu_e \\ e^- \end{pmatrix}_L , \begin{pmatrix} \nu_\mu \\ \mu^- \end{pmatrix}_L , \begin{pmatrix} \nu_\tau \\ \tau^- \end{pmatrix}_L \tag{2.1}$$

The neutrinos have zero electrical charge and therefore only interact via the weak interaction, whereas the charged leptons (e.g. the electron) also interact using the electro-magnetic force.

The six quarks are also described in three families (again omitting the anti-particles).

$$\begin{pmatrix} u \\ d \end{pmatrix} , \begin{pmatrix} c \\ s \end{pmatrix} , \begin{pmatrix} t \\ b \end{pmatrix} \tag{2.2}$$

Their interaction with each other via the strong force and the corresponding color-charge. The nature of the QCD leads to the so called confinement and asymptotic freedom. Therefore quarks cannot be observed alone, but only in the form of hadrons that consist of a $q\bar{q}$ pair (Mesons such as the pions) or in groups of three (Baryons such as protons and neutrons). Recently there is evidence from the LHC for other more exotic composite particles like qlueballs and pentaquarks. The quarks have electric charge and will also take part in electro-weak interactions. But in order to describe the flavor changing weak decays, the mass eigenstates of the quarks have to be rotated into the weak eigenstates by the CKM[2]-quark-mixing matrix.

Since the neutron decay is a weak decay, the discussion will be limited to the weak interaction. Fundamentally there are two processes that have to be differentiated: Processes with the exchange of the neutral Z^0 boson are so called neutral currents like elastic neutrino scattering in matter. In processes that involve one of the $W^{\pm}$ bosons also electric charge is transferred from one current to the other.

Since the $W^{\pm}$ bosons can couple to leptons and to quarks, one can separate the charged current interactions into the three categories depending on the participating currents: leptonic, hadronic and semi-leptonic. The decay of the neutron into proton, electron and electron anti-neutrino is a semileptonic decay and will be described in detail in the next chapter. The decay of the muon

[2] named after Cabibbo, Kobayashi and Maskawa

into an electron is an example for a pure leptonic weak interaction from which one can extract the important parameter G_F.

2.3. Neutron Decay in the Standard-Model

The notation of this chapter follows the discussion in the review paper of Dubbers and Schmidt [DS11].

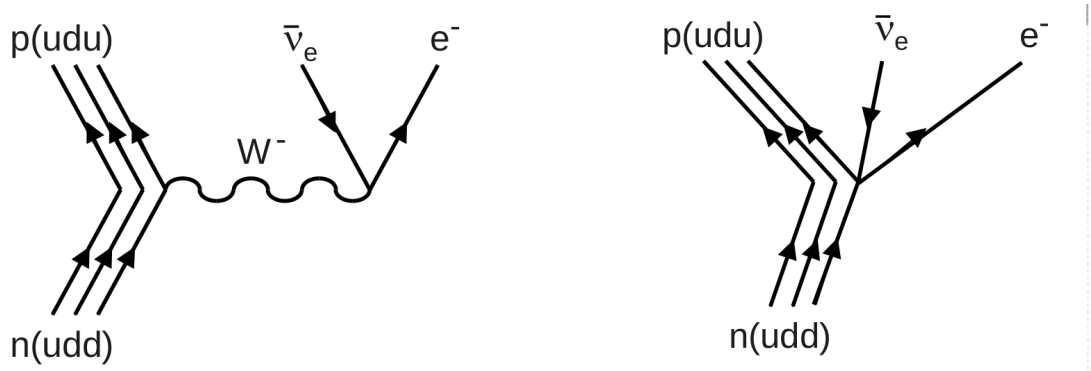

(a) Neutron decay on quark level is mediated by a W^--boson. The other quarks are spectator quarks.

(b) Low energy approximation of the neutron decay as a four current point interaction

Figure 2.1.: Feynman graphs of neutron decay

The semi-leptonic decay of the neutron $n \to p^+ + e^- + \overline{\nu_e}$ via the W^- boson (see Figure 2.1a) has only a small momentum transfer q and can therefore be described as a point interaction (see Figure 2.1) by approximating the propagator $\left(\frac{p^2}{c^2} - M^2\right)^{-1} = M^{-2}$.

In this point interaction with the $V - A$ structure of the weak interaction in the SM these currents can be written as

$$j_\mu = g_w \psi' \gamma_\mu \left(1 - \gamma_5\right) \psi \tag{2.3}$$

with $(1 - \gamma_5)$ as the left handed chirality operator. Due to the different behaviour of the V and A parts under parity transformation the current becomes

$$\mathbf{P}\, j_\mu = -g_w \psi' \gamma_\mu \left(1 + \gamma_5\right) \psi = -\left(V_\mu + A_\mu\right) \tag{2.4}$$

which is then completely right handed. This behaviour is called maximal parity violating nature of the weak interaction. Its origin remains still a mystery, but might be a consequence of a new theory beyond the SM.

With this currents one can write the transition matrix element of the neutron decay as

$$\mathcal{M}_{\text{quark}} = \left(G_F/\sqrt{2}\right) \left[\mathrm{u}\, \gamma_\mu (1 - \gamma_5)\, \mathrm{d}\right] \left[\mathrm{e}\, \gamma_\mu (1 - \gamma_5)\, \nu_e\right] \tag{2.5}$$

Since we do not observe the decay of one quark into another, but have to work with the hadrons neutron and proton, the final matrix element has to account for hadron-structure effects. Therefore several form factors are introduced, which due to the low energy nature of the decay can be taken at zero momentum transfer $q^2 \to 0$. Several of those are connected to SM-forbidden

currents or can be neglected due to the low energy. g_v is set to exactly one due to the so called "conserved vector current hypothesis" (CVC), which causes the hadronic effects to be summarized in one form factor, the relative strength of the axial-vector current. Using $\lambda = \frac{g_A}{g_V} < 0$ the new matrix element for the decay of the neutron into the proton can be written as:

$$\mathcal{M}_{\text{hadrons}} = \left(G_F/\sqrt{2}\right) V_{ud} \left[\text{p}\ \gamma_\mu(1+\lambda\gamma_5)\ \text{n}\right]\left[\text{e}\ \gamma_\mu(1-\gamma_5)\ \nu_e\right] \tag{2.6}$$

From measurements of the triple correlation coefficient, that could not find a violation of the **T** symmetry one can conclude that λ is purely real and has no imaginary part. The most precise way to measure λ is the electron asymmetry in polarized neutron decay. The value of $\lambda \approx -1.27$ can also be deduced from lattice-QCD calculations albeit with a lower precision.

To describe the flavour changing weak decays the decaying d quark from the neutron has to be substituted by d' the flavour-eigenstate of the quark. This flavour-eigenstate is connected to the mass-eigenstates by the CKM-Matrix[3] [KM73; Cab63].

$$\begin{pmatrix} d' \\ s' \\ b' \end{pmatrix} = \begin{pmatrix} V_{ud} & V_{us} & V_{ub} \\ V_{cd} & V_{cs} & V_{cb} \\ V_{td} & V_{ts} & V_{tb} \end{pmatrix} \cdot \begin{pmatrix} d \\ s \\ b \end{pmatrix} \tag{2.7}$$

Since we only observe the flavour conserving decay the matrix element $V_{ud} \approx 0.97$ appears in the formula.

Using that one can calculate the decay rate for different final states. Typically the spins of the outgoing particles cannot be observed. Integrating out all free observables except for the energies and momenta of the electron and neutrino gives the classical "Jackson formula" for the decay of polarized neutrons.

$$\begin{aligned} \mathrm{d}\,\Gamma =& \frac{{G_\mathrm{F}}^2\,|V_{ud}|^2}{(2\pi)^5}\,\mathrm{F}\,(E)\,|M_\mathrm{fi}|^2\,\mathrm{d}\,\Omega_e\,\mathrm{d}\,\Omega_\nu \\ &\times\left[1 + a\frac{\mathbf{p}_e\cdot\mathbf{p}_\nu}{E_e E_\nu} + b\frac{m_e}{E_e} + \langle\sigma_n\rangle\cdot\left(A\frac{\mathbf{p}_e}{E_e} + B\frac{\mathbf{p}_\nu}{E_\nu} + D\frac{\mathbf{p}_e\times\mathbf{p}_\nu}{E_e E_\nu}\right)\right] \end{aligned} \tag{2.8}$$

This formula was first derived in 1957 by Jackson, Treiman, and Wyld [JTW57]. It contains Fermi's constant (G_F) which can be measured in µ-decay. $F(E)$ describes the spectral shape of the electron's energy. M_fi provides the general decay probability. The parameter a is the correlation coefficient that describes the angular correlation of the electron and the anti-neutrino. This value is parity conserving and is a result of the momentum conservation of the three decay particles. It can be measured by its influence on the shape of the proton recoil spectrum.

A and B both describe the angular correlation of the electron and neutrino with respect to the spin of the neutron ($\langle\sigma_n\rangle$). A is called β-asymmetry and has been measured to very high precision by several experiments. B, the so called neutrino asymmetry, can be measured in several ways and was also measured in the same measurement as the last measurement of **C** by Schumann et al. [SSD+07].

b is the so called Fierz interference term. It changes the shape of the electron spectrum and is zero in the Standard Model but could be an interesting probe for non-SM interactions, since it depends on left handed scalar and tensor interactions. If the Fierz interference term is not zero it will change the electron correlation coefficient by

$$\widetilde{A} = \frac{A_{SM}}{1 + b\,\langle m_e/w_e\rangle} \tag{2.9}$$

[3] Cabibbo-Kobayashi-Maskawa-Matrix named after the scientists who developed its formulation

with the average over the observed energy range $\langle m_e/w_e \rangle$. In the formula for the neutrino asymmetry a second Fierz term appears.

$$\widetilde{B} = \frac{B_0 + b_\nu \langle m_e/w_e \rangle}{1 + b \langle m_e/w_e \rangle} \tag{2.10}$$

The so called triple-correlation constant D would be time-symmetry violating and has been found to be compatible with zero as expected by the SM.

Within the SM, all those parameters only depend on λ and can therefore be used to precisely determine it. Equation 2.11 shows these dependencies.

$$a = \frac{1-\lambda^2}{1+3\lambda^2}, \qquad A = -2\frac{\lambda\,(\lambda+1)}{1+3\lambda^2}, \qquad B = 2\frac{\lambda\,(\lambda-1)}{1+3\lambda^2} \tag{2.11}$$

From that the SM values of the parameter can be calculated as $a = -0.106$, $A = -0.118$ and $B = 0.987$.

Section VI.B of the review by Dubbers and Schmidt [DS11] and the references therein describe recent and historic measurements of many of those parameters.

Additional recent results of the electron asymmetry A are UCNA [MPB+13] and the newly published PERKEO II result [MMD+13]. The measurement of A from Mest [Mes11] with the additional analysis of Saul [Sau16] with a relative precision $\Delta A/A < 2 \times 10^{-3}$ will be published soon. The aSPECT collaboration is still analysing the data from their measurement of a. Currently several experiments (such as PERC) are planed to further decrease the errors on all parameters.

Until now the formula did not contain the proton as a free parameter in the final state. Its energy and momentum had been integrated out. The proton asymmetry parameter **C** was first defined in 1958 by Treiman [Tre58] in general terms for recoil spectra in all β-decays. Since the proton is kinematically coupled to the electron and neutrino, its momentum can always be reconstructed from the energies and momenta of the neutrino and the electron. The angular distribution of the protons shows the typical $\cos(\theta)$ dependency also known from the electrons:

$$W(\theta) = 1 + 2\,\mathbf{C}\,\cos(\theta) \tag{2.12}$$

Furthermore the proton asymmetry parameter can be expressed in terms of the electron and neutrino asymmetry.

$$\mathbf{C} = -\chi_C\,(A+B) = \chi_C \frac{4\lambda}{1+3\lambda^2} \tag{2.13}$$

Here χ_C is a kinematic constant that was first calculated in the same paper [Tre58]. It only depends on the electron's endpoint energy and mass and has a numerical value of $\chi_C = 0.27484$. Depending on the definition of the proton asymmetry χ_C can either be positive or negative.

In the case of a non-zero Fierz term the proton asymmetry can be expressed as

$$\widetilde{C} = \frac{-\chi_C(A+B_0) - \chi'_C b_\nu \langle m_e/w_e \rangle}{1 + b \langle m_e/w_e \rangle} \tag{2.14}$$

For the interpretation of precision measurements it is important to know all corrections that can be calculated from theory to be able to relate the measured quantity to the fundamental parameter of the theory.

Glück [Glü96] calculated numerical values for the recoil-order, Coulomb and model independent order-α corrections. Additionally the influence of non-SM models on the proton asymmetry were calculated. In a detailed paper [GJL95] these calculations are collected for many of the neutron decay parameters.

In 2008 Gudkov [Gud08] revisited the problem of the theoretical corrections to the integral proton asymmetry. In a consistent model of an Effective Field Theory, the corrections are calculated including all possible non-SM contributions.

Within the SM the corrections can be split into three distinct parts.

$$\Delta C = \Delta C_\alpha + \Delta C_\delta + \Delta C_{rec} \tag{2.15}$$

All corrections originating in the nucleon structure, so called inner corrections, are summarized in ΔC_δ whereas ΔC_α contains the Coulomb- and outer-corrections. The effects of the recoil are expressed in ΔC_{rec}. Many factors of these corrections again only consist of the electron's mass and maximal energy and can therefore be collapsed into numerical values. Other constants are λ and the fine structure constant as well as the neutron mass and μ_V from the mangetic moments of proton and neutron which are all known quite precise. So all corrections can be expressed as ([Gud08])

$$\Delta C = 0.0065 - 0.00022\, e_v^R \tag{2.16}$$

where the low energy constant of the EFT e_v^R can be calculated using LatticeQCD or extracted from other measurements. Ando et al. [AFG$^+$04] show extensive details of the derivation of these corrections and estimate the low energy constant to $e_v^R \approx 20$.

2.4. Possible Extensions of the Standard-Model

2.4.1. Problems with the SM

The Standard Model is not considered a final theory, because there are several effects and observations that cannot be descried in the framework of the SM. There are many cosmological and astronomical observations that require dark matter and dark energy. Those make up about 27 % and 69 % of the observable universe. The SM has no particle that could be the dark matter and there is no explanation for the dark energy from the SM.

In the last years several experiments proved that neutrino oscillations exist and mix all the flavours of the neutrinos. This oscillations require a non-zero rest mass for at least two of the three known light neutrino masses, which is in direct contradiction to the assumptions of the SM.

Another big problem is the matter/anti-matter asymmetry in the universe which cannot be explained by only the small CP-violating effects already found in the SM. Closely related is the absent CP violation in the strong interaction which could be explained by a fine tuned theory which in itself is also not satisfactory.

Additionally there are also some more philosophical problems with the SM. In its current state the SM is defined by 19 Variables, that cannot be deducted from theory. This great number and the relative fine tuning between parameters sparks the search for a overlying theory with less parameters.

Also the forth fundamental force of the universe, gravity, is not included in the SM and up to now there is no clear way to describe gravity in the framework of a quantum field theory.

If an overlying theory also could unify the electroweak theory with the strong interaction, it would be called a Unified theory. A possible quantum theory of gravity that could be unified with the other forces would then be called the GUT (Grand Unified Theory)

Therefore a search for physics Beyond the Standard Model (BSM) is ongoing for several years. So far it has not been successful, even though there are several candidates proposed. Since the start of the data-analysis of the LHC experiments the bounds for extension models have shrunk

significantly. Several super-symmetric models are already excluded, since their predicted particles have not been found. Additional measurements of rare decays or precision measurements of branching ratios and correlations can give strong bounds on BSM physics. Also searches for the electric dipole moment of the neutron give strong bounds on some proposed models.

2.4.2. Effective Field Theories - VAST Model

In order to be able to search for non-SM physics in a model-independent way, so called EFTs (Effective Field Theories) are used. These describe the effective low energy Lagrangian in terms of various coupling constants. Those constants can directly be constrained by experiments. Possible theories can than calculate the expected values for those coupling constants. This allows to globally compare the experiments and the EFT acts as a mediator between the experiments an the theory. Directly constraint parameters of certain models or theories might lead to a fixation on this specific subset of theories and might cause one to overlook the right theory. Additionally the EFT approach decouples the experiment from possible wrong interpretations of the theory.

This section follows the notations of the paper "Asymmetry of recoil protons in neutron beta-decay" by Gudkov [Gud08]. Another good summary of the usage of neutron decay measurements in the search for new physics can be found in [NG13]. The most general Lorentz-invariant Lagrangian can be written in the following way:

$$\begin{aligned} H_{int} = &\left(\overline{\psi}_p \psi_n\right)\left(C_S \overline{\psi}_e \psi_\nu + C'_S \overline{\psi}_e \gamma_5 \psi_\nu\right) \\ &+ \left(\overline{\psi}_p \gamma_\mu \psi_n\right)\left(C_V \overline{\psi}_e \gamma_\mu \psi_\nu + C'_V \overline{\psi}_e \gamma_\mu \gamma_5 \psi_\nu\right) \\ &+ 1/2\left(\overline{\psi}_p \sigma_{\lambda\mu} \psi_n\right)\left(C_T \overline{\psi}_e \sigma_{\lambda\mu} \psi_\nu + C'_T \overline{\psi}_e \sigma_{\lambda\mu} \gamma_5 \psi_\nu\right) \\ &- \left(\overline{\psi}_p \gamma_\mu \gamma_5 \psi_n\right)\left(C_A \overline{\psi}_e \gamma_\mu \gamma_5 \psi_\nu + C'_A \overline{\psi}_e \gamma_\mu \psi_\nu\right) \\ &+ \left(\overline{\psi}_p \gamma_5 \psi_n\right)\left(C_P \overline{\psi}_e \gamma_5 \psi_\nu + C'_P \overline{\psi}_e \gamma_\mu \psi_\nu\right) \\ &+ h.c. \end{aligned} \tag{2.17}$$

The indices V, A, S, T and P denote interactions of vector, axial-vector, skalar, tensor and pseudoscalar nature. When reasonably assuming non-relativistic nucleons the pseudoscalar interaction vanishes. Each of the interactions can couple to left and right handed currents. The Left-Right structure is easier to see in the formulation of Konrad et al. [KHB+12].

They write the Matrix element as:

$$\mathcal{M} = \frac{2G_F V_{ud}}{\sqrt{2}} \sum_{j\in\{V,A,S,T\}} \mathbf{L}_j \langle p|\Gamma_j|n\rangle\langle e^-|\Gamma_j \frac{1-\gamma_5}{2}|\nu\rangle + \mathbf{R}_j \langle p|\Gamma_j|n\rangle\langle e^-|\Gamma_j \frac{1+\gamma_5}{2}|\nu\rangle \tag{2.18}$$

The different interactions are then written as

$$\Gamma_V = \gamma_\mu, \qquad \Gamma_A = i\gamma_\mu\gamma_5, \qquad \Gamma_S = 1, \qquad \Gamma_T = \frac{i\left[\gamma_\mu, \gamma_\nu\right]}{2\sqrt{2}} \tag{2.19}$$

Due to the direct appearance of the projection operators the Matrix element is split in an interaction with the left handed neutrino an another interaction with the right handed neutrinos. Within the SM all $\mathbf{R}_j$ are zero due to the (nonexistance of right handed neutrinos).

In order to express $C_{j\in\{V,A,S,T\}}$ and $C'_{j\in\{V,A,S,T\}}$ from Equation 2.17 in terms of those explicitly left and right handed couplings see the following equation.

$$C_j = \frac{G_F V_{ud}}{\sqrt{2}}\left(\mathbf{L}_j + \mathbf{R}_j\right) \qquad C'_j = \frac{G_F V_{ud}}{\sqrt{2}}\left(\mathbf{L}_j - \mathbf{R}_j\right) \tag{2.20}$$

Again following the previous formulation, one writes the coupling constants as a combination of the SM values C_i^{SM} and a small new physics contributions δC_i. The resulting change in the proton asymmetry due to the new physics can be written as

$$\delta C_{new} = \frac{1}{X\left(1+3\lambda^2\right)} * \left(\frac{X_1}{2} L_1 + \frac{X_3}{2} L_3 - X_1 2\lambda * \left(\frac{L_0}{1+3\lambda^2} + \frac{X_2 L_2}{X * \left(1+3\lambda^2\right)} \right) \right) \tag{2.21}$$

The factors X_i again only depend on masses and energies where as the L_i depend on the new physics coupling constants, λ and α. Inserting the known values for those constants Gudkov [Gud08] arrives at the final sensitivity of **C** to the new physics coupling constants.

$$\begin{aligned} \delta C_{new} = 0.05657 \left(\delta C_V + \delta C'_V\right) + 0.04456 \left(\delta C_A + \delta C'_A\right) \\ - 0.06234 \left(\delta C_S + \delta C'_S\right) + 0.02132 \left(\delta C_T + \delta C'_T\right) \end{aligned} \tag{2.22}$$

Similar equations can be calculated for each of the observables from neutron decay. Therefore one has to combine several independent observables in order to be able to fit the many parameters of the effective field theory. In that way a combined analysis of all measurements can be used to constrain possible values for the new physics. Recently this was done by Konrad et al. [KHB+12]. After a careful selection of input experiments, they find that the SM is included in the 1σ errors for the relative strengths L_S/L_V and L_T/L_A. The selection of the data excludes the last measurement of the proton asymmetry C, since it was derived from the same data set as the measurement of B. In a future scenario of improved precision on all neutron parameters limits can be improved considerably, especially for L_T/L_A (this caused mainly by expected improvements in the lifetime and the correlation B). Additionally an independent measurement of **C** is assumed. A final analysis of our measurement will provide this result, but with an accuracy of a factor 10 higher than assumed in the future scenario.

The current limits of right handed scalar and tensor couplings for each value independently include the SM at 68 %CL but the combined plot shows two most likely values at $(-0.05, -0.05)$ and $(0.05, 0.05)$ for $(R_T/L_A, R_S/L_V)$ with the SM at $(0, 0)$ excluded at the 90 %CL. Again, future experiments can improve the limits and reveal if the exclusion of the SM persists.

2.4.3. Manifest Left-Right Symmetric Models

Often the influence of the neutron measurements on manifest left-right symmetric models is studied. A detailed discussion in the scope of neutron measurements was collected by Schumann [Sch07].

Here the left and right handed coupling constants are assumed to be equal [BBM+77] but not necessary the same as in the SM, which could give a new $\lambda' = g'_A/g'_V$. This theory assumes a spontaneous broken left-right theory. Therefore the left handed $W_L^{\pm}$ boson has a right handed partner $W_R^{\pm}$. After symmetry breaking the two bosons mix with a mixing angle ζ.

$$W_1 = W_L \cos\zeta + W_R \sin\zeta \qquad \text{and} \qquad W_2 = -W_L \sin\zeta + W_R \cos\zeta \tag{2.23}$$

W_1 is the SM W after symmetry braking which then has a right-handed admixture. W_2 is a yet undiscovered much heavier boson that has mainly a right handed interaction. The mass of this boson is an important parameter of the theory in addition to the mixing angle.

Three free parameters $\delta = (m_1/m_2)^2$, ζ and λ' then appear in the different formula of the correlation coefficients and other observables (see [GJL95]).

Recent analysis of the particle data group [pdg15] (Section "Searches for New Heavy Bosons") set the limit of the mass of the W_R to 715 GeV from combined Electroweak analysis (see [CGZ99])

and above 592 GeV from muon decay (see [BBD+11]). The limit derived from the Schumann measurement [SKD+08; SSD+07; Sch07] is no longer included.

The study of Konrad et al. [KHB+12] also explores the impact of neutron measurements on this model and they conclude that the current results include the SM and that the limits derived are inferior to the other measurements. The future scenario could become comparable and new physics might be in reach for the next generation of neutron experiments.

2.4.4. Neutrons as a Probe for Lorentz-Violation

Recent studies by Díaz, Kostelecký, and Lehnert [DKL13] propose a study of the effects of a possible Lorentz-violation especially in the neutrino sector. Since a neutrino is involved in the beta decay some of the observables in neutron decay might be sensitive to Lorentz violating effects as presented by Díaz [Día14].

2.5. Spectra and Angular Distributions

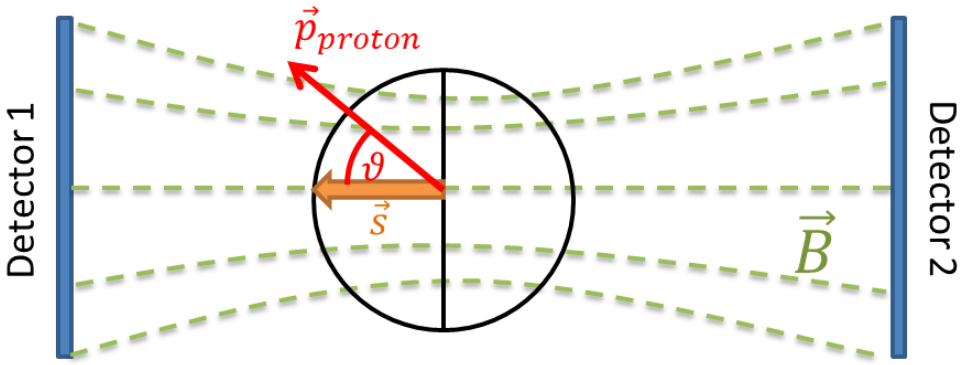

Figure 2.2.: Separating the two hemispheres using a magnetic field. Particles emitted in direction of the spin are observed on detector 1 and particles emitted against the spin direction are detected on detector 2. Employing a spin-flipper to reverse the direction of the neutron spin allows to measure both particle counts in the same detector.

To measure the differential decay rate with respect to the neutron spin, we utilise the common concept of all PERKEO measurements. The neutrons decay in a magnetic field with their spin parallel or anti-parallel to the magnetic field. The charged decay products then gyrate along the magnetic field lines on a helix trajectory. The magnetic field lines guide the electrons and protons towards two detectors. The drift movement clearly separates particles from each of the hemispheses defined by the sign of the projection to the spin. A full detection of all decaying particles is therefore possible.

The angular distribution $W(\theta) = 1 + X\cos(\theta)$ with an asymmetry parameter X is then integrated over each hemisphere.

$$N^{\uparrow,\downarrow} = \int \frac{\mathrm{d}\,\Gamma}{\mathrm{d}\,\Omega}\,\mathrm{d}\,\Omega \propto \int (1 \pm X\cos(\theta))\,\mathrm{d}\,\Omega = 1 \pm \frac{1}{2}X \tag{2.24}$$

Those count rates are then combined to the experimental asymmetry

$$X_{exp} = \frac{N^{\uparrow} - N^{\downarrow}}{N^{\uparrow} + N^{\downarrow}} = \frac{1}{2} X_{theo} \tag{2.25}$$

For the asymmetries appearing in Equation 2.8, namely A and B this formula holds. The situation for the proton asymmetry is slightly different. Since **C** is defined instead of appearing in the Jackson formula (Equation 2.8), this factor $1/2$ and the sign of the asymmetry vary from paper to paper. The definition of **C** as

$$C = \frac{N_p^{\uparrow} - N_p^{\downarrow}}{N_p^{\uparrow} + N_p^{\downarrow}} \tag{2.26}$$

will be used in this thesis as it is also used in recent publications. The general angular distribution of recoil nuclei in beta-decay can be found in [JTW57]. There the factor 2 is absorbed in a different definition of the kinematic factor, also as later authors (Glück, Gudkov and other) mention, there is a misprint in the formula of X_1.

The energy spectra of the electron and the proton are quite different, since the masses of both particles differ by three orders of magnitude. Adapting a Monte Carlo neutron decay event generator from [Rei91] to modern `C++` with updated values for the constants, a set of proton decay events was created. The resulting spectra were checked against literature.

From that data set one can extract the energy correlation of the proton and the electron for each event see Figure 2.4. Also the single spectra of the protons (Figure 2.3b) and the electrons (Figure 2.3a) were generated. One can see that the endpoint energy of the electron is slightly above 780 keV whereas the protons maximum energy is only 0.75 keV. Also the shape of the spectrum is quite different.

From the same MC simulation, the proton spectra for the different spin directions can be extracted. Those can be used to calculate the value of the proton asymmetry as a function of the proton energy (Figure 2.5). In the same plot also the integrated proton asymmetry is plotted for protons above the corresponding energy. The new experimental setup was able to collect measurement data for a few points on that curve as later described in section 10.2.

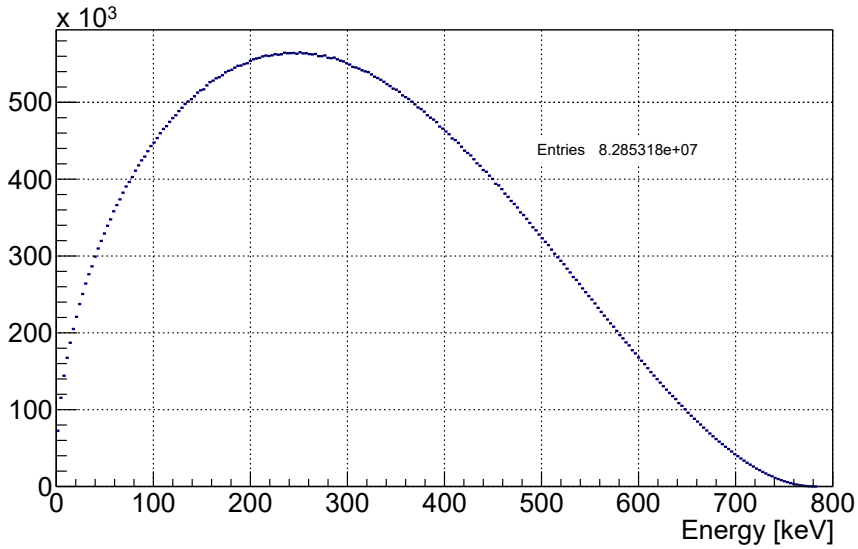

(a) Electron spectrum

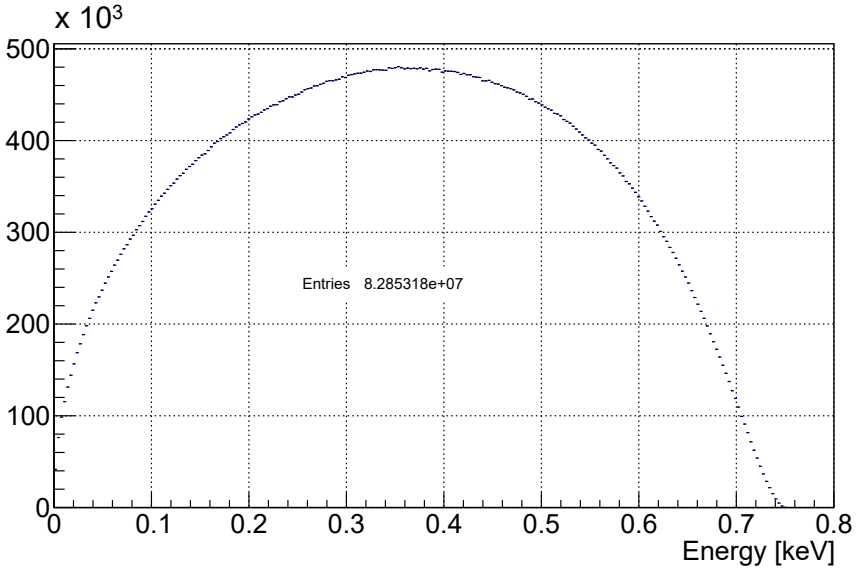

(b) Proton spectrum

Figure 2.3.: Energy Spectra of the charged decay particles. Generated without any theoretical corrections (e.g. recoil or radiative)

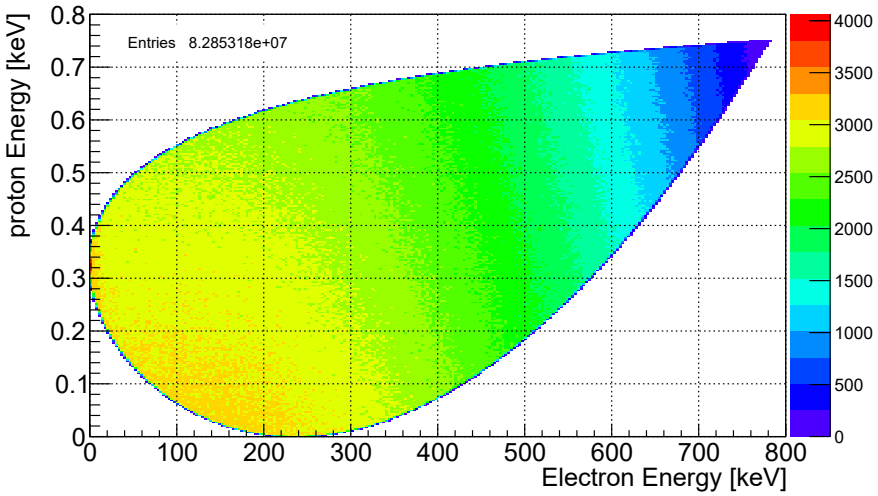

Figure 2.4.: Scatter plot of the neutron decay shows the correlation of energies of electron and proton. Data from the described Monte Carlo Generator without recoil or radiative corrections.

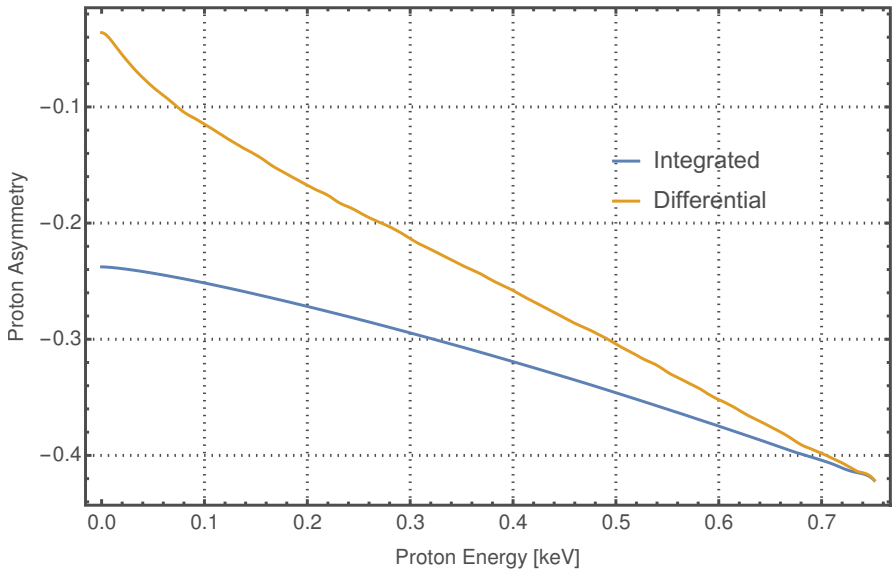

Figure 2.5.: Proton Asymmetry as a function of the proton energy. The integrated proton asymmetry for protons above a certain energy is also plotted.

3. Magnetic Mirror Effect

The Lorentz force applied to a charged particle in a constant magnetic field causes the particle to move in the typical gyration motion with the radius depending on the momentum perpendicular to the magnetic field ($p_\perp$) and the strength of the magnetic field.

$$r = \frac{p_\perp}{q\,B} \tag{3.1}$$

But since the particles move along field lines of varying field strength, it is useful to present the concept of adiabatic invariances of motion.

In a mechanical system the general action integral J_i can be expressed in terms of the general canonical variables q_i and p_i.

$$J_i = \oint p_i \,\mathrm{d}q_i \tag{3.2}$$

If the system is changed slowly (adiabatic) for the moving particle, those integrals are constant. For a charged particle in a magnetic field the change in field strength is considered adiabatic, if the change of $B(z)$ along z is small for one cycle of the gyration movement. From the classical discussion of this effect by Jackson [Jac99] we get the two invariants of the motion inside an inhomogeneous magnetic field.

$$B\,r^2 = \text{const.} \quad \text{and} \quad \frac{p_\perp^2}{B} = \text{const.} \tag{3.3}$$

Together with the conservation of momentum both components of the momentum of a particle starting at z_0 can be written as a function of z

$$p_\parallel^2(z) = p^2 - p_\perp^2(z) = p^2 - p_\perp^2(z_0) * \frac{B(z)}{B(z_0)} \tag{3.4}$$

Those invariants lead to interesting and useful effects: When drifting towards a slowly rising field the pitch angle increases further and further and the drift velocity decreases until the angle reaches it maximum and the drift velocity is zero. At that point the particle is reflected at the rising magnetic field. This effect is used in particle traps and magnetic bottles.

Particles drifting towards a lower magnetic field strength gyrate on increasing radii and their pitch angle decreases while the pitch of the helix lengthens. This can be used to accelerate the drift of those particles that are emitted almost perpendicular to the magnetic field.

The usage of the inverse magnetic mirror effect is typical for the PERKEO experiments. The magnetic field inside the decay volume has a slight gradient towards the detectors which accelerates the drift from the central volume. But this increases the number of wrongly assigned particles since it is possible that particles are reflected and counted in the wrong detector. For example a particle with high pitch angle emitted at a position downstream of the maximum of magnetic field strength but with initial momentum pointing towards the upstream detector can be reflected at the maximum. This introduces a systematic correction that is suppressed if one averages the results of the both detectors. Another effect of the reduced field at the detector is to avoid gracing incident of the particles on the detector, since the angle of the particle with

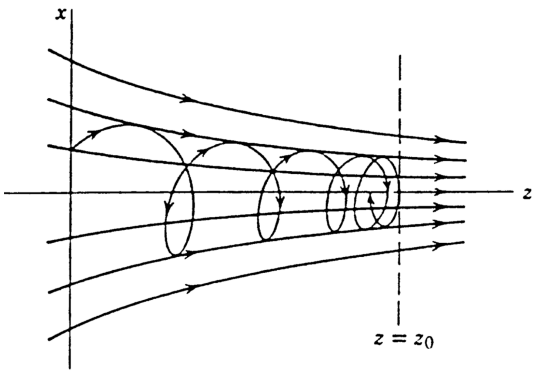

Figure 3.1.: Trajectory of a particle reflected at a magnetic mirror from [Jac99]

respect to the magnetic field is boosted to smaller values. Backscattering of particles from the detector is suppressed since it strongly depends on the incident angle. Nevertheless some particles can undergo multiple scattering in the detector and leave the detector before depositing all their energy. Those particles then have to travel against an increasing magnetic field, which then reflects a part of the backscattered particles back onto the primary detector. Since both detectors are connected via the magnetic field lines, those backscattered particles that can overcome the magnetic barrier, can be detected on the opposite detector. A full energy reconstruction of those events is therefore possible. The measurement of the real field configuration is described in subsection 5.3.1 and in section 10.2 the transmission function of the retardation electrode is calculated taking the magnetic mirror effect into account which changes the measured integrated asymmetry considerably (see Figure 3.2).

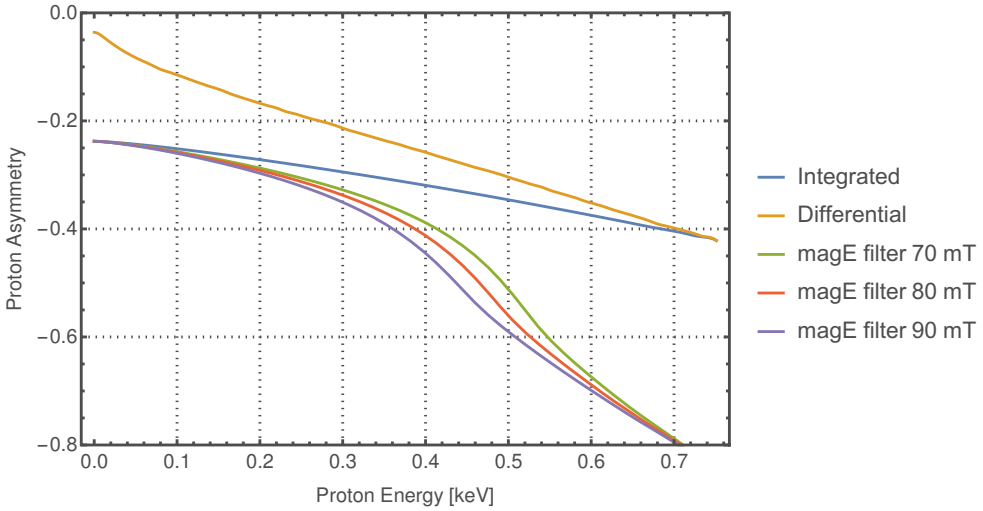

Figure 3.2.: The magnetic mirror effect in the retardation system changes the measured integral asymmetry depending on the magnetic field ratios by cutting into the angular and energy distributions. See the full calculation in section 10.2.

4. Current Status of Experiments on Neutron Decay

4.1. Other Experiments Used as Inputs

In order to interpret the measurements of the correlation coefficients one has to combine measurements of G_F and the neutron lifetime.

The neutron lifetime is an important independent measurement, that has to be used in order to extract a value for λ from the correlation coefficients. Unfortunately, there is a discrepancy in the measurements of the neutron lifetime. In the review of Wietfeldt and Greene [WG11] the status of the measurements in 2011 is presented. After that review there were three new papers [SPK+12; ABM+12; YDG+13] that presented new values or re-evaluated old data. Disappointingly, the discrepancy is still not resolved and a difference between beam and bottle experiments can be seen. However several new measurements are planed or currently running including new magnetic bottle measurements that do not have to correct for wall losses.

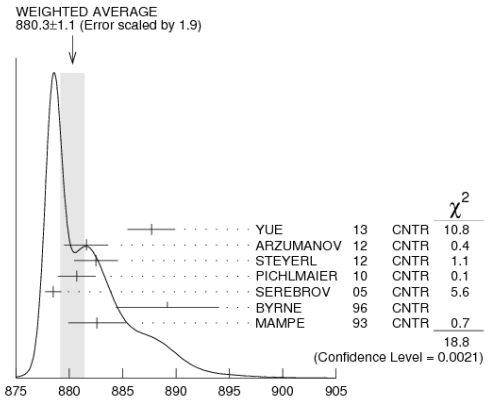

Figure 4.1.: Status of the neutron lifetime measurements used in the PDG average (from [pdg15])

Recently the Particle Data Group has shifted their value to (880.0 ± 1.1) s [pdg15]. This value is 5.4 s lower than the previous value that excluded the 2005 measurement of Serebrov et al. [SVK+05] due to the discrepancies with the older measurements. Since then the evidence for a shorter lifetime is increasing which is reflected in the revisited new average.

The value of G_F is best determined by measurements of the muon decay $\mu \rightarrow e + \overline{\nu_e} + \nu_\mu$. Here no hadronic form factors influence the measurement and therefore the observables have no dependence on λ. Recently this value was determined with below ppm precision [WTP+11].

Another set of experiments related to precision measurements in the weak interaction are so called superallowed fermi decays. They can be used to test the conserved vector current hypothesis (CVC) that is used to fix the value of $g_V = 1$. Up to now there is no reason to mistrust the CVC and therefore the previous used definition of λ. In 2009 a detailed review by Hardy

and Towner [HT09] combined the results of 20 decays and finds them in astonishing agreement with each other and the SM. In a combined analysis those measurements can also be used to constrain scalar and tensor interaction.

4.2. Previous Measurement of the Neutron Correlation Coefficients

The electron asymmetry was measured many times and the current PDG average of $-0.1184(10)$ (with scale factor 2.4) is deducted from five measurements [MMD+13; MPB+13; LSK+97; YKM+97; BDH+86]. The two more recent measurements differ from the earlier measurements, but agree with each other. This can be seen in the ideogram of the values (see Figure 4.2) from [pdg15]. The soon to be published result from Perkeo III based on the measurement and analysis by Mest [Mes11] and Saul [Sau16] might help to clear the confusion.

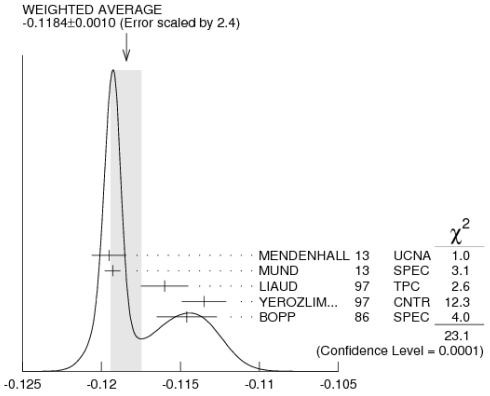

Figure 4.2.: Values of the measurements used to combine the PDG average of the electron asymmetry parameter A (from [pdg15])

PDG average of B is 0.9807 ± 0.0030 based on six measurements with the last two [SSD+07; KSB+05] beeing measured by Perkeo II.

The proton asymmetry has been measured by M. Schumann using the predecessor experiment Perkeo II. The setup of the experiment is described in detail in the dissertation of M. Schumann [Sch07]. This has been the first precision measurement of C detecting the electron and proton of the decay in coincidence [SKD+08]. The value of **C** was found to be -0.2377 ± 0.0026 and therefore compatible with the SM. The extracted value for λ fits the newer and therefore lower values obtained by UCNA [MPB+13] and the latest Perkeo II measurement [MMD+13], albeit the much bigger error. From the same data also an analysis of the neutrino asymmetry B has been performed [SSD+07].

The PDG average of a is -0.103 ± 0.004 and was derived from the three measurements [BDG+02; SDW78; GGV+68].

Additionally three of the many possible triple correlation coefficients have been measured to be compatible with the SM. The measurement of R and N, both correlations involving the polarization of the electrons, are found in [KBB+12]. The coefficent D from Equation 2.8 would be **T**-violating and was averaged by the PDG from several experiments [LHA+00; SBP+04; CCC+12] to be $(-1.2 \pm 2.0) \times 10^{-4}$ as expected by the SM.

Part II.

Experiment and Detector

5. Setup of the Experiment

This chapter will provide an overview of the experiment and name all necessary parts of the detection system. Those components will be discussed in more detail in the following sections and chapters.

To describe relative positions in the experiment, several coordinate systems are used. Because of the geographical layout of the ILL and our experiment, the upstream direction towards the reactor is called "Grenoble", while the downstream direction is called "Lyon" or just "beamstop side". Both names will be used in the further descriptions of the experiment. Also the directions left and right of the beam have geographical names. Left of the direction of flight of the neutrons is called "Vercors", named after the mountains south of the experiment. Right in the direction of flight is then called "Chartreuse", named after the mountains north of the ILL.

5.1. Overview

Since this is the third generation of PERKEO spectrometers and especially it is the third time that PERKEO III has been set up, there are several paper and dissertations describing the general setup. The general design of the PERKEO III spectrometer was first published in the dissertation of B. Märkisch [Mär06] and in the corresponding instrument paper [MAD+09]. A measurement of the beta-asymmetry in 2008/09 was described in detail in the dissertation of H. Mest [Mes11]. The analysis of this data was further improved by H. Saul whose dissertation is not yet published [Sau16]. A paper with the results is in preparation. Our general setup copies the successful setup of that measurement but uses a different and newly designed detector system as well as other improvements that will be discussed later.

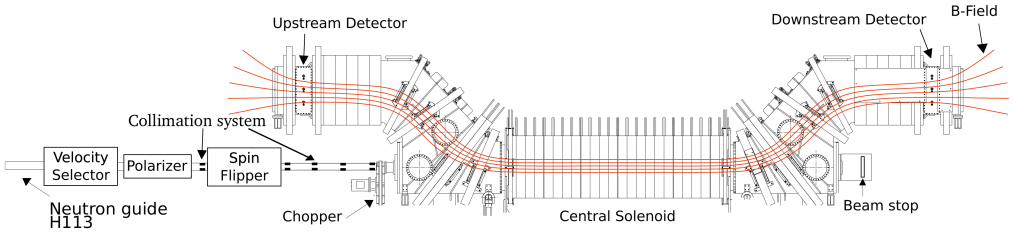

Figure 5.1.: General setup of the beamline and the spectromerter from [Mes11]. The reactor core and most of the 76 m long neutron guide are not shown. The magnetic field lines that separate the charged particles from the neutron beam are shown in red.

The neutrons are produced at the reactor core and are transported towards the experimental area using super mirror neutron guides. Before arriving in the decay volume of the spectrometer the neutrons have to be prepared. After a selection of the energy, the neutrons are polarized and the beam is shaped in transverse direction by a set of absorbing apertures. A spin flipper is used to reverse the direction of the spin in order to cancel certain corrections on the final

asymmetry. At the entrance of the spectrometer, the beam is separated into bunches by a rotating disk chopper.

These bunches of slow and polarized neutrons now traverse the central, homogeneous field region of the spectrometer depicted as the central solenoid in Figure 5.1. The charged decay products that are created in this region follow the magnetic field lines and are separated from the neutron beam by the s-shape of the magnetic field (see Figure 5.1). The two parts of the spectrometer that are separated from the beam are called detector vessels which itself consist of the transition part and a part that is again parallel to the beam. The detector system is installed in the horizontal part of the detector vessel.

After exiting the decay volume the neutrons are absorbed in a neutron backscatter suppressing beam stop that is located in a vacuum tube under the downstream detector.

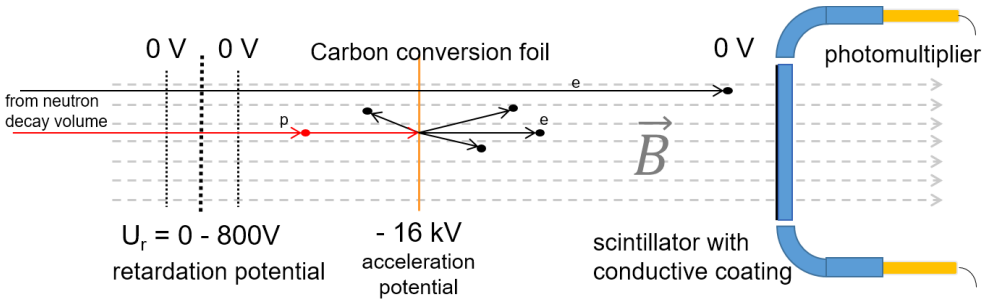

Figure 5.2.: Sketch of the combined proton and electron detector including all HV systems

The electrons and protons now have to be separated in the discussion since they have opposite charge and very different energies. As a reminder, the end point energy of the electron spectrum is about 780 keV where as the end point energy of the protons is about 0.75 keV. In order to guarantee a long enough mean free path of the low energetic protons, an ultra high vacuum is desired. After separation from the neutron beam, at the entrance of the upper detector vessel, the protons are accelerated towards a thin carbon foil held at a high negative electrostatic potential. The now higher energetic protons are able to ionize secondary electrons from the foil. The same electric potential is then used to accelerate these secondary electrons away from the foil and towards the electron detector. This setup is sketched in the center of Figure 5.2.

In the later discussion of the data those 'secondary electrons from the protons' are often just refereed to as protons or the proton-signal. Nevertheless one should not forget, that we never directly detect protons in the scintillator. Also almost all energy information of the proton is lost in the acceleration and conversion process. For a foil voltage of 15 kV the energy of the protons ranges from 15 keV to 15.8 keV. This small energy spread does not change the statistical distribution of the few secondary electrons on the detector[1].

Primary electrons from the neutron decay follow the same magnetic field-lines and also arrive at the entrance of the detector vessel. Since they have energies of up to 1000 times higher than the protons, most electrons can overcome the electrostatic barrier of the foil potential. The exact transmission function will be calculated also taking into account the magnetic field as a so called mag-E filter.

[1] Recent test measurements [Ber16] have shown that this assessment might be wrong and that the conversion efficiency as a function of the acceleration voltage can be quite steep. Nevertheless the results of the preparation measurements of the last **C** measurement suggested no such effect [Bra00; Kre04; Sch07]. A final analysis must certainly consider this effect.

Both the electrons and the protons from the neutron decay are now detected as electrons on the detector as seen in the test spectra in Figure 5.3. Hence a method to distinguish the contributions of both particles is needed. In the previous PERKEO II measurement, electrons and protons have been detected in coincidence and could be identified by the different drift times. Due to the increased decay volume and drift times a coincident detection in PERKEO III is difficult, but the larger dimensions of the spectrometer allow for a different approach to separate the protons from the combined proton and electron signal.

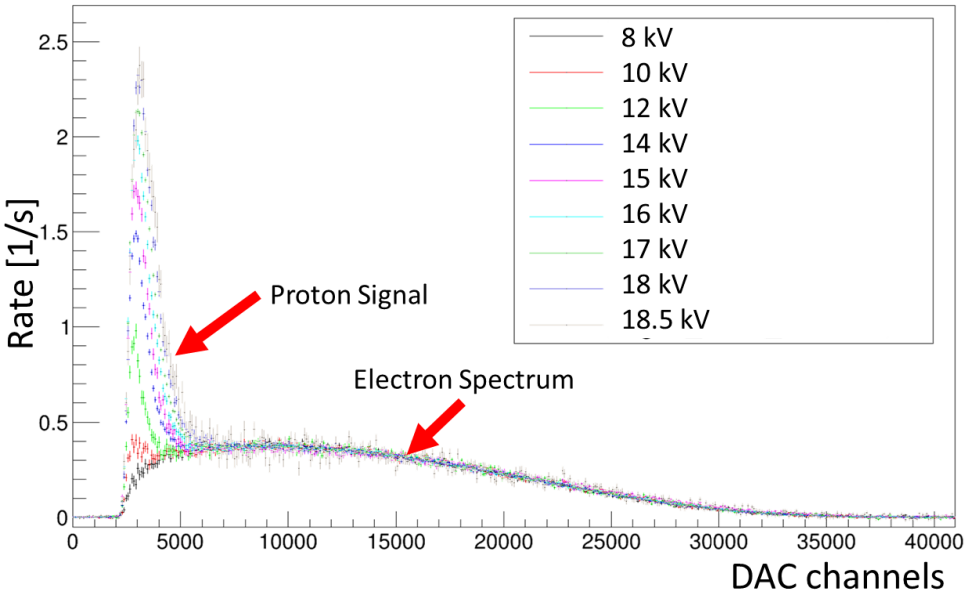

Figure 5.3.: With the conversion foil at high voltage a proton peak appears in the low energetic part of the spectrum. As discussed in the main text, the proton signal consists of the conversion electrons emitted from the thin carbon foil.

An additional electrostatic potential created by a positive voltage can be used to completely block the protons from reaching the conversion foil. Without this blocking-potential, electrons and the proton signal are both detected simultaneously on the detector. Applying a voltage above 850 V stops the protons and one can measure the pure electron signal which, in the context of the proton asymmetry, is only a background.

5.2. Beam Preparation

The ILL research center operates a nuclear reactor that provides neutron beams to about 40 experiments. Only a few experiments study the neutron itself, instead most experiments use the neutron for studies of soft and solid state matter, chemistry and biological systems.

A very detailed description of the reactor source and the beam line can be found in [Mes11]. The neutrons that are created in the 54 MW reactor core originate from nuclear fission processes and have very high energies (MeV). They quickly thermalize in the surrounding cooling water to an average speed of about 2200 m s^{-1}. For several reasons the neutrons used for this experiment need to be slower and therefore cooler. Most importantly the number of decays inside the

central volume is inversely proportional to their velocity. Additionally cold neutrons are easier to transport and to polarize. Scattering instruments also benefit from the accessible energy range of cold neutrons.

The neutrons guided towards the experiment therefore originate from a cold source made from liquid deuterium at 25 K [Age89]. Now an average velocity of 1000 m s^{-1} corresponding to a wavelength of ca. 4 Å is reached. It is common to describe the energy of the neutron in terms of their wavelength which relates to the velocity as shown in Equation 5.1.

$$\lambda \approx \frac{3956}{v} \mathrm{m\,s^{-1}\,\text{Å}} \tag{5.1}$$

The guide H113 transports the neutrons towards the experimental zone using super-mirror guides in evacuated beam tubes. These neutron mirrors are made from 80 layers of Nickel and Titanium coatings that are able to use total reflection of the neutrons with incident angel smaller than the critical angle. The guides' mirrors have a critical angle of twice the size of the classical pure Nickel coated guides ($m = 2$) [HKF$^+$02]. In order to block the direct sight on the reactor core and its γ radiation, the guide is sightly bent. A characterization of the H113 beam that feeds the PF1B experimental beam site can be found in [ADH$^+$06].

At the end of the 76 m long guide the beam has a cross section of $6 \times 20\,\mathrm{cm}^2$ and a divergence of 7 mrad. The beam then has to be prepared for the experiment by selecting an energy range, polarizing, shaping and chopping.

Beamline, velocity selector and polarizer are provided by the ILL and are shielded in the case-mate. The spinflipper, the apertures and the chopper belong to the experimental setup. The neutrons exit the vacuum of the guide and pass through the velocity selector and the polarizer in air, before entering the vacuum system of the beamline and spectrometer. Thin aluminium windows allow for a almost undisturbed transmission of the neutrons.

5.2.1. Velocity Selector

The velocity selector is realized as a rotating bladed axis with neutron absorbing blades that form helical channels. Those channels appear straight for those neutrons that travel with the right velocity with respect to the turning frequency of the axis.

The basic working principles of such velocity selectors was described in three papers [FWW89; WFW92; WFW95]. In section 3.1.2 of the dissertation of H. Mest [Mes11] the characteristics of the velocity selector of PF1B are described in detail.

The velocity selector absorbs about 80 % of the flux which produces huge amounts of γ radiation that has to be shielded for biological and background reasons.

For our measurement the selector was set to run at 25 470 rpm which corresponds to a neutron wavelength of $\lambda = 5$ Å with a width of $\Delta\lambda/\lambda \cong 10\,\%$.

5.2.2. Polarization

In order to observe the proton asymmetry **C** or other spin correlation coefficients the neutrons have to be spin-polarized. The polarization is defined using the numbers of the desired spin state $X^\uparrow$ and the admixture of the wrong spin state $X^\downarrow$:

$$\mathbf{P} = \frac{X^\uparrow - X^\downarrow}{X^\uparrow + X^\downarrow} \tag{5.2}$$

(a) Picture of the blades from [Dai]

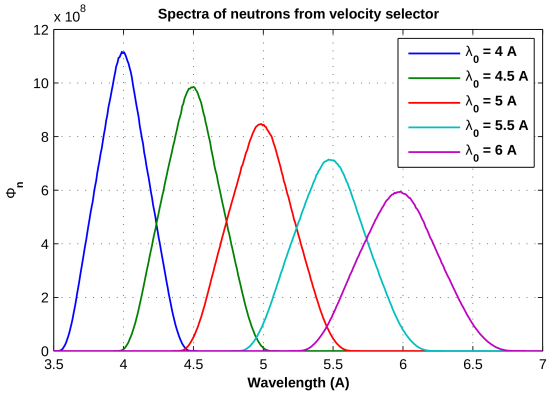

(b) Simulated velocity spectra after the selector from the dissertation of X. Wang [Wan13]

Figure 5.4.: The neutron velocity selector

This allows to write the spin state of the neutron beam (N) that is observed in the detectors as a function of the polarization ($\mathbf{P}$) and the pure spin states (n).

$$N^{\uparrow} = \frac{1}{2}\left((1+\mathbf{P})\, n^{\uparrow} + (1-\mathbf{P})\, n^{\downarrow}\right) \tag{5.3}$$

$$N^{\downarrow} = \frac{1}{2}\left((1-\mathbf{P})\, n^{\uparrow} + (1+\mathbf{P})\, n^{\downarrow}\right) \tag{5.4}$$

This causes the polarization to appear in every experimental asymmetry.

$$C_{\text{exp}} = \frac{N^{\uparrow} - N^{\downarrow}}{N^{\uparrow} + N^{\downarrow}} = \frac{n^{\uparrow} - n^{\downarrow}}{n^{\uparrow} + n^{\downarrow}} \times \mathbf{P} = C_{\text{theo}} \times \mathbf{P} \tag{5.5}$$

Within any experimental setup that does employ a non-perfect polarizer the contributions of the wrong spin state cause a dilution of the true asymmetry.

The measurement and analysis of the polarization is blinded in this analysis and has been performed by other parts of the collaboration. As a final step after the determination and correction of all other systematic effects, the polarization value will be un-blinded and the true value of $\mathbf{C}$ be revealed.

The polarizer used in this experiment was constructed following the principles discussed in [SS89]. A stack of super mirrors made with layers of magnetic material is placed inside a magnetic field. The potential seen by the neutrons in the material then differs for the two possible spin directions. This causes one spin direction to be reflected while the other component is transmitted through the layer stack and absorbed by the base layer of the stack of coatings.

A single polarizer can achieve a polarization of $\mathbf{P} \approx 98.5\,\%$ while transmitting about $25\,\%$ of the incoming neutrons. This again is a big source of background radiation, that is shielded like the radiation from the velocity selector by the housing of the casemate consisting of led and concrete.

5.2.3. Adiabatic Fast Passage Spin Flipper

In order to cancel certain systematic corrections on the asymmetry it is useful to be able to flip the spin state of the neutron beam. This allows to measure both particle counts, with and against

spin direction, in the same detector. This cancels the dependency of the detector functions from the denominator in the asymmetry.

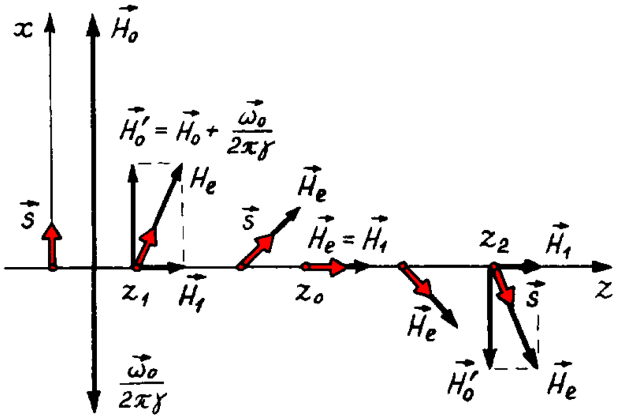

Figure 5.5.: Principle of operation of the spin flipper from [BLP+93]

Bazhenov et al. [BLP+93] described the type of spin flipper used in our experiment. The neutron travels trough a static magnetic gradient while beeing influenced by an additional radio frequency magnetic field. In the frame of the neutron this causes the spin to be rotated into the opposite direction. The original sketch of the working principle can be found in Figure 5.5.

The spin flipper is made from a (nonmagnetic) glass tube with the coil wrapped around. The tube is sealed with several layers of tape in order to keep the inside of the vacuum chamber dark so that the photo multiplier tubes (PMTs) can be used in the detector. To connect the flipper to the vacuum system of the beam line, the glass tube is glued to stainless steel flanges. This exposes parts of the glue to the vacuum system. Even good vacuum compatible glue still has significant outgassing. This caused us to add a spectrometer entrance window from aluminium foil after the chopper. Even though this window was not really tight and at several points even showed cracks, the differential pumping cross-section was small enough to shield the UHV in the spectrometer from the higher pressure in the beam line. The vacuum inside the beam line is needed to minimize neutron scattering and therefore also preserves the spin polarization.

Before entering the spectrometer the vertical aligned spin states have to be rotated slowly into a longitudinal polarization by a careful design of the magnetic field to couple the spin into the spectrometer.

5.2.4. Apertures

Distributed within the whole evacuated beamline a set of apertures with a quadratic opening of 6 cm width and height made from neutron absorbing Li^6F ceramics and lead were installed. Their positions are presented in Figure 5.6. They shape the beam in transverse direction and they have to be aligned precisely to each other. This was done without the possibility to measure the resulting neutron profile, since the beamline had to be installed in a reactor shutdown phase. Even the position of the spectrometer had to be determined only with laser and optical measurement systems and was aligned using wool-thread crosses in the flanges that were checked with the laser. The laser itself was placed using a lynette and a theodolite.

To verify the absolute positioning of the spectrometer with respect to the neutron beam, a copper foil was activated with running selector and chopper. The foils was placed inside the

setup with fully connected vacuum system including the beamline and only one window at the beamline entrance[2]. At the connection flange of the central part and the beamstop detector vessel the beam was found to be only 0.8 mm too low and 1.8 mm too close to the right side (in flight direction) of the spectrometer with respect to the center of the flange. An earlier measurement at the end of the first detector vessel and behind a Al-window and the whole polarization measurement setup also estimated a displacement of (2 ± 2) mm mm to low and (2 ± 2) mm to the right. Therefore we had no angular displacement and the horizontal displacement was well within our limits for the critical systematic corrections. Detector and HV-system could be adjusted to match the measured displacement.

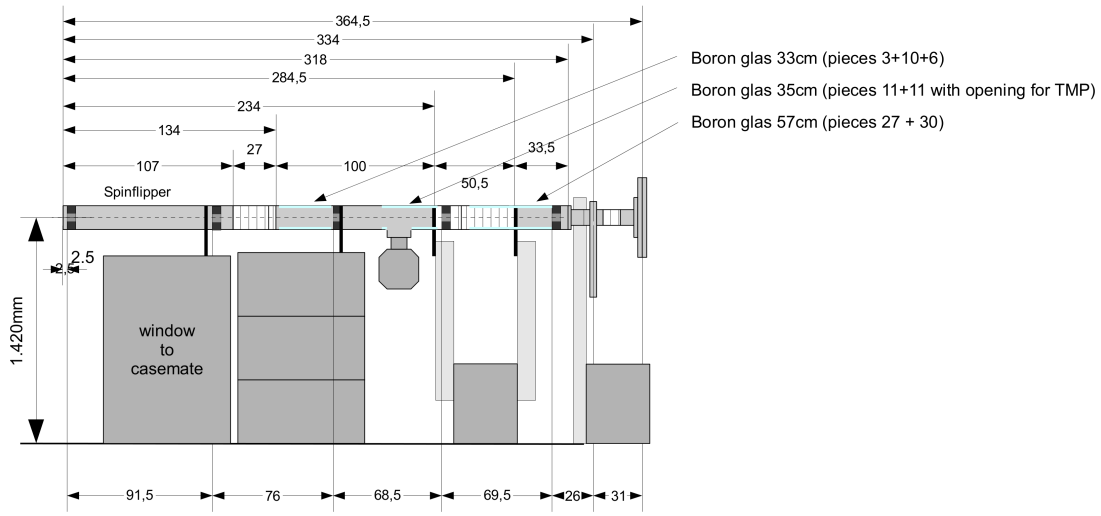

Figure 5.6.: Dimensions of the beamline setup. The positions of the apertures is indicated by the distances displayed under the sketch.

5.2.5. Chopper

The chopper is the same rotating disk chopper that was used in the previous measurement with PERKEO III. It was constructed by Werder [Wer09] and is described in detail in the dissertation of H. Mest [Mes11] who also discusses advantages and disadvantages of a pulsed measurement in detail including event rate considerations.

Its diameter is about 50 cm and the opening angle is 22.2° and it uses the same type of Li^6F ceramics to absorb the neutrons. The dimensions of the chopper are shown in Figure 5.7a. The rotation speed was fixed to 76 Hz and the measured frequency histogram is normal distributed with a mean of 76.004 Hz and a sigma of 0.010 Hz. Due to the high rotation speed, the chopper is guarded by a monitoring system that can stop the chopper if vibrations get too big. The vacuum characteristics of the chopper itself are also not compatible with the decay volume requirements. Therefore we placed the entrance window separating beamline and spectrometer vacuum in between chopper and spectrometer.

Measuring with the chopper has the main disadvantage, that one looses almost all neutrons except for the about 6 % that can pass in each rotation. But the advantages outweigh this disad-

[2]The window between chopper and spectrometer was not yet installed.

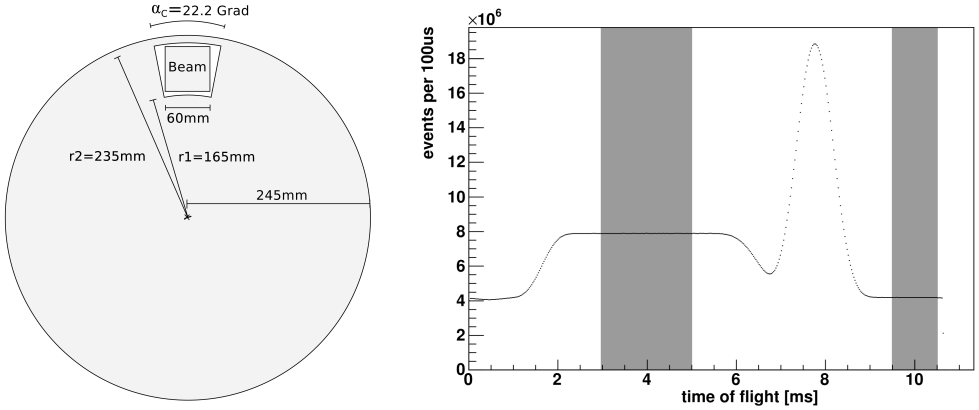

(a) (b)

Figure 5.7.: The left picture shows the dimensions of the chopper disk. In the right picture is an ideal ToF spectrum of both detectors combined of a chopped measurement taken from [Mes11]. The grey areas indicate the time cuts for the signal and the background window. The real situation in our measurement is different, since we observed a significant difference in count rate for both detectors.

vantage, since it allows (together with the slow speed of the neutrons and their small velocity distribution) to limit the analysis to those decay particles that decay within the homogeneous central volume by cutting on the ToF (Time of Flight) after the chopper opening. Additionally it is possible to measure the beam independent background continuously at the end of each chopper cycle after the neutrons are absorbed in the beam stop and before the chopper opens again to let the next pulse enter the spectrometer.

Figure 5.7b shows the combined signal rate of electrons and γ-radiation of both detectors for an ideal setup. After opening of the chopper, the pulse has to travel for about 1.5 ms before reaching a part of the spectrometer where some of the magnetic field lines can guide the particles to the detector. Once the pulse is fully contained in the central decay volume the count rate is constant. There the signal time window is placed in the later offline analysis. The neutron pulse then exits the homogeneous field region and the count rate (almost) decreases to the previous level. Around the 8 ms mark the neutron pulse is getting absorbed in the beam stop which creates lots of γ radiation that is also detected. After this beamstop peak, the signal is back to ambient background level. Here the time window for the background measurement is placed.

Weighted for the different measurement times, the spectra obtained in the two time windows can be subtracted to get the background free spectra of the decay products as shown in Figure 5.8.

5.2.6. Beamstop

The neutrons have to be stopped after they have traversed the central decay volume. When neutrons are stopped by a material with a high absorption, they create secondary radiation that can be detected in our detectors. Therefore the placement of the beam stop is crucial. The signal from the beamstop should not arrive simultaneously with the protons and neutrons from the decay volume. Placing the beamstop too far away shifts its signal into the time window in which the background is measured. These considerations lead to the placement of the beamstop close to the exit of the last part of PERKEO III and therefore under the downstream detector. An external

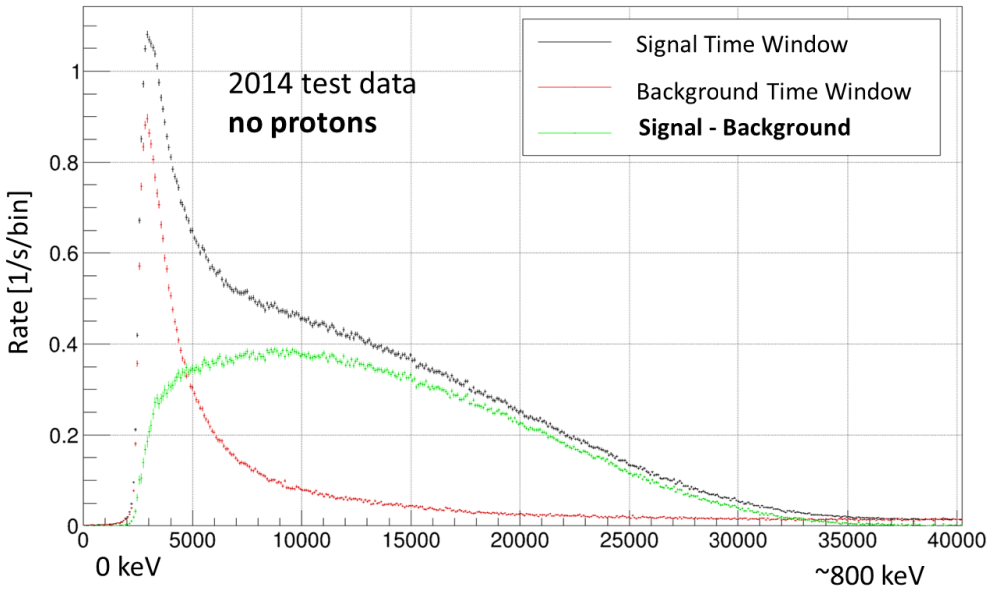

Figure 5.8.: Typical spectra from the signal and background time window. Subtracting the background reveals the electron spectrum.

beamstop is not feasible, since the neutrons then have to exit the vaccuum vessel. In this case a neutron transparent window is needed, for example made from aluminium.

In the tight space between the beamstop tube and the detector vessel a sufficient shielding for the fast neurons and gamma-radiation had to be installed.

An additional disadvantage of the window is the possibility of backscattering neutrons into the decay volume. These could again decay there and produce unfavourable non polarized background to the original measurement. The same problem can be caused by the beamstop itself, which can be suppressed by an advanced design.

The old beamstop of the previous measurement could not be used since it was made from strongly outgassing components. Hence a new beamstop had to be construced using a UHV suitable material. H. Saul [Sau16] designed the new beamstop using boron-carbide as the absorbing material in conjunction with a neutron backscattering suppressing structure in front made from di-met. The back plate is supported from the back and thus exposes no other material to the neutron beam. This prevents the activation of parts of the beamstop. The backscatter suppressing structure in the front is simply stuck together using a set of slits eliminating the need for metal screws or other mounting material that could be activated (see Figure 5.9).

Later while performing test measurements of proton signals there was the suspicion that some alpha-particles are emitted from the beamstop. Those could then drift towards the decay volume and produce fake proton signals. In order to stop those, a thin aluminium foil was placed in front of the back-plate of the beamstop.

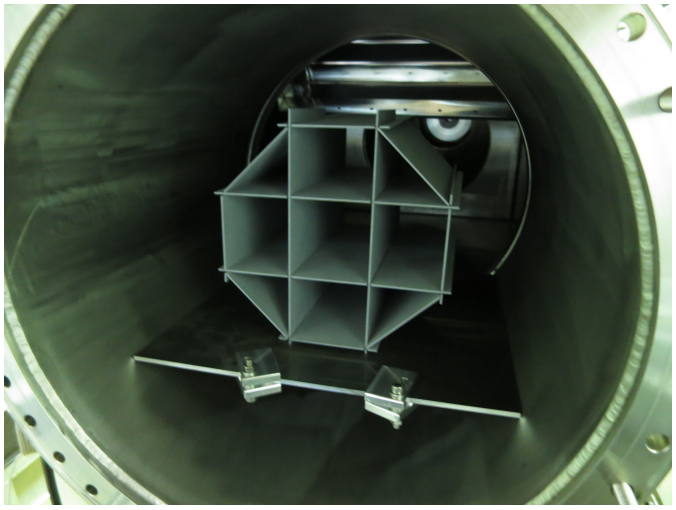

Figure 5.9.: A picture of the backscatter suppressing part of the beamstop inside PERKEO III

5.3. The PERKEO III Spectrometer

The PERKEO III spectrometer is the successor of PERKEO II which was used in the first determination of the proton asymmetry. Its mayor advantage is the increased decay volume with the usage of a chopper to precisely measure the time dependent background. This leads to a mayor increase in statistics while controlling the systematic effects [Mär06; MAD+09].

The spectrometer is build from water cooled square copper coils around a non-magnetic stainless steel vacuum chamber. In the standard configuration, the magnetic field strength is around 150 mT in the central part and 80 mT at the detectors. Overall size is about 8 m × 3 m × 3 m and it can be separated into three parts: the central solenoid and two symmetric detector vessels. When disassembled, the whole system including the water cooling circuit and the power supplies can be transported using a standard 40T-truck. Therefore the spectrometer can be installed at different neutron sources and in different laboratories in order to test and improve the system.

5.3.1. Magnetic Field

The general shape of the magnetic field is defined by the central volume and the s-shape to guide the particles to the detectors. Inside the central volume the magnetic field is around 150 mT strong with a small gradient to smaller values at both ends of the central volume. This corresponds to a gyration radius of about $r_{decay}^{max} = 2.6\,\text{cm}$ for electrons with the maximal energy and pitch angle. At the end of the central volume, the magnetic field lines are bend upwards and then parallel again in the detector vessel. In this transition region the field strength is reduced due to the coil arrangement. At the detector the field is configured to about 80 mT. Here the maximum radius of particles arriving at the detector is approximately $r_{det}^{max} = 3.7\,\text{cm}$.

In non-uniform magnetic fields, charged particles behave as described in chapter 3. The falling magnetic field strength causes the gyration radii to increase while the pitch angel decreases. This accelerates the drift movement away from the maximum. In the presence of an electric field other forces start to act on the charged particles. These include a $E \times B$ drift for perpendicular electric fields and the $R \times B$ effect for particles moving on curved field lines.

The charged particles are collected onto the field lines within the central volume. The separation from the neutron beam is done by a double curve that leaves the decay particle beam parallel shifted above the neutron beam. Since the particles trajectories are bent twice the corresponding $R \times B$ drift is compensated in first order. The adiabatic decrease of the magnetic field towards the detector focusses the particles forwards so they can impinge the detector at higher angles of incidence. This suppresses possible backscattering from the detector surfaces.

Additionally those particles that are emitted almost perpendicular to the magnetic field are only drifting very slowly towards the detectors, since the parallel component of their momentum is very small. Therefore the magnetic field slowly decreases to both sides from the central volume to start focussing and accelerating these particles.

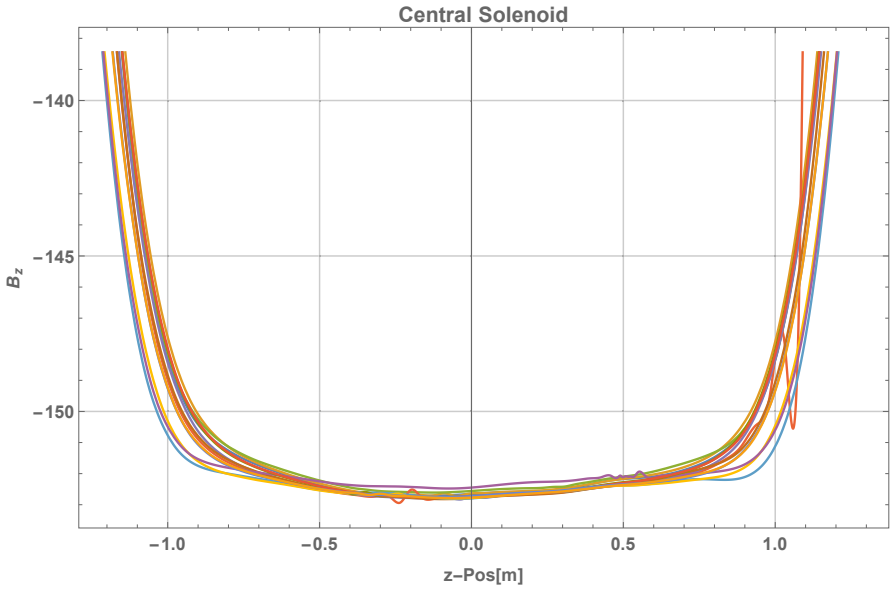

Figure 5.10.: Magnetic Field (B_z) in the central volume measured on 13 positions. In the read line a non-physical interpolation artefacts can be seen. Careful analysis of all curves shows that there are no local minima in the central volume.

Possible minima of magnetic field strength in the central volume could trap high pitch decay products created in the volume around the minimum. Theses could then, after an arbitrary time in the trap, be released from the trap by a collision with a rest-gas particle. Those will then not necessarily on the right detector according to their initial direction. These minima are avoided by providing a small but non-zero gradient in field strength.

These advantages outweigh the disadvantage of introducing a major systematic effect called the magnetic mirror effect. High pitch particles emitted towards the magnetic field maximum will be reflected by the rising magnetic field and will be detected on the wrong detector.

Compared to other measurements with PERKEO III the current detector is quite small (240 mm instead of 400 mm) and therefore edge effects and alignment problems are becoming more important. Additionally the transmission function of the retardation system as well as the field degrader strongly depend on the knowledge of the magnetic field in this regions. They operate in two very different combinations of the E and B fields. Inside the retardation plane the electric barrier acts only on the parallel component of the already boosted momentum and we are interested in the angular distribution and the energetic spectrum of the transmitted particles. In

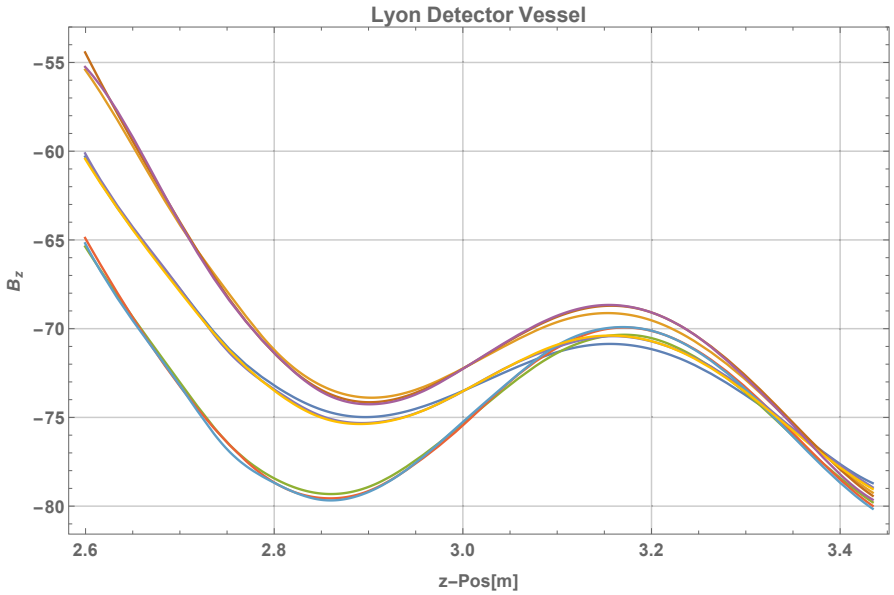

Figure 5.11.: Magnetic Field (B_z) in the downstream (Lyon) detector volume measured on 9 positions.

contrast to that, in the case of the field degrader the electric field is quite strong and especially between degrader and retardation not always parallel to the magnetic field lines. This causes secondary effects like drifts of the gyration center and therefore the electric field cannot be ignored when calculating the effect of the small foil as a baffle for the protons.

A simulation of the magnetic field is available from the design phase of the instrument, but it is known to not describe all features observed in the real magnetic field. Previously this model was sufficient, but in order to calculate our transmission functions a better model has to be constructed. Hence some of the effects of the simulations of the magnetic field have to be validated by measurements. Therefore we measured a map of the magnetic field in the central volume and in the horizontal parts of the detector vessels. Additionally some point measurements have been taken in the separation part especially with respect to the installed electrode system. The measurement collected all components of the field vector along several tracks through the vacuum chamber. In comparison to earlier maps of the magnetic field, we used a probe that was capable of measuring at full magnet strength to avoid the need for scaling. Even though this probe is temperature compensated we logged the probe temperature through all measurement days. The precise position along the main axis of the spectrometer was measured using a laser distance meter with a precision of below 1 mm. This should provide enough data to validate any simulation of the magnetic field. A plot of such a single measurement is presented in 5.13 showing the typical range for each component ($B_x \approx 0.5\,\mathrm{mT}$, $B_y \approx 5\,\mathrm{mT}$ and $B_z \approx 150\,\mathrm{mT}$). A new finite elements simulation of the whole magnetic field including shielding and measured coil shifts is currently prepared and validated by D. Moser [Mos15].

5.3.2. Vacuum Requirements

To study the influence of the vacuum quality on the decay protons U. Schmidt [Sch15] investigated interaction of the decay protons with the rest gas molecules. The simulation software `TRIM`

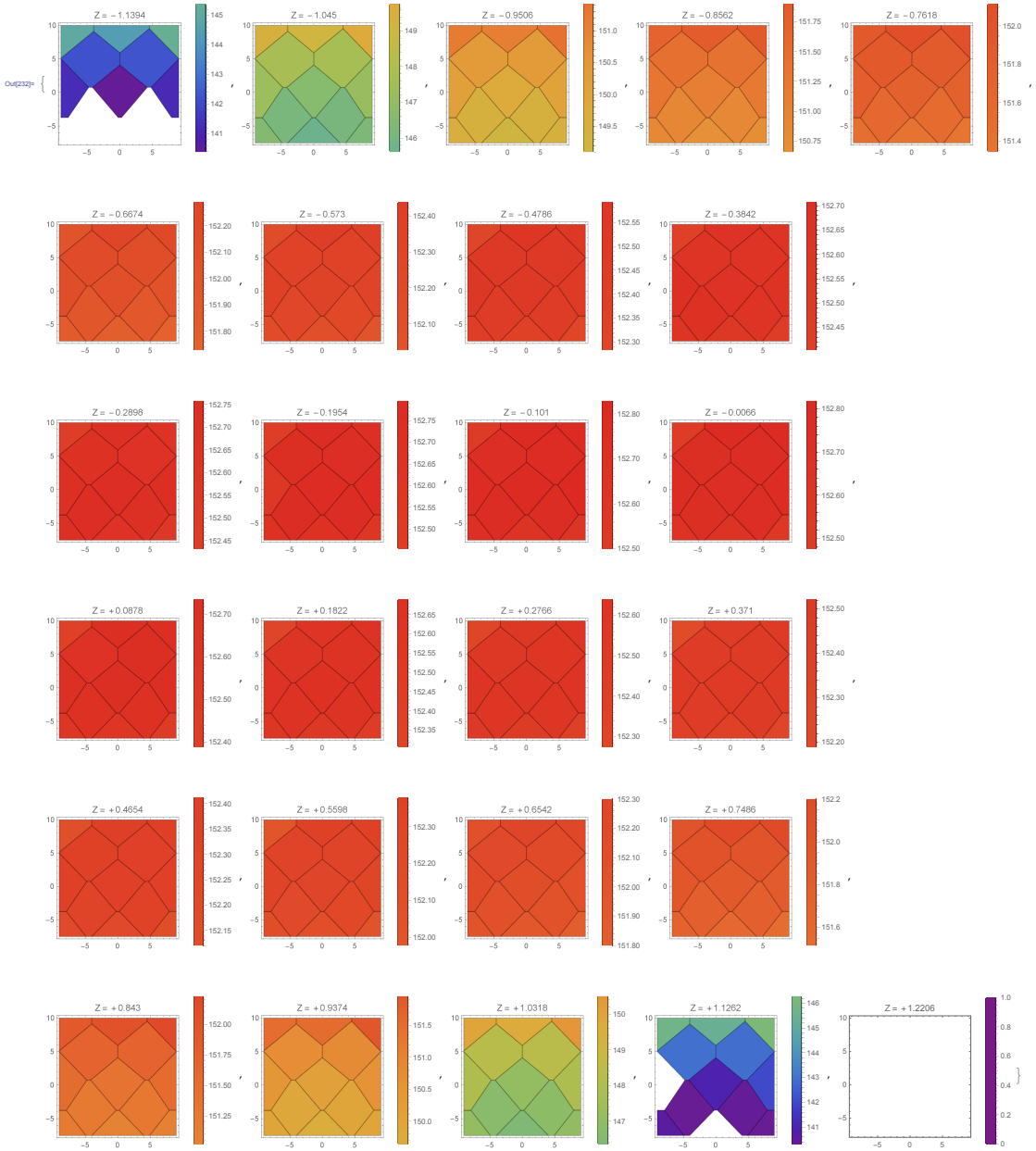

Figure 5.12.: Magnetic Field (B_z) in the central volume seen in the x-y-plane for several z cuts. Similar field maps also exist for the detector vessels. The color scale ranges from 140 mT to 155 mT (blue to red).

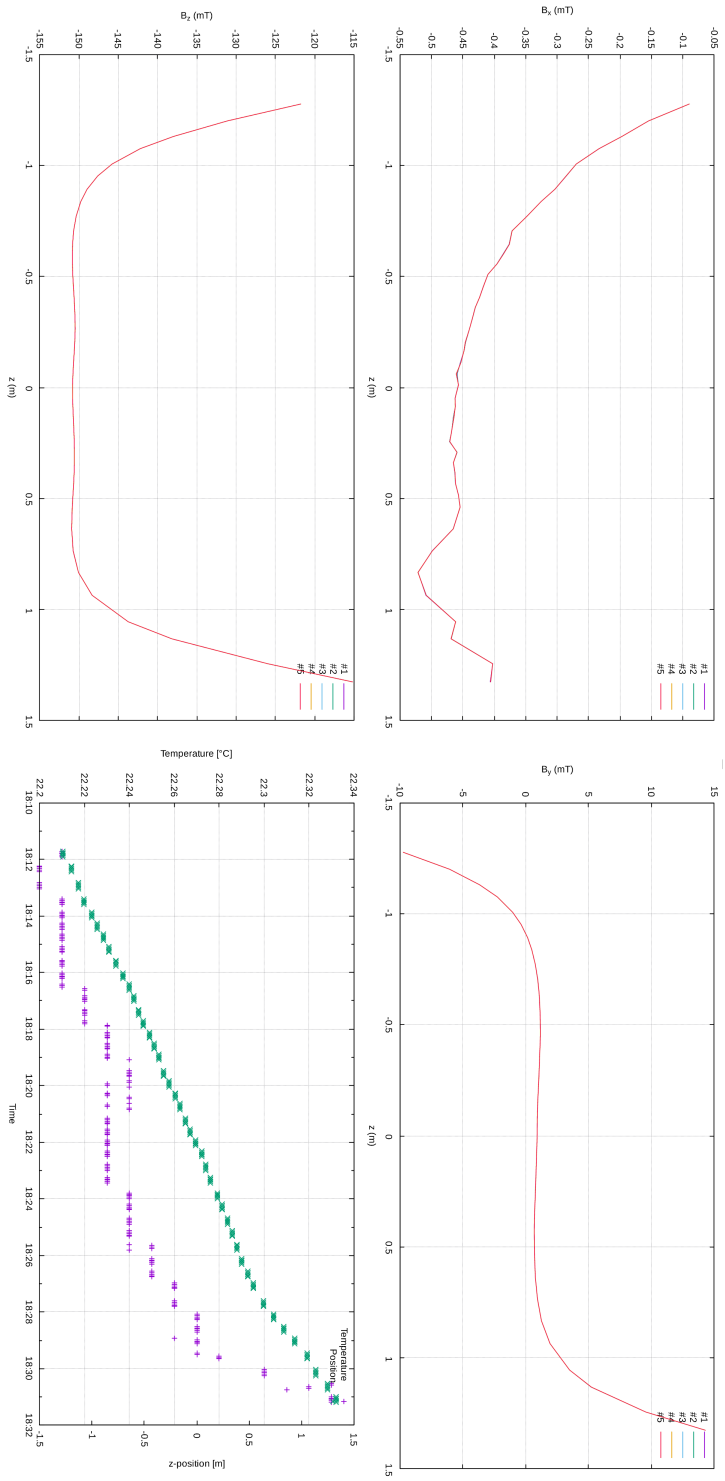

Figure 5.13.: Typical measurement of a single field profile. All three components of the magnetic field are recorded, as well as the temperature of the probe.

[ZZB10] that can calculate the stopping power of any ion in any material was used. The calculations assumes 1×10^{-6} mbar water vapour and 4 m flight path. In this regime the interaction probability rises linear with flight path length and linear with the pressure. Table 5.1 presents this results for four different proton energies. The values for ionization of the rest gas are just an upper limit.

proton energy	50 eV	100 eV	200 eV	500 eV
rel. transmission	0.999 68	0.999 79	0.999 93	0.999 96
rel. backscattering	2.20×10^{-4}	2.15×10^{-4}	7.50×10^{-5}	4.00×10^{-5}
rel. ionization	4.10×10^{-4}	3.30×10^{-4}	3.05×10^{-4}	3.30×10^{-4}

Table 5.1.: Interaction probability of protons in 1×10^{-6} mbar water vapor for a flight path of 4 m. Simulation by [Sch15] using `TRIM` [ZZB10]

Also the energy spectrum of the transmitted and backscattered protons can be extracted from the simulation. For a single energy of 200 eV this spectra are shown in Figure 5.14. For this measurement of the proton asymmetry, the achieved vacuum is sufficient, but for future measurements that aim at $<10 \times 10^{-3}$ accuracy, one should investigate those effects further and improve the vacuum.

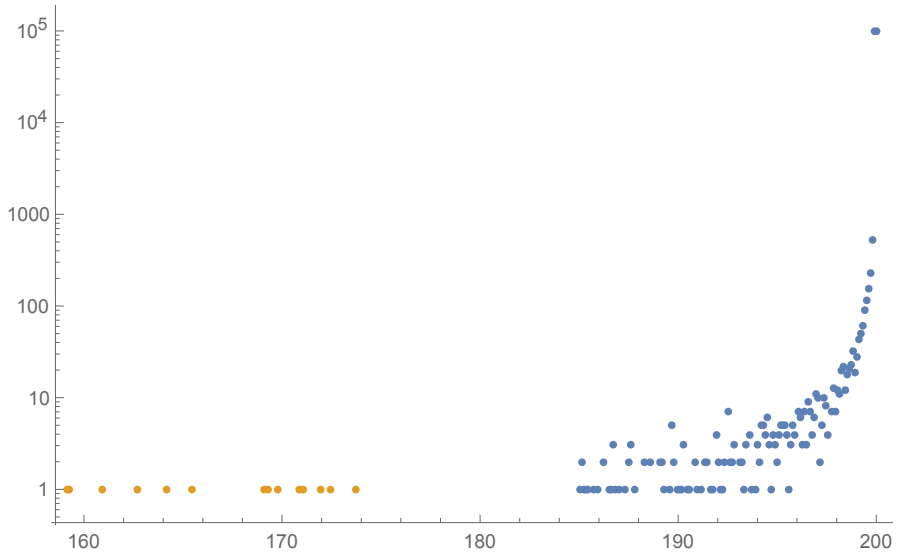

Figure 5.14.: Energy spectrum of 200 eV protons for transmission (in blue) and backscattering (in yellow) from the same simulation as in Table 5.1.

The real pressure during the last beamtime was monitored with two cold cathode gauges. One was attached downstream and the other at the upstream end of PERKEO III. A plot of the pressure can be found in Figure A.1 in Appendix A. We had to switch the cathodes off while measuring the proton asymmetry, but at the end of the beamtime we reached a final pressure of 5×10^{-7} mbar on one sensor and 7×10^{-7} mbar on the other.

5.3.3. Background and Shielding

Since many parts in the beam line absorb parts of the neutron beam, they produce radiation that has to be shielded. Especially the γ radiation could reach the detector and are detected as background. The parts that are exposed to the biggest flux of neutrons are the velocity selector and the polarizer. Those are enclosed by the casematte and are therefore especially well shielded. The further beamline with the apertures was covered in a shielding made from lead and boron enriched plastic. The strength of the shielding was constrained by the requirements of the radio-protection service to act as a biological shielding.

An additional source of background is the beamstop. The shielding towards the downstream detector is especially difficult because they are close to each other and there is not much space in between the beamstop tube and the detector vessel. Here a table was constructed and packed with lead and plastic.

Other background sources are the neighbouring experiments in the guide hall. This background cannot be controlled, but is measured continuously in each chopper cycle.

5.3.4. Changes to the Spectrometer

Several changes to the spectrometer were necessary to be able to detect protons. In order to place the detector inside the spectrometer, the original flange with a diameter of about 500 mm at the back of the detector vessel had to be replaced. A new rectangular vacuum flange was installed in its place. This new opening is now 540 mm × 470 mm big and allows the installation of the whole detector system. Compared to the inner size of the detector vessel of 596 mm × 526 mm this was the maximum opening that could be manufactured into the backplate of the vacuum vessel.

The goal of achieving an Ultra High Vacuum inside the spectrometer lead us to the removal of all viton seals. All parts of the spectrometer, with the exception of the chopper and the beamstop flange, are now connected with metal seals. The big parts are joined by an aluminium seal that was prepared during construction but was now used for the first time. A similar seal was used at the new detector flange which itself was equipped with a standard CF-250 flange. All additional accessory flanges of the spectrometer are CF-250 flanges with copper seals.

This allowed us to equip the both detector parts of the spectrometer with heating bands in order to be able to speed up the outgassing and pumping of the vacuum. On the central solenoid heating bands were already installed in the initial assembly of the magnet. Additionally, for the first time a cryogenic vacuum pump was connected to Perkeo III.

Since the additional transversal rectangular chambers of the spectrometer were not needed for the new detector we replaced them with simple flanges. For the first time all accessory flanges were equipped with either turbo molecular vacuum pumps, vacuum gauges or electrical feedthroughs.

5.4. High Voltage (HV) Systems

The high voltage system was a major source of uncertainty in the last measurement of B and C. Some sources of instability were suspected to originate in the high voltage parts or in converted ions from the rest-gas. Since the design of Perkeo II placed the detectors very close to the decay volume, the HV-system had to be very compact. Therefore the foil was directly suspended from a holder that was set to a high potential. The electron detector with its aluminium surface was placed quite close to the foil as one of the grounding electrodes. On the other side of the foil, the close proximity of the decay volume made it necessary to reduce the electrical field in a

controlled way to zero in order to not disturb the initial angular distribution of the protons. A set of thin wire grids was therefore installed to reduce the residual electric field in the decay volume.

The much bigger detector vessels of PERKEO III allowed a completely new design of the system. The high electric potential of the foil is now raised in a controlled manner over a distance of about 25 cm by a series of electrodes. This design is much larger but was thought to be more stable. Additionally the free space in the transition part of the spectrometer allowed the installation of the retardation electrode system. This is a new concept since the previous measurement of **C** could not separate the effects of the protons and electrons that easily. The retardation system allows to measure with partially blocked protons to study the energy dependence of the proton asymmetry.

5.4.1. Conversion Foil Supporting High Voltage System

The high voltage system was designed by P. Lennert from the Physikalisches Institut. [Len14] The main idea was to construct a smooth and controlled gradient using a set of electrodes on intermediate voltages. This system is called "field degrader" or just short "degrader" and I will continue to use this name to clearly distinguish it from the (retardation-) electrode system.

Design gradient is around $1\,\mathrm{kV\,cm^{-1}}$ which is realized by a symmetric setup of 15 electrodes on each side of the central foil holding electrode. Considering that the HV has to be fed into the vacuum chamber, the degrader is sourced by only one voltage. A series of HV-resistors, configured as voltage dividers, connect the electrodes to the central foil voltage. The whole system is held together by four ceramic rods in each corner. The electrodes are isolated against each other by teflon disks resting on those rods. Isolation to the surrounding vacuum vessel is achieved using copper plated mylar foils. Those are connected so that all potential differences appear only via the mylar layer and not via the vacuum. This should eliminate flash over arcs or field emissions in the tight spaces.

The inner opening of the degrader is 33 cm wide and high. On the central electrode the foil is installed on a plate with a hole depending on the foil size.

The system was tested on air and in vacuum to be stable up to at least 35 kV. A further test was not possible since this was the maximum voltage of our power supplies. Unfortunately the system was less stable when it was used in the final configuration. Turning on the magnetic field destabilized both degraders and the many voltage drops with tripping current protection forced us to reduce the voltages. Additionally we saw a high rate of low energetic background on both detectors. This could be caused by low energetic electrons from field emission from sharp edges or corners, or even direct light from flashes or small discharges.

In the time between the beam times several improvements to the degrader had to be implemented. While inspecting the system we found that one isolator had signs of a flash over arc. With the goal to increase the distance for surface currents on the isolators, they were all dismantled and had several approximately 1 mm deep and wide trenches cut into their surface. At the same time they were cleaned thoroughly to decrease the outgassing in order to increase the vacuum compatibility.

One suspected source of the low energetic background signal was field emissions from sharp edges at high voltage. This prompted us to rework and polish all the edges of the electrodes on the inside of the field degrader. Due to time constraints this could not be completely finished for one degrader.

Another suspicion was the possibility of trapped particles that travel on the magnetic field lines and are constrained by the electric field of both field degraders. The temporary installation of a very coarse and irregular grid in the central volume stabilized the degraders so much, that

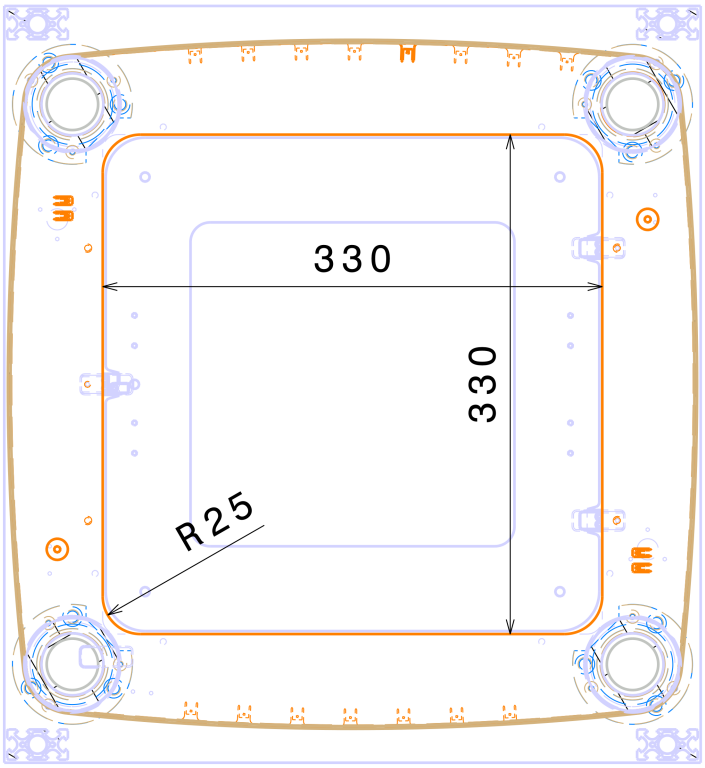

Figure 5.15.: Cross-section of the middle electrode of the degrader system

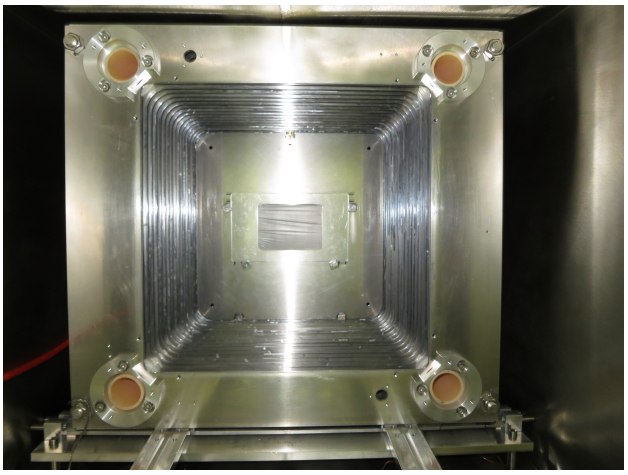

(a) Degrader with small foil as seen from the detector

(b) Voltage divider and Isolator

Figure 5.16.: The left picture shows the degrader system with a small foil installed. The different electrodes used to ramp up the potential can be seen on the inside of the system. The right picture shows a close up of the already improved isolating rings and the resistors of the voltage divider.

a simultaneous operation at voltages above 15 kV with magnetic field was possible. This result started the design and construction of two very thin regular one dimensional grids that were installed in each retardation electrode system (see subsection 5.4.3).

To prevent low energetic particle emissions from one of the outer electrodes, a small additional baffle was mounted at the exit of the field degrader. The very low energetic particles have very small gyration radii and could be absorbed by this baffle.

5.4.2. Conversion Foil

The conversion foil is an integral part of the detection system. Unfortunately it was also the part of the detector that caused the most problems and its size might limit the final result of this measurement.

Earlier designs of proton conversion foils systems used by J. Reich ([Rei99]), M. Kreuz ([Kre04]) and M. Schumann ([Sch07]) optimized the thickness to about 20 $\mu g\,cm^{-2}$. This foil was coated with MgO.

In the PERKEO II measurement of **C** the foil had a size of 120 mm × 90 mm. We originally planed to use a foil size of 220 mm × 220 mm, but production and transport problems forced us to measure with much smaller foils. Some tests were done with the same foil holders as the PERKEO II measurement and the final measurement even with a smaller foil of size 110 mm × 80 mm with an edge radius of 5 mm. Additionally it was not possible to produce coated foils, since they were extremely fragile. Therefore we only used bare carbon foils.

The foil only sticks to the aluminium holder and the edge of the foil can be crumpled or partially peel off and point into the electric gradient. This might release electrons from the foil in the form of field emissions. Hence we countered the foil with an empty foil holder. Additionally all edges of the foil holding system were rounded off and polished.

5.4.3. Retardation Electrodes

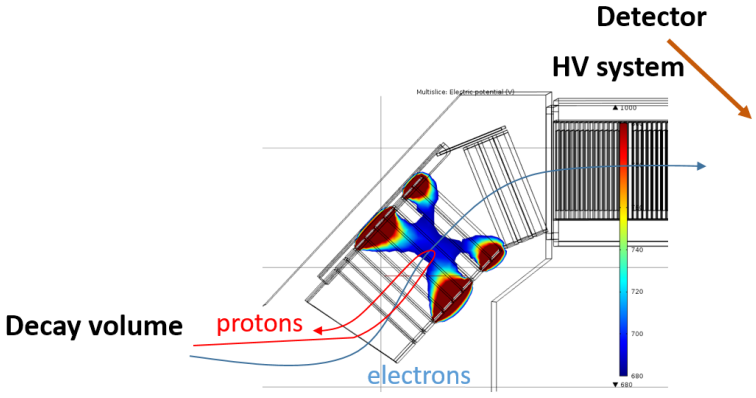

Figure 5.17.: Position and working principle of the retardation electrode system [Klo15]

Between the central decay volume and the detector vessel a system of retardation electrodes is installed. This system was designed by M. Klopf of our Collaboration and consists of 12 rectangular Electrodes that can be controlled individually with voltages up to 2 kV. Each electrode has its own vacuum feedthrough as well as a sensing line. Two electrodes are split in order to be able

to create a orthogonal electric field to empty possible particle traps with $E \times B$ drifts. But those had no influence on our measured background rates. The electrostatic field around the center electrode is used to block the protons on their way to the detector as depicted in Figure 5.17.

By selecting the appropriate voltages on the other electrodes the potential barrier can be shaped. The optimal configurations were determined by simulations. It had to be ensured that no residual electric field enters the decay volume, because this would disturb the angular distributions of the protons. On the other side of the retardation system, the last electrodes interact with the high voltage from the field degrader. The last electrode is therefore grounded.

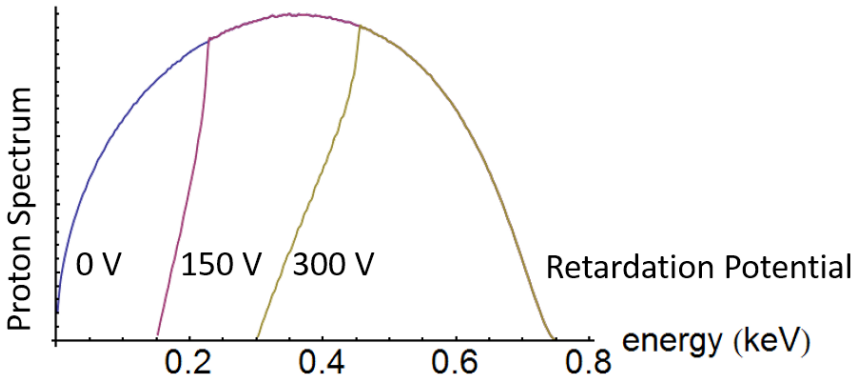

Figure 5.18.: Simulated spectra of the protons after a retardation system.

Inside the electrode with the highest voltage, in the retardation plane, a grid made of 25 µm thick aluminium wires with a pitch of 5 mm was installed. This grid makes the field in the retardation plane more homogeneous and allows a complete blocking of protons across the plane with lower voltages applied to the central electrode.

The combined effect of the magnetic and the electrostatic field has to be simulated with a finite element simulation in order to be able to describe the effect on the protons. A full blocking or a free passage of the protons does not require this calculations, which allows a basic measurement of the proton asymmetry without too many Monte Carlo corrections. A first simple calculation of such transmission functions can be found in Figure 5.18.

5.5. The Electron Detector

Since the construction of the electron detector was an important part of this thesis, it will be described in detail in the following chapter 6. Primary components of the detector are the plastic scintillator, the light guides and eight photo-multiplying tubes (PMTs).

The detector is grounded by a transparent conductive coating and serves as a reference point for the acceleration voltage. Electrons and γ particles are stopped in the scintillator where they emit light of a specific spectrum. This light is then coupled into the light guides that transport the scintillation light to the PMTs. The photons enter the PMT via a glass window and knock out electrons out of the cathode. Inside the PMTs a cascade of high voltage electrodes is then used to multiply the electrons. The resulting charge is proportional to the impinging light intensity.

The housing of the PMTs is water cooled with a UHV tight water system. Each detector needs eight SHV and eight BNC feedthroughs as well as the water cooling feedthroughs. Additionally on each detector there were two PT-100 temperature resistors connected.

5.6. Event Based Data Acquisition

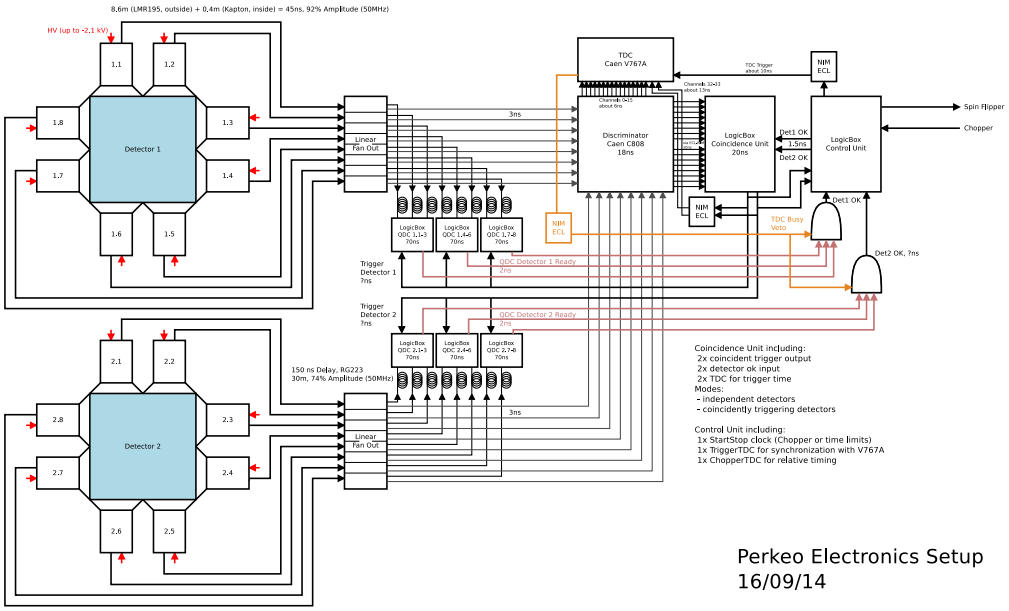

Figure 5.19.: The configuration of the electronics of the experiment [Roi15]

The charge signals from the PMTs arrive in the electronics cabinet and are split using a linear fan out. One part of the signal is then fed into the constant fraction discriminator that triggers the digital and analogue electronics that handle the signal. This trigger signal of all PMTs is fed into the FPGA (Field Programmable Gate Array) system that implements the coincidence unit. If a coincident signal on two or more sides of the scintillator (each at least one PMT) is detected, a gate and veto signal are generated. Those activate the integration of all QDCs (charge to digital converter) of both detectors. Then the analogue signal arrives after being held in the delay cables. Those QDCs are read out by the FPGA system and the data is send to the measurement PC via an optical link. Usually two samples per PMT are stored, one just before the integration and another as the true measurement value. This second sample can be used alone as it was done in the last beamtime. One can also work with the difference of those in order to avoid the baseline in the analysis. This system works well into the 10s of kHz event rates.

The ADC cards have been developed for the previous PERKEO III measurement and are described by H. Mest [Mes11]. The electronics system of this measurement will be described in more detail by my colleague Ch. Roick in his thesis [Roi17] as he developed the final configuration of the electronics as well as the readout and measurement program. It is programmed in C++ and is used to control and configure the whole readout electronics. Several counters provide the timing information in coarse or fine resolution of up to 0.8 ns.

Data is stored in cycles that each collect the data of 700 chopper turns and last for approximately 9.5 s. Eight cycles are combined to build a spin-flipper pattern (01101001 or 10010110) and several (usually 1 to 4) flipper pattern are grouped together in a file. At the beginning and the end of a file a pedestal measurement is performed. At a first step of every cycle the voltages of the retardation electrodes are measured.

Most files are files with a fixed configuration of the retardaton electrodes but in order to observe the effects of the ramping the electrodes this is done while data taking. Therefore there

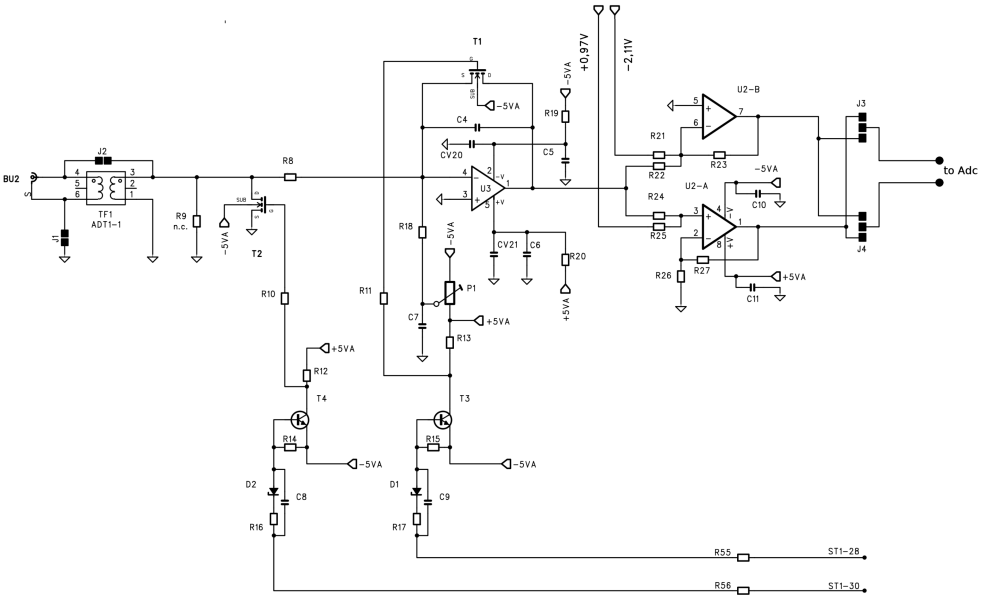

Figure 5.20.: Schematic of the QDC card from [Mes11]

are files with changing electrode configurations. Those are called ramping files. Since the power supplies of the electrodes are quite fast, some cycles in these files are already valid cycles of the target voltage. These valid cycles are always at the end of a flipper pattern, so using the ramping files could introduce a bias. If those ramping files are skipped this will be called `'NO_RAMPING'`.

Each data file has the format of a "root TFile" compatible with the CERN ROOT data analysis program. It was generated with a stable version of root5 [BR97]. Data is stored in different trees, the most important one being the data tree that contains all information for the events (see Listing 5.1).

Important information of each event are the values from the ADCs for both samples, the information which detector triggered first, the trigger time of the event and the TDC data for all the PMTs.

Similar trees exist for the chopper monitoring, the cycle information, the pedestal measurements and the measured values of the retardation system.

In the detailed analysis of the data from the 2008/09 beam time ([Mes11]) some rate dependent effects were found in the ADC cards. Those will be published in [Sau16] and should not play any role at the precision of this proton measurement.

During the whole measurement campaign we collected 1015 GB of data (60 % systematic tests and 40 % data for the analysis). Additionally 50 GB of detector calibration data were recorded.

```
*******************************************************************************
*Tree    :dataTree  : Data                                                    *
*******************************************************************************
*Br    0 :Cycle             : Cycle/i                                         *
*Br    1 :PMT               : PMT[16][2]/S                                    *
*Br    2 :DetSum            : DetSum/I                                        *
*Br    3 :Detector          : Detector/b                                      *
*Br    4 :CoinTime          : CoinTime[2]/i                                   *
*Br    5 :TriggerTime       : TriggerTime/i                                   *
*Br    6 :DeltaCoinTime     : DeltaCoinTime/i                                 *
*Br    7 :DeltaTriggerTime  : DeltaTriggerTime/i                              *
*Br    8 :TDC               : TDC[72]/I                                       *
*Br    9 :ChopperTime       : ChopperTime/i                                   *
*Br   10 :SpinFlip          : SpinFlip/O                                      *
*Br   11 :EventNumber       : EventNumber/i                                   *
*Br   12 :TypeGuess         : TypeGuess/b                                     *
*Br   13 :RelatedEventGuess : RelatedEventGuess/i                             *
*.............................................................................*
```

Listing 5.1: Available data branches for each entry in the `dataTree`

6. Design and Construction of the Electron Detector

The design of the detector is based on the earlier detectors used in the different PERKEO experiments but almost all components have been improved.

The scintillator is now the more temperature resistant type BC-440 [Sai14] and coated with a transparent conductive coating that was specifically matched to maximize the internal reflectivity. For the first time, we manufactured the light guides using a five-axis milling process in order to reduce manufacturing variability. Additionally the shape of the light guides has been simulated extensively to equalize the losses for each sub-strip. The scintillator is read out from all four sides to increase the light output and therefore improve the low energy response of the detector. When using a 4-side readout, one has to pay special attention to not disturb the homogeneity of the 2D-response of the detector and leave a gap in-between the scintillator and the light guide. Inside the vacuum vessel there is enough space for a planar detector with two sided readout, but for a four-sided readout the light guides had to be bend to be able to place everything inside. This all together gives hard constraints on the design of the detector support system. On the detector assembly the PMTs are supported in a steel housing that can be water-cooled in order to stabilize the gain against the daily drifts due to the high spread in temperatures in the guide hall. To convert the photons, this detector uses the R5504 and R5924 PMTs produced by Hamamatsu. The PMTs have production years stretching from 1999 to 2015 and show different stages of ageing. Therefore the relative calibration was challenging.

The construction of the detector had three major steps. First a suitable coating had to be found that enables the four-side readout, then the bent light guides had to be simulated and designed and finally a support structure had to be designed including the PMT cooling.

6.1. Comparing the Current Detector to the Previous PERKEO II Detector

The detector used in the last measurement of the proton asymmetry was also based on a scintillator. To provide a ground electrode for the acceleration voltage, the front of the scintillator was coated with about 50 nm of aluminium. Aluminium reduces the reflectivity of the scintillator-vacuum interface so much, that a scintillator readout from the edges is no longer feasible. Therefore the six PMTs were placed on the back side of the scintillator. The thin (5 mm) scintillator does not distribute the light good enough leading to a insufficient homogeneity of the detector. Adding a block of 3 cm thick plexiglas between the scintillator and the PMTs was one of the improvements that allowed the final measurement. Additionally the exposed plexiglas between the PMTs was painted with reflective paint. The size of the detector was $(13 \times 19)\,\mathrm{cm}^2$ with a slightly smaller conversion foil size [Kre04; Sch07].

The size of the electron/proton beam in PERKEO III and the need for a good low energy performance of the detector determined the main design criteria for the new combined electron proton detector. Also the new detector should be designed to ft as a detector for future measurements at the new experiment PERC. Readout should be switched to a edge readout of the scintillator

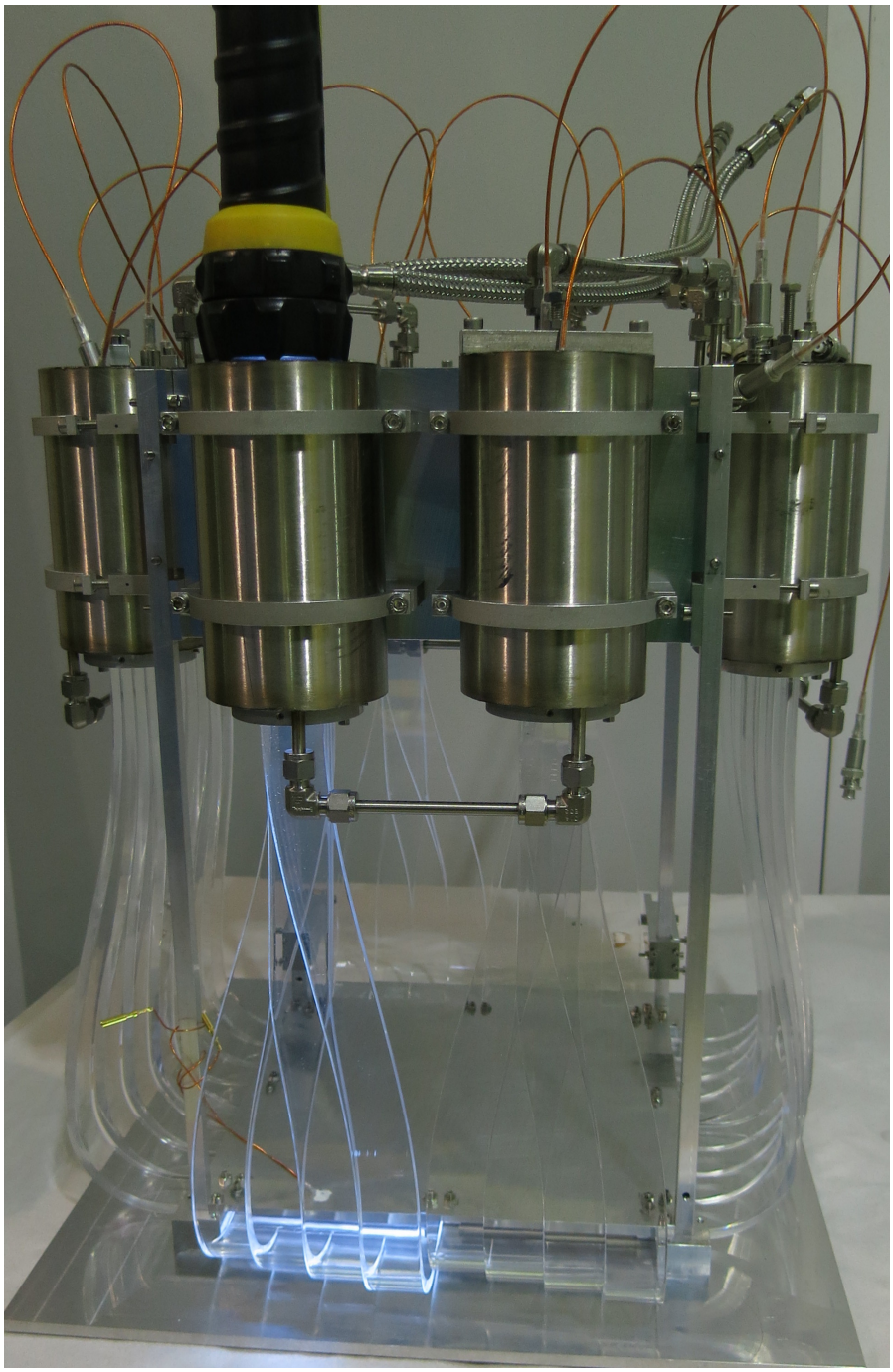

Figure 6.1.: Picture of the final detector assembly including water cooling

in order to increase the spacial homogeneity of the detector. Additionally extracting the light from the scintillator on all four sides can increase the amount of light detected in the PMTs and therefore improve the low energy response. This required us to find a new, more suitable electrically conductive coating. The size of the detector was planned to use most of the available space in the detector vessel while allowing enough room to shift its position by a few cm in order to account for shifts of the beams of decay particles.

6.2. Four-Side Readout

The critical angle of the total reflection (defined against the normal of the contact surface) is calculated from the refractive index of the material as

$$\sin(\theta_{crit}) = 1/n = 1/1.59 \quad \text{therefore} \quad \theta_{crit} \approx 39° \tag{6.1}$$

In order to increase the light-output, the scintillator is read out from all four sides. One has to pay special attention to homogenize the 2D-response. If the light guides are just directly attached to the scintillator the probability of the light to arrive in any of the PMTs strongly depends on the position. Especially off center positions loose much of their light as seen in the example in Figure 6.2. In this example the light that is emitted in the bottom right direction leaving the system via the side of the right light-guide instead of the bottom side of the scintillator. In a two-sided readout this light would reflect and exit the scintillator through the bottom light-guide.

In a two-side readout most of the lost angles would reflect at the scintillator-vacuum interface and be detected on a perpendicular side. This problem of spacial inhomogeneity can be solved by introducing a gap between the scintillator and the light guides.

In such a configuration every ray impinging steeper than the critical angle can pass the boundary. Rays with grazing incident are reflected and arrive at the perpendicular boundary with an angle of incidence of $90° - \theta_{old}$. So almost grazing incidence with 89° impinges the perpendicular surface with an angle of 1° and can thus leave the scintillator on that surface. For emission angle between 39° to 51° the ray will never leave the scintillator and reflect until absorbed. So all light, except for the infinitely reflecting rays, can leave the scintillator and the amount of exiting light does not depend on the position of emission.

The light propagation was simulated using a self developed ray-tracing python program in a model consisting of a 240 mm × 240 mm scintillator with refractive index of $n_{scinit} = 1.59$ and two rectangular light guides at each side with a refractive index of $n_{LG} = 1.49$. For a classical arrangement of light guides that are coupled with optical grease, a direct scintillator light guide interface is assumed. In the simulations including the gap its width was set to 1 mm. Crosstalk between the light guides is suppressed by introducing a very small gap[1] between the light guides.

The origin of the coordinate system is placed in the middle of the scintillator. A randomly or systematically created ray is propagated through the medium until it intersects with a boundary shape, where the formulas from Snell's law are applied. Additional random absorption at each interface can be included, but its probability was set to zero for the presented results. The intensities of reflection and transmission from the Fresnel equations are not yet implemented, but can be added by ray splitting with the probability as a weight factor[2]. The transmission through the two interfaces and the gap for angles below the critical angle averages to 90 % and only deviates near the critical angle (compare Figure 6.4).

[1] Gap has to be bigger than the intersection search radius and the step size.
[2] A first implementation is not yet thoroughly tested, but results seem promising and will be improved.

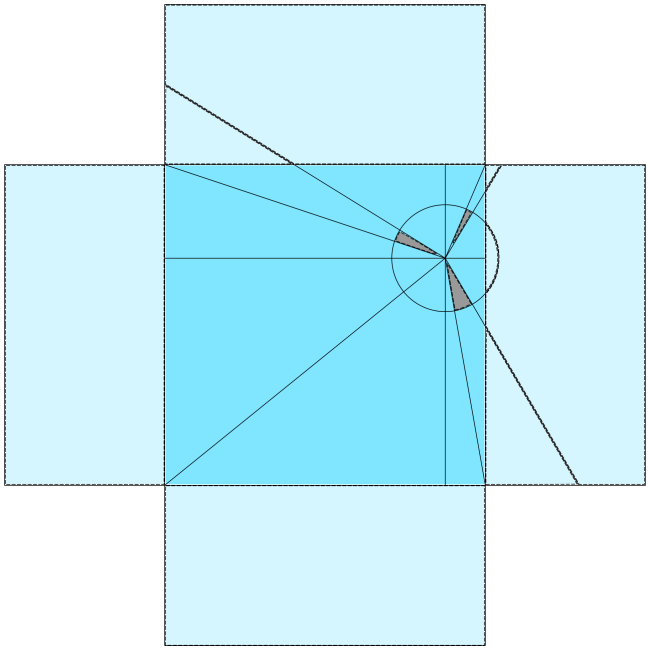

Figure 6.2.: For non center emission light is lost on the edges of the scintillator. Grey angles cannot be detected in the PMTs. Those angles vary greatly depending on the position.

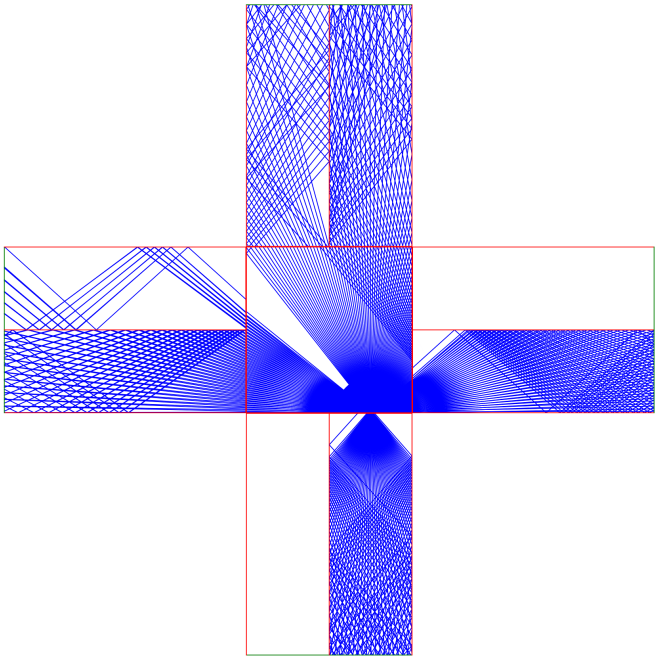

Figure 6.3.: Simulation with gap and emission near the bottom edge shows the unequal distribution in the PMTs even though the combined signal of each side is the same.

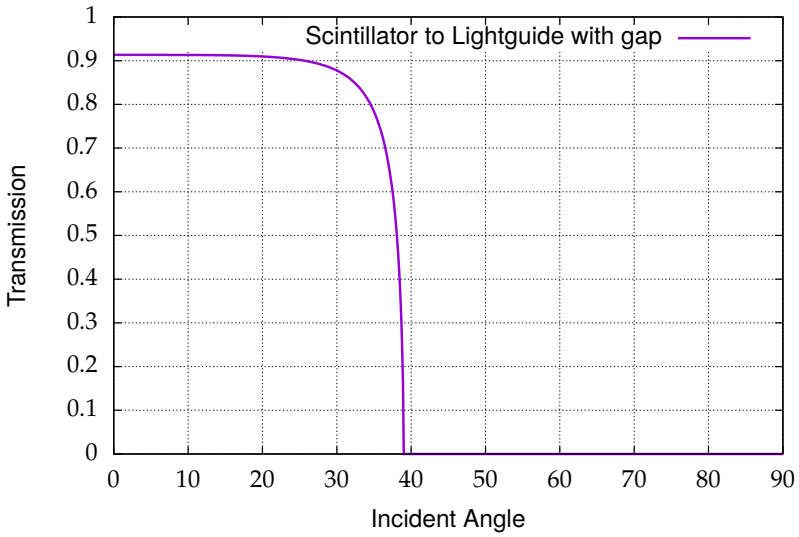

Figure 6.4.: Transmission of 400 nm rays from the scintillator through a gap into the light guide under the assumption of incoherent scattering for gaps bigger than the typical wavelength. Calculated with `tmm` [Byr16]

First result of the simulation from this simple model is the amount of lost rays. Those are shown in Figure 6.5, where the fraction of lost rays is plotted for four simulated scans along the x-axis at different y-positions. Those positions correspond to 0 %, 20 %, 50 % and 80 % of the distance from the center to the upper edge of the scintillator. As seen in Figure 6.5a with no gap the losses strongly depend on the position as expected from the drawing in Figure 6.2. When leaving a gap between scintillator and light guide (Figure 6.5b) the losses are constant for all positions within the scintillator.

Another analysis is the expected signal strength in each PMT especially in the gap case since it was used in the experiment. This is important for the calibration of the PMTs with respect to each other. As one can see in Figure 6.6, the amount of light per PMT varies greatly with the emission position. But a pair of PMTs on one side together will always add up to a constant value. In extreme cases, all rays that will exit on one side of the scintillator are detected in only one of the two PMTs.

This has a mayor influence when one of the PMTs, or its electrical connection, fails. In that case one cannot just take the signal of the others to extrapolate the total energy of the event. Similar effects happen if one PMT is badly calibrated, shows a different efficiency or is insufficiently coupled to the light guide. On the other hand, the strong dependence on the position could be exploited to exactly determine the positioning of the detector relative to the calibration sources. The relative signal strength of the PMTs can be used to estimate the position of the impinging electron. This might enable interesting studies of systematic effects.

For an improved future detector this effects should be studied in detail and a way to optimize the problems originating from this effects should be found. In a perfect detector those effects do not matter, since the full energy can always be reconstructed.

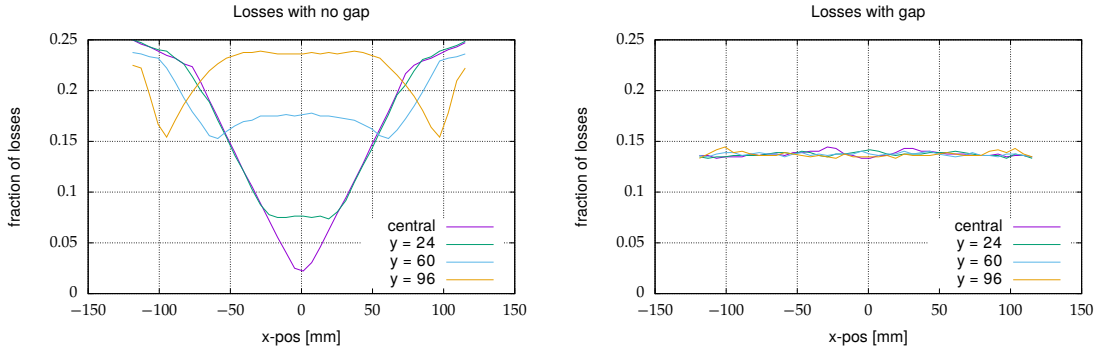

(a) Without a gap between scintillator and light guides

(b) With a 1 mm gap between scintillator and light guides

Figure 6.5.: Simulated losses in a four side readout.

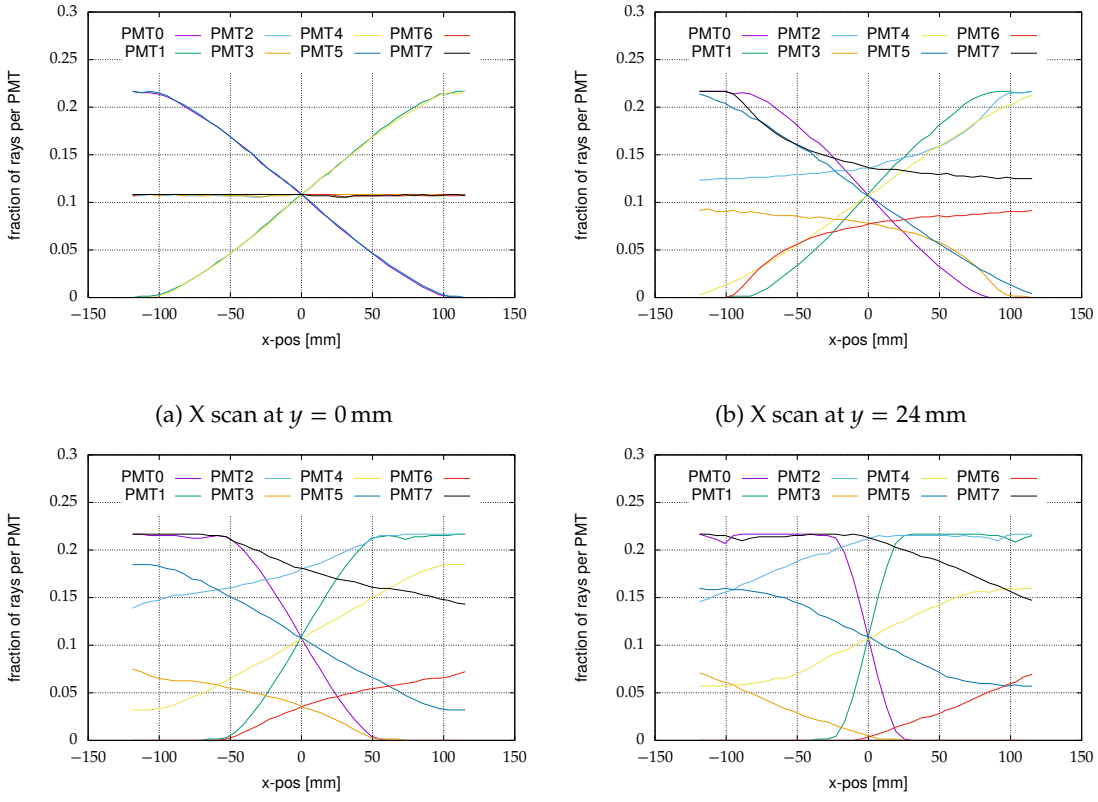

(a) X scan at $y = 0$ mm

(b) X scan at $y = 24$ mm

(c) X scan at $y = 60$ mm

(d) X scan at $y = 96$ mm

Figure 6.6.: Single PMT signals in a four-side readout arrangement

6.3. Transparent Conductive Coating of the Detector

6.3.1. Necessity of a Conductive Coating

In order to establish a uniform acceleration of the secondary electrons towards the detector, the electric potential on the detector has to be defined properly.

The field degrader system itself builds most of the gradient, but is insufficient to provide a clear border potential over the whole cross-section.

Towards the decay volume the gradient is controlled by the first electrodes of the retardation system. Since the bare detector is an isolator situated directly behind the opening of the field degrader system, it cannot provide a suitable potential to fix the electrostatic conditions for the acceleration of the secondary electrons. Additionally the isolator could float to very high values of static electricity in this setup. This static electricity could also be varying with time or be correlated to other variables. Any static electricity of the scintillator would repel low energy electrons from the detector surface. The expected signals from secondary electrons from the proton conversion are very low energetic and even static potentials of a few thousand Volts could easily disturb the count rate. Also a slight shift in energy could change the position of the proton signal with respect to the trigger function of the electronics system.

Furthermore since we convert the protons to electrons we are left with only negative charges impinging onto the detector. This could worsen the static electric potential problem.

6.3.2. Method of Investigation

The possible coatings have to be compared with respect to three characteristics. First of all the coating has to provide a reasonable reflectivity for scitillation light (about 420 nm). An ideal material would not interfere with the total internal reflection properties of the scintillator.

Secondly the coating has to be reasonably thin with respect to the absorption length of the decay electrons with below 1 MeV energy. Minimizing the thickness effects also the optical and electrical properties.

As a last step the resistivity of the coating has to be considered. Since the coating is not used to disperse a bigger current, even a big resistance of order $k\Omega$ can be used to ground the detector surface.

Furthermore the manufacturing has to be included in the discussion, as a uniform distribution of the coating should be achieved in order to have a smooth and flat 2D-response of the detector. The coating process has to work with the extremely sensitive scintillator surface. Any cleaning solutions, high temperatures and mechanical stress have to be avoided in order to preserve the smoothness of the surface.

The optical properties have been studied using the python library `tmm` [Byr16] using several data sets of reflectivity values. Most values are found with the help of an online database of refractive indices [3]. These calculations are based on spectral curves of the real and imaginary part of the refractive index obtained from the data base and based on [KLK+14; RDE+98]. Typical thickness used for the analysis ranged from 5 nm to 100 nm. In Figure 6.7 the results for a 15 nm simulation are plotted.

First of all the properties of aluminium have been studied, since it is the reference material of the previous detector. Other obvious candidates are metallic materials. Gold, Copper and Titanium have the problem that their average reflectivity is only of the order of 40 %. Silver is a more promising candidate with a reflectivity of above 70 % for angles that normally undergo total internal reflection. Over the several reflections of the light within the scintillator on the front and

[3] `http://refractiveindex.info/`

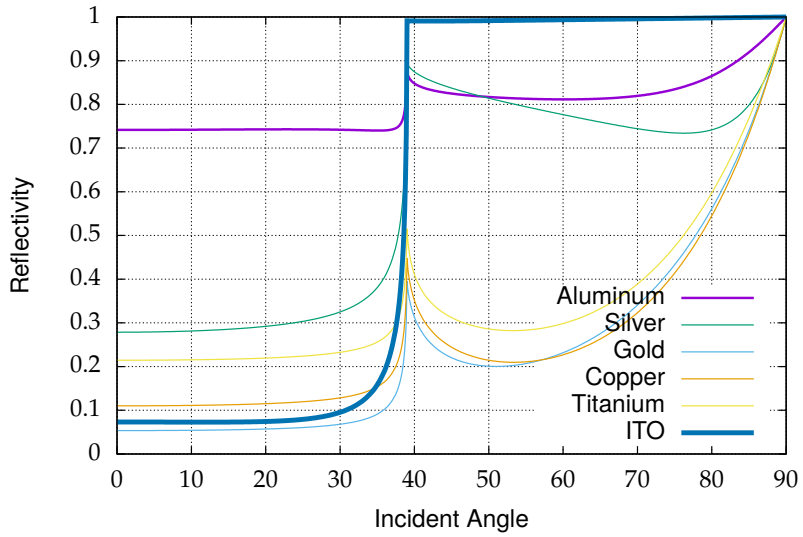

Figure 6.7.: Comparison of different coatings with 15 nm thickness. Simulated with the `tmm` python package[Byr16] and ITO data from [KLK+14] and metallic data from [RDE+98].

back surfaces this leads to a huge loss of intensity and therefore also a non-uniform 2D-response. The last material is Indium-Tin-Oxide (ITO) that is used in touch screens and anti-glare coatings of consumer electronics. The results (based on data from [KLK+14]) are incredibly good and the reflectivity seems to be similar to the total internal reflection. The maximum deviation from 100 % is only about 2 %.

We also planed to study multi layer super mirror structures tuned for optimal reflectivity in the desired wavelength using conductive materials, but the good performance of just a single coating and the difficult optimisation process for super mirrors caused us to stop the investigation. Also the increased thickness might absorb part of the energy of the electron and therefore act as an additional dead layer on the scintillator.

6.3.3. Final Selection and Validation

The very good optical properties for very thin coatings (10 nm) and the availability of industrial processes convinced us to use ITO as a conductive coating. Several test coatings of scintillator pieces (BC-400 type) have been done by the Fraunhofer Institute in Jena. The scintillator showed no obvious signs of damage and the finally used scintillator type (BC-440) is even more temperature resistant.

To analyse these samples a reflectivity test bench powered by a pulsed blue LED light source and a photo diode detector has been constructed. The LED is mounted with a fitting focussing lens to limit the divergence. Four different angular positions of the light source and a defined aperture on both sides of the scintillator allowed to study the intensity at the end of the scintillator for different number of reflections. The pulsed LED allowed to subtract the varying background on the photo diode caused by different surrounding conditions. The LED was driven by a constant current source that allowed a precise control of the light intensity. The circuit could be enabled using a function generator with an appropriate square wave pattern. The signal at

the end of the scintillator was measured using a photo diode sensitive to the low wavelengths of the LED (420 nm). Within the systematic errors and the repeatability of the setup no difference in reflectivity could be observed when comparing two uncoated samples with two coated ones.

6.3.4. Outlook on Possible Future Coatings Concepts and Materials

While researching conductive coatings, several exotic concepts have been discarded in favour of the ITO coating. Other coatings used in similar applications like AZO, GZO or IZO (aluminium, gallium or indium—doped zinc oxide) could be studied for future detectors.

One possibility are aluminium nano-wires [LY11]. Those are sold in a water solution and can be used like a paint on many surfaces. The wires then build a fine mesh on the surface. One disadvantage would be the inhomogeneous surface. An electron that has to traverse a heap of nano-wires surely looses more energy than an electron that just passes by all wires. Those also exist as carbon coated aluminium nano-wires [CDJ+13] with increased conductivity.

Similar carbon nano tubes could be a possible material for future detectors [KHS+11]. This approach will have similar disadvantages as the aluminium nano-wires. A coating made of graphene could be the thinnest and most homogeneous conductive coating. Technical feasibility of such coatings onto a scintillator is not clear, but should be tested in the far future.

Also the whole field of conductive polymers [Inz08] could offer possibilities for the design of conductive scintillators, but I cannot estimate the feasibility of an intrinsically conductive scintillator, since the performance of the scintillator is governed by many parameters. Those could also be used as a coating see [XSO12; SFS15].

6.4. Light-Guides

The classical approach to produce light-guides is to use sheet material (transparent Plexiglass) and bend it around predefined shapes after warming it locally. This process preserves the good surface quality from the sheet material that was cast between two mirrors like glass sheets. Since this process relies on bending by hand it is difficult to achieve a consistent light-guide performance over a longer production run. This approach also does not allow tight tolerances for each part.

All these considerations together with the complicated bending in different planes in my design required us to find a new solution to the production.

The light guides were produced from blocks of Plexiglas of the type ”GS 222 (farblos)”. This material is the only Plexiglas available in the required thickness with optical properties allowing a production of light-guides. Since each light-guide consists of four different strips and a joined block at the beginning and the end, each part of a light-guide can be manufactured independently. Each of this six different parts is cut directly out of the block by a 5-axis CNC mill using special tools suitable for Plexiglas. The parts are then individually polished until the required surface quality is reached. This often included a fine sanding to remove the remaining facets in the outer curvature of the bends in the shape. The pieces are then joined using a two component special glue for Plexiglas (ARCIFIX). In the end a surface quality equal to classic light-guides bended from sheets could be achieved.

6.4.1. General Shapes

The light-guides start with a small diverging section to increase the thickness from 5.0 mm to 6.4 mm. The further parts of the light-guide are four different strips each with a width of 30 mm.

A straight section of varying length follows, before the guide is bent by a quarter circle with an inner radius of 50 mm. Here the truly three dimensional bending begins that shifts the outer strips into the middle to join the sightly shifted inner strips. At the same time all strips move inwards by 29.5 mm and are then united in a final rectangular block on top with a size of 30 mm × 28 mm × 10 mm. All single strips are separated by a 0.8 mm gap. A three sided view of the final light-guide design is shown in Figure 6.8.

The diverging section helps to accept slight angular deviations from the parallel mounting with a gap. Additionally it shifts those angles that are very close to the critical angle towards a smaller incident angle. This helps to prevent losses, especially in the following quarter circle. In the round surface one looses angles that are close to the critical angel in the straight section. That circle has the same radius for all strips which helps to equalize the losses and makes the slight differences in the straight section in front of it necessary. The sideways bending is necessary in order to collect all light on a surface that can be coupled to the PMT. The outer strips are shifted 45 mm to the side on a distance of 250 mm whereas the inner strips are shifted by 15 mm on a distance of 130 mm. In order to provide enough space for the PMT holders, such that those have the same maximum extension to the outside as the light-guide, the shift towards the inside is necessary. This shift is 29.5 mm on the full 250 mm distance. Each strip has the same constant cross-section over the whole length after the diverging part. The gap between the strips is necessary to prevent losses of light that could exit to one of the other strips. The opposite edge of the next strip is not necessarily parallel to the previous edge of reflection but often even converging, which would increase the losses.

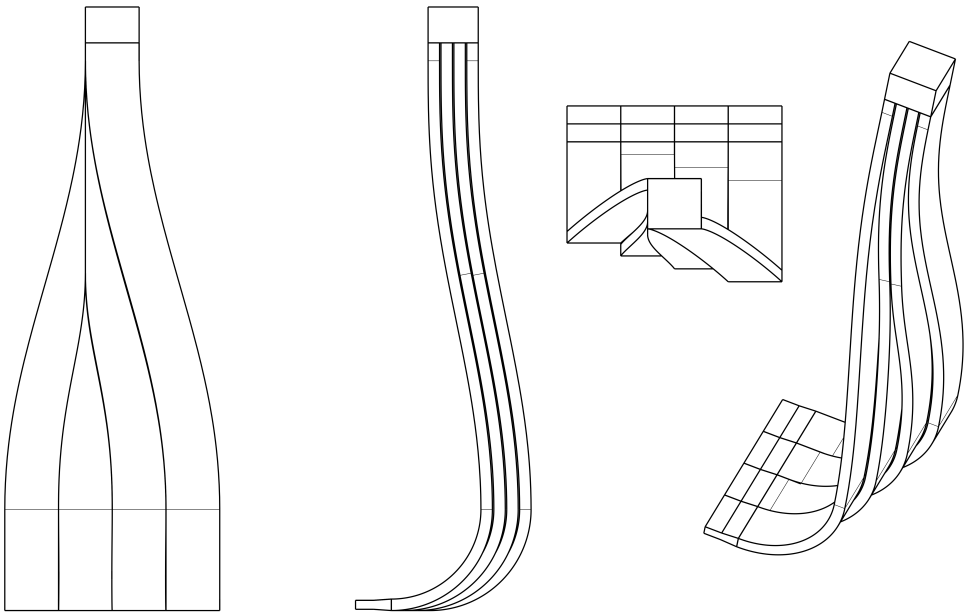

Figure 6.8.: Three side view of the light guides. In the final version the diverging part is moved to the contact surface and is followed by a short steight piece.

The top block of the light guide is rectangular, but it might be better to couple a circular light-guide to the round PMT cathode. We developed a prototype solution for the last block to slowly shift from a rectangular shape to a circle of same area. This free form is difficult to manufacture,

but using a spark eroding machine one can produce a negative form of such a shape. This could then be used to cast that shape from liquid Plexiglas. Of course the surface quality of the cast has to be improved in order to get a good surface quality on the light guide. This approach requires experience with casting of Plexiglas and was therefore postponed for future light-guides.

6.4.2. Simulating Light Losses in Free Geometries

As a tool to study the shapes of light guides, a python program to simulate the light propagation through such shapes was developed. This program was the precursor of the program used to simulate the propagation on light in the four-sided readout concept (see section 6.2). Therefore it has the same limitations and uses only Snell's law to calculate the interaction with the interface. Especially it can only be used for flat two-dimensional structures, but all projections of the shape could be simulated.

One mayor difference to the other ray-tracing program is the possibility to directly enter cubic splines as a border definition. Additionally the program can produce histograms of lost angles, the distance through the light-guide and the number of reflections. A typical output is shown in Figure 6.9. Especially the S-shape sifts to the side were simulated extensively and the dimensions of the outer and inner strips were matched to produce the same loss rate of about 7.4 %.

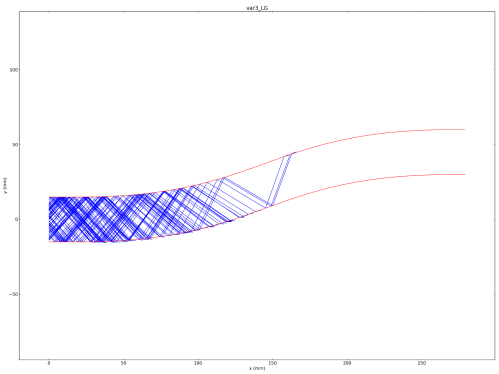

(a) All lost rays in a simulation of the outer strips of the light guide.

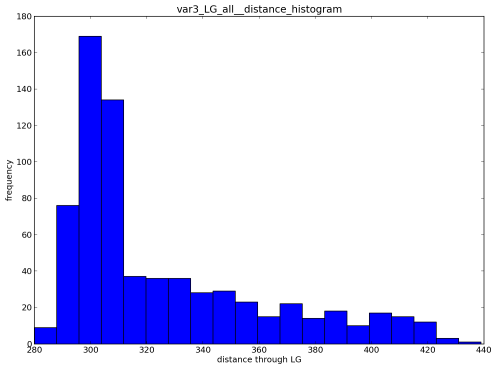

(b) A histogram of the distances the light has to travel through the light-guide

Figure 6.9.: Typical results of the lightguide ray tracing simulations

6.4.3. Manufacturing Light-Guides Using 5-axis Mills

To manufacture the light guides with a milling process is quite difficult and needs special care. It is best to involve the manufacturer early in the design phase, since the manufacturing tools constrain the bending radii and the shape of inner edges.

Transferring the final design to the CNC-mill can produce more problems than one might naively expect. On the mill there is a quite long optimization process to ensure that each step is run with the right revolutions and speed of the mill. The optimal order of the steps has to be found so that optimal quality or production speed is reached. Free forms will be translated into polygons and depending on the setting of the mill, those can be quite coarse.

To achieve nice surfaces, the last run along a surface has to be performed carefully with the right parameters. Special tools suitable for plexiglass have to be used and it has to be ensured that

Figure 6.10.: Producing a part of a light-guide using the 5-axis mill at the institute

they are in good condition and have not been used for other materials before. While advancing further towards the final light guide the material gets thinner and the chance of vibrations or bending increases. Vibrations in one case caused a fine ripple structure along the large side of the light guide and bending of the light guide can result in a non optimal shape of the later. Supporting the light guide for the final steps helps to minimize those problems.

The surface of each element of the light guide has to be polished using a rotating polishing wheel. In order to minimize the likelihood of uneven polishing and material removal, the radius of the polishing wheel should be maximized, but it is constraint by the minimal radius on the light guide that has to be polished from the concave side. Also, the minimal diameter of the available polishing wheels might be too big and should have been already considered in the design process.

Plexiglass can be damaged very easily by micro cracks caused by solvents like acetone or petroleum, so a completely solvents free work environment has to be ensured. In the past there were also problems due to residual oil from touching the plexiglass with bare hands, which therefore should be generally avoided. For the same reason a suitable air tight storage containers for the final light guides have to be provided.

In order to glue the six polished pieces of the light guide a special form had to be build. Equal pressure has to be applied without damaging the final surface since additional polishing after assembly is not possible for all surfaces.

The choice of glue can have a great influence on the final product. From earlier tests, it was concluded that conventional superglue is suited very well for its optical properties [Plo00]. In the beginning we used Loctite 406, but we experienced blooming in between the small gaps at the upper end of the light guide strips. Blooming is the name for a slightly matte appearance of surfaces near the gluing contact area. Another especially low-blooming superglue was tested but also failed the blooming test. In the end the surfaces were glued using the recommended

two-component reactive cement "ACRIFIX® 2R 0190". The manufacturer describes it as follows:

> "It offers the best bonding quality (strength and optical quality) for bonding acrylic (PMMA) to itself and to other substrates. The joint cures in an invisible water clear. It is UV stabilized so there is no yellowing." [4]

One disadvantage of this glue is the long time to final strength of about 24 h (we already removed the final part from the holder after 12 h and allowed it to dry without the holder) and the strongly reduced curing time for closed or almost closed cavities. Additionally, the material slightly contracts while drying so enough material has to be applied on the outside of the gluing slit by building a small reservoir from masking tape. This led to a small ridge around the contact area that had to be milled and polished again.

For other geometries where all surfaces are better exposed to the surrounding air, the superglue might again be the better solution, especially since the time to final strength is much shorter.

The whole process, especially when including polishing and final mounting, was quite work intensive. Using the 5-axis mill exclusively and employing a minimum of two workers for the full time we achieved a production of one to two light guides per week.

Final cleaning of the surfaces was done using special tissues, that are suitable for optical elements and chemically pure iso-propanol. This was later also used to remove excessive amounts of optical paste from the mounting of the PMTs.

6.4.4. Performance Measurements

We performed some test measurements with the first prototype light-guides. With small pieces of scintillator and two light-guides, a miniature detector was constructed recycling old mounting clamps from the old detector from the Mund [Mun06] measurement of the beta asymmetry. The tunable electron spectrometer "ELISE" designed by Ch. Roick [Roi12] was used as a source. In the end, we concluded that the performance of the prototype light-guides in this simple detector matches the performance of the detector used by H. Mest [Mes11] in the last PERKEO III measurement.

6.5. Design and Construction of the Support System

Designing the support system for the detector was a task involving many constraints. The unique shape of the bent light guides together with the four sided readout leaves not much room for a support structure. Furthermore the design had to allow the mounting or exchange of a single PMT or light guide without disturbing the alignment of the others.

In order to minimize light losses, all transparent parts should be fixed with the minimal amount of material in contact with reflective surfaces. In earlier detectors the contact areas were quite large and attributed to the light loss in the system.

Vacuum compatibility of the whole system has to be considered in the construction. Any dead volume that can only be pumped via small slits or holes has to be avoided. Especially in the UHV range, outgassing from such volumes can contaminate the vacuum of the system. Therefore all screws were slit and all blind holes got an addition venting hole.

The final design of the support structure (see Figure 6.11) features a 7 mm thick aluminium base plate (with size $(440 \times 440)\,\mathrm{mm}^2$) with a square hole in the middle with the exact dimensions of the scintillator ($(240 \times 240)\,\mathrm{mm}^2$). Four square beams are connected with plates further

[4] http://www.acrifix.com/product/acrifix/us/products/reactive-cements/acrifix-2r0190/pages/default.aspx retrieved on July 14th, 2016

up provide the basis for the light guide and PMT support structures. The side that was exposed to the impinging particles and the high voltage system had polished edges and countersunk screws. Above the scintillator the upper support plate was mounted and fixed. This prevented direct sight from the PMTs to light from the backside of the scintillator and provided the threads for the screws that fixed the scintillator and the light guides. The square rods in combination with a thick support block at each corner fixed the base plate allowing no shifts or rotations.

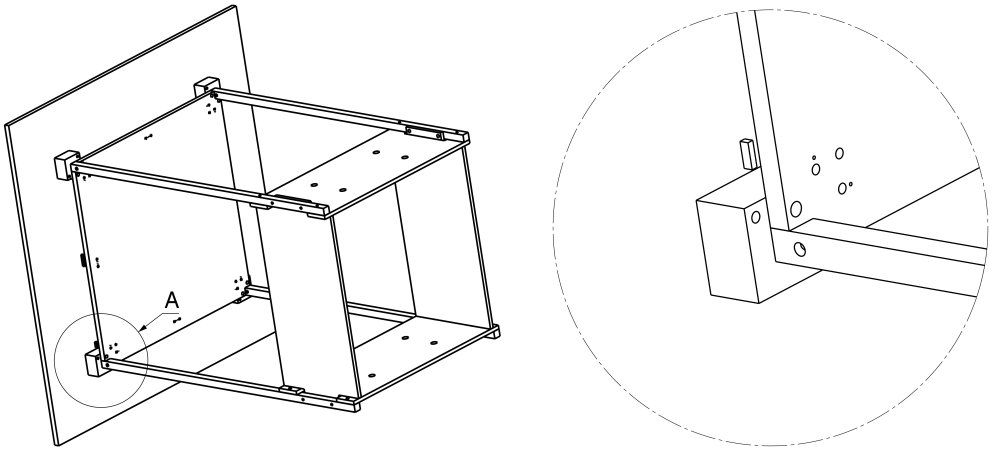

Figure 6.11.: Drawing of the basic structure of the detector mounting.

The scintillator cannot be supported by the small sides, since the whole circumference is used to extract the light. Therefore the scintillator is supported in each of the corners by an area of $(8 \times 8)\,\mathrm{mm}^2$ with the respective movable counterpart to clamp the scintillator onto the basic support structure.

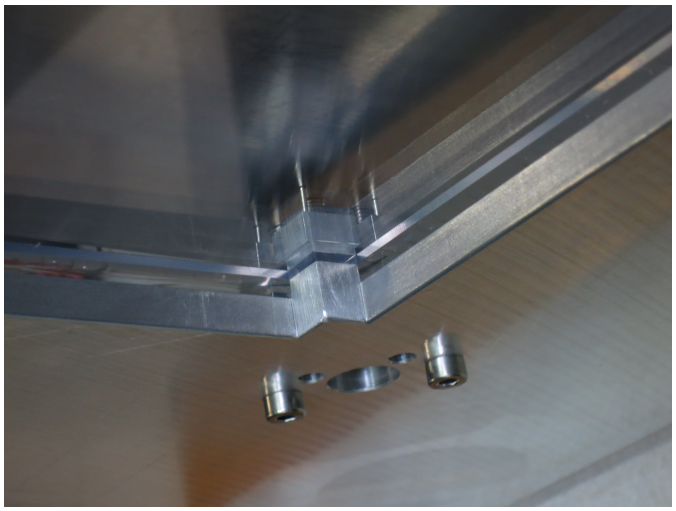

Figure 6.12.: The scintillator is mounted on quadratic polished aluminium with an equivalent counterpart on top. View from the coated side of the scintillator.

The support of the scintillator has to be independent of the support of the light guides, so that

it stays fixed while installing the other light guides. After adjusting the position of the scintillator it was fixed by tightening the screws in all four corners.

In order to protect the scintillator from pressure cracks and to provide a defined contact, all screws have a cap with a polished face which is secured against rotation by a pin with 1 mm diameter. This hugely complicates the assembly of the detector, but provides good support to the scintillator. A picture from the coated face of the scintillator can be found in Figure 6.12.

Similar caps were used to fix each light guide next to the scintillator. In the current system each light guide is only supported by two small rectangular cuboids each sized $(2 \times 8)\,\mathrm{mm}^2$ with an additional corresponding part on the other side of the light guide. By also fixing the top of the light guide it could be ensured that the exit surface of the scintillator and the entry surface of the light guide are as parallel as possible. In order to implement the four-side readout with a gap, a piece of paper was inserted in the space between the two parts while mounting and tightening of the screws.

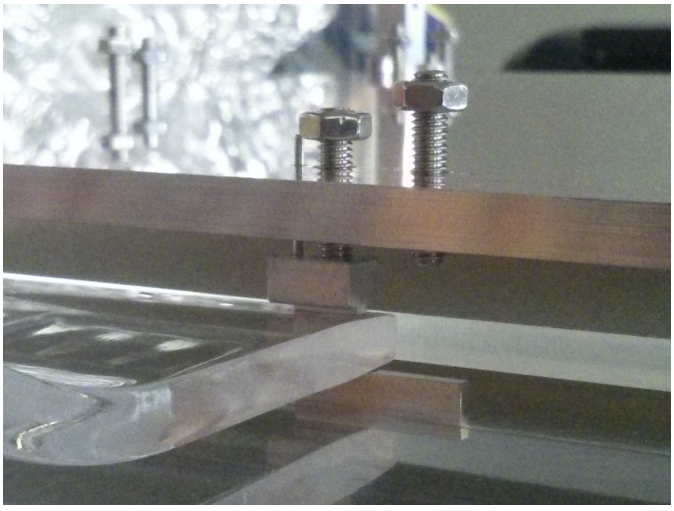

Figure 6.13.: Close-up of the screw and cap that are used to fix the light guide on the small contact areas from polished aluminium.

The upper fixation of the light guide is combined with the PMT holder. In order to be able to cool the PMT, the holder is made from two concentric tubes of non-magnetic stainless steel. On the smaller tube a thin strip made from a steel sheet is attached in form of a spiral. This guides the cooling water around the inner tube. The top and bottom surface of the cylinder is welded to be vacuum tight. One each of the sides at opposite angle the connection tubes of 6 mm are welded in. At the bottom the aluminium part that fixes the light guide can be installed at different angles. The part itself is shown in Figure 6.14. The light guide is touched by small polished parts and a few small screws.

Inside the PMT holder, the top part of the light guide protrudes into the tube. This ensures that the PMT is in perfect contact to the light guide. Using an optical grease [5] at the contact area minimizes the losses at this interface. A screw held by a crossbeam presses the PMT onto the light guide. In order to center the light guide in the tube and to adapt for the slight variations in PMT diameter, an adapter ring with screws was installed.

The PMT holder is fixed by two clamps that allow an adjustment by rotating the PMT holder

[5] EJ-550 Optical Grade Silicone Grease produced by ELJEN TECHNOLOGY

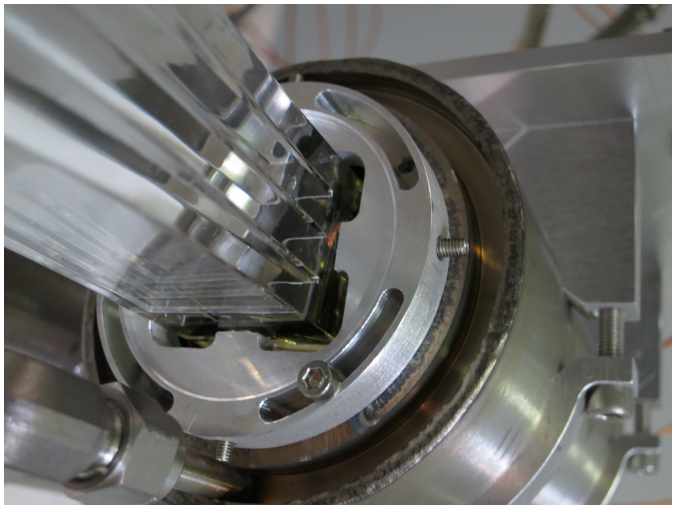

Figure 6.14.: Detailed view of the upper light-guide mount. Contact area is only the tip of the screw or the small polished aluminium surface.

and by sliding it up and down along the upper part of the light guide. Since the best procedure to fix the light guides was to first clamp at the bottom and then sliding the PMT holder over the top of the light guide, the PMT holder cannot be fixed before installation.

In order to minimize the number of necessary water feedthroughs, all PMT holders were connected in series. The two PMTs on each side are connected at the bottom and the connection to the next side of the detector is made on top where the tubes could be placed diagonally. The connections are made with non-magnetic stainless steel Swagelok ferules. After installing a disconnection should be avoided in order to preserve the best vacuum tightness. Therefore the water cooling connections were made after all light guides were installed.

The PMT holder is quite heavy when filled with water and that causes the center of gravity of the detector to shift very far towards the back. Nevertheless the four legs of the detector support, attached to the square beams, could support the detector without the risk of tilt. The legs had small wheels made from PEEK parts left over from the construction of the retardation electrodes. Those were supported by a rail system that could be adjusted with a few screws in order to shift the detector position inside the detector chamber. The rolls on the detector are necessary to protect the installed foil from vibrations and sudden air movements while the detector is installed in front of the foil[6].

6.6. Installing the Detector and HV System

To install the very fragile foil some experience with the movement of those foils is needed. One should never attempt to install the foils without a thorough training of all movements. Even inside the transport box, all vibrations from putting down the box or touching it should be as soft as possible. Movement of the transport box has to always be parallel to the foil surface to prevent the air movement inside the box from destroying the foil. For the same reason corners have to be taken with the biggest radius that is possible.

[6] as seen from the point of the operator that installed everything from the big flange behind the detectors

Removing the foil from the transport box is a critical moment since the foil has to be moved in free space before laying it down on a support structure inside the vacuum chamber. At that point no air movement is tolerable. From that point onwards we used a rail and a fishing line with low ductility to slowly pull the foil on the holder towards the center of the field degrader. There the lower part of the holder was softly inserted into the central electrode and the foil holder was put into the vertical position by slowly winding up the fishing line. This allows to stop in case some vibrations or movement is detected in the foil.

The detector is placed very slowly in front of the detector onto the rail system and pushed towards the final position close to the degrader. After that all connections have to be made to the feed-through flange. Here the length of the extremely fragile cables has to be optimized. The clamped capton BNC cables can be very easily separated from the connectors.

In order to be able to reconnect the water cooling several times, we installed fixed fitting to each the detector and the feedthrough and use a throw away piece of tube between those. This ensures perfect connection each time, even though it is possible to re-use this piece at least three times if it is possible to use a bit more torque each time. It is useful to check the connection of the HV-supply for the PMTs by measuring the resistivity of the connection. If possible, the next user of the cables should find a way to also check the connection of the BNC signal cable before closing the vacuum chamber.

Pumping speed of the vacuum is also crucial and the necessary flow is best achieved by using a membrane valve and a mechanical pressure gauge. Pumping overnight from 1000 mbar to 100 mbar was always slow enough to conserve the foil and allowed to start the turbo pumps within 24 h of the initial start of the pumping.

6.7. Measuring the Detector Performance

6.7.1. Improvements of the Calibration Device

In order to calibrate the detectors inside PERKEO III D. Wilkin [Wil07] constructed a calibration robot with five arms. This device is installed in the central decay volume and is build such that it does not disturb the neutron beam or the decay particles including their gyration radius. All components have to be absolutely non magnetic in order to not disturb the carefully configurated magnetic field in the decay volume. The system is therefore driven by ultra-high vacuum compatible piezo-ceramic motors "HR-1-VN" from the company Nanomotion. On each arm one can install calibration sources on carbon foils. When the neutron shutter is closed, the main arm can then be driven in the middle of the decay volume. The different sources can then be raised out of their housing. With the typical electron sources ^{109}Cd, ^{139}Ce, ^{113}Sn, ^{137}Cs and ^{207}Bi, electron energies from 78.1 keV to 997.9 keV are available.

In order to improve the reliability of the system, several changes were implemented. The sliding system of the arms was based on a Teflon glider on an aluminium rod. This works reasonably well and was used in the previous measurement with PERKEO III. In vacuum the thin film of moisture on the Teflon is missing, so friction is increased. This sliding system has been replaced by the commercial available low profile linear guide system "drylin® N" that is based on an anodized aluminium rail and a fitting plastic glider made from the vacuum compatible polymer "iglidur® J"[7]. Those reduced problems with jamming while driving and added stability against rotations of the source holder.

Additionally, all plastic bearings were replaced by pure ceramic ball bearings. This decreased the force necessary to move the horizontal arm and in the pulleys of the drive system of the

[7] all products of the igus GmbH company

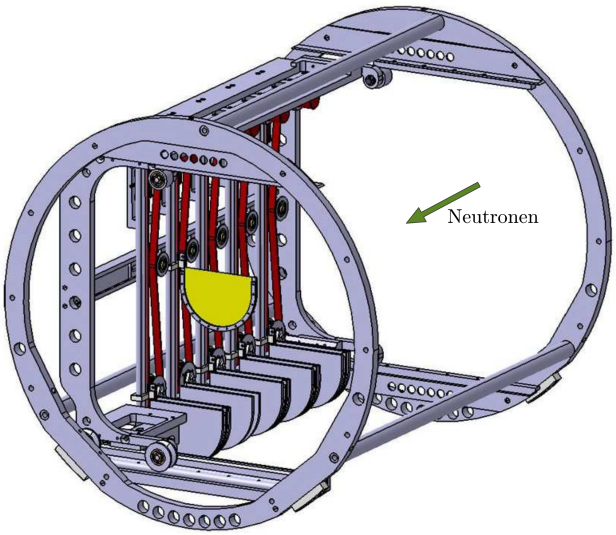

Figure 6.15.: Rendering of the scanning system before the improvements.

arms. At the same time, an additional stabilizing aluminium profile was installed to minimize warping of the horizontal system in order to minimize necessary forces.

The drive system of the arms was most critical for the achievement of our vacuum goals. Initially it utilized a rubber belt drive and a ten-turn precision potentiometer to measure the position. Both are unsuitable materials for the desired vacuum pressure. After struggling to find a solution, Ch. Roick [Roi15] invented a replacement for the belt drive using a steel wire and a double threaded cylinder. This system was more vacuum compatible, but has still room for improvement. It was prone to slipping and loosing contact to the source holder.

Additionally, it was very difficult to find a suitable replacement for the potentiometer, but we manufactured a crude system based on a resistive wire wound around a rod that was contacted by a spring loaded aluminium glider.

All together the system could only be used in the calibration of the detector. We were able to mainly collect calibration and homogeneity data from the ^{207}Bi source. Additional data from measurements with ^{137}Cs is only available for a non-final PMT-voltage configuration. We did not install the system for the final beam time, since its vacuum compatibility was still not sufficient and we were not sure if possible material potentials and isolators could disturb the protons in the decay volume (see section 10.7). Also the reduced reliability of the drive generated the fear of a calibration source getting stuck in the middle of the beam.

This system has to be further improved for future measurements. One has to discuss if it is useful to install another system near or even behind the detector for the drift control measurements. The full device would then only be used for the calibration and 2D-mapping of the detector prior to the real measurement using neutrons.

One idea for the construction of a non-magnetic position sensitive device is to use a small snake-like track on a flexible capton PCB. Aluminium based PCBs might also be a good carrier, but the vacuum compatibility of both materials has to be verified first. In a standard process [8] the minimal width of a track is 0.15 mm with a minimum gap of also 0.15 mm. Such a track has

[8] like the one available at `www.bcb-pool.com`

a resistivity of $3.86\,\Omega\,\mathrm{m}^{-1}$. The maximum length of a zig-zag structure that one could fit on a 25 cm × 3 cm PCB is 30 m which then results in a total resistance of the strip of about 100 Ω. The voltage drop along the strip could then be measured by a spring loaded glider on the PCB.

6.7.2. PMT-Calibration

In order to calibrate the PMTs with respect to each other, we did alternating calibration measurements in the center of the detector and at off-center positions. The single PMT spectra were then fitted with a simple parabola formula. A typical output can be seen in Figure 6.16 Combining the center of the peaks of the two PMTs per side and of all PMTs on the detector one could identify an imbalance in the gain of the PMTs. An automated program suggested new settings for the high voltage of the PMTs after also considering the information of the last few scan positions.

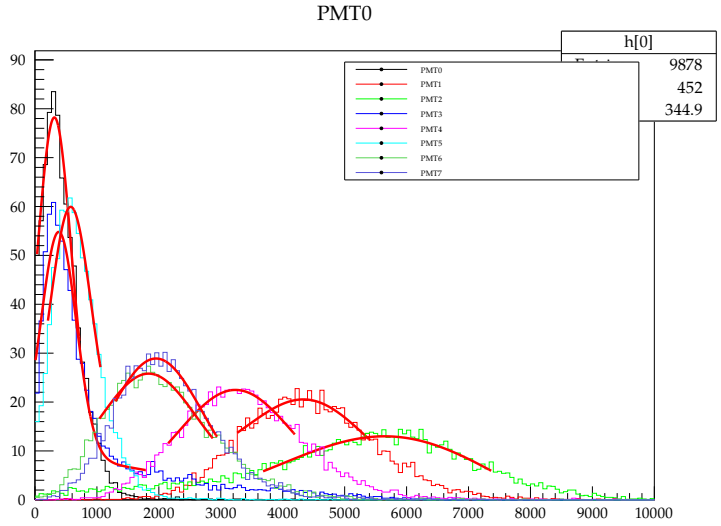

Figure 6.16.: Fitting the single PMT spectra for a calibration measurement using ^{137}Cs helped to identify misbalances in the PMT gain.

6.7.3. Uniformity

The analysis of the uniformity of the detector is performed by Ch. Roick. The goal is a recalibration using scaling factors for each PMT. Sophisticated analysis of the collected data, including a reconstruction of the light position, results in a map of scale factors for the PMTs. The initial variety of the signal of 8.9 % on the upstream (Grenoble) detector could be reduced to 4.0 %. On the downstream (Lyon) detector an even better improvement from 13.6 % to 5.0 % could be achieved.

6.7.4. Light Output and Energy Resolution

The analysis of the energy resolution and calibration is also done by Ch. Roick. Therefore a preliminary result from the ^{207}Bi measurement is presented. On the downstream detector the

data was fitted using a Birks-5/3 non-linearity model that is directly applied to the photo electrons. This is the most advanced model fit of the detector characteristics that was developed for the measurement of the electron asymmetry [Mes11]. The trigger function does not fit, since the new trigger scheme was not jet implemented. Additionally the background spectrum mas measured several minutes later.

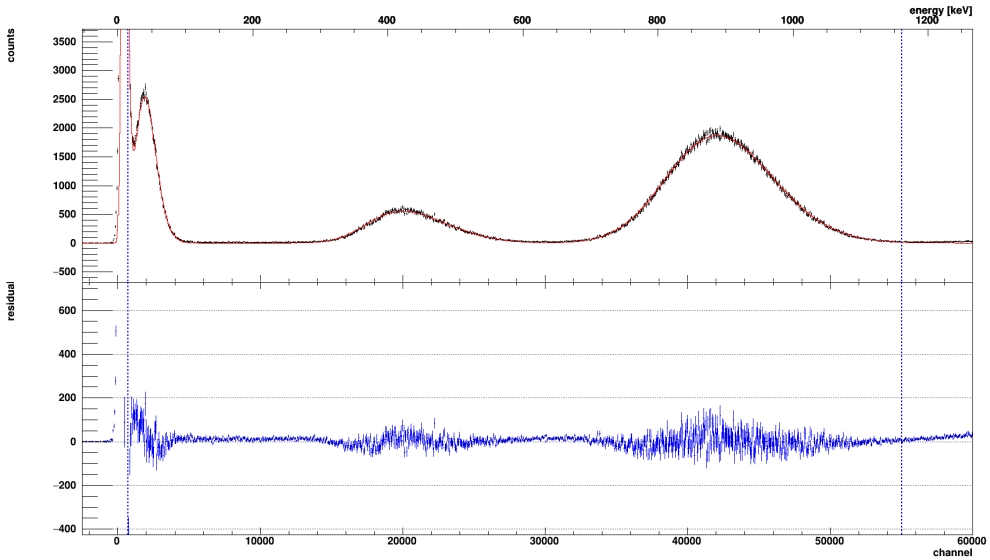

Figure 6.17.: Preliminary fit of the downstream (Lyon) detector to the ^{207}Bi calibration source [Roi15]. The light output of the detector is so high, that the energy resolution is sufficient to resolve the flat part of the spectrum between the peaks.

The fit presented in Figure 6.17 is impressive. The previous detectors were just able to distinguish the very low energetic Auger-electron peak (here around 200 ch) from the background, but it was impossible to include it in the fit. This shows the good low energy performance of the detector due to the improved homogeneity and the four-side readout. Especially having over 200 PE/keV is a real improvement. Additionally the coating really does not seem to have a big influence on the detector performance. In order to compare the parameters from the fit with other fit data their values are presented in Table 6.1.

	parameter	value	error
0:	gain	47.397	fixed
1:	offset	0.000	fixed
2:	PE	0.222	0.001 30
3:	pe_nonlin_k	12.6	fixed
5:	sigma_electric	145.0	fixed
6:	sigma_drift	0.0366	0.000 47

Table 6.1.: Results of the fit parameters from the ^{207}Bi calibration fit.
red. Chi2 = 3027.5/1084 = 2.8, probability: 0.00

7. Point Spread Function and Edge-Effect as a Major Systematic Effect

One general problem of all PERKEO type measurements is the broadening of the beam of secondary particles due to the gyration motion caused by the guiding field. The gyration radius depends on the field strength of the guiding magnets. If one chooses a detector larger than the neutron beam by an additional two gyration radii on each side, all decay particles can be detected. Unfortunately such a big detector is not always feasible and a large one is also susceptible for background signals, whose intensity scales with the size of the detector. Also depending on the used technology a large detector may have a bigger spacial inhomogeneity or might be infeasibly expensive. Especially in the case of PERKEO III the magnetic field is quite low (150 mT) since a superconducting and therefore stronger magnet was not practicable in the required size. The losses and corrections on the asymmetry for a smaller detector were therefore studied earlier in 2008 and published to the ArXiv. The planing of this measurement with an even smaller detector caused us to investigate the problem further.

To study such problems, the image of a mono-energetic point source on the detector is defined as the Point Spread Function (PSF). This response can then be folded with the energy spectrum of the source as well as the spacial source density in order to fully express the image of the source on the detector plane.

A new mathematical deviation of the point spread function was found and applied to the PERKEO III setup. This investigation was then published in 2014 [DRM+14].

Further investigation of singularities in the mono-energetic PSF are discussed in the next paper by Dubbers [Dub15]. The influence of a inhomogeneous magnetic field and the generalization to anisotropic sources can be found in more detail in the preprint of the paper (see arXiv:1501.05131v3).

Sjue et al. [SBM+15] evaluate the influence on their UCNA experiment and verified the effects in a low field test measurement. Especially in their next generation experiment with a pixelated detector, the spectral effects in single pixels have to be considered for a 10^{-3} relative accuracy measurement.

Backe [Bac15] provides a series expansion of the PSF and shows the practicality of the numerical and Monte Carlo investigations of the detector effects of the PSF.

In another paper ([Bac16a] with corrigendum [Bac16b]) Backe discusses some issues with approximations, some of which still remain even after the corrigendum. Additionally the behaviour of the PSF in a inhomogeneous magnetic field is discussed, with the conclusion that the small singularites are shifted. This could be explained by the different quality of the adiabatic approximation. Future experiments should investigate the particle trajectories in detail using Monte Carlo methods as recommended in the paper.

7.1. Deriving a Point Spread Function for Charged Particles in a Magnetic Field

The general setup is constructed as a point-source inside a homogeneous magnetic field in z-direction $\vec{B}(\vec{x}) = (0, 0, B_z)$. We are interested in the spacial resolved image on a detector plane that is situated a distance z_0. To describe the initial direction of emission two angles are introduced. The pitch angel towards the magnetic field line (polar angle) is called θ and the angle in the orthogonal plane (azimuthal angle) shall be called ϕ. The general motion inside a homogeneous magnetic field can be separated in a gyration motion caused by the orthogonal momentum component and a drift of the so called guiding center of this spiral motion. The projected motion of a single particle is a circle around a guiding center with distance r_{gyr}. Allowing all possible emission angles ϕ while keeping a fixed θ gives the maximal extend of the projected motion. A circle with a diameter of $4\,r_{gyr}$.

The trajectory of a single particle in the magnetic field can be calculated as

$$\begin{aligned}\vec{r}(t) = \hat{x}\ &[r(1-\cos(\omega t))\cos(\phi) + r\sin(\omega t)\ \sin(\phi)] \\ -\,\hat{y}\ &[r(1-\cos(\omega t))\sin(\phi) + r\sin(\omega t)\cos(\phi)] \\ +\,\hat{z}\ &(p/E)t\cos(\theta)\end{aligned} \tag{7.1}$$

with the radius of gyration $r = r_0 \sin(\theta)$ depending on the maximal gyration radius $r_0 = \frac{p}{qB}$ and the pitch angle θ [SBM+15]. The angular frequency is given by $\omega = qB/m$ and for negatively charged particles only the sign of either the x- or the y-component has to be switched.

The calculations in our paper are based on the total phase angle α of the gyration movement derived from the pitch d of the helix.

$$d = 2\pi\, r_0\, \cos(\theta) \tag{7.2}$$

For each starting condition (energy and pitch angle) one can find the exact phase angle for the arrival at the detector to be

$$\alpha = \frac{z_0}{r_0\, \cos(\theta)} \tag{7.3}$$

The displacement of the particle from the projected source can be expressed as a very rapidly oscillating function of this phase angle.

The classical approach was to assume that all phase angles are distributed evenly. In that case the probability for a displacement R (wrongly called PSF in our first paper [DRM+14]) is constant

$$g(R) \equiv \frac{\mathrm{d}P}{\mathrm{d}R} = \frac{1}{2\,r_0} \tag{7.4}$$

Taking into account that the area of detection at R given $\mathrm{d}R$ happens in an area $\mathrm{d}A = 2\pi R\,\mathrm{d}R$, the PSF therefore can be written as

$$f(R) \equiv \frac{\mathrm{d}P}{\mathrm{d}A} = \frac{g(R)}{2\pi R} = \frac{1}{4\pi\, R\, r_0} \tag{7.5}$$

Unfortunately this result is only an approximation, since in the deviation θ and α are treated as independent. Caused by the fixed distance of source and detector, there is only one phase angle for each pitch angle with the relation

$$\cos(\theta) = z_0/(r_0\,\alpha) \tag{7.6}$$

Deriving the PSF under this assumption is more complicated and requires the careful usage of approximations. The resulting PSF shows a remarkable feature, namely spikes or infinities at certain displacements whose positions strongly depend on the distance of the detector and the source[1]. This strong dependence helps to average out the singularities as seen in this quote from Dubbers [Dub15].

> "This parameter sensitivity of n_0 may average out the singularities of the PSF: These singularities are no longer individually resolved experimentally if n_0 changes by $n_0 > 1$. This happens when either $\Delta B/B$ (e.g., for extended sources), or $\Delta z_0/z_0$ (for axially extended sources), or $|\Delta p/p|$ (for continuous spectra) in $[n_0 = eBz_0/(2\pi p)]$ exceeds $1/n_0$."

In the final case of the proton asymmetry measurement, we will have a voluminous source with a whole energy spectrum and all possible emission angles. This integration will average out some of the features of the mono-energetic point spread function.

7.2. Calculation for a Realistic Neutron Profile

For our initial paper we calculated the particle loss and the "lost asymmetry" for a realistic beam profile. For that the integrated PSF of the whole electron and proton spectra was numerically folded with a symmetric beam profile. This two-dimensional source image is calculated for a certain set of points arranged in a regular grid. Integrating over these points within the limits of the detector of variable size, allows to calculate the number of missed electrons and protons. Additionally the PSF of the first Legendere polynom (1,0) is folded in order to calculate the correction for the asymmetry value.

As shown in the second Dubbers paper [Dub15], the distribution after an adiabatic transport of the decay particles through a magnetic gradient towards the lower field at the detector can be calculated from the stretched original PSF.

$$f'(R') = f(R\sqrt{B'/B}) \tag{7.7}$$

This is due to the inverse magnetic mirror effect (for $B' < B$) that increases the radii of the particles to $r' = r/\sqrt{B'/B}$ while boosting the pitch angle closer to the magnetic field line with $\sin\theta' = \sqrt{B'/B}\sin\theta$.

The major result from this calculation is shown in Figure 7.1. The differences in the proton and electron curves originate in the non-relativistic behaviour of the proton compared to the electron and their different spectra. This calculation prompted us to enlarge the detector from 220 mm to the maximum possible size of 240 mm.

7.3. Monte-Carlo Simulations of Energy Dependent Edge-Effects

In order to understand the effects of a small baffle or detector it is useful to investigate this effect further. The survival probability of the particles through the different baffles is the first parameter to study. The thickness of the baffle has an influence on the effects. A particle with a big pitch of its helix can gyrate around the baffle and be detected at positions behind the

[1] more accurately the minimal number of gyration revolutions $n_0 = eBz_0/(2\pi p)$ from the limit $\theta \to 0$

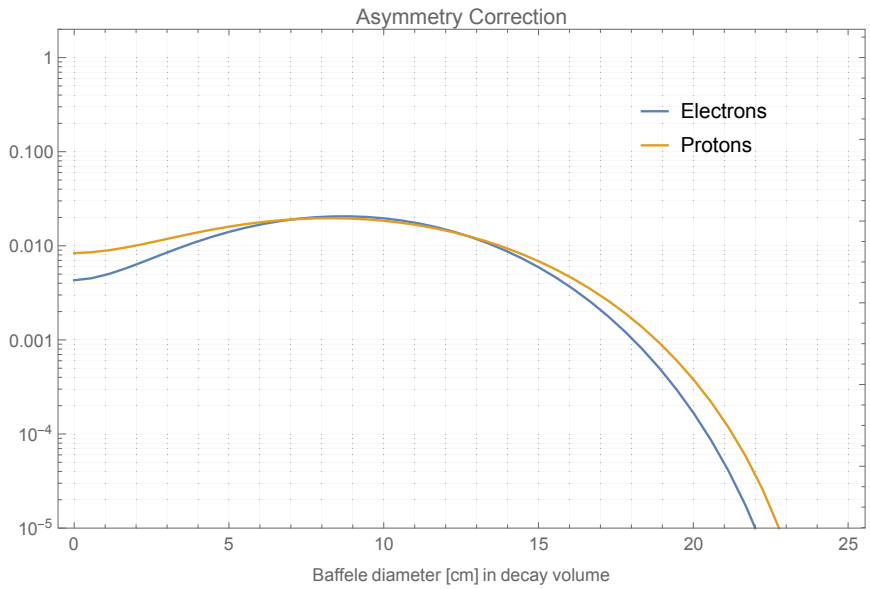

Figure 7.1.: Correction factor for the asymmetries as calculated in [DRM+14] for a realistic neutron profile. For baffles in the detector vessels the size of the baffle has to be multiplied with $\sqrt{B'/B}$.

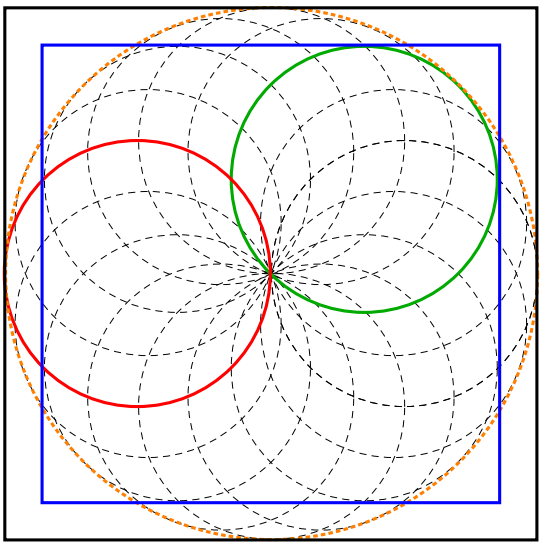

Figure 7.2.: Sketch of several gyration curves (dashed) originating in the center. The maximum extend of the point spread function is indicated by the orange circle with radius $2r_{max}$ and the maximum square baffle in black. Introducing a smaller square baffle (blue) shows that depending on the azimuth angle ϕ some gyration curves never touch the baffle (green) or partially overlap with the baffle(red). Particles with less energy or a smaller polar angle towards the magnetic field θ have smaller gyration radii.

baffle, whereas a thick baffle also absorbs along the side walls and stops all particles that have a projected trace that at one point touches or enters the baffle.

A real baffle is likely to be a mix of both. Especially for small angles to the magnetic field the pitch of the helix is so big, that any real baffle can be treated as a thin baffle. To estimate how thin the baffle is it might be useful to calculate the phase difference $\Delta\alpha$ that occurs while the particle flies through the baffle thickness Δz. A thin baffle therefore samples only a very small part of the whole gyration motion of a single particle.

Using Equation 7.1, one can integrate the number of absorbed particles numerically using Mathematica [Math10] with the Adaptive Monte Carlo Method.

This calculations assume a quasi point source that is extended along the magnetic field line, such that the singularities are all averaged out and the classic assumption of independent θ and α is valid again. The source can emit the characteristic β-spectrum of neutron decay and therefore has a maximum energy of $E_0 = 783\,\mathrm{keV}$. A square baffle with a maximum width of four times the maximal gyration radius at E_0 is added. This situation is sketched in Figure 7.2. It shows several possible trajectories of a single emission with constant energy and angle in dashed lines. The orange circle shows the maximal extend of the trajectories. In blue a smaller baffle is drawn.

The transmission probability of electrons is the relevant quantity and it depends on the size of the baffle opening and the energy of the source. Therefore two sets of plots are generated, the transmission as a function of the baffle size for several energies and the other way around the transmission spectra as a function of energy for several widths of the baffle. Figure 7.3 shows these plots for the thin baffle and the plots for the thick baffle can be found in Figure 7.4. The first type of plot is also generated as the average for energies weighted with the Fermi spectrum of neutron β-decay (see Figure 7.5). Here the fraction of lost or absorbed electrons is plotted instead of the transmission because the transmission is almost 1 at baffle sizes of $2r_{max}$.

For the thin baffle the integral runs over $\theta \in [0, \pi/2]$, $\phi \in [0, 2\pi]$ and $\alpha \in [0, 2\pi]$. Integrand is a bool function that returns 0 if the absolute value of one of the coordinates is bigger than half the size of the baffle opening. This has to be weighted with $\sin(\theta)\,\mathrm{d}\theta$. This numerical integration can be speed up by setting the appropriate precision and accuracy goals as well as the right integration method. In this case the method "AdaptiveMonteCarlo" was chosen. The corresponding code can be found in the appendix in Figure C.2

To calculate the thick baffle all cycles that have a part of their projected motion extending beyond the baffle opening have to be excluded from the integration. As seen in Figure 7.2 the maximum x- or y-coordinate of a cycle not only depends on α but also on ϕ. To find the maximum value we set the derivative to zero.

$$0 = \partial_\alpha x(r_0, \theta, \phi, \alpha) = r_0 \sin(\theta)\, \sin(\alpha + \phi) \tag{7.8}$$

$$0 = \partial_\alpha y(r_0, \theta, \phi, \alpha) = r_0 \sin(\theta)\, \cos(\alpha + \phi) \tag{7.9}$$

The extreme values are then found at $\alpha = 2\pi - \phi$ and $\alpha = \pi - \phi$ for the x-coordinate and $\alpha = -\phi \pm \pi/2$ for the y-component. This allows to write the integrand again as a bool function but omitting the integration over α (see Figure C.1 in the appendix for the code).

The calculated case is not completely realistic, since it is only calculated for a point-like source and the results for a realistic source profile, that extends in all three dimensions and has a soft edge, will probably differ. Also the magnetic field is constant and does not vary in strength like in Perkeo III and other similar experiments. In those experiments the distribution of the pitch angle is shifted which influences this calculation.

Our square detector can be seen as a thin baffle since the aluminium base plate of the detector absorbs all particles with positions out of the active area. If one has a free standing arrangement

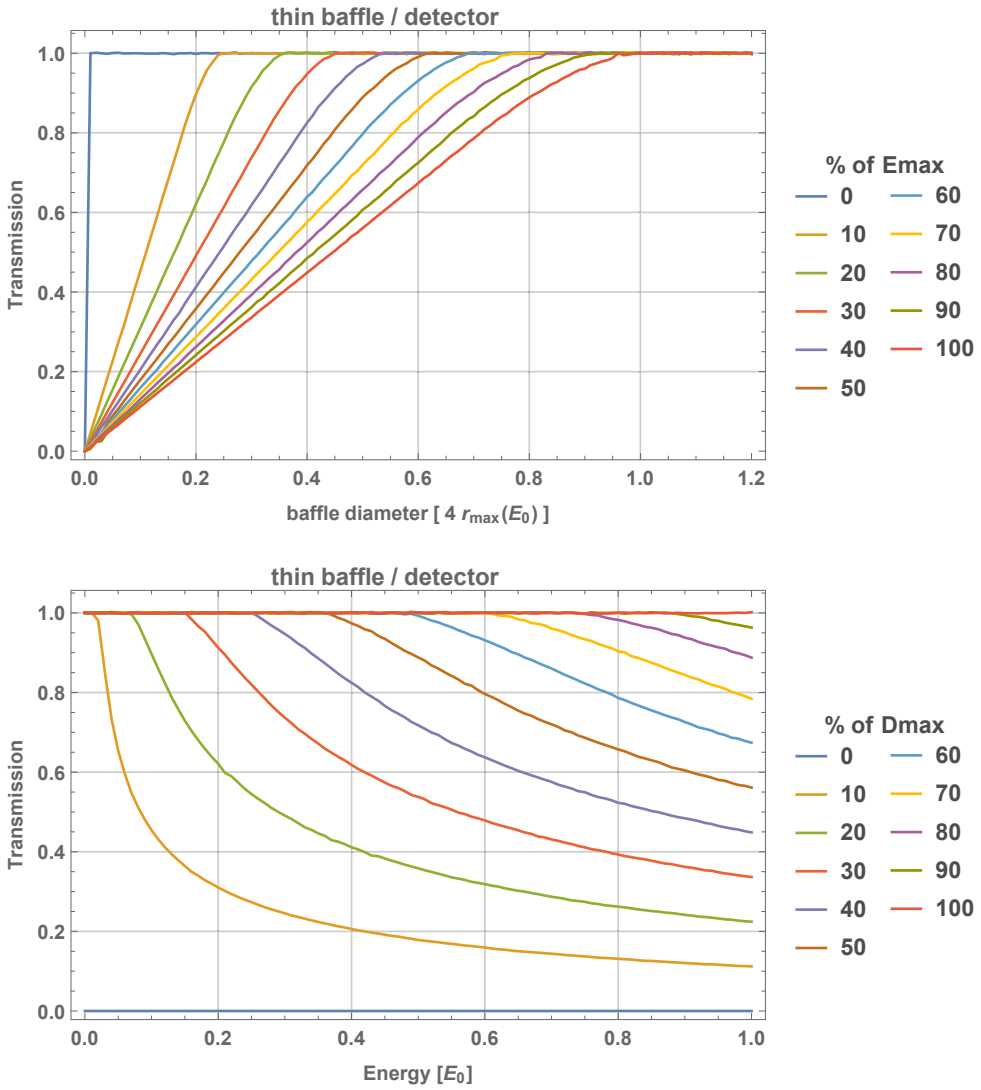

Figure 7.3.: Electron transmission of a thin square baffle or detector. The upper picture shows the transmission as a function of the baffle/detector size for different electron energies. The lower pickture shows transmission spectra for different baffle/detector sizes. E_0 is the end point energy of the electron spectrum and baffle size is given in units of 4 times the maximal radius.

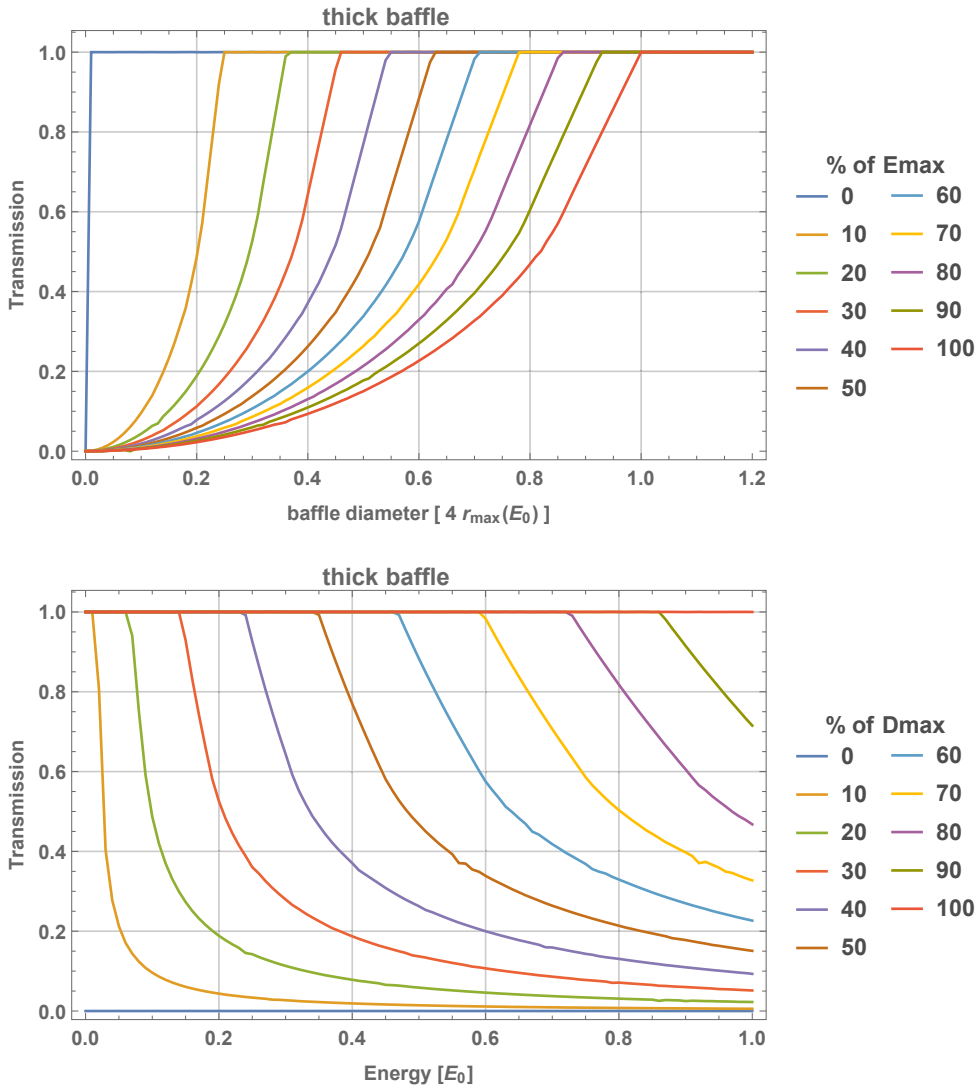

Figure 7.4.: Electron transmission of a thick square baffle. The upper picture shows the transmission as a function of the baffle/detector size for different electron energies. The lower pickture shows transmission spectra for different baffle/detector sizes. E_0 is the end point energy of the electron spectrum and baffle size is given in units of 4 times the maximal radius.

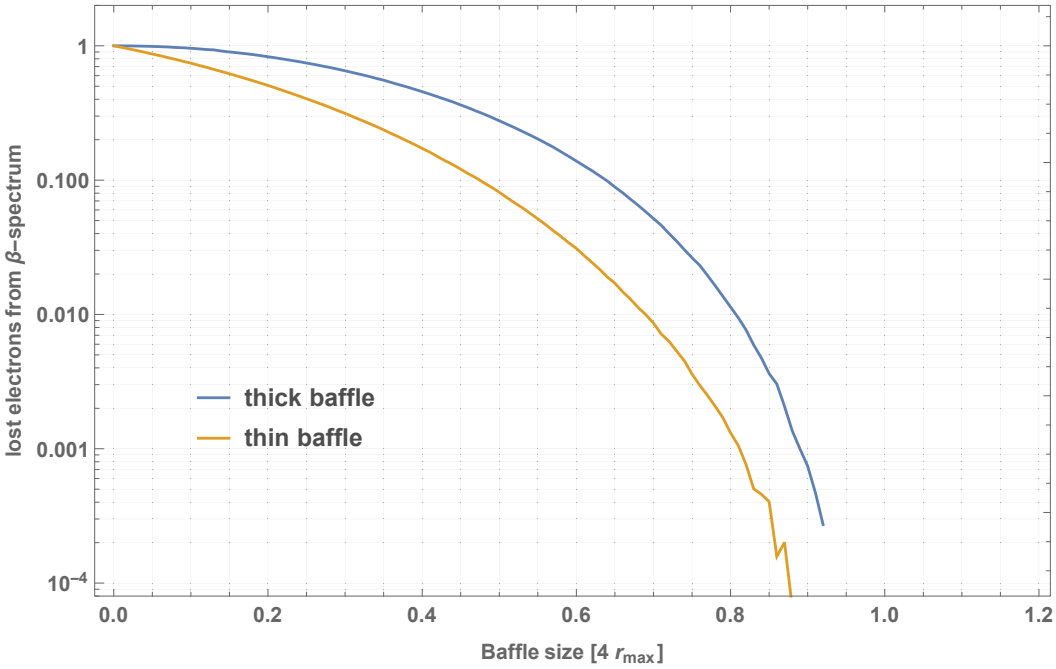

Figure 7.5.: Loss factor of the β-spectrum from a point source through a square baffle with width relative to $4r_{max}(E_0)$. The plot shows numerical fluctuations at the 10^{-4}-level.

of scintillator and light-guides, the not scintillating light guides act as an absorber. In a real case, the scattering on baffle surfaces and the multiple scattering inside absorbing material have to be considered. Also in the case of a thick detector that allows gyrating particles to enter from the side faces has to be calculated differently.

If one wants to include such effects, also the real magnetic field configuration has to be considered including $R \times B$ drifts and inhomogeneities as they have a strong influence on the low energetic protons. For the protons also the transmission function of the retardation electrodes and the combined effects of the electric and magnetic fields surrounding the high voltage conversion system have to be considered.

7.4. Lost Protons in the Final Geometry

Another result from the calculations with the realistic neutron profile is the fraction of the lost particle flux that does not hit the detector. The assumed neutron profile is symmetric in horizontal and vertical direction, this is an acceptable simplification. The real neutron field is slightly asymmetric in horizontal direction and the vertical profile differs a bit from the horizontal. The maximum width of the neutron profile is 15.6 cm (13.0 cm at 10 %Φ_{max}) and the central homogeneous part is approximately 7.06 cm (at 90 %Φ_{max}) wide. Full width at half maximum is 10.0 cm

A two dimensional plot of the density can be found in Figure 7.6. Since the profile is symmetric only one quadrant is plotted. To improve the visibility of the low flux parts, the plotted value is $\log_{10} \Phi_n$. As one can see, the resulting flux profile of the protons is less steep and extends $2r_{\text{max}}$ further in every direction.

To calculate the losses in a detector, this flux profile has to be integrated over the area of the

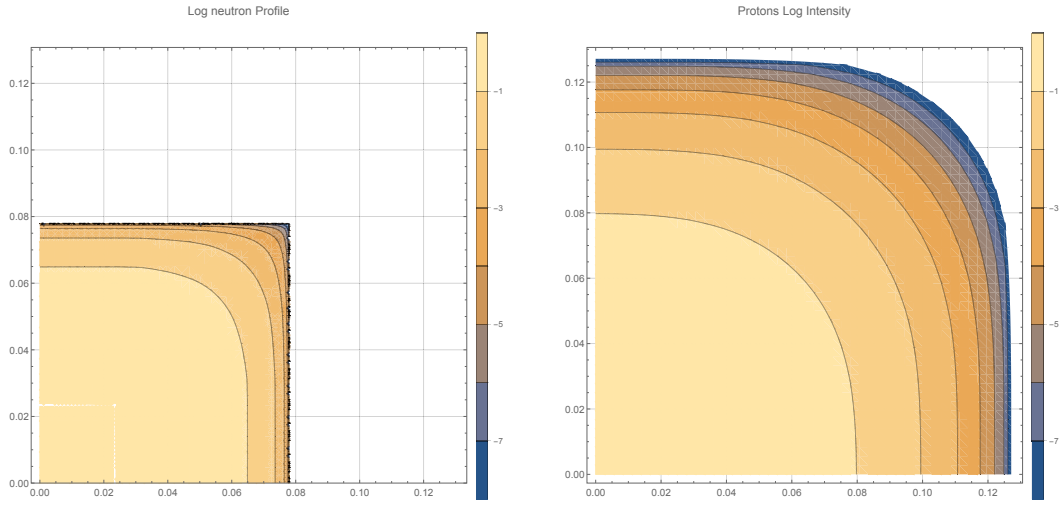

(a) $\log_{10}$ Neutron density (b) $\log_{10}$ Proton density

Figure 7.6.: The density distributions of the protons is broader and its maximal extend is bigger by two gyration radii. Both plots have the same axis scaling and can directly compared.

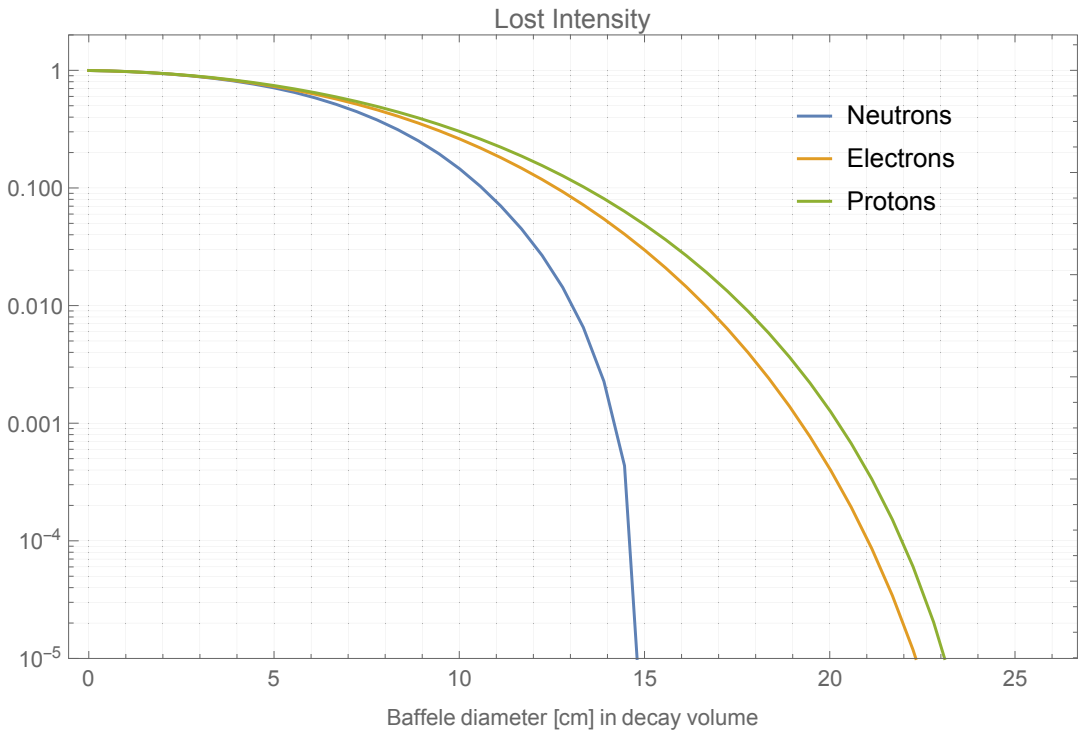

Figure 7.7.: Lost particles for a centered square baffle or detector.

detector and be compared with the integral of the maximum possible area. Those results for the electron and the proton beam are shown in Figure 7.7. The differences of electrons and protons is caused by the different energy spectra and by the secondary effect of the different momentum calculation. For the electron relativistic effects have to be considered.

Both plots discussed in this section are calculated in the decay volume. In order to transform this distributions into conditions in the detector vessel, the distribution has to be stretched by the factor of the magnetic mirror ($\sqrt{B'/B}$). The maximum extend of the secondary particles is 26.16 cm for both particles.

7.5. Uncertainty of the Correction

For the used 10 cm × 8 cm foil the correction on the asymmetry is $C_{\text{meas}}/C_0 - 1 = 0.0181$ and for the older foil holder with 11 cm × 9 cm $C_{\text{meas}}/C_0 - 1 = 0.0188$. For the square foil holder of the big foil 21.5 cm × 21.5 cm the correction is only 0.005 57.

To estimate the influence of the uncertainty of the magnetic field and the absolute foil size, both were varied independently and the absolute shift in the correction is plotted in Figure 7.8 and Figure 7.9. These plots again assume a square baffle or detector to ease the calculation.

Even for huge uncertainties in the size of the baffle or the magnetic field at the baffle, the correction stays small for the used foil sizes. The usage of the small foils placed us near the maximum correction, which seems a bad spot for a measurement. Fortunately the correction is very flat in this region, which allows to calculate the asymmetry quite accurately.

For a reasonable accuracy of 1 mT near the detector the correction can be calculated with $<1 \times 10^{-4}$ precision. The uncertainty due to the size (and positioning) of the baffle is approximately $<1 \times 10^{-3}$ for ± 0.5 cm.

Again this calculation does not take the electric fields, $R \times B$ or combined electric and magnetic fields into account. Those are only available in a full tracking simulation of the experiment.

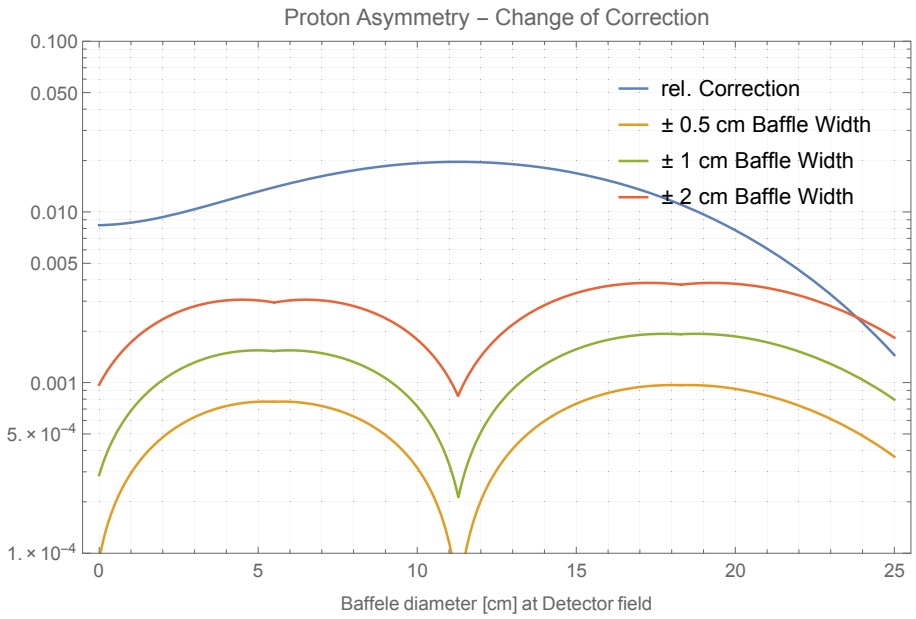

Figure 7.8.: Dependence on width of the baffle. The correction and the shift in correction for different uncertainties in the width of the baffle are plotted. Even for an "uncertinaty" of ± 2 cm the changes in the correction factor stay unexpectetly small.

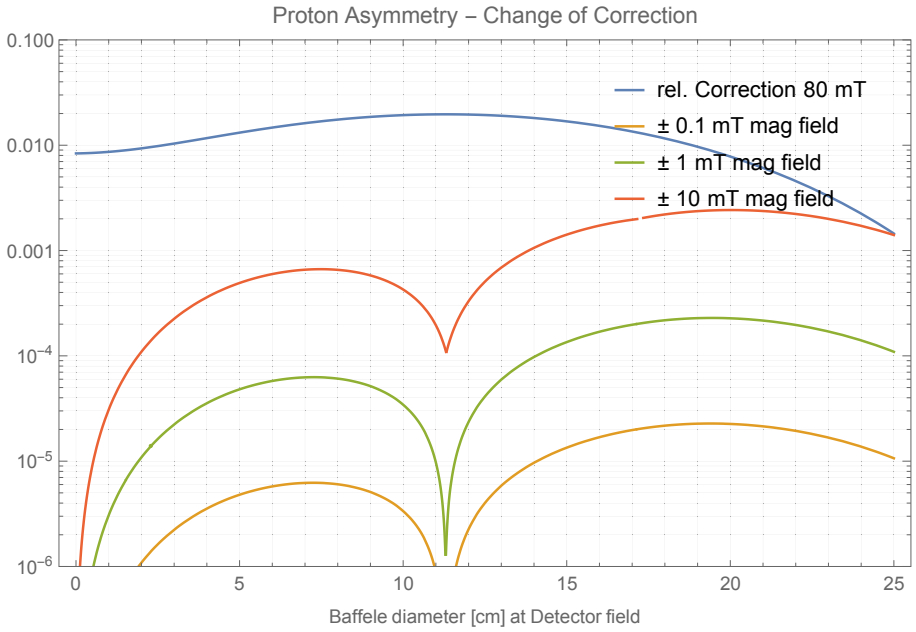

Figure 7.9.: Dependence on the accuracy of the magnetic field. The correction and the shift in correction for different uncertainties in the strength of the magnetic field at the baffle are plotted.

7.6. Observation the Energy Dependent Edge Effect

In order to back up the calculations with measurement data we returned to one of the test measurements in December 2014 where we used the full magnetic field strength and one big foil on the Grenoble detector. The smallest baffle inside the system is the conversion foil holding frame. Unfortunately it is only 1 mm thin and might not absorb all very high energetic electrons. This measurement can be compared with the electron spectra from the end of the beam time in July 2015.

Other differences are the missing energy calibration of the big foil data and the completely different HV-settings of the PMTs. Additionally the upstream detector (Det 1) had one disconnected PMT due to issues with the high-vacuum compatible cable.

Nevertheless one can try to compare the two measurements. The signal from the measurement with the big foil had to be scaled with 7/8 to compensate for the inoperable PMT. Due to the strong 2D-response inhomogeneity of the single PMT signals (see the chapter about the 4-side readout section 6.2), this scaling is only a very rough estimate.

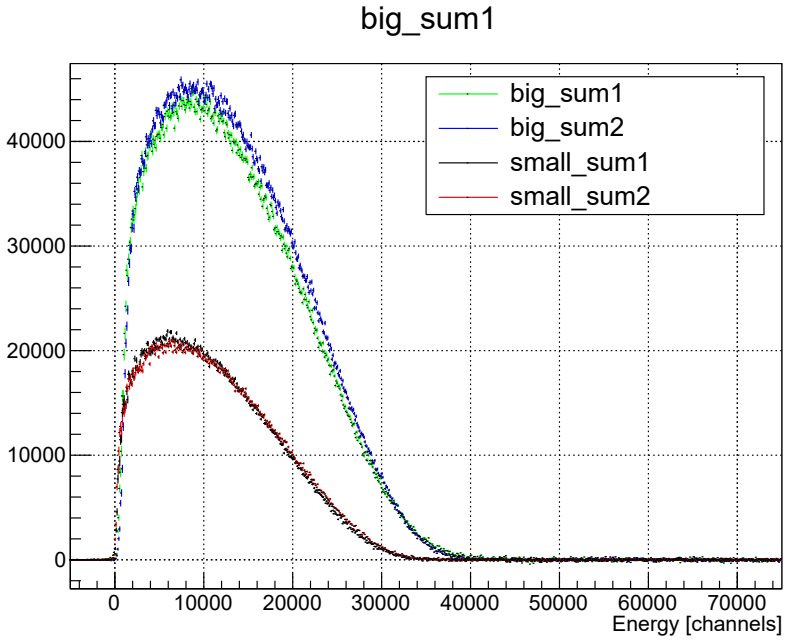

Figure 7.10.: Spectra from the both measurmements with the small and big foil.

The spectra of both measurements are shown in Figure 7.10. They have been normalized for the different measurement time and on the small foil we detect only about 40 % of the events with the big foil. Also we can observe that the end point energy of the spectra are not comparable. This is strange, because even for very small apertures one can expect to see a fraction of the highest energetic particles (compare Figure 7.3).

Even though we can suspect that the data is not really comparable, we can try to see the relative factor between the two measurements. Dividing the spectrum of the small foil by the spectrum of the big foil, should give a transmission spectrum of the small foil. This is presented in Figure 7.11

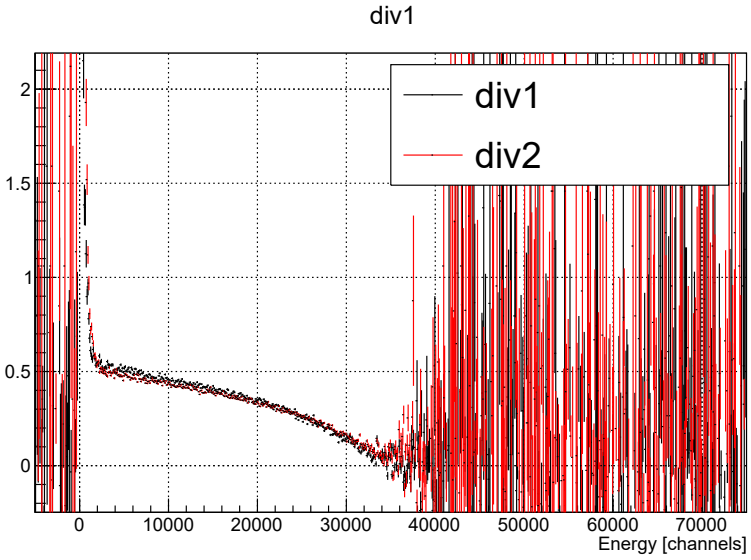

Figure 7.11.: Spectra from the division of the small and big foil.

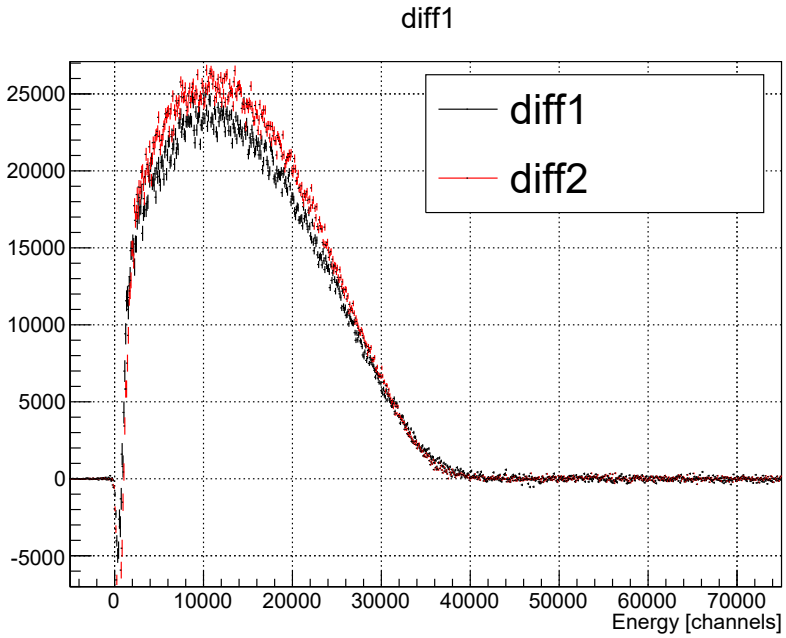

Figure 7.12.: Spectra from the difference of the small and big foil.

Part III.

Measurement of the Proton Asymmetry

8. Beamtime Overview

The instrument was set up at the ILL in Grenoble from March 2014 until July 2015. Due to delays in foil production and several hardware failures, including the loss of one 600 A power supply and the cooling water purification system, it took until December 2014 to proof that the system was indeed detecting protons. Together with a detailed plan for further improvements, this allowed us to extend the stay at the ILL for another cycle of data taking in May 2015. After a thorough measurement of the polarization and many datasets of systematics studies, the first asymmetry data was collected. A unforeseen reactor shut down lead to a final extension of 13 days of beam time in June. The data collected in these days is the main source for this analysis.

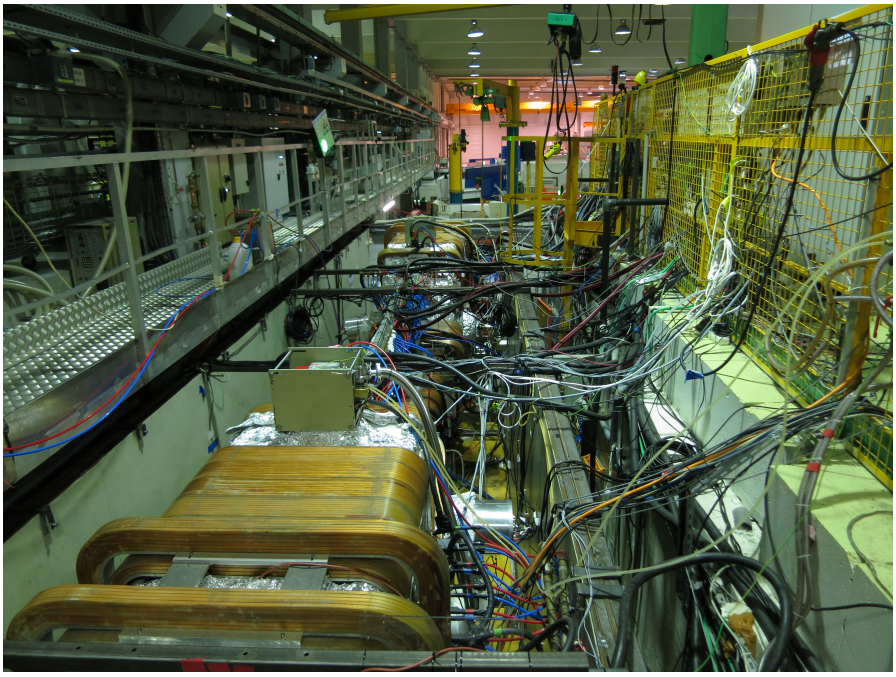

Figure 8.1.: Picture of the spectrometer installed at the beamsite

In addition to the hardware failures, other things also slowed down the progress of the beamtime. Many tests required a sufficient vacuum that took at least one day of pumping, which increased the feedback time of the tests. The HV-System was tested to be stable at atmospheric pressure as well as under vacuum, nevertheless when combined in the final geometry using two HV-Systems and the Perkeo magnetic field geometry the field in the HV-systems would break down at low voltages (<1 kV) under vacuum. Many tests required a sufficient vacuum that took at least one day of pumping, which increased the feedback time of the tests but finally most of the problems could be resolved.

Another source of delays was the extremely fragile conversion foil. In the previous measurement of Perkeo II it was possible to transport approximately ten foils from Munich to Grenoble

while only breaking two of them on the way. The production of the big foils was additionally much more dependent on the right weather conditions during the production. Currently the foils can only be produced in Munich, which made us strongly dependent on the status of the lab and the conditions of the production environment. A first successful transport of foils in 2104 caused us to underestimate the dangers of the foil transport. All other transports of the big foils failed even though we tried our best to maximize safety on the transports. Therefore we had to use small foils for the final measurement which will contribute to our systematic error.

In addition to the author three PhD students were involved in the beamtime. C. Roick (Heidelberg / Munich) and M. Klopf (Vienna) attended the full beamtime. H. Saul (Vienna / Munich) worked full time on site until the end of 2014 and he assisted the polarization measurement in 2015. Dr. T. Soldner (ILL) was involved as the local contact and beam site responsible. He coordinated the measurement with the ILL and was involved in all major decisions. Dr. G. Konrad (Vienna) attended all beam times and supervised the improvements in the beginning of 2015. Prof. Dr. B. Märkisch (Heidelberg / Munich) is the project leader of the PERKEO III experiments. Additional support in weekly discussions came from Apl. Prof. U. Schmidt (Heidelberg) and Prof. Dr. H. Abele (Vienna). W. Mach, a PhD student from Vienna, assisted during the initial mechanical setup of the beamline and spectrometer and performed the polarization measurement together with T. Solder and H. Saul. Three interns helped with various tasks while setting up the experiment. D. Moser (Vienna) started his master thesis on the project after finishing his internship and is currently working on a simulation of the magnetic field. D. Berruyer (ILL) was the technical assistant of the PF1B beamsite. For several heavy tasks we had temporary assistance from technicians from Heidelberg, Munich and the ILL.

9. Data Analysis

9.1. Methods

The data analysis is mainly handled by the custom made program named `p3reduce` that was developed by H. Saul [Sau16]. It is based on several earlier analysis programs from previous PERKEO measurements and adapts the ideas of configuration files and several intermediate output files that can be generated independently. This approach was very useful in the past. The new program extensively uses modern features of `C++` like templates. Therefore it was relatively easy to add the capability to handle the new data from the proton measurement. The new detector has more PMTs per detector, utilizes another TDC and has a different data file structure. This modifications of the `p3reduce` software were done by H. Saul. I implemented several plugins for the analysis software and made existent plugins compatible with the new proton data.

Useful functions of the ROOT framework are encapsulated in the software and all intermediate and final output files are compatible ROOT files. For each analysis step an input list is needed that specifies the location of the data files. Additional information such as invalid cycles are also coded in the input file. A global configuration specifies common settings such as the number of energy bins in the spectra. Other options can be set globally and locally for each analysis. Such settings include filter settings, ToF-window definitions, relative scaling factors and several output options.

This proton measurement is different from a stable electron measurement with constant measurement schedule. Several times we had to optimize the high voltage settings and we measured at different retardation electrode settings. The analysis program is not suited for such a high number of configurations. Therefore the input lists are pre-selected and categorized by an external script. Careful study of the measurement logbook helped to separate data files that were used to debug or optimize the system from the real measurement data. Additionally, all cycles with failed water cooling, power supply or neutron beam had to be sorted out. The external script then reads all the meta data from the ROOT files from the accepted master list. This script then detects the different electrode settings used in the cycles of the file. It respects the mapping of electrodes to HV channels whose definition changed sometimes.

If a retardation setting is stable over the whole file, this file is added to the prime list of files that all have this retardation setting. In case that a data file contains events that were collected while the retardation system was ramped up or down, that file is only added to a secondary list that also accepts files with non constant retardation settings. The few cycles with unstable voltages while ramping are marked invalid. This might introduce a bias, since it is always the first cycles that are removed. The retardation settings are named after the highest voltage they provide. For example `FULL850_BT` is designed to completely block the protons, while `PROTONBLOCK10_BT` and `PROTONBLOCK10_BT_NO_RAMPING` are collected with a maximum potential of 10 V. If the retardation system is grounded the setting is called `DEFAULT`.

Unused functionality of the main analysis program (`p3reduce`) is the grouping in calibration and drift sets that are independently handled. This cannot be used because the calibration device was not installed during the measurement. But the grouping is now used to distinguish different settings of the foil's high voltage. The many changing configurations are divided into five major datasets. Table 9.1 shows the cycle ranges and a short characterization of the datasets.

No.	first cycle	last cycle	No. cycles	comments
0	0	417 813		before the start of the last beamtime
1	417 814	434 621	16 807	both degraders above 15 kV
2	434 750	484 474	49 724	Grenoble 15 kV; Lyon varied around that
3	484 894	511 301	26 407	Grenoble and Lyon varied <15 kV
4	511 302	519 329	8027	Lyon degrader shut down
5	519 510	523 733	4223	Both degrader off; only electrons

Table 9.1.: Grouping of the cycles in the last beamtime. Groups 1 to 3 are often grouped as the full data set for proton asymmetry data. This is then called group −1. Grenoble is the upstream degrader and Lyon the downstream degrader.

9.2. Pedestals

The natural noise in the analogue part of the readout system leads to an extended distribution of ADC values even for events with no energy deposition in that ADC. To avoid to cut into parts of this spectrum, the ADC adds a small signal to each integration. This shifts the noise distribution by the amount of the so called pedestal. Each individual ADC has a slightly different pedestal value. The width of the pedestal signal distribution in each ADC is very gaussian and is $\sigma_{\mathrm{ADC}} \approx 30\,\mathrm{ch}$. When combining eight ADCs to a detector signal, the with of the combined pedestal is expected to be $\sigma_{\mathrm{det}} \approx \sqrt{8}\sigma_{\mathrm{ADC}} \approx 85\,\mathrm{ch}$

As an additional and previously unused feature we stored two samples of the ADC values per trigger event. One sample before the integration and the other after the integration. Usually we use the difference of both ADC samples. This reduces the amplitude of the pedestal that we have to subtract but does not get rid of the pedestal completely. Taking only the second sample of the ADC is comparable to the way the ADC signal was recorded in the previous measurement.

In this previous measurement with the current ADC-boards [Mes11] the pedestals were extracted from events in which only one detector triggered. There the signal on the not triggered detector can be taken as the pedestal. We introduced another way to measure the pedestals. At the beginning and the end of each measurement file the electronics just recorded signals with an artificial trigger. The data of those measurements was collected in two pedestal trees called first and last, which were measured at the start and end of the data file respectively.

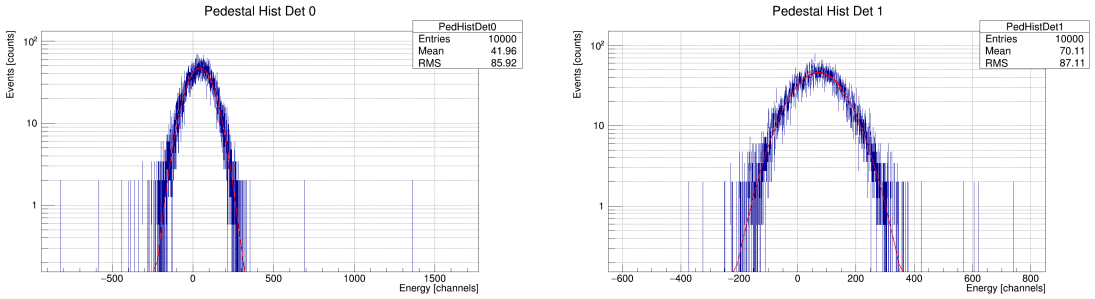

(a) Upstream Detector (Grenoble)

(b) Downstream Detector (Lyon)

Figure 9.1.: Fit of the detector pedestal of a single data file from the lastPedestalTree in diff mode.

The pedestals can be extracted from this measurements. For each data file the pedestal of each

PMTs is collected from the pedestal tree and then fitted with a gaussian distribution. Typical results of those fits are presented in Figure 9.1. The central value is considered the pedestal and its value slowly drifts with time as seen in Figure 9.2a. The amount of fluctuation is comparable to the last measurement where the pedestal changes were approximately 40 ch around the value of about 7250 ch extracted from the non-differential measurement mode. The width of the pedestal fit is very constant over the whole measurement time (see Figure 9.2b). The average width on the Grenoble detector is 80.4 ADC Units and 83.9 ADC Units on the Lyon detector as expected from the characterization of the ADC modules in the last beamtime.

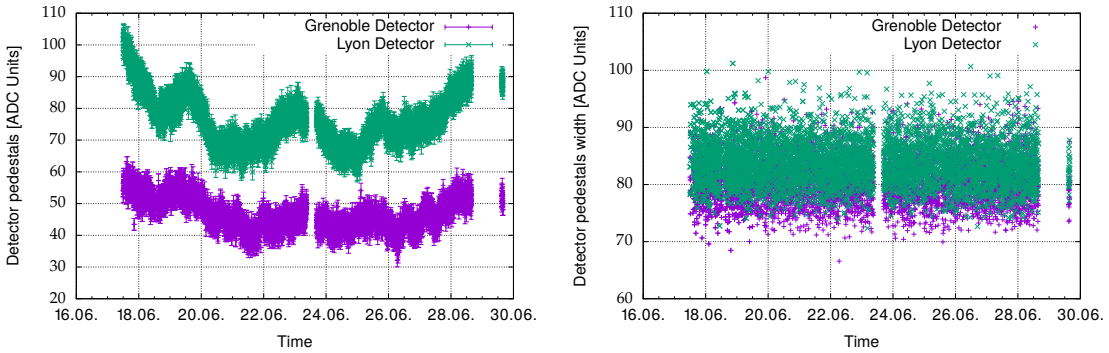

(a) Plot of the combined detector pedestal over the last beamtime.

(b) Plot of the combined detector pedestal width over the last beamtime.

Figure 9.2.: Plots of the pedestal over the last beamtime.

In every further analysis, this pedestal value of each PMT in the specific data file is subtracted from the measured ADC value. Those pedestal corrected ADC values are then combined to the signal of the respective detector. At the same stage it is also possible to scale each PMT individually for the recalibration of the 2D-response.

9.3. ToF and Rates

The next step is to check the Time of Flight spectra, since for a good background subtraction the count rate in the background window should be flat. Those ToF spectra vary with each retardation setting and analysis group. As an example the combined ToF spectrum of the third data group for the retardation settings `PROTONBLOCK10_BT` and `FULL850_BT` are presented in Figure 9.3. The position of the signal ToF window is determined by the analysis of the velocity spectrum of the neutrons beam, which can be calculated from the settings of the velocity selector and the chopper. The signal window is centred around 4.7 ms and currently extends 1 ms in both directions. The time window for the background measurement can usually be placed somewhere between 11 ms and 13 ms. In the further analysis we take this whole range as the background ToF window.

Generally we can find the optimal background window by fitting a linear slope to the background. For the data sets presented in Figure 9.3 the background fits good with a zero slope in the range from 11 ms to 13 ms For the `FULL850_BT` retardation off the third data group the slope is $2.0(31) \times 10^{-4}$ (Chi2/ndf $= 72.4377/78$) for the upstream detector and $-3.3(45) \times 10^{-4}$ (Chi2/ndf $= 90.0564/78$) for the downstream detector. The fits of the `PROTONBLOCK10_BT` dataset

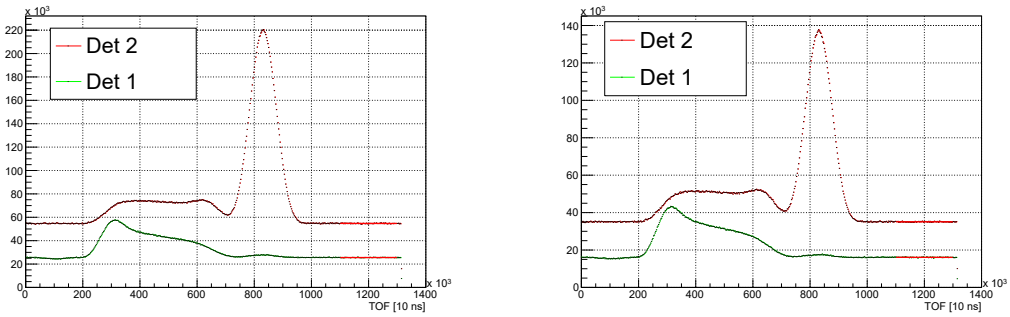

(a) Electron data set (FULL850_BT) (b) Proton data set (PROTONBLOCK10_BT)

Figure 9.3.: Different ToF Spectra from the third HV configuration dataset.

are similar with a slope of $-1.9(24) \times 10^{-4}$ (Chi2/ndf = 89.5489/78) for the upstream detector and $4(36) \times 10^{-5}$ (Chi2/ndf = 77.1935/78) for the downstream detector.

When extracting the rates for the different retardation settings it can be seen that the rates are very high. A typical plot of the number of signal events per cycle over the last beamtime is shown in Figure 9.4. This plot only contains the data from the FULL850_BT retardation setting. Plots of the other settings all look similar with a small absolute shift caused by the blocking of proton intensity.

From the combined analysis of the different retardation settings it can be concluded, that the high fluctuation of the rates does not effect the true signal rate after the subtraction of the background event rate (see Figure D.2). This is a good sign and allows the further analysis of the data. The high rates therefore are not correlated with the beam but seem to be correlated to the configuration of the degraders. When separating the detectors (see Figure D.1 in the appendix) one can see that most of the background triggers are detected on the downstream (Lyon) detector, however both detectors are triggered by an event on one of them. The significant rate for the analysis is the combined trigger rate as plotted in Figure 9.4. Later we introduced the delta time cut which reduces the measured rates, but only partially reduces the big range of rates.

9.4. Drifts

During the final bematime the calibration robot was not installed and thus we could not recalibrate the detector. All analysis of the drift data is only based on simple fits to the electron spectrum. The Spectrum itself is quite featureless and therefore offers no real sensitivity at low counts. Therefore only a simple fit of the Fermi spectrum with two free parameters (pseudo-gain[1] and norm) was fitted. In a first run the Fermi Function is fitted between 1×10^3 to 30×10^3 ADC channels. As a second step the ADC channels for $0.1\,E_{max}$ and $0.9\,E_{max}$ are calculated and then used as the range for a second fit.

In Figure 9.5 the extracted pseudo-gain is plotted over time. The error in the determination of the drift is very big. A Fourier analysis of the data did not show any significant periodicity in the drift. Comparing the data with the measured temperature of the spectrometer did also not provide any correlation.

[1] this gain is not the real gain of the PMT, but more an effective gain

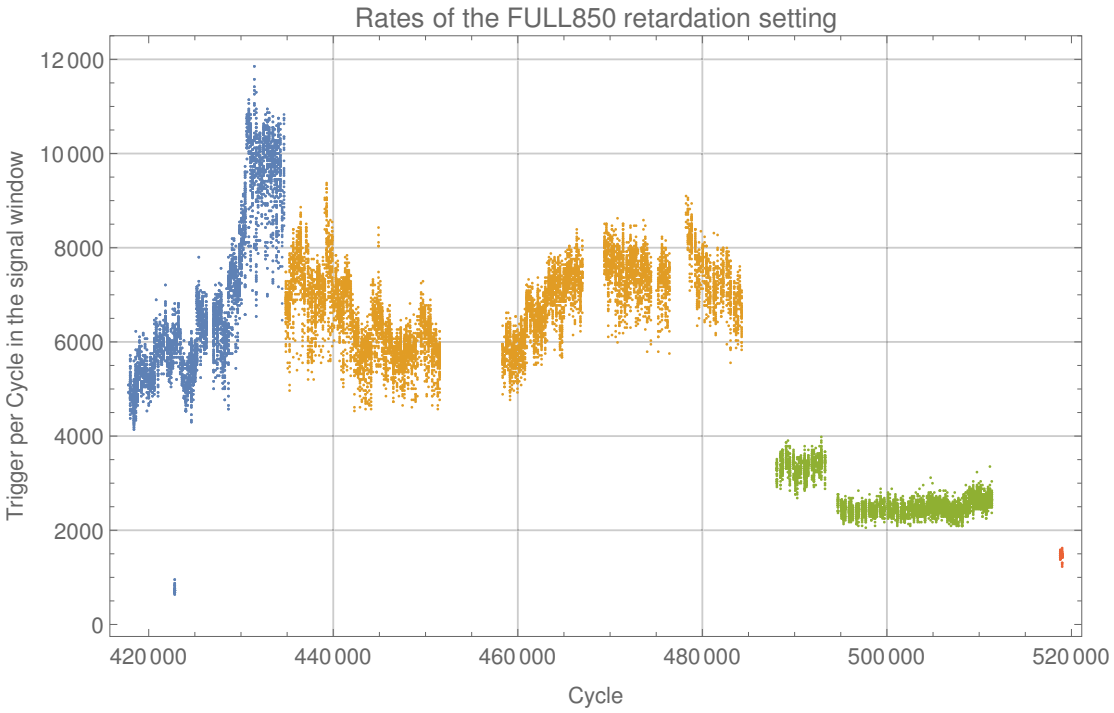

Figure 9.4.: Events per cycle of the last beamtime. Only the electrode settings `FULL850_BT` (no protons) are shown. The colors shows the different data groups. Blue is set 1, orange set 2 and green set 3.

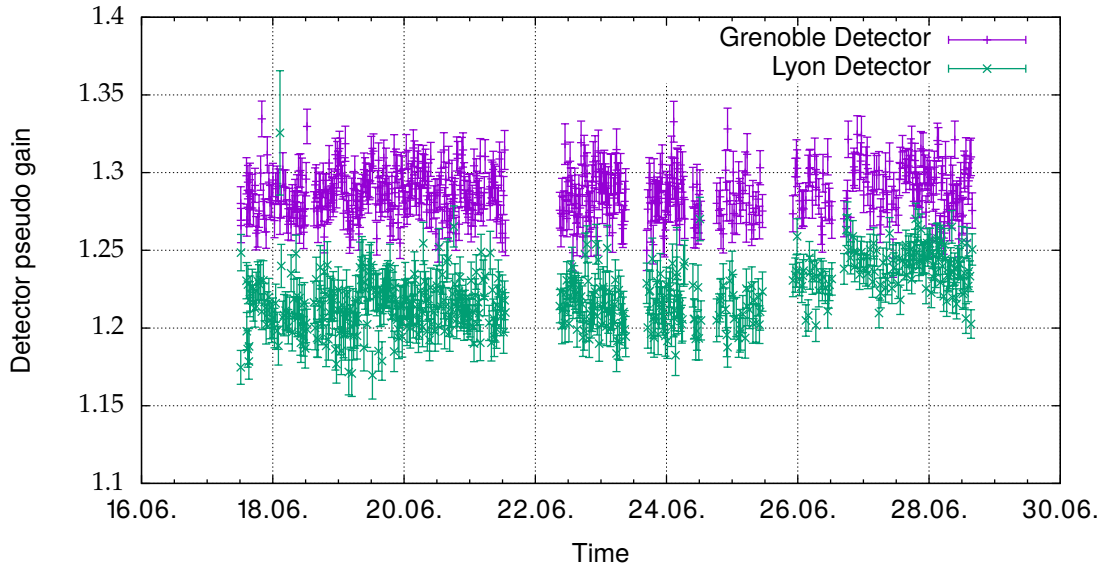

Figure 9.5.: Time evolution of the detector drift on the downstream (Lyon) and upstream (Grenoble) detector

9.5. Time Structure of the Background

To analyse the time structure of the background, we studied the two dimensional (delta time and energy) histogram of all pairs of events that happen right after each other. When plotting the energy of the second event of the pair against the time difference of the two triggers, interesting structures emerge.

For the dataset 2 and the FULL850_BT retardation setting (no protons) the histograms of both detectors are shown in Figure 9.6, but the plots for other retardation settings such as PROTONBLOCK10_BT do not differ except for statistics. Additionally, no difference in the effects can be seen when comparing the plots for the signal and background time window.

On the upstream detector (Figure 9.6a) an unexpected structure appears for delta times below 2 µs. This huge excess of events with very low energies and even negative channels (after pedestal subtracion) is attributed to effects in the ADC card that occur at very short time differences. An additional source of highly temporal correlated events with short delta time are the result of afterpulses in the scintillator or the PMTs. Further studies of those effects are currently done in the lab.

On the downstream detector (Figure 9.6a) the situation is worse (please note the different scale of the color coding). All rates are much higher and another unexpected structure appears for delta times below 6 µs. These events all have energies above 0 ch but below 5000 ch. For specific delta times the number of events is strongly increased and it extends into high energies. In order to identify the source of the problem, the same analysis was performed on the pure electron dataset from group 5. In this reference data set from the end of the beamtime all high voltage system were tuned off and a pure electron spectrum with the foil holder as an aperture was measured. As presented in Figure B.1 (in the appendix on page 135) this effect vanishes and the histogram of the downstream detector is comparable to the Grenoble detector including the swinging structure at delta times below 2 µs.

In order to exclude those signals from the further analysis we introduced the possibility to filter events by their delta time to the previous or next event. The influence of such a filter on the spectra was studied and the results are shown in Figure 9.7. The big low energetic peak of the afterpulses can be suppressed by the cut on the delta time without influencing the higher energetic parts of the spectrum.

For the further analysis, a delta-time cut at 6 µs was chosen. This is reasonable since the proton signals are expected more than 6 µs later than the corresponding electron. This can be seen in the histograms of the delta-time in the signal window for the FULL850_BT (no protons) and the PROTONBLOCK10_BT retardation settings (10 V) on the upstream (Grenoble) detector. The low background on that detector enables us to observe this effect. Those histograms (Figure B.2 and Figure B.3) can be found in the appendix on page 136. In the same place also the histograms of the downstream detector can be found, but the low energetic background from the HV makes it difficult to see the electrons and protons in these histograms.

But those delta-time cuts influence the quality of the background subtraction. To quantify this problem, the spectrum is fitted with a constant function for energies beyond the electron spectrum from 40 000 ch to 60 000 ch. The distance of the fit constant from perfect zero is expressed in units of the errors of the fit. For this analysis a relative scaling between the signal and background spectrum is not applied. In section 9.7 the so called deadtime effects are discussed that introduce such a scaling. For the huge range of delta-time cuts from 0 µs to 100 µs the quality of the background subtraction is plotted in Figure 9.8. This almost linear behaviour might help to understand the dead-time scaling factors better.

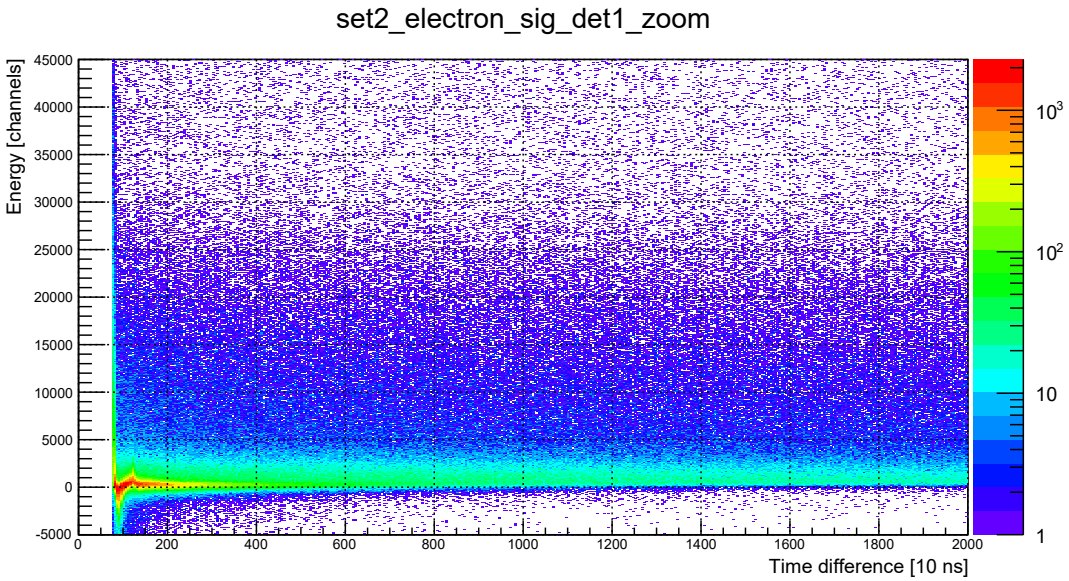

(a) Upstream Detector (Grenoble)

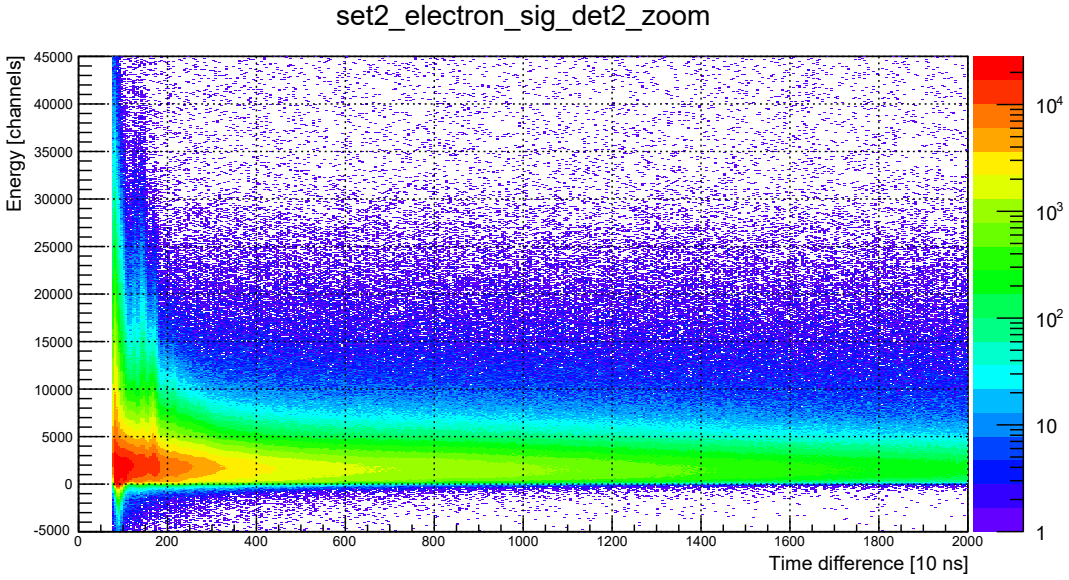

(b) Downstream Detector (Lyon)

Figure 9.6.: Correlated histograms of the `FULL850_BT` retardation (no protons) data from group 2 (both degraders around 15 kV). The time difference of the two events and the energy of the seconnd event are plotted. The delta time axis has a range of 0 µs to 20 µs.

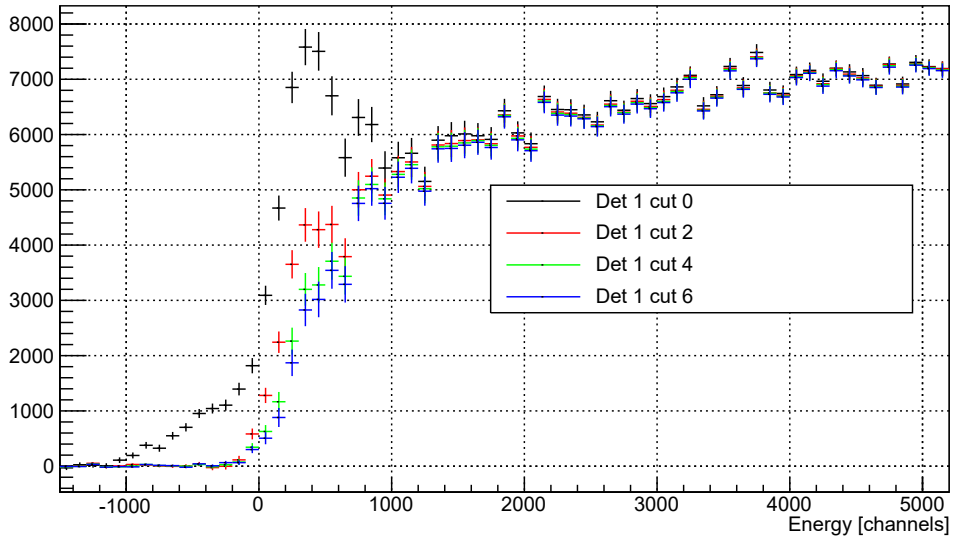

Figure 9.7.: Spectra of the upstream (Grenoble) detector depending on the minimum allowed delta time to the previous event. Shown are the cuts for 0 µs, 2 µs, 4 µs and 6 µs.

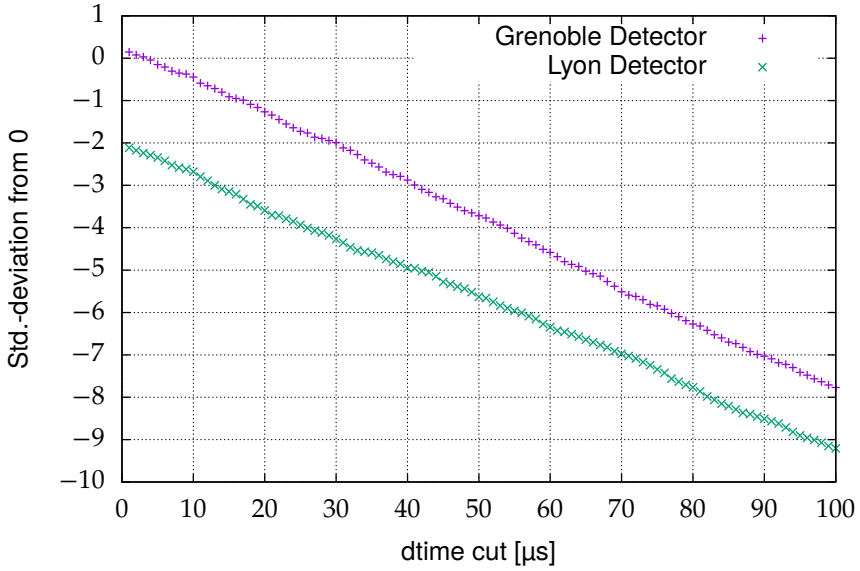

Figure 9.8.: Influence of the delta time cut on the background subtraction. Plotted is the difference of the flat part of the spectrum in units of standard deviations. From the pure electron spectrum with all HV systems off (group 5).

9.6. Backscattering

Electrons that backscatter from the detector surface do not deposit all their energy in the scintillator and thus disturb the measured spectra. For PERKEO II this has been studied by Schumann and Abele [SA08]. From all possible combinations in the backscatter decision tree (Figure 9.9) only one alters the asymmetry. If a backscatter event only triggers in the second detector it is wrongly assigned to that detector. In the other case of an event that triggered the first detector but not the second detector, the energy information can be recovered by triggering both detectors simultaneously.

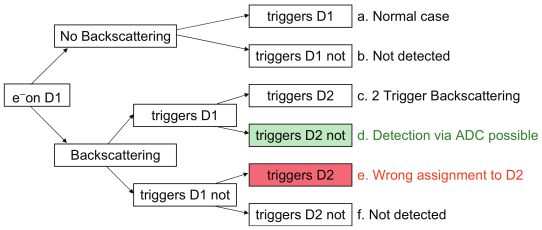

Figure 9.9.: All possible results for an event. Only case *e* has an influence on the asymmetry parameter

For the secondary electrons from the conversion process, the backscatter probability is strongly suppressed. Such an electron is very low energetic and its only energy originates from the acceleration in the electrostatic field. If it backscatters from the detector it looses a part of its energy and cannot overcome the electric potential from the same field degrader.

Nevertheless the primary electrons can backscatter and are detected on the opposite detector. But they are also suppressed by the electrostatic potential since they might exit the detector with energies so low that they cannot overcome the electrostatic barrier. Figure 9.10 shows this spectrum and the small shift to higher energies if the backscattered energy is added to the primary signal. For fits of the electron spectrum this correction has to be made, but the backscattering does not impose any correction on the proton asymmetry measurement.

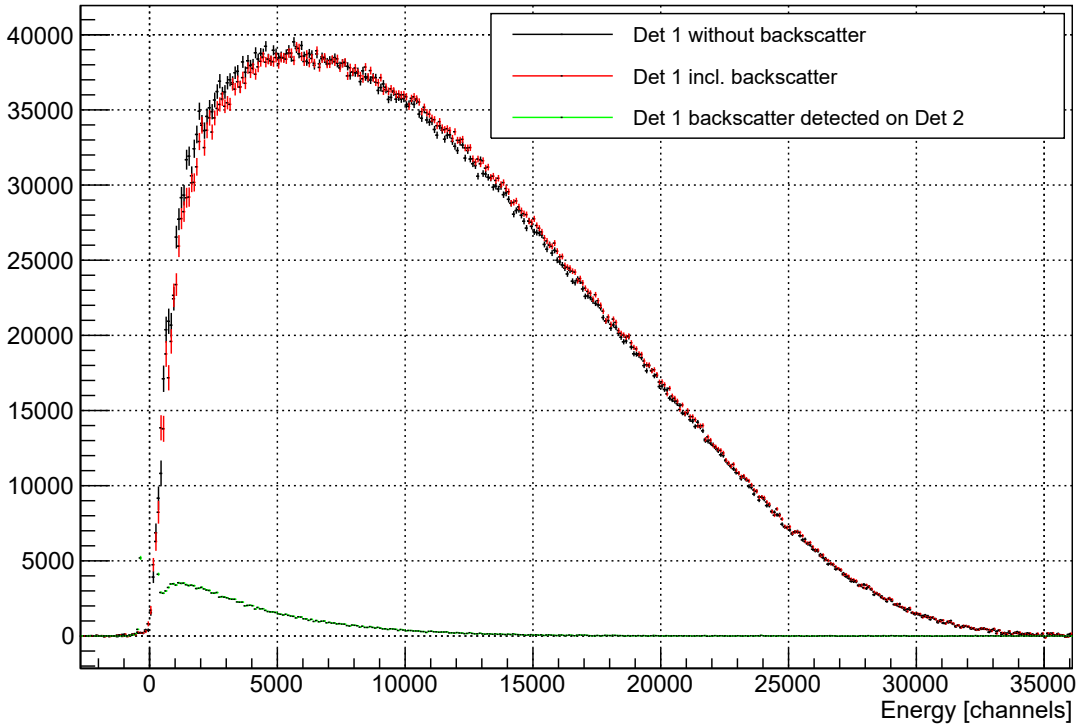

Figure 9.10.: Plot of the backscatter spectrum of the Grenoble detector for the electron data set. The green curve is the spectrum that is detected in coincidence on the opposite detector.

9.7. Deadtime Correction

After each trigger the measurement electronics is blind for further events. Because of this deadtime of the detector, the measured rates are not the true event rates of protons and electrons. More importantly, the correction factor to convert to a real rate depends on the measured rate. This correction factor has to be taken into account if spectra with different rates are subtracted from each other.

9.7.1. Calculating the Deadtime Scaling

The problem of correcting a measured rate for deadtime effects is extensively discussed in the literature. For this simple approach I closely follow the book *Techniques for nuclear and particle physics experiments* by Leo [Leo94, p. 122 ff] and the dissertation of H. Mest [Mes11]. For more complicated cases follow the references in [Leo94]. The general assumption is that the process has purely poisson distributed events. The frequency of the time difference of two events then falls exponentially.

One has to distinguish two basic cases of deadtime. The first case is the so called "non-extendible" deadtime. In this case the detector is blind for any event within the deadtime and therefore deadtimes cannot overlap. The second case is an "extendible" deadtime which, in the case of a second event within the deadtime of the first, is prolonged. For extremely high rates this can lead to an almost completely blocked detector.

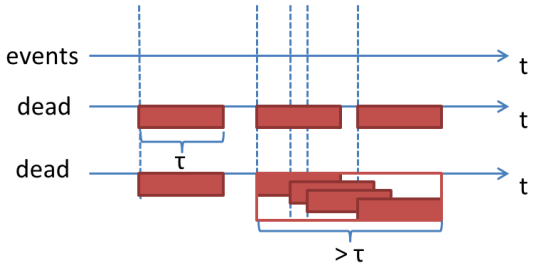

Figure 9.11.: The two deadtime models, non-extendible in the middle and extendible on the bottom adapted from [Leo94]

Figure 9.11 shows the difference of both cases for a series of five detector triggers. When the deadtime is non-extendible (upper case in the plot) the last event of the burst is registered in the detector even though it followed its predecessor after less than the deadtime. Therefore from the five events in the time frame only events 1, 2 and 5 are registered. This model corresponds to the electronic veto logic in the data acquisition system.

The extendible deadtime model blocks the last event and therefore has to be used to describe the cuts on the delta time[2]. Here only the events 1 and 2 follow the previous event later than the deadtime and are not filtered in the delta time filter of the analysis software.

Since the cuts on the delta time are done using a bigger time constant (6 µs) than the electronic deadtime of the DAQ system (800 ns), the discussion is limited to the extendible case. For the rates present in our system (below 12 000 s^{-1}) both models are equivalent on the 0.8×10^{-3} level.

Following the nomenclature from [Leo94] the true rate is called m and within the measurement time T a total of k events are detected. The deadtime is called τ and in the extendible case describes the minimal time.

[2] when comparing to the previous event. Comparing to the next event should be similar but is not used in the analysis.

In the non extendible case, the true rate can be calculated by equation 9.1

$$m = \frac{k/T}{1 - (k/T)\,\tau} \tag{9.1}$$

In case of an extendible deadtime with a minimal deadtime τ after every event, the true rate can be found by the numerical solution of equation 9.2.

$$k = mT \exp(-m\tau) \tag{9.2}$$

For each number of events in the detector there are two solutions of real rates. For very high rates the detector is blocked most of the time and can only register another event if there is a gap of at least the minimal deadtime. This behaviour is expected for rates above $m = 1/\tau$, which in the case of a delta-time filter of 6 µs corresponds to rates above 167 MHz.

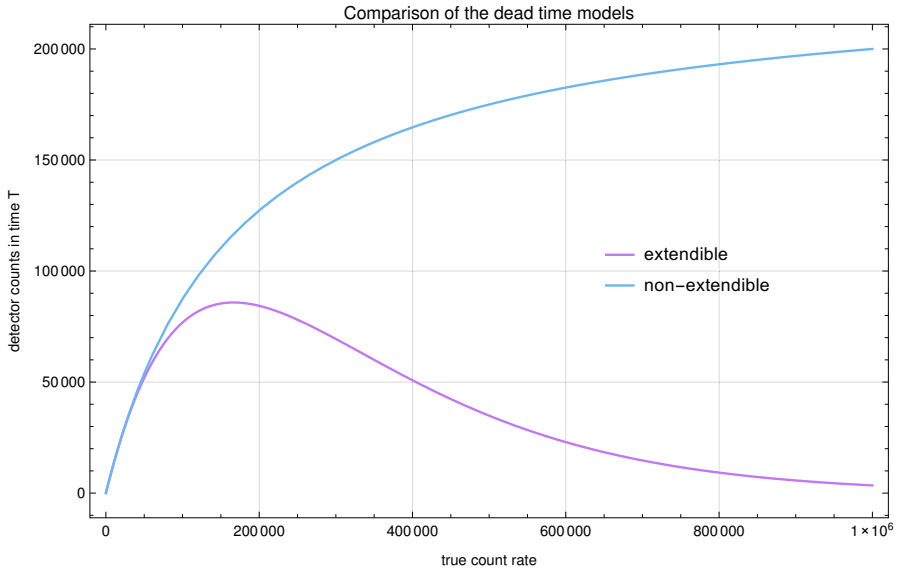

Figure 9.12.: Comparing the two different deadtime models

Comparing the detected rates of up to 15 000 s^{-1} one can observe that both models show a very similar functional behaviour. For a true rate of 10 000 s^{-1} the measured counts on the detector for the different deadtime models only differ on the 10×10^{-4} level. If for further measurements the numerical speed of the calculation is important, the extendible model can be approximated by the non-extendible model.

As seen in section 9.3 the events per cycle within the signal or background window (from now on also called signal and background rates) vary by a large amount. This variation can be described by a strong fluctuating part and a slower overall drift or variability. The long term variability is hugely influenced by the setting of the conversion foil potential. Short time fluctuations seem to be more stable in their amplitude and show no apparent time structure.

When comparing the signal and background rates for a constant electrode setting as a function of time one can see that both scatter by the same amount. This confirms the hypothesis, that this fluctuating background is not correlated with the signal.

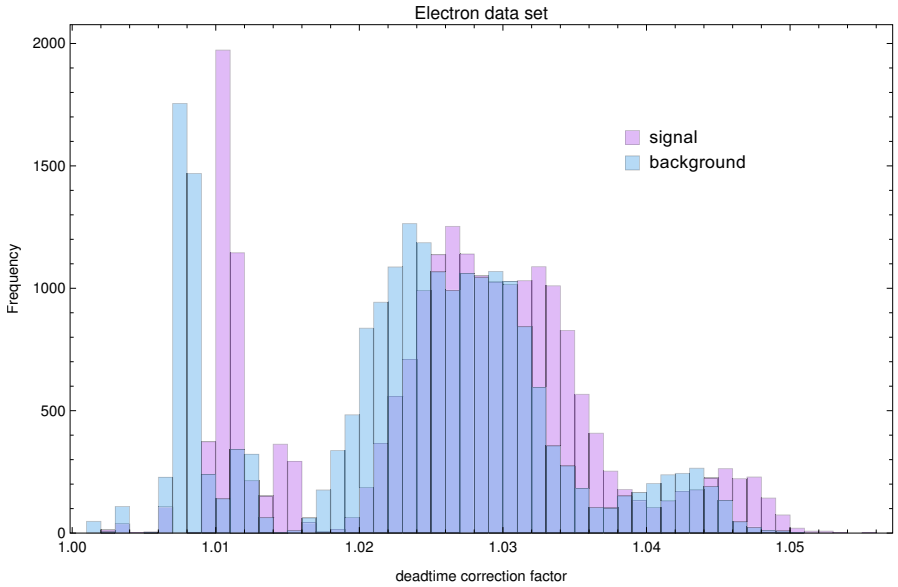

Figure 9.13.: Histogram of the deadtime correction factors for the electron data set (`FULL850_BT`). In cyan k_{sig} for the signal rate and in blue k_{bkg} for the background rate.

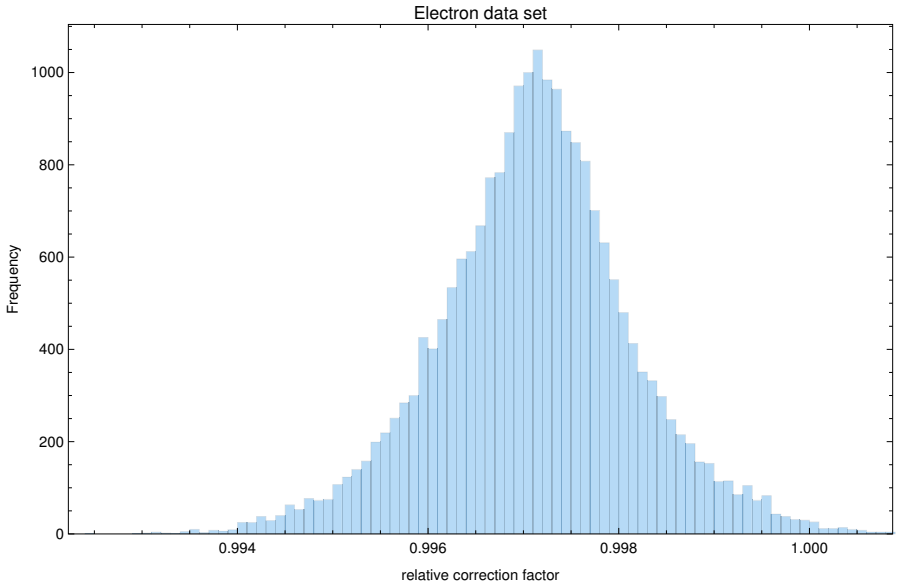

Figure 9.14.: Histogram of the relative correction factors for the scaling of the Electron data set with respect to the different rates of signal and background time window.

In order to be able to correctly subtract the background spectrum from the signal, the measured rates first have to be converted into the true rates. The resulting clean, background subtracted, spectrum (R_{clean}) can be determined.

$$R_{clean} = k_{sig} \cdot R_{sig} - k_{bkg} \cdot R_{bkg} \tag{9.3}$$

Those correction factors (k_{sig} and k_{bkg}) vary by a huge amount since they depend on the rate. However, the determination of the asymmetries does not rely on the absolute true rate. Therefore it is allowed to only scale the background relative to the signal rate.

$$\widetilde{R}_{clean} \equiv R_{clean}/k_{sig} = R_{sig} - \frac{k_{bkg}}{k_{sig}} \cdot R_{bkg} \tag{9.4}$$

This gives a slightly scaled rate $\widetilde{R}_{clean}$ but with correctly subtracted background.

Fortunately this relative correction factor (k_{bkg}/k_{sig}) is smaller and varies less than the single factors.

As seen in the histogram of those values (see Figure 9.14) this relative correction factor does not show the huge range of values as one would naively expect from the histogram of the rates. This is caused by the still linear behaviour of the correction factor as well as the almost constant difference between signal and background rates.

For the electron dataset with retardation electrode setting `FULL850_BT` one can then find a normal distributed relative scaling factor with a mean of 0.9958 and a sigma of 0.001 as seen in Figure 9.14. The correction factor and the standard deviation for the other electrode settings can be found in Table 9.2. Also skewness[3] and kurtosis[4] are listed to complete the picture of the distributions. All Histograms can be found in Appendix E.

Electrode Setting	Cycles	Mean	Std. Dev.	Skewness	Kurtosis
FULL850_BT	21506	0.9972	0.0010	0.03	3.8
DEFAULT	7009	0.9958	0.0010	−0.26	3.6
PROTONBLOCK10_BT	17723	0.9957	0.0011	−0.13	3.4
PROTONBLOCK20_BT	6956	0.9959	0.0009	−0.23	3.8
PROTONBLOCK50_BT	5902	0.9958	0.0011	−0.21	3.4
PROTONBLOCK200_BT	5488	0.9963	0.0010	−0.17	3.7
PROTONBLOCK400_BT	5755	0.9970	0.0010	−0.06	3.8

Table 9.2.: Correction factor for the signal to background deadtime effect

For the subtraction of the background free electron spectrum (setting `FULL850_BT`) from the also background free, combined proton and electron spectrum it is necessary to perform a similar correction of the deadtime effects.

Getting a relative correction factor is difficult, since those spectra are not measured simultaneously but, depending on the electrode setting, with a variable delay. In order to compare the correction factors of those data sets, one has to group them in bins of cycles and use the average rates. The bin width was optimised to yield the maximum amount of bins with both proton and

[3] "A positive skewness indicates a distribution with a long right tail. A negative skewness indicates a distribution with a long left tail." [Math10]

[4] "Kurtosis measures the concentration of data around the peak and in the tails versus the concentration in the flanks." [Math10] Kurtosis < 3 for flatter than normal and Kurtosis > 3 for more peaked than normal.

electron cycles. For the DEFAULT setting this bin width is set to 50 cycles and for all other settings to 100 cycles.

For the subtraction again the true rates, as defined in Equation 9.4, have to be used.

$$R_p = k_{sig}^{ep} \cdot \widetilde{R}_{sig}^{ep} - k_{sig}^{e} \cdot \widetilde{R}_{sig}^{e} \tag{9.5}$$

Again a scaled proton rate is defined, but this time by scaling the combined electron-proton spectrum to fit the pure electron spectrum.

$$\widetilde{R}_p \equiv R_p / k_{sig}^{e} = \frac{k_{sig}^{ep}}{k_{sig}^{e}} \cdot \widetilde{R}_{sig}^{ep} - \widetilde{R}_{sig}^{e} \tag{9.6}$$

This definition allows to directly compare the spectra of the different electrode settings ($\widetilde{R}_{p\,(0V)}$, $\widetilde{R}_{p\,(10V)}$, etc.), since they all are scaled by the same constant k_{sig}^{e}.

Since in this case the higher rate gets scaled, the relative scaling factor is bigger than 1. A sample histogram for the dataset PROTONBLOCK10_BT can be found in Figure 9.15. The characterizing values of all histograms can be found in Table 9.3.

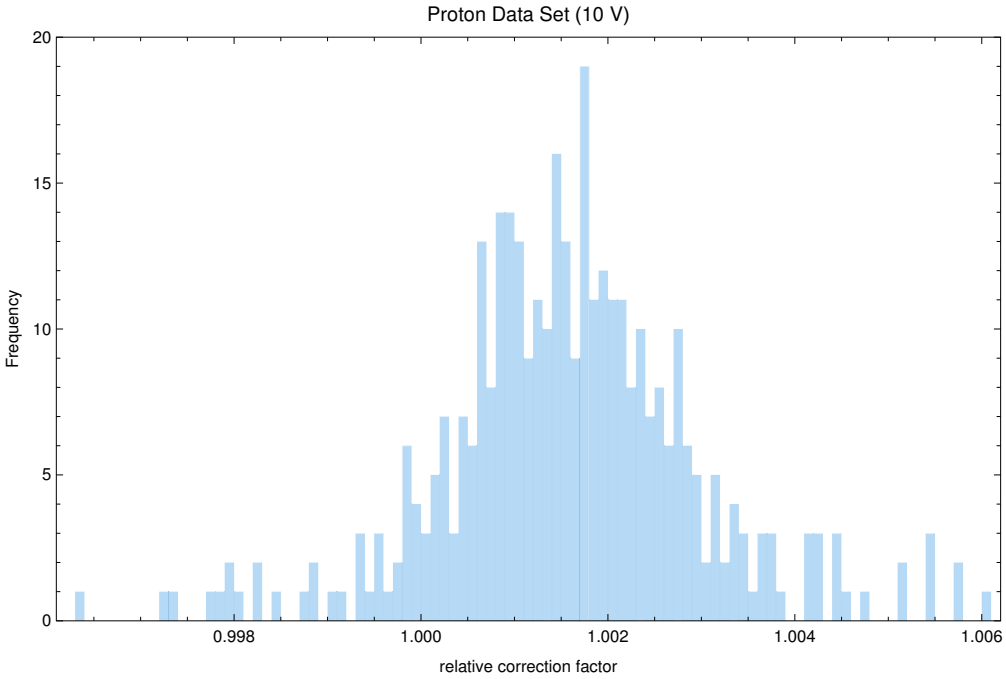

Figure 9.15.: Histogram of relative deadtime correction factors for electrons and PROTONBLOCK10_BT

9.7.2. Problem with the Deadtime Scaling

When applying the calculated scaling to the different data sets, it can be seen, that the background subtracted signal is not compatible with zero in the region behind the electron spectrum.

Electrode Setting	Cycle-bins	Mean	Std. Dev.	Skewness	Kurtosis
DEFAULT	769	1.0014	0.0017	−0.99	9.2
PROTONBLOCK10_BT	366	1.0017	0.0019	5.75	75.7
PROTONBLOCK20_BT	240	1.0013	0.0011	−0.25	5.4
PROTONBLOCK50_BT	158	1.0015	0.0014	−0.17	9.1
PROTONBLOCK200_BT	151	1.0012	0.0014	−0.58	7.1
PROTONBLOCK400_BT	174	1.0003	0.0020	2.88	30.8

Table 9.3.: Deadtime corrections for the proton to electron scaling.

ret. setting	group	calc. factor	σ_{Det1}	σ_{Det2}
FULL_850	1	0.9972	1.44	2.44
FULL_850	2	0.9972	−0.34	0.87
FULL_850	3	0.9972	2.0	1.54
PROTONBLOCK_10	1	0.9957	−0.13	1.5
PROTONBLOCK_10	2	0.9957	−1.28	−1.09
PROTONBLOCK_10	3	0.9957	−2.4	−0.9
pure_electrons	5	0.991	0.14	−2.9

Table 9.4.: Compatibility of the background from channel 36 k to 60 k. Tested with 6 µs delta time cut for sets 1 to 3 and 20 µs delta time cut for the pure electrons. Highlighted values differ more than 1σ from zero.

This behaviour is not consistent, but appears in all sets and all tested retardation electrode settings as shown in Table 9.4.

A first assumption was that the effect comes from the non-poisson behaviour of the delta-time distribution. Therefore another test was performed with a delta time cut of 50 µs, which is clearly in the pure exponential part of the delta time distribution. For such a long deadtime the correction factors are no longer linear and the calculation had to be separated for the different sets. For that data set the effects are even worse as seen in Table 9.5.

9.7.3. Fitting the Deadtime Scaling

In order to get a feeling for the correct values of the relative scaling, a fitting algorithm was implemented. By varying the scaling factor and fitting the resulting background behind the spectra, the algorithm finds the scaling that causes the fitted constant to be zero. In order to estimate the uncertainty of the automatic scaling, the same algorithm is used to vary the scaling such that the resulting constant fit of the background is exactly $\pm 1\sigma$ away from the optimal zero. Those values are taken as the error of the optimized automatic scaling.

We know that there are no signal related events beyond the electron spectrum, therefore the correct scaling can be determined in this way. A similar argument also holds for the protons. The proton signal is sharply peaked around the low energies, so that only extremely few events can be found in the higher parts of the electron spectrum where we place the fit region for the relative fit of the electron and proton spectra.

The typical output of such a fit is presented in Listing 9.1. The first two columns present the names of the histograms that are optimized. The combined electron proton data set is written

ret. setting	group	calc. factor	σ_{Det1}	σ_{Det2}
FULL_850	1	0.970	4.0	4.6
FULL_850	2	0.971	4.0	2.8
FULL_850	3	0.975	2.8	2.5
PROTONBLOCK_10	1	0.955	4.5	6.1
PROTONBLOCK_10	2	0.956	3.2	2.6
PROTONBLOCK_10	3	0.965	−1.3	0.12
DEFAULT	1	0.952	5.7	5.2
DEFAULT	2	0.957	5.6	0.7
DEFAULT	3	0.965	−2.3	1.4

Table 9.5.: Compatibility of the background from channel 36 k to 60 k. Tested with 50 µs delta time cut for all sets. Highlighted values differ more than 1σ from zero.

short as ep, the completely blocked spectrum with only the electrons is shortened to e. The status of the spin flipper for the signal spectrum is abbreviated as up or down, whereas the background spectrum is taken from both spin direction and shortened as bg. The trailing number denotes the detector. In the square brackets follow the values of the optimization for $-\sigma$, 0 and $+\sigma$ distance to the zero. The fit range is presented in the second set of square brackets at the end of the line.

As one can see, the scaling factors from the first four lines differ from each other and they are not compatible with each other. Their uncertainties however are similar. The scaling factor for the spectrum e_up1 is even bigger than one. In order to estimate the influence of the fit region of the constant fit, its borders are changed by $\pm$5000 channels. As one can see in the following lines, the values scatter and are often not compatible with each other on the one sigma level.

After the scaling with the extracted values, now the electron spectrum has to be subtracted from the combined electron proton spectrum. Again the correction factor is fitted, but this time in the region of the electron spectrum. As one can see in Listing 9.2 the values are now bigger than one, as expected from the definition of the scaling factor. The two values of the scaling for the up and down pure proton signal are now comparable on the two sigma level. But the dependence on the fit range is even bigger for those scaling factors.

Overall the results from the downstream detector produce similar results. Comparing the fitted scaling factors for different data groups and electrode settings gives no clear structure of these values. A better understanding of the possible effects causing this behaviour is clearly necessary. Possible reasons are the not yet understood influence of short event bursts with short time differences. Also the influence of the high trigger rates and the non poisson distribution of delta times on the same detector has to be studied.

A further improvement would be to make more fine grained deadtime corrections. This is probably useful on a data file level or in groups of hours or days.

```
****************** DET 1 *********** 1 sigma fits ***********
ep_up1    ep_bg1  :  [ -0.995, -0.991, -0.987 ] = -0.991 +-  0.004 [40000 - 70000]
ep_down1  ep_bg1  :  [ -0.985, -0.980, -0.976 ] = -0.980 +-  0.004 [40000 - 70000]
e_up1     e_bg1   :  [ -1.005, -1.001, -0.998 ] = -1.001 +-  0.003 [40000 - 70000]
e_down1   e_bg1   :  [ -0.998, -0.995, -0.991 ] = -0.995 +-  0.003 [40000 - 70000]
Check stability against changes in fit range
ep_up1    ep_bg1  :  [ -0.995, -0.991, -0.987 ] = -0.991 +-  0.004 [40000 - 70000]
ep_up1    ep_bg1  :  [ -1.002, -0.997, -0.992 ] = -0.997 +-  0.005 [45000 - 65000]
ep_up1    ep_bg1  :  [ -0.998, -0.994, -0.990 ] = -0.994 +-  0.004 [35000 - 65000]
ep_up1    ep_bg1  :  [ -0.995, -0.990, -0.986 ] = -0.990 +-  0.005 [45000 - 75000]

ep_down1  ep_bg1  :  [ -0.985, -0.980, -0.976 ] = -0.980 +-  0.004 [40000 - 70000]
ep_down1  ep_bg1  :  [ -0.989, -0.984, -0.979 ] = -0.984 +-  0.005 [45000 - 65000]
ep_down1  ep_bg1  :  [ -0.989, -0.985, -0.981 ] = -0.985 +-  0.004 [35000 - 65000]
ep_down1  ep_bg1  :  [ -0.986, -0.981, -0.977 ] = -0.981 +-  0.005 [45000 - 75000]

e_up1     e_bg1   :  [ -1.005, -1.001, -0.998 ] = -1.001 +-  0.003 [40000 - 70000]
e_up1     e_bg1   :  [ -1.009, -1.005, -1.001 ] = -1.005 +-  0.004 [45000 - 65000]
e_up1     e_bg1   :  [ -1.009, -1.005, -1.002 ] = -1.005 +-  0.003 [35000 - 65000]
e_up1     e_bg1   :  [ -1.007, -1.003, -0.999 ] = -1.003 +-  0.004 [45000 - 75000]

e_down1   e_bg1   :  [ -0.998, -0.995, -0.991 ] = -0.995 +-  0.003 [40000 - 70000]
e_down1   e_bg1   :  [ -0.999, -0.994, -0.990 ] = -0.994 +-  0.004 [45000 - 65000]
e_down1   e_bg1   :  [ -1.004, -1.001, -0.997 ] = -1.001 +-  0.003 [35000 - 65000]
e_down1   e_bg1   :  [ -0.992, -0.988, -0.984 ] = -0.988 +-  0.004 [45000 - 75000]
```

Listing 9.1: Output of the automatic scaling fit for the Grenoble detector with retardation setting `PROTONBLOCK_10` of group 3.

```
ep_clean_up1    e_clean_up1   :  [  1.061,  1.063,  1.066 ] = 1.063 +- 0.003 [12000 - 25000]
ep_clean_down1  e_clean_down1 :  [  1.053,  1.057,  1.060 ] = 1.057 +- 0.003 [12000 - 25000]
Check Stability of the Proton vs Electron fit
ep_clean_up1    e_clean_up1   :  [  1.061,  1.063,  1.066 ] = 1.063 +- 0.003 [12000 - 25000]
ep_clean_up1    e_clean_up1   :  [  1.042,  1.048,  1.053 ] = 1.048 +- 0.005 [17000 - 20000]
ep_clean_up1    e_clean_up1   :  [  1.054,  1.056,  1.059 ] = 1.056 +- 0.002 [ 7000 - 20000]
ep_clean_up1    e_clean_up1   :  [  1.058,  1.062,  1.067 ] = 1.062 +- 0.005 [17000 - 30000]

ep_clean_down1  e_clean_down1 :  [  1.053,  1.057,  1.060 ] = 1.057 +- 0.003 [12000 - 25000]
ep_clean_down1  e_clean_down1 :  [  1.043,  1.049,  1.055 ] = 1.049 +- 0.006 [17000 - 20000]
ep_clean_down1  e_clean_down1 :  [  1.056,  1.058,  1.061 ] = 1.058 +- 0.002 [ 7000 - 20000]
ep_clean_down1  e_clean_down1 :  [  1.045,  1.050,  1.055 ] = 1.050 +- 0.005 [17000 - 30000]
```

Listing 9.2: Part two of the output of the automatic scaling fit for the Grenoble detector with retardation setting `PROTONBLOCK_10` of group 3.

10. Systematic Effects

Several systematic effects have to be studied in order to be able to correct for their influence on the measured asymmetry. Some of the effects are so small that they do not have to be considered in a final analysis.

10.1. Stability of the HV-System

One issue is the general stability of the high voltage system. The highly varying trigger rates, especially the extreme variability on the downstream (Lyon) side, make a clean description of the background very difficult. Several things have been tried in order to suppress the background. Fine tuning of the both voltages of the degraders with respect to each other only helped to reduce the background marginally. A part of the background can be blocked with the retardation system. Running at 10 V instead of 0 V stabilized the background on a high level.

In the beginning of 2015 several tests of configurations of the degraders were performed. While conducting those tests, it was observed that the pressure, measured in the cold cathode, spiked when a small breakdown of the voltage was observed. We came to the conclusion that all observed effects could be explained by particles that are confined in different traps until they reach a density that allows a discharge. Particles could be trapped on the magnetic field lines between the high voltages of both field degraders. Another trap for some particles is on the magnetic field lines between the electrostatic potential from the degrader and the maximum of the magnetic field in the central volume (magnetic mirror). The installation of the wire grid in the central retardation electrode helped to reduce this problem. Unlike the decay protons that can just pass the grid (see section 10.8 on page 113), trapped particles pass the grid numerous times until they are absorbed or scattered out of the trap.

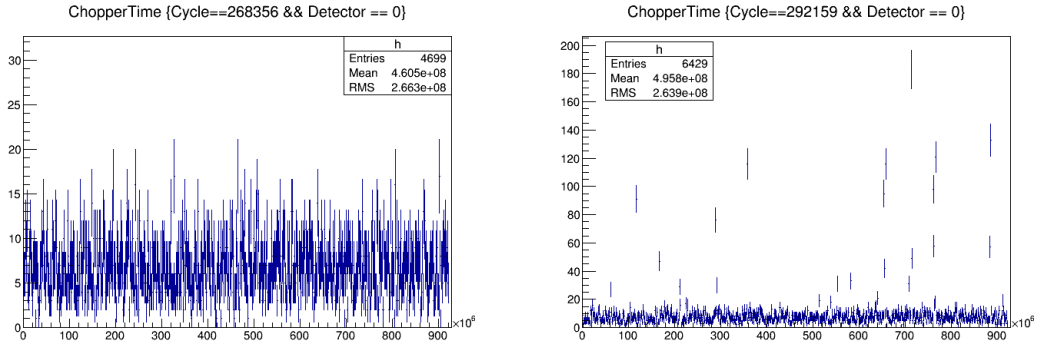

(a) Before the breakdown

(b) After the breakdown

Figure 10.1.: Events per chopper turn. Showing only events where the Grenoble (upstream) detector triggered first.

After an especially violent breakdown of the degrader Voltage in May 2015 a change in background time structure could be observed. Instead of a homogeneous distribution of the events as seen in Figure 10.1a, now there are single chopper turns with extremely increased trigger rate. This behaviour was probably caused by a small part of the foil that did not stick to the holder and pointed towards the detector. This observation led to the improvement of the second aperture that was used to shield those parts of the foil that are attached to the holder. In later measurements the problem of the single chopper turn event rate was still present.

For the future it is planed to implement a filter that cuts away those chopper turns, but the implementation requires interventions in the core code of the analysis software. Also it has to be proven, that such a filter does not change the measured proton asymmetry. Therefore this implementation is deferred to the further analysis of the data in [Roi17].

For a future measurement the instabilities of the HV system should be investigated thoroughly. Additional smoothing of surfaces can be tried as a first step. Probably a further decrease in vacuum pressure can reduce the background, but we did see changes in background rate that were not correlated with the slow change of the vacuum pressure. It has to be ensured that those test are preformed under realistic condition with two HV potentials connected with a magnetic flux tube.

10.2. Transmission Function of the Retardation Potential

One major systematic effect for all measurements with intermediate voltages is the real transmission function of the retardation potential. It depends on the magnetic and electric field at the retardation plane. In order to estimate the size of the correction as well as the sensitivity to variations in magnetic and electric field strength some simplifications have to be made. A constant magnetic field around the central electrode with a lower fields strength than in the decay volume is assumed. Also the electrical field is assumed to be constant in the transversal direction.

The electrostatic potential only affects the longitudinal energy of the proton. Since the proton arrives from a higher magnetic field the pitch angle is smaller and therefore more of its energy is parallel. This longitudinal energy of the proton can then be expressed as a function of the initial energy E_p and the pitch angle of emission θ_{decay}.

$$E_{\parallel} = E_p \cos(\theta_{ret.}) = E_p \cos\left(\arcsin\left(\sqrt{B_{ret.}/B_{decay}}\,\sin(\theta_{decay})\right)\right) \tag{10.1}$$

In order to calculate the measured asymmetry one has to numerically integrate the initial decay distribution over the two hemispheres. To implement the retardation potential the integrand is multiplied by the boolean value of the comparison of the parallel energy with the value of the electric potential U_{cut}.

$$\begin{aligned} N^{\uparrow}_{cut} = 1/2 \int_0^{E_{max}} \int_0^{\pi/2} & w_p(E_p)\ \left(1 + 2C(E_p)\cos(\theta_{decay})\right) \\ & \cdot \text{Boole}[(E_p\ \cos(\arcsin(\sqrt{B_{ret}/B_{decay}}\sin(\theta_{decay})))) \geq U_{cut}]\,\mathrm{d}E_p \sin(\theta_{decay})\mathrm{d}\theta_{decay} \end{aligned} \tag{10.2}$$

To calculate the value for $N^{\downarrow}_{cut}$ on has to change the integration borders to $\int_0^{E_{max}} \int_{\pi/2}^{\pi}$

The values of the relative correction $(C_{cut} - C_0)/C_0$ extracted from this calculation can be found in Table 10.1 in the fifth column. In the last two columns, the sensitivity to changes in the electric or magnetic field strength is shown. These values are calculated for two different accuracies. This constraints the needed accuracy of the field simulations in the retardation electrode for all transversal positions along the surface of maximum voltage.

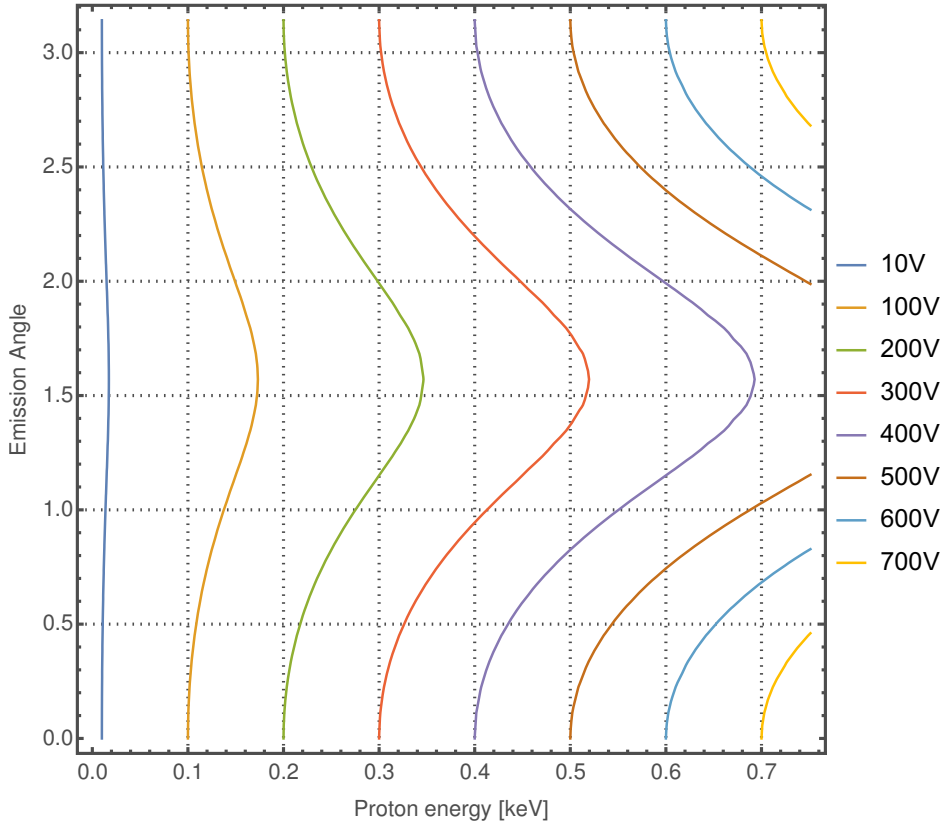

Figure 10.2.: Integration borders for a 150 mT to 80 mT magnetic field ratio. Due to the increased blocking of particles with high initial angles a bigger asymmetry as naively expected is measured.

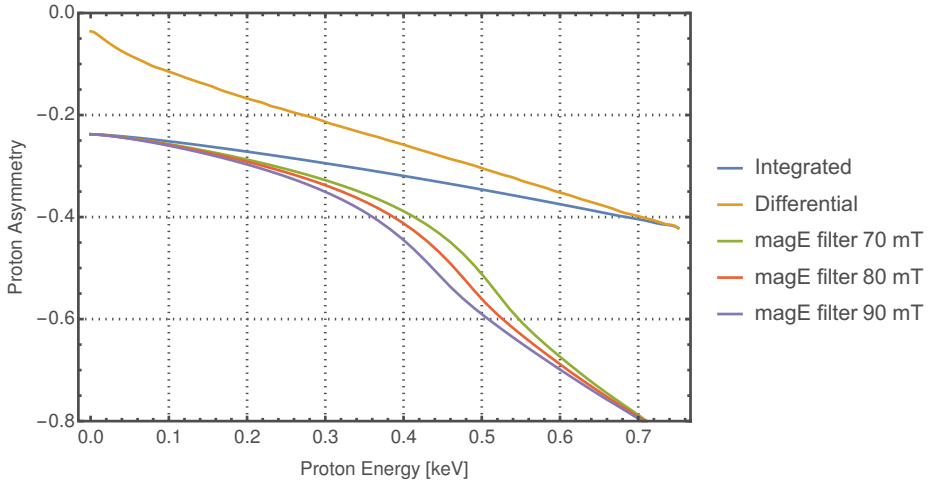

Figure 10.3.: Effect of the magnetic mirror effect on the measured integral asymmetry for different field ratios.

U_{cut} [V]	δU_{cut} [V]	B_{ret} [mT]	δB_{ret} [mT]	rel. corr	δ corr mag.	δ corr el.
10	$\pm$1	60	$\pm$1	3.006×10^{-3}	$\pm 1.6 \times 10^{-5}$	$\pm 4.4 \times 10^{-4}$
		70		3.184×10^{-3}	$\pm 1.9 \times 10^{-5}$	$\pm 4.7 \times 10^{-4}$
		80		3.397×10^{-3}	$\pm 2.3 \times 10^{-5}$	$\pm 5.0 \times 10^{-4}$
	$\pm$0.1	60	$\pm$0.1	3.006×10^{-3}	$\pm 1.6 \times 10^{-6}$	$\pm 4.3 \times 10^{-5}$
		70		3.184×10^{-3}	$\pm 1.9 \times 10^{-6}$	$\pm 4.7 \times 10^{-5}$
		80		3.397×10^{-3}	$\pm 2.3 \times 10^{-6}$	$\pm 5.0 \times 10^{-5}$
20	$\pm$1	60	$\pm$1	8.218×10^{-3}	$\pm 4.9 \times 10^{-5}$	$\pm 6.1 \times 10^{-4}$
		70		8.703×10^{-3}	$\pm 5.3 \times 10^{-5}$	$\pm 6.2 \times 10^{-4}$
		80		9.281×10^{-3}	$\pm 6.4 \times 10^{-5}$	$\pm 6.6 \times 10^{-4}$
	$\pm$0.1	60	$\pm$0.1	8.218×10^{-3}	$\pm 4.6 \times 10^{-6}$	$\pm 6.2 \times 10^{-5}$
		70		8.703×10^{-3}	$\pm 5.4 \times 10^{-6}$	$\pm 6.2 \times 10^{-5}$
		80		9.281×10^{-3}	$\pm 6.2 \times 10^{-6}$	$\pm 6.6 \times 10^{-5}$
50	$\pm$1	60	$\pm$1	2.972×10^{-2}	$\pm 1.6 \times 10^{-4}$	$\pm 8.2 \times 10^{-4}$
		70		3.150×10^{-2}	$\pm 1.9 \times 10^{-4}$	$\pm 8.7 \times 10^{-4}$
		80		3.363×10^{-2}	$\pm 2.3 \times 10^{-4}$	$\pm 9.3 \times 10^{-4}$
	$\pm$0.1	60	$\pm$0.1	2.972×10^{-2}	$\pm 1.7 \times 10^{-5}$	$\pm 7.9 \times 10^{-5}$
		70		3.150×10^{-2}	$\pm 2.0 \times 10^{-5}$	$\pm 8.6 \times 10^{-5}$
		80		3.363×10^{-2}	$\pm 2.2 \times 10^{-5}$	$\pm 9.6 \times 10^{-5}$
200	$\pm$1	60	$\pm$1	1.944×10^{-1}	$\pm 1.3 \times 10^{-3}$	$\pm 1.3 \times 10^{-3}$
		70		2.088×10^{-1}	$\pm 1.6 \times 10^{-3}$	$\pm 1.5 \times 10^{-3}$
		80		2.265×10^{-1}	$\pm 2.0 \times 10^{-3}$	$\pm 1.6 \times 10^{-3}$
	$\pm$0.1	60	$\pm$0.1	1.944×10^{-1}	$\pm 1.4 \times 10^{-4}$	$\pm 1.4 \times 10^{-4}$
		70		2.088×10^{-1}	$\pm 1.7 \times 10^{-4}$	$\pm 1.6 \times 10^{-4}$
		80		2.265×10^{-1}	$\pm 1.8 \times 10^{-4}$	$\pm 1.5 \times 10^{-4}$
400	$\pm$1	60	$\pm$1	5.591×10^{-1}	$\pm 6.5 \times 10^{-3}$	$\pm 2.6 \times 10^{-3}$
		70		6.340×10^{-1}	$\pm 8.6 \times 10^{-3}$	$\pm 3.2 \times 10^{-3}$
		80		7.347×10^{-1}	$\pm 1.2 \times 10^{-2}$	$\pm 4.3 \times 10^{-3}$
	$\pm$0.1	60	$\pm$0.1	5.591×10^{-1}	$\pm 6.8 \times 10^{-4}$	$\pm 3.2 \times 10^{-4}$
		70		6.340×10^{-1}	$\pm 9.0 \times 10^{-4}$	$\pm 3.4 \times 10^{-4}$
		80		7.347×10^{-1}	$\pm 1.1 \times 10^{-3}$	$\pm 3.8 \times 10^{-4}$

Table 10.1.: Relative correction factors for the different retardation settings. Last two columns show the sensitivity of the correction to a change in the magnetic or electric field of the specified value.

For the lower retardation settings the uncertainty in the correction due to the accuracy in the magnetic field ranges from 1×10^{-5} to 1×10^{-4}, if the magnetic field is known on the $\pm 1\,\mathrm{mT}$ level. Those can be lowered to 1×10^{-6} to 1×10^{-5}, if the accuracy of the simulation can be lowered to $\pm 0.1\,\mathrm{mT}$, which is already below the accuracy of the measurement described in subsection 5.3.1. However, the correction depends only on the ratio of the magnetic field which is known better due to the precision of the magnetic probe.

The uncertainty in the correction due to the accuracy of the electric field is higher than the magnetic uncertainty. A simulation on the $\pm 1\,\mathrm{V}$ level is not precise enough for a further analysis. Reducing the accuracy to $\pm 0.1\,\mathrm{V}$ gives a uncertainty on the correction that is comparable to the magnetic uncertainty at the $\pm 1\,\mathrm{mT}$ level.

The measurements at a retardation of 200 V and 400 V should not be interpreted as a measurement of the pure integral asymmetry, but rather as a measurement of the partially integrated asymmetry. This reduces the correction factor, but not its uncertainties.

10.3. Stern-Gerlach effects

Since the spin of the neutron interacts with the magnetic gradients, the Stern-Gerlach effects have to be estimated. The potential energy of a magnetic dipole in a magnetic field is given by $U = -\vec{m} \cdot \vec{B}$ and in an inhomogeneous field a force acts on the magnetic moment. That force is given by the gradient of $\overrightarrow{\nabla}\left(\vec{m} \cdot \vec{B}\right)$ and for our longitudinal polarization and magnetic field configuration results in

$$F = \overrightarrow{\nabla}\left(\begin{pmatrix} 0 \\ 0 \\ \mu_z \end{pmatrix} \cdot \begin{pmatrix} B_x(x,y,z)) \\ B_y(x,y,z) \\ B_z(x,y,z) \end{pmatrix}\right) = \mu_z \begin{pmatrix} \partial_x \\ \partial_y \\ \partial_z \end{pmatrix} B_z(x,y,z)) \approx \mu_z \partial_z B(z) \tag{10.3}$$

Force components in transversal direction are one order of magnitude lower than the z component. For an estimation of the strength, a gradient of $0.15\,\mathrm{T\,m^{-1}}$ with length of 1 m has been chosen. The force acting on the neutron entering the decay volume is then $\pm 1.45 \times 10^{-27}\,\mathrm{N}$ which results in an acceleration of $\pm 0.87\,\mathrm{m\,s^{-2}}$, depending on the sign of the spin. Together with the approximate velocity of the neutron of $800\,\mathrm{m\,s^{-1}}$ that takes about 1.25 ms to pass that gradient this results is a relative change in velocity of about $\Delta v/v = 1.4 \times 10^{-6}$.

The effect on the asymmetry in a continuous beam measurement is then caused by the different time that it takes the components to pass through the decay volume (see [Kre04]).

$$C_{exp} = \frac{N_1(1 + \Delta v/v) - N_2(1 - \Delta v/v)}{N_1(1 + \Delta v/v) + N_2(1 - \Delta v/v)} = \frac{N_1 - N_2 + (N_1 + N_2)(\Delta v/v)}{N_1 + N_2 + (N_1 - N_2)(\Delta v/v)} \tag{10.4}$$

Which results in a correction δC on the true asymmetry when deriving the measured asymmetry $C_{exp} = C + \delta C$. This correction can be expressed as a function of the asymmetry and the shift in velocity.

$$\delta C = \frac{\left(C^2 - 1\right)(\Delta v/v)}{C\,(C\,(\Delta v/v) + 1)} = -\frac{3.96928(\Delta v/v)}{0.2377\,(\Delta v/v) + 1} \approx -5.6 \times 10^{-6} \tag{10.5}$$

Any influence of the integration over the true neutron velocity distribution and the real magnetic gradient will not change this by orders of magnitude, and therefore this effect is negligible.

In our case of a pulsed measurement with a ToF cut, each spin component is slightly shifted for each ToF time. But the shift is very small and its only influence is via the magnetic mirror effect and therefore further suppressed.

10.4. Effect of the Moving Neutron - Doppler Effect

The neutron decays in its rest frame and all angular distributions are also described in the rest frame. The neutron traverses the decay volume with approximately 800 m s^{-1}. The decay electrons with their low mass already have relativistic velocities for quite low energies. But the heavy protons have a velocity spectrum (see Figure 10.4) that in some parts is comparable to the neutron velocity. This changes the angular distribution of the protons in the lab frame and therefore influences the measured asymmetries.

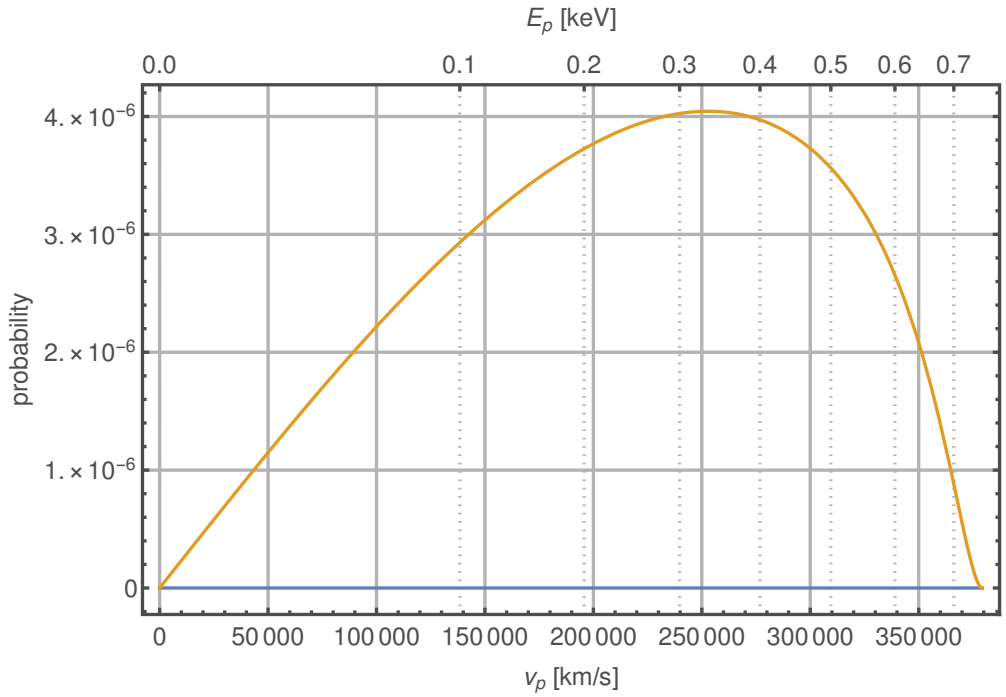

Figure 10.4.: Velocity spectrum of the protons from neutron beta decay.

For a first approximate discussion, we neglect the magnetic mirror effect. In the extreme case of protons with a velocity lower than the neutron velocity, all protons are detected on the forward detector. For each proton velocity one can calculate the maximum pitch angle $\theta \in [\pi/2, \pi]$ in the rest frame of the neutron that is detected on the downstream detector.

$$\theta_{crit} = \begin{cases} \pi & \text{for} \quad v_\mathrm{p} < v_\mathrm{n} \\ \arccos(-v_\mathrm{n}/v_\mathrm{p}) & \text{for} \quad v_\mathrm{p} \geq v_\mathrm{n} \end{cases} \tag{10.6}$$

This angle is very close to the optimal 90° for most of the spectrum, but at low energies the difference can be quite big as shown in Figure 10.5. At the protons end-point energy the critical angle is 90.1208°.

In order to calculate the effect on the measured asymmetry, the angular distribution of the protons is integrated on $[0, \theta_{crit}]$ and $[\theta_{crit}, \pi]$. This allows to plot the measured asymmetry as a function of the protons velocity. Depending on the method of defining the experimental asymmetry the effect has a different strength.

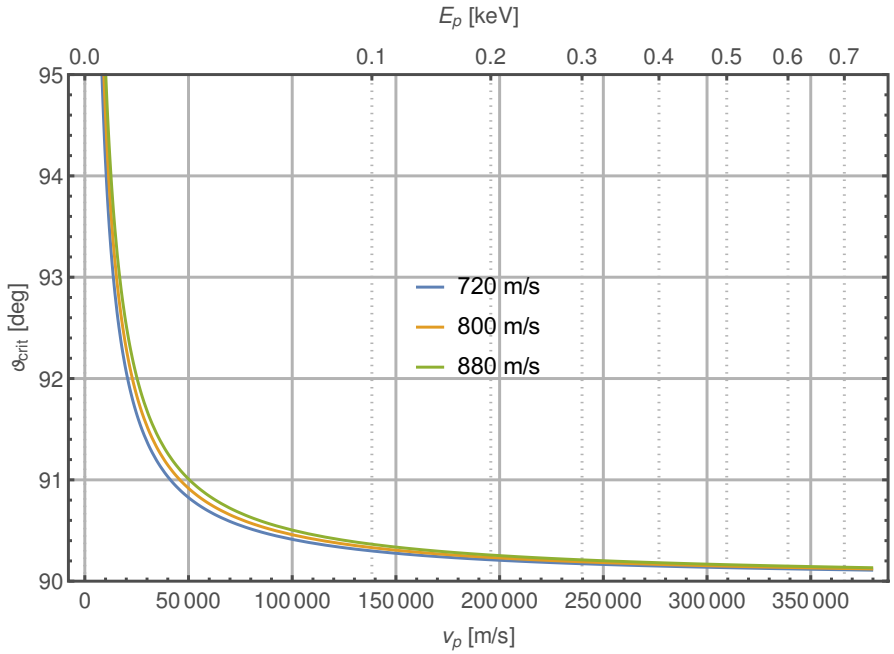

(a) Full energy scale

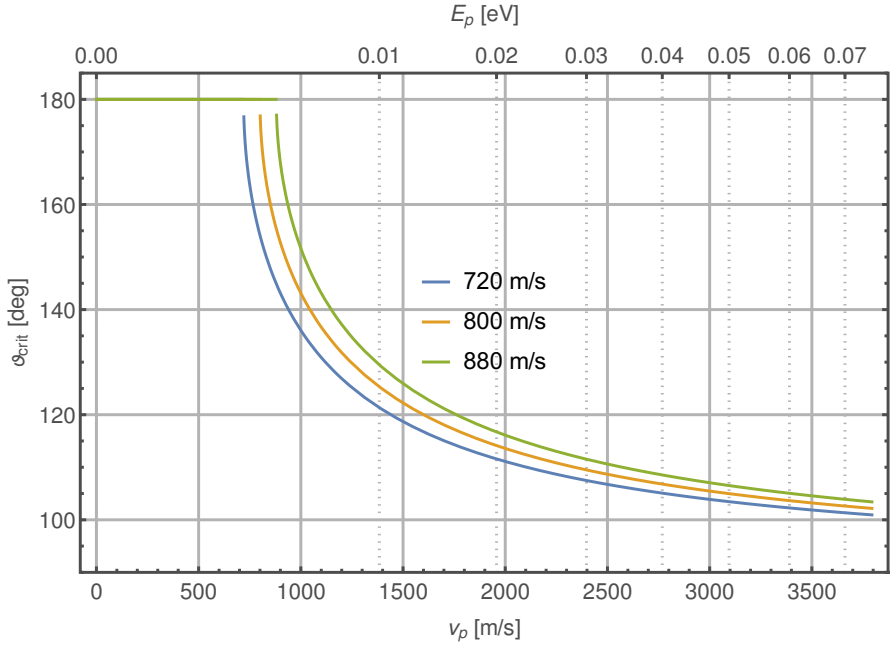

(b) Zoom into the very low energies

Figure 10.5.: Critical angle for detection in the downstream detector plotted for three different neutron velocities.

For the following discussion a neutron velocity of $(800 \pm 80)\,\mathrm{m\,s^{-1}}$ is assumed. If one extracts the asymmetry as the difference of the two detectors for a fixed spin flip status, the relative correction on the asymmetry is $(3.15 \pm 0.31) \times 10^{-2}$ for the one spin direction and for the other spin direction $(-3.14 \pm 0.31) \times 10^{-2}$. Both uncertainties are slightly asymmetric, but not on the level displayed here. When averaging the both asymmetry measurements the combined correction is $\left(1.95^{+0.41}_{-0.37}\right) \times 10^{-5}$.

The normal approach is to extract the asymmetry in each detector independently using the spin-flipper. In that case the relative correction of the asymmetry in the downstream detector is $(3.74 \pm 0.37) \times 10^{-3}$ and in the upstream detector $(-3.74 \pm 0.37) \times 10^{-3}$. Combining both detectors then reduces the systematic correction due to the moving neutron to a negligible $\left(1.85^{+0.59}_{-0.50}\right) \times 10^{-8}$ .The dependence of the measured proton asymmetry on the proton velocity is shown in Figure 10.6.

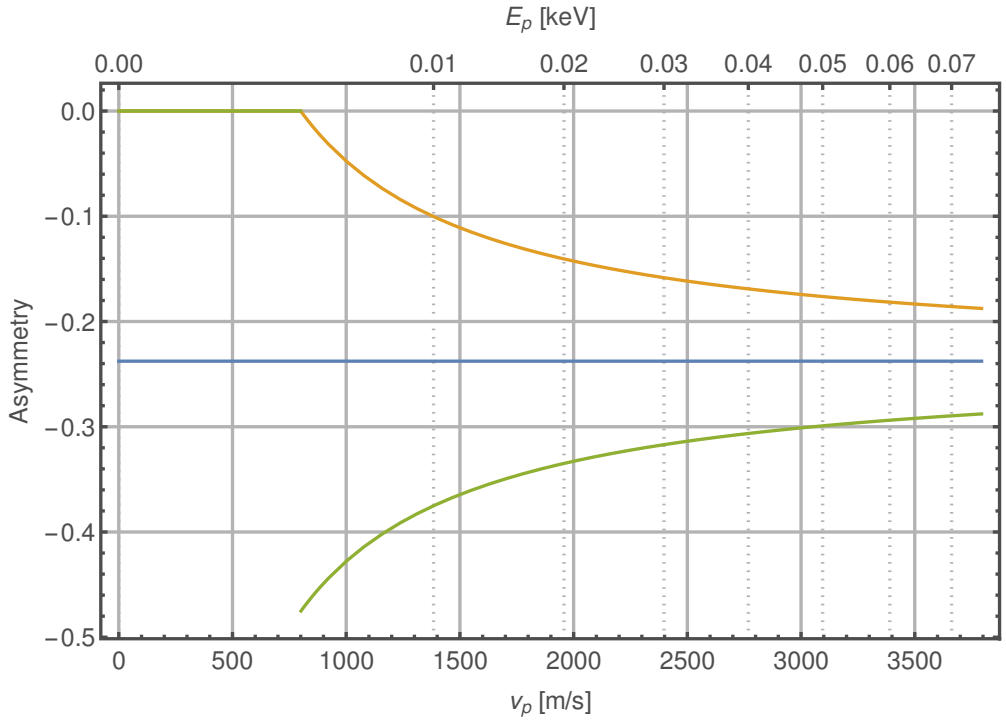

Figure 10.6.: Proton asymmetry as function of proton velocity. The blue line marks the true asymmetry, in yellow the measured asymmetry in the downstream detector is plotted and in green in the upstream detector.

Therefore this effect only has to be considered if a determination in one of both detectors is impossible. In that case a full calculation should take the real velocity distribution of the neutron pulse into account. An influence on the correction of the magnetic mirror effect due to the moving neutron cannot be excluded, but for the calculation one just has to transform the emission angle distribution in the rest frame of the neutron into the corresponding distribution in the lab frame.

10.5. Edge Effect and Beam Profile

As calculated in chapter 7 the effect of the PSF is significant for the small foil. But the final geometry has several possible edge effects and other influences that cannot be calculated using this simple method. From the particle tracking in a preliminary model of the magnetic field, we can see, that a part of the beam might scratch on the lower edge of the entry aperture of the field degrader. Additionally the calculations in chapter 7 ignore all effects from the electric fields. The gradient field of the entrance of the field degrader might have a focussing influence on the protons. This effect will be different from the effects on the electrons, since they have hugely different energies. Also the system does not consist of only one baffle. The first and last electrode of the field degrader have a slightly different edge radii, but those effects should be masked by the size of the foil. For the electrons at least the size of the detector and the foil have to be considered and the fact that they are situated at different magnetic fields.

The situation of the protons is more complex and necessitates the consideration of all electric and magnetic fields along the flight path in a full particle tracing simulation. The combined forces of a variable magnetic field (along the flight path and also in transverse direction) and the bending in the s-shape ($R \times B$ drifts) and the highly varying electric potential at the retardation electrodes cannot be calculated analytically. Additionally, the transverse size of the neutron beam has to be considered in all those calculations since the magnetic field shows a variation in this direction. Plots of the transversal field maps can be found in subsection 5.3.1.

10.6. Magnetic Mirror Effect

The magnetic mirror effect (see chapter 3) is caused by the shape of the magnetic field in the central volume. This field is strongest in the center and slowly decreases towards the end of the central volume where it decreases stronger and bends towards the detector vessels. For a particle decaying in on the maximum of the magnetic field this has no effect and all decay particles can arrive at the detector that belongs to the right hemisphere.

The situation is different for decays that are situated in a lower field. Decay particles with very high angle towards the magnetic field that are emitted in the direction of the field maximum can be reflected at the maximum and therefore be detected in the wrong detector. To first order this effect has the same amplitude on both sides of the maximum and therefore the effect is reduced when both detectors are averaged. Since the field gradients are not exactly the same on each side of the maximum and the neutron pulse is diverging while traversing the central volume a small correction remains.

The following equations for the correction of the magnetic mirror effect have been derived by Raven [Rav95] and especially for the case of PERKEO III they are presented in [Wan13] (see also [Mär06] and [Mes11]). The calculation is similar to the previous calculation of the moving neutron. Biggest difference is that the critical angle depends on the magnetic field strength and therefore the position of decay. Additionally the effect is strong enough, that one has to account for the density of the pulse with time of flight effects.

For an extended neutron density $\rho(\mathbf{r}, t)$, one can define the properties M and k. They are defined by combinations of integrals over the space left and right of the magnetic field maximum with trigonometric functions of $\theta_{crit}(\mathbf{r})$. The parameter M is slightly lower than 1 and describes the gradient and homogeneity of the magnetic field. The value k describes the asymmetry of the magnetic field weighted by the neutron density and is one order of magnitude smaller than M.

With those parameters the experimental asymmetries in the single detectors including the

magnetic mirror effects can be expressed as

$$C_{exp}^{1,2} = C \frac{M}{1 \pm k} \tag{10.7}$$

The correction is further reduced by averaging the both detectors.

$$C_{exp}^{avg} = C \frac{M}{1 - k^2} \tag{10.8}$$

The different slopes of the two detectors in the ToF-spectra can be explained with this effect and the associated corrections. To illustrate the time dependence of those parameters, a calculation of the size of those parameters as a function of the time of flight inside PERKEO III is presented in Figure 10.7.

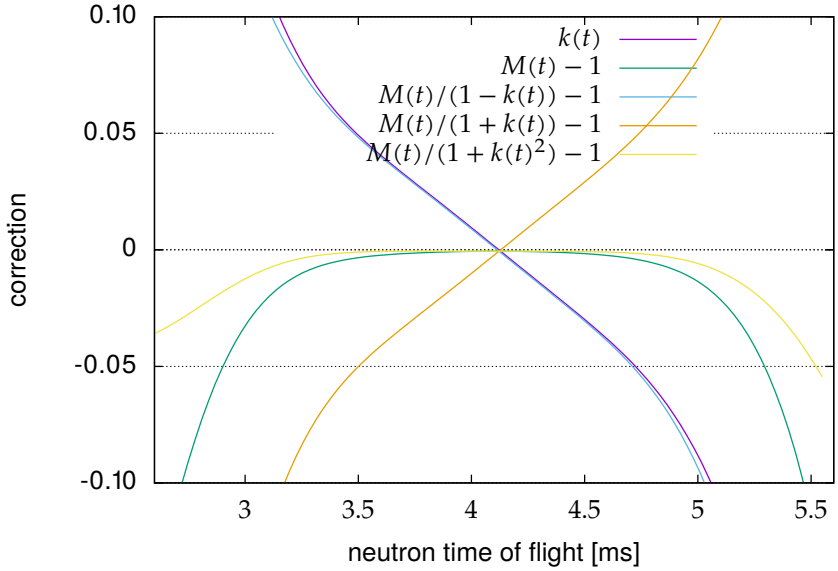

Figure 10.7.: Calculaton of the time dependence of the parameters and corrections from the magnetic mirror effect from fieldmaps and neutron pulse shape analysis from the 2009 measurement. Plot from [Mär15].

10.7. Electrostatic Potentials

Since the protons have relatively low kinetic energies, they are easily disturbed by relatively small electrostatic potentials. A localized potential of only a few volts can already influence and repel a good fraction of the proton beam. Those potentials cannot be measured and can therefore not be corrected for.

Thus the influence of the retardation potential in the decay volume was studied by Klopf [Klo17] and considered while designing the electrode settings. Additionally no isolating material is allowed near the neutron beam inside the decay volume. The same is true for electric components as they were present in the calibration scanner. This was one of the reasons we did

not employ it while measuring protons. On a smaller level the differences in the work function of different materials can also create an electrostatic potential.

By blocking protons below a certain threshold voltage, one can avoid to detect those protons that have possibly been disturbed. We measured at several different voltages but especially at 10 V, 20 V and 50 V. This introduces an additional correction as calculated in section 10.2.

10.8. Grid-Effect

Installing the wire grid in the retardation system has its advantages and disadvantages. On the one hand it stabilized the electric field of the degraders so much, that a simultaneous operation of both degraders above 12 kV was feasible. On the other hand protons can scatter on the wires. This could change the momentum of the protons as well as their direction. Small changes in direction are not that harmful as long as they are still detected on the right detector. Absorbed protons are a bigger problem if the absorption probability depends on the energy or the momentum of the proton. This then changes the measured value of the proton asymmetry since the asymmetry is energy dependent.

A first calculation was done by G. Konrad [Kon15] with the conclusion, that such a wire grid does not influence the value of the proton asymmetry at our then planned level of precision.

In order to provide an estimation of this effect, one can calculate the probability of a wire hit. The regular wire grid of 25 µm wires with a 5 mm pitch covers 0.5 % of the cross-section of the electrode. Since the particles that arrive at the wire already have travelled along a gradient, their maximum pitch angle is boosted to approximately 50° with a diameter of gyration of about 7 mm. This big pitch of the helix decreases the hit probability.

To arrive at the maximum hit probability helix pitch of the particle with the biggest angle to the magnetic field has to be compared with the wire thickness. With the previous parameters a helix pitch of 14 cm can be calculated. Compared to the width of a wire this translates to a probability of 1.8×10^{-4} of being at the right z-position. Multiplying both values gives a maximum probability of about 1×10^{-6}. Even if this probability is energy dependent it does not matter.

11. Extracting the Proton-Asymmetry

11.1. Method

The proton asymmetry of a retardation setting can be extracted by first collecting the signal and background spectra from the data set of the corresponding retardation setting. Naturally those must be split into the two spin configurations `up` and `down`. The same is done for the spectra of the `FULL850_BT` retardation setting, which is the reference setting with only electrons.

A step by step calculation of the asymmetry is then started by subtracting the time-of-flight background from the spectra of the signal window. At that point it is necessary to include the correct background scaling of the deadtime effects. Those clean spectra can then be used to subtract the electron signal from the combined electron proton signal. At this stage, spectra of different data files are combined and the spectra have to be scaled with the ratio of the measurement time of the respective data set. That scaling is mainly dependent on the number of files for the proton data set compared to the number of electron files. An additional scaling factor comes from the fact, that both spin states are not measured for exactly the same time due to the validity of the cycle or the retardation electrode setting[1]. The remaining four spectra are the pure proton events on the upstream detector (`up1` and `down1`) and the downstream detector (`up2` and `down2`). For the `proton_up2` spectrum this subtraction is shown in Figure 11.1. The number of proton events is then the integral of this proton peak. From the number of events in each spectrum, one can calculate the proton asymmetry as

$$C = \frac{N_{\text{prot}}^{\text{up}} - N_{\text{prot}}^{\text{down}}}{N_{\text{prot}}^{\text{up}} + N_{\text{prot}}^{\text{down}}} \tag{11.1}$$

For a full error propagation, it is better to find the full formula of the asymmetry since in the denominator some influences almost cancel under certain assumptions. This can be seen best in the simple formula of the electron asymmetry.

$$A = \frac{N^{\uparrow} - N^{\downarrow}}{N^{\uparrow} + N^{\downarrow}} = \frac{\left(S^{\uparrow} - B^{\uparrow}\right) - \left(S^{\downarrow} - B^{\downarrow}\right)}{\left(S^{\uparrow} - B^{\uparrow}\right) + \left(S^{\downarrow} - B^{\downarrow}\right)} \overset{B^{\uparrow} \equiv B^{\downarrow}}{=} \frac{S^{\uparrow} - S^{\downarrow}}{S^{\uparrow} + S^{\downarrow} - 2B} \tag{11.2}$$

Similar effects can also be found in the calculation of the proton asymmetry. Therefore the proton asymmetry is written in terms of the single spectra of the signal and background time window and the several scaling factors. The proton spectra for up and down are then written as

$$N_{\text{prot}}^{\text{up}} = \left(\left(S_p^{\text{up}} - B_p^{\text{up}} k_p^{\text{up}}\right) k_{\text{ep}}^{\text{up}} - \left(S_e^{\text{up}} - B_e^{\text{up}} k_e^{\text{up}}\right)\right) \tag{11.3}$$

$$N_{\text{prot}}^{\text{down}} = \left(\left(S_p^{\text{down}} - B_p^{\text{down}} k_p^{\text{down}}\right) k_{\text{ep}}^{\text{down}} - \left(S_e^{\text{down}} - B_e^{\text{down}} k_e^{\text{down}}\right)\right) \tag{11.4}$$

[1] For a further analysis it is planned to invalidate those cycles symmetrically with respect to the spinflip pattern. Then again all linear drifts vanish and both data sets are measured with the same statistics

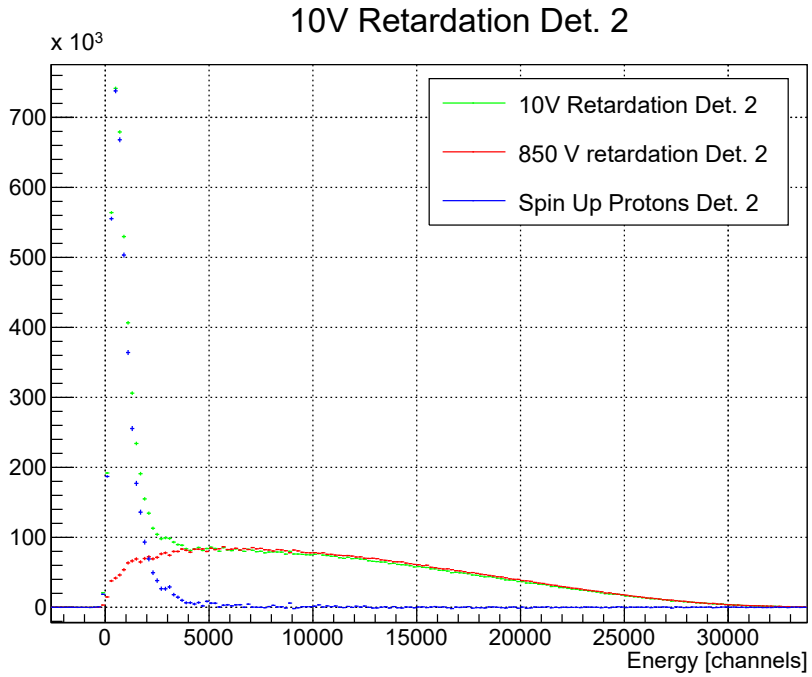

Figure 11.1.: Subtracting the electrons from the combined spectrum produces the proton spectrum. In this case the extraction of the `proton_up2` spectrum on the downstream detector is shown for the combined data set -1 that is the full measurement data.

For spin independent background spectra ($B_p^{\text{up}} = B_p^{\text{down}} = B_p$ and $B_e^{\text{up}} = B_e^{\text{down}} = B_e$, but with different spectra for the electron and proton dataset $B_e \neq B_p$) the equation can then be written as:

$$C = \frac{N_{\text{prot}}^{\text{up}} - N_{\text{prot}}^{\text{down}}}{N_{\text{prot}}^{\text{up}} + N_{\text{prot}}^{\text{down}}} = \frac{2\left(-B_e k_e^{\text{down}} + B_p k_{\text{ep}}^{\text{down}} k_p^{\text{down}} + S_e^{\text{down}} - k_{\text{ep}}^{\text{down}} S_p^{\text{down}}\right)}{B_e\left(k_e^{\text{down}} + k_e^{\text{up}}\right) - B_p\left(k_{\text{ep}}^{\text{down}} k_p^{\text{down}} + k_{\text{ep}}^{\text{up}} k_p^{\text{up}}\right) - S_e^{\text{down}} + k_{\text{ep}}^{\text{down}} S_p^{\text{down}} - S_e^{\text{up}} + k_{\text{ep}}^{\text{up}} S_p^{\text{up}}} + 1 \tag{11.5}$$

From that equation all partial derivatives can be used to calculate the contribution of each error on the final uncertainty. It is useful to combine the uncertainties from the signal and background spectra to a combined statistical error. The only other uncertainty contribution in the extraction originate then in the errors of the fitted scaling factors.

11.2. Error Tables

The results of those extractions for the `PROTONBLOCK10_BT` retardation setting are summarized in Table 11.1 for the upstream detector and in Table 11.2 for the downstream detector. The values extracted from the different sets on the upstream detector are much more stable than on the

downstream detector. The errors on both detectors for all data sets are dominated by the systematic contribution of error of the automatic scaling. The downstream detector in general has a much worse performance with ten times increased errors of the automatic fit and a slightly higher statistic uncertainty. When combining all the data a statistic uncertainty in each detector of about 0.0018 can be reached which is approximately 0.76 % depending on the value of C.

set	C	comb. error	syst. error	stat. error	% syst.	% stat.
1	0.2407	$\pm$0.0061	$\pm$0.0059	$\pm$0.0015	$\pm$2.4	$\pm$0.63
2	0.2326	$\pm$0.0105	$\pm$0.0101	$\pm$0.0027	$\pm$4.4	$\pm$1.2
3	0.2417	$\pm$0.0150	$\pm$0.0145	$\pm$0.0040	$\pm$6.0	$\pm$1.7
all	0.2406	$\pm$0.0070	$\pm$0.0068	$\pm$0.0018	$\pm$2.8	$\pm$0.75

Table 11.1.: Upstream detector (Grenoble) for the automatic scaling and no other systematic corrections. (`PROTONBLOCK10_BT` with integration boundary 15000)

set	C	comb. error	syst. error	stat. error	% syst.	% stat.
1	0.2265	$\pm$0.0412	$\pm$0.0411	$\pm$0.0028	$\pm$18	$\pm$1.2
2	0.1844	$\pm$0.0637	$\pm$0.0635	$\pm$0.0048	$\pm$34	$\pm$2.6
3	0.1636	$\pm$0.0517	$\pm$0.0512	$\pm$0.0067	$\pm$31	$\pm$4.1
all	0.2053	$\pm$0.0213	$\pm$0.0212	$\pm$0.0016	$\pm$10	$\pm$0.79

Table 11.2.: Downstream Detector (Lyon) for the automatic scaling and no other systematic corrections. (`PROTONBLOCK10_BT` with integration boundary 15000)

The asymmetries can also be extracted with no such automatic scaling correction. Then the value of the extracted proton asymmetry depends on the integration borders of the single proton spectra. Those have a different not vanishing background that is then included in the integration. For the calculation of the uncertainties this assumes an error of 1×10^{-4} on the constant scaling. This results are presented in Table 11.3 and Table 11.4. As one can see, the values vary strongly and additionally depend on the integration border. So without the background scaling the data is not usable. Therefore a thorough understanding of the background is needed for a further analysis to fully exploit the good statistic uncertainty.

All other retardation settings can be extracted in the same way. Since the higher retardation settings were not as often measured as the `PROTONBLOCK10_BT` and `PROTONBLOCK20_BT` settings, it is only useful to analyse the complete data set that consists of group 1 to 3. For the upstream

set	C	comb. error	syst. error	stat. error	% syst.	% stat.
1	0.2204	$\pm$0.0015	$\pm$0.0002	$\pm$0.0015	$\pm$0.11	$\pm$0.67
2	0.1903	$\pm$0.0029	$\pm$0.0004	$\pm$0.0029	$\pm$0.22	$\pm$1.5
3	0.2700	$\pm$0.0050	$\pm$0.0005	$\pm$0.0050	$\pm$0.18	$\pm$1.9
all	0.2283	$\pm$0.0022	$\pm$0.0005	$\pm$0.0021	$\pm$0.22	$\pm$0.92

Table 11.3.: Upstream Detector (Grenoble) with no corrections and assumed 1×10^{-4} errors on the scaing. `PROTONBLOCK10_BT` and integration border 15000

set	C	comb. error	syst. error	stat. error	% syst.	% stat.
1	0.2999	$\pm$0.0034	$\pm$0.0014	$\pm$0.0031	$\pm$0.47	$\pm$1.0
2	0.4373	$\pm$0.0071	$\pm$0.0024	$\pm$0.0067	$\pm$0.55	$\pm$1.5
3	0.1832	$\pm$0.0094	$\pm$0.0015	$\pm$0.0093	$\pm$0.81	$\pm$5.0
all	0.3453	$\pm$0.0023	$\pm$0.0012	$\pm$0.0020	$\pm$0.35	$\pm$0.57

Table 11.4.: Downstream detector (Lyon) with no corrections and assumed 1×10^{-4} errors on the scaing. PROTONBLOCK10_BT and integration border 15000

detector the results of thee automatic scaling are presented in Table 11.5 and for the downstream detector in Table 11.6. Again the systematic error of the automatic scaling fit dominates the combined error. For example the 3 % measurement at retardation setting PROTONBLOCK200_BT offers a great possibility to explore the proton energy dependent proton asymmetry. Those values have never been measured and in a next beamtime could be determined with lower uncertainties. On the downstream detector the statistical uncertainties are a about a factor four higher than on the upstream detector. The fits of the automatic scaling factors do not work satisfactory on the downstream detector. This is also the reason the PROTONBLOCK400_BT data is omitted in the table.

ret. V	C	comb. error	syst. error	stat. error	% syst.	% stat.
10	0.2406	$\pm$0.0086	$\pm$0.0083	$\pm$0.0021	$\pm$3.5	$\pm$0.89
20	0.2609	$\pm$0.0123	$\pm$0.0119	$\pm$0.0031	$\pm$4.6	$\pm$1.3
50	0.2366	$\pm$0.0156	$\pm$0.0151	$\pm$0.0039	$\pm$6.4	$\pm$1.6
200	0.3163	$\pm$0.0292	$\pm$0.0282	$\pm$0.0074	$\pm$8.9	$\pm$3.1
400	0.3513	$\pm$0.1047	$\pm$0.1013	$\pm$0.0265	$\pm$28	$\pm$11

Table 11.5.: Overview of the current status of the analysis in the upstream detector (Grenoble) for the automatic scaling and no other systematic corrections. Extracted from the combined data of set 1-3.

ret. V	C	comb. error	syst. error	stat. error	% syst.	% stat.
10	0.2048	$\pm$0.0219	$\pm$0.0219	$\pm$0.0017	$\pm$10	$\pm$0.70
20	0.1962	$\pm$0.1347	$\pm$0.1343	$\pm$0.0102	$\pm$68	$\pm$4.3
50	0.2458	$\pm$0.1661	$\pm$0.1656	$\pm$0.0127	$\pm$67	$\pm$5.3
200	0.2472	$\pm$0.3536	$\pm$0.3526	$\pm$0.0267	$\pm$124	$\pm$11

Table 11.6.: Overview of the current status of the analysis in the downstream detector (Lyon) for the automatic scaling and no other systematic corrections. Extracted from the combined data of set 1-3.

11.3. Dependence on the Integration Region

Especially the uncorrected data shows a strong dependence on the upper integration border. The non vanishing background gets integrated and shifts the values. For some spectra the back-

ground is below zero and for others above as presented in subsection 9.7.2.

A graphical representation of that behaviour can be found in Figure 11.2. For each of the data sets the extracted asymmetry with the combined error is plotted. The grey bar represents the previous measurement of the proton asymmetry with PERKEO II. Of course one cannot compare the absolute value of our pure uncorrected asymmetry with the final value of the measurement. However, the error bar of the old measurement can be used to compare with our new measurement. For the first dataset in Figure 11.2a the uncorrected upstream detector (Det 1) shows a strong dependence on the integration border until 20 k Ch. The behaviour of the downstream detector however is relatively flat but shifted to much higher values. When automatically fitting the scaling factors the values get shifted by a significant amount. This is caused by a different scaling for the up and down components.

Due to the different influence of some of the systematic corrections the not completely corrected values of the both detectors cannot be compared.

For the second data set in Figure 11.2b the uncorrected value of the downstream detector is even higher but gets corrected to a value that is similar to the value in the first data set. The dependence of the upstream value on the integration border has again a similar strength. In the third data set (Figure 11.2c) the uncorrected data set on the upstream detector shows now a higher value and the opposite behaviour as a function of the integration border. However the downstream detector in that data set shows values that are much lower than in the previous data sets.

The full combined data set shows again a huge uncorrected value for the downstream detector that is shifted down by the automatic scaling. The uncorrected values from the upstream detector still have a dependence on the integration border.

A similar representation of the data from the other retardation settings can be found in Figure 11.3. Here only the results of the full data set are presented. Again the values of the upstream detector are strongly dependant on the integration border. The values errors on the downstream detector are much higher and in most cases are just included for completeness. After the automatic scaling correction the values are stable and the errors on the downstream detector decreased. Still it might only be possible to analyse the values of the upstream detector. If it is possible to filter much of the low energy background by a burst filter in the future the errors on the downstream detector might decrease.

11.4. Discussion of the Results

Generally, we have collected data for an analysis with below 1 % statistical uncertainty in each detector. Averaging over the detectors might result in a approximately 0.6 % statistical uncertainty. Considering the circumstances of the beamtime, this is a satisfactory result. Currently the results are limited by the uncertainty in the background scaling. If we can improve our understanding of the background and the deadtime effects, this will lead to a measurement that is comparable to the measurement of Schumann et al. [SKD+08]. A better filtering of the background that is created by the high voltage of the field degrader might help to improve the results on the downstream detector.

For the first time the proton energy dependent proton asymmetry has been measured at five energy points. Those measurements have a statistical uncertainty of a few percent on the upstream detector. The further analysis of those values is possible once the real transmission function of the retardation potential is simulated.

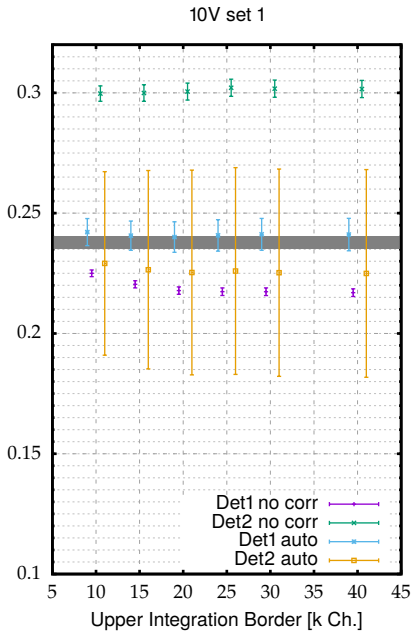

(a) From the first groups of cycles.

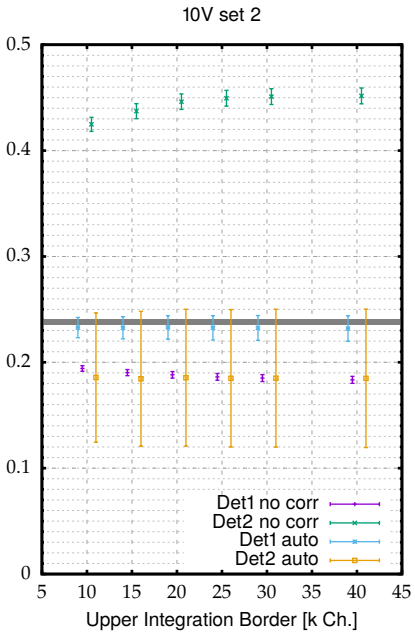

(b) From the second group of cycles.

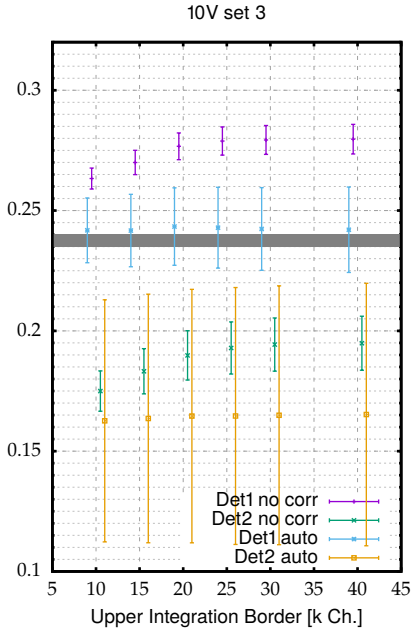

(c) From the third group of cycles.

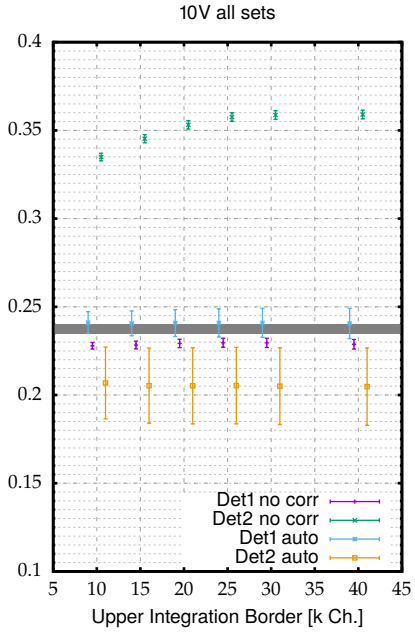

(d) From all groups of the beamtime.

Figure 11.2.: Extraction of the bare proton asymmetry from the `PROTONBLOCK10_BT` retardation setting. The gray bar indicates the value and total error of the last measurement of the proton asymmetry, used to compare the errorbar, not the absolute value.

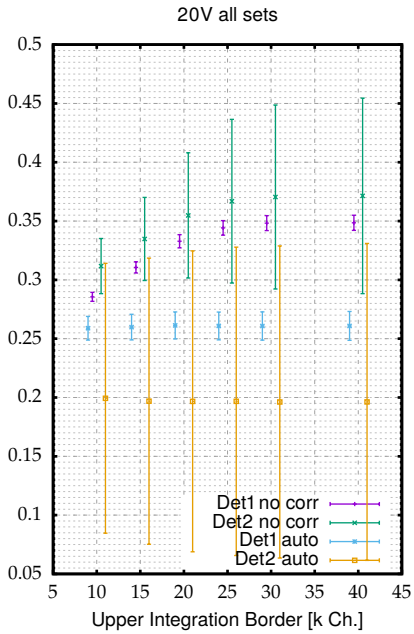

(a) PROTONBLOCK20_BT full beamtime

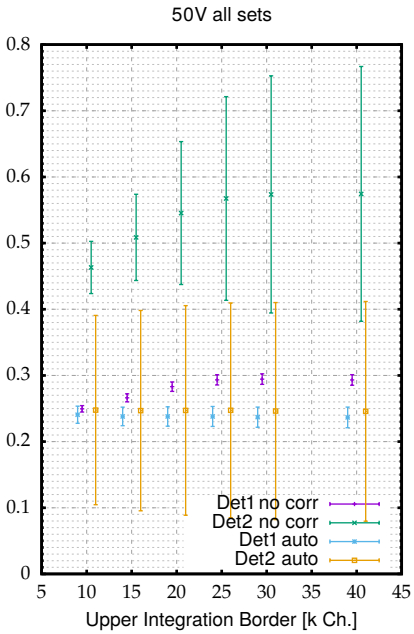

(b) PROTONBLOCK50_BT full beamtime

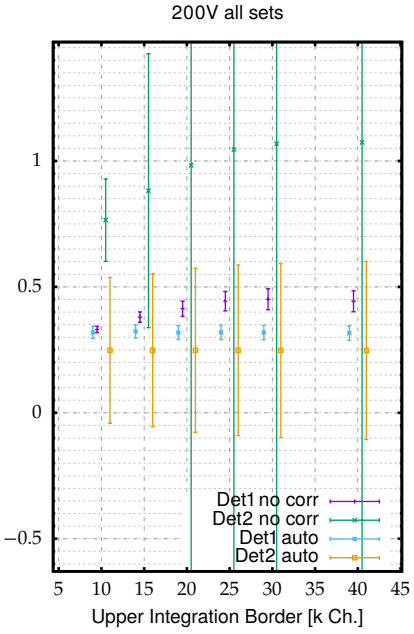

(c) PROTONBLOCK200_BT full beamtime

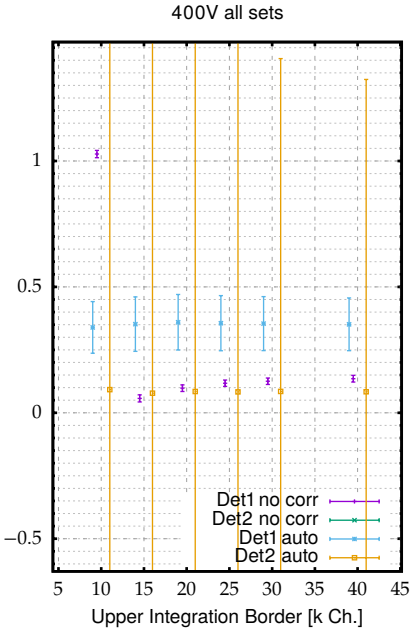

(d) PROTONBLOCK400_BT full beamtime

Figure 11.3.: Extraction of the bare proton asymmetry from the the other retardation settings.

Part IV.

Conclusions

12. Results

12.1. Detector Performance

When designing and constructing the new detector several new concepts were implemented. For the first time we used a *transparent conductive coating* on the scintillator surface. The optical properties of the 15 nm ITO coating were studied in detail and the high reflectivity of the surface allowed to read out the detector from the sides. This increased the light yield and the detector homogeneity.

Using a *four-side readout of the scintillator* by coupling light-guides to each side, helped to further increase the low energy performance of the detector. In order to avoid an inhomogeneous response function of the detector, the mounting has to leave a small gap between light guide and scintillator. With the gap the amount of light on each side of the scintillator is equal and independent of the position. This is not true for the ratio of the signal of the two PMTs on each side which is strongly dependent on the position of the incident electron. This has been verified using a *self-developed ray tracing simulation* and could be used for the studies of the homogeneity of the detector.

The four side readout made it necessary to use light guides that bend by 90° and are shifted towards the center of the detector in order to fit into the vacuum chamber of the spectrometer. This led to a complicated three-dimensional shape of the light guides, which could only be manufactured by *five-axis milling the light guides* from a block of Plexiglass. We improved this technique until the light guides achieved a quality not less than the light guides of the previous beamtime that were manufactured traditionally. The shape of the light-guide has been simulated extensively also using the self-developed ray-tracer to a consistent performance of 93 % integrated light transmission.

The detector mounting was optimized to fix the positions of the scintillator and the light guides with the minimum amount of contact area. *Water cooling the PMTs* stabilized the amplification against daily drifts of the temperature in the experimental hall.

In order to correctly dimension the detector, the *magnetic Point Spread Function* of the system has been studied and simulated. Parts of these results were already published in [DRM+14].

The detector performance is very satisfactory and the light output is higher than in any of the previously used detectors. The low energy response of the detector allows to successfully fit the low-energetic Auger-electrons from the ^{207}Bi source for the first time. This great performance of the detector allows to use it in future measurements with higher precision.

12.2. Performance of the Experiment During the Beamtime

Several unforeseen problems impacted the performance of the experiment during the beamtime. The failure of one of our 600 A power supplies as well as interim problems with the water cooling system caused delays. Additionally severe, previously un-testable problems with the high voltage conversion system appeared in the final configuration. Several test of the conversion foil supporting the voltage systems revealed that the cleaning of the implicitly existing particle trap had to be improved. The foreseen $E \times B$ drift electrodes could not compensate for particle

emission, mostly due to field emissions from surfaces. Those surfaces had to be reworked and wire grids inserted to allow a symmetric measurement with two detectors at the same time.

The conversion foils in the originally planned size could not be manufactured reliably and the transport of the few intact foils from Munich to Grenoble was very problematic. Fortunately we were able to measure with smaller, uncoated foils that are easier to produce and transport.

Using those small uncoated foils we were able to measure the proton asymmetry with a sufficiently small uncertainty. During the final measurement cycle the retardation system, the high voltage and the detector worked reasonably well.

12.3. Proton-Asymmetry

We have successfully collected data for a measurement of the integrated proton asymmetry **C** that allow a statistical uncertainty in each detector of $<0.8\,\%$. In combination both detectors could reach $0.6\,\%$ statistical uncertainty. Several *systematic effects* have been studied, and their influences on the proton asymmetry can be found in Table 12.1.

Two very big effects dominate the error budget. First of all the exact transmission function of the combination of retardation and conversion foil system has to be simulated in order to fully calculate the *edge effect* of the foil aperture and the retardation correction. The other big effect is the not fully understood background subtraction scaling as presented in subsection 9.7.3. A better calculation of the effects and a correction that groups and corrects hours or days might help to reduce the errors in the background scaling. Just fitting the scaling introduces uncertainties in the range of several percent or worse. Further studies of the behaviour of the background could help to reduce the problem.

While the uncertainty of the final result will only show little improvemnt over the first measurement, this *methodically different determination* of **C** with a different spectrometer, a pulsed beam and the possibility to block protons, provides more controll over systematic effects than its predecessor. This will enhance studies of combined neutron decay parameters. Since the last measurement of the proton asymmetry was extracted from the same data set as the measurement of the neutrino asymmetry, usually only the later is used in combined fits of the SM. Our measurement will allow to also include the proton asymmetry data in such analyses. Together with the soon to be published new precise measurement of λ the proton asymmetry can be used to constraint left handed scalar and tensor interactions. The different dependence of the two asymmetries on λ and b (the Fierz interference term) allows to determine the value of b.

With the retardation system it was possible to measure the *proton energy dependant proton asymmetry* for the very first time. The statistics of the measurement are not great and the exact values strongly depend on the simulations of the transmission function of the retardation system. Nevertheless this proof of concept allows future measurements of the energy dependence of the proton asymmetry. Right now it is unclear how that data can be useful in future fits of non-SM physics from neutron decay. Currently there is no analytical description of the proton energy dependent proton asymmetry available. Now that this observable is experimentally accessible, it might be interesting to study the theoretical implications of a more precise determination.

	Effect	relative correction	uncertainty	comment
1	rest-gas back-scattering[a]	$<2.2 \times 10^{-4}$		energy dependent, at 1×10^{-6} mbar
2	Stern-Gerlach effects	6×10^{-6}		
3a	mov. neutron single det	3.7×10^{-3}	3.7×10^{-4}	
3b	mov. neutron avg. det.	1.9×10^{-8}	5×10^{-9}	
4	grid effect[b]	approx. 5×10^{-3}		simple estimation
5	Backscattering from detector	approx. 0		
6	magnetic mirror	approx. 1×10^{-3}		independent analysis
7	Transmission ret. pot	3×10^{-3}	4.5×10^{-5}	± 0.1 V and ± 0.1 mT
8a	deadtime calculated[c] sig/bkg	1×10^{-3}		
8a	deadtime calculated el/prot	5×10^{-2}		
8b	deadtime fittted	2.4 % to 30 %		
9	PSF / edge effects	1.8×10^{-2}	1×10^{-4}	
10	background uncertainty	unknown		to be investigated, dominated by the deadtime scaling

Table 12.1.: Table of the systematic effects on the proton asymmetry. Some values are only estimations and have to be replaced by full calculations. Especially the results of the electro-magnetic field simulations and the tracking have to be added.

[a] Only the probability of scattering, not directly the effect on the asymmetry
[b] probability of hitting the wire, energy dependent and further analysis needed
[c] calculated deadtime correction cannot be used at the moment

13. Outlook

13.1. Improvements of the Detection System

For a future measurement with a similar system several improvements can be proposed. Major limitations currently originate in the vacuum, the stability of the high voltage and the size and mechanical stability of the foils.

In order to achieve a better vacuum all sources of outgassing have to be removed or their impact reduced. Without the calibration robot, the remaining problematic parts are the field degrader and the detector itself. The most problematic part of the field degrader are the several layers of isolating material used to separate the high voltage from the inner surfaces of the spectrometer. The thin gaps between them are dead volume that cannot be pumped efficiently, so reducing them or closing them completely might be necessary. Additionally, one could exchange all teflon parts with PEEK that has a better vacuum compatibility. The huge surface area of the detector including the light guides has a big influence on the vacuum. One might study the possibility of coating the whole detector with a coating that hinders the outgassing from the plastic. Another possibility is to increase the local pumping power near the detector, for example by using the side flanges to install small turbo pumps. Those could help to keep a good local vacuum in the central volume and around the high voltage. It might be helpful to additionally install a metal aperture in the detector chamber that only leaves a small opening for the scintillator. This would then separate the bad vacuum near the light guides from the rest of the spectrometer.

The foil production and transport can be improved. Measuring with a big foil would decrease the systematics, but the failure rate in foil production has to be lowered considerably. The originally planned foil size is obviously very close to the absolute maximum of the current technology. Further studies of the coating processes that could increase the conversion efficiency could help to get better statistics. In order to secure the safety of the transport, the foils could be shipped at an intermediate production step when they are still on the substrate. The mounting of the foil on the holder could then be done close to the experiment, reducing the chance of breaking on the way. Exchanging the carbon foil completely for example with a coated polyimide foil [HYA+06] or other materials might also be possible. Those are so stable, that they can be shipped with standard postal services. Further studies of the conversion process might aid this analysis but can also be used to gain experience with the foil parameters. First studies were already conducted at TUM [Ber16]. It was also shown, that the surface quality of the electrodes has a big influence on the performance of the system.

Several small ideas exist how the calibration robot could become more vacuum compatible, but the problem of the electric potentials near the decay volume can hardly be avoided.

13.2. Comparison of Measurements with PERC and with PERKEO III

Currently a successor experiment is being constructed at the MEPHISTO beam facility of the Forschungs-Neutronenquelle Heinz Maier-Leibnitz (FRM-II) in Munich. The "clean, bright and

versatile source of neutron decay products" called PERC will provide a beam of neutron decay products to exchangeable detectors and experiments. The name PERC is short for Proton Electron Radiation Channel. Its goal is to enable measurements of the several neutron decay observables on the 1×10^{-4} level.

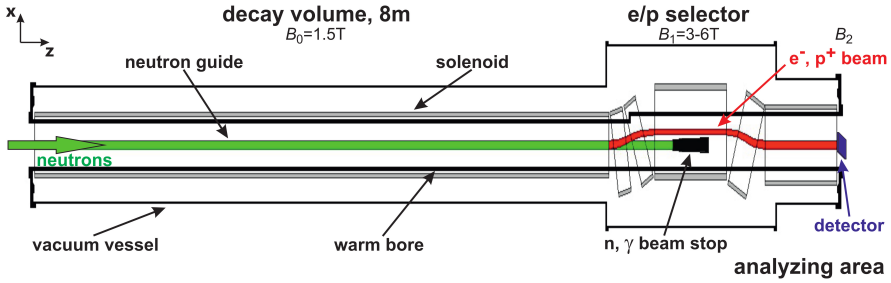

Figure 13.1.: Schematic of PERC from [KAB+12]

The first case study of PERC was published in 2008 [DAB+08] with a more reccent update in [KAB+12]. Inside a 8 m long superconducting solenoid with a magnetic field strength of 1.5 T a non-depolarizing neutron guide [Reb14] is placed. This neutron guide limits the divergence of the neutron beam and therefore also the size of the beam of the decay products. Those are collected by the strong magnetic field and transported along the solenoid also inside the neutron guide. Using several coils with varying field strength of 3 T to 6 T the beam of decay products is guided around the neutron beamstop. Details on the design of the magnetic field including the shielding can be found in [Zie15]. The high magnetic field thereby acts as a magnetic mirror and filters out all decay products that have an angle larger than the critical angle defined by the ratio of the both magnetic field strengths. This allows to cut into the angular distribution which helps in the final determination of the asymmetries by reducing the sensitivity to some systematic effects. The beam of decay products is then provided to exchangeable external instruments that are optimized to measure one or several of the observables.

When used with a polarized neutron beam, PERC can only feed one detector with the proton beam of approximate width of 10 cm. Therefore a similar detector as used in this measurement can be used to measure the proton asymmetry. One could reuse the new good lightguides by building a new detector with a size of 12 cm × 12 cm and only one lightguide per side. Also the foil size can be about the same size as the small foil in our measurement. The same detector with its good light output, could also be used for a measurement of the electron asymmetry as one of the first measurement with PERC.

One big problem of our beamtime, the particle trap between the two degraders, does not exist in this asymmetric setup. But a new trap between the degrader and the selector field is created and its impact on a proton measurement with high voltage conversion foils has to be studied.

Since it might take a while until PERC is completely commissioned and a proton measurement is scheduled, one might consider another beamtime with Perkeo III in a similar setup as this measurement. Necessary improvements in the stability of the high voltage might be achieved with the things we learned from this measurement. If the foil transport problem can be reduced or if the final step of the foil production can be done near the experiment, the system has the capability to make a better measurement. Other more stable foils are currently tested and characterized. Otherwise the same time could be used to fully optimize the detection system for a measurement with PERC. Of course also the usage of other detectors for low energetic protons has to be studied, but the current system has not reached its maximum possible performance.

Part V.

Appendix

A. Plot of the Vacuum Pressure

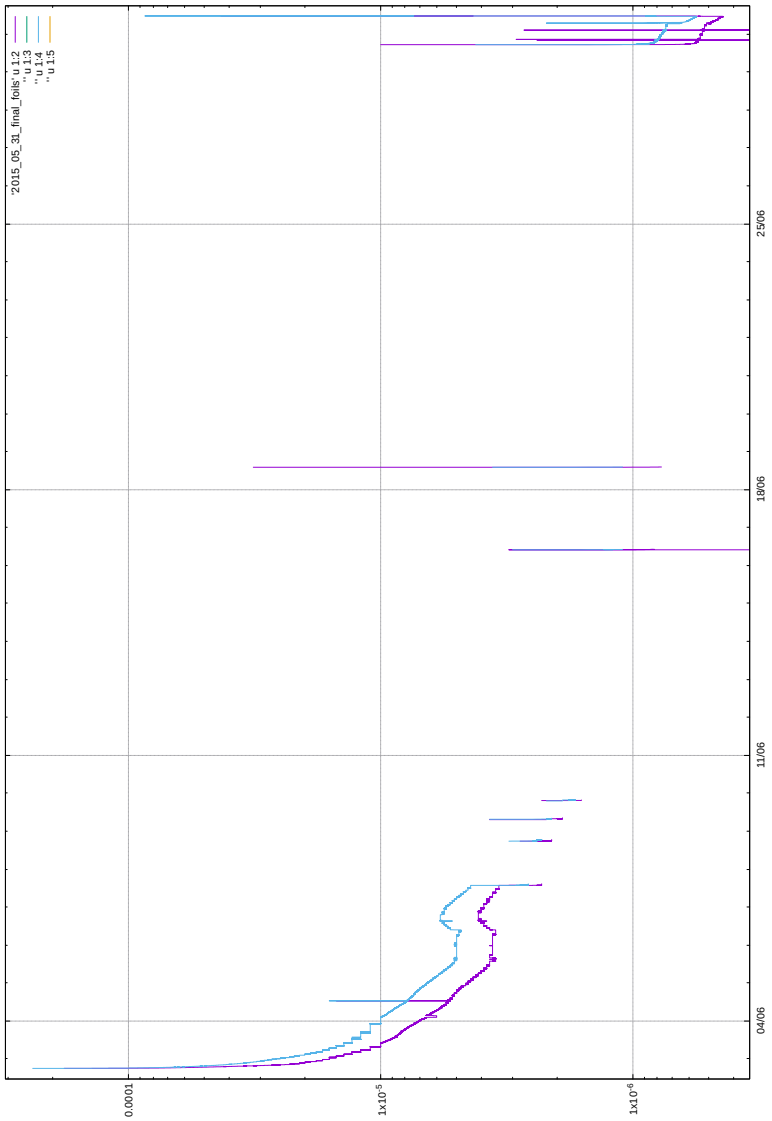

Figure A.1.: Pressure measured during the last beamtime

B. Additional Plots of the Delta-Time Investigation

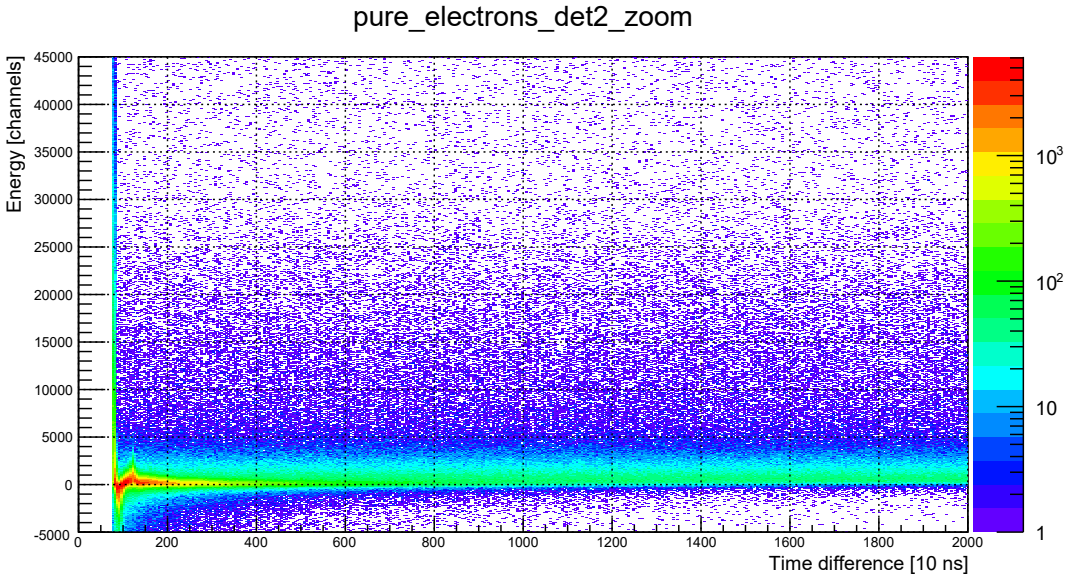

Figure B.1.: Same Plot as Figure 9.6b (downstream detector) but with all HV systems turned off.

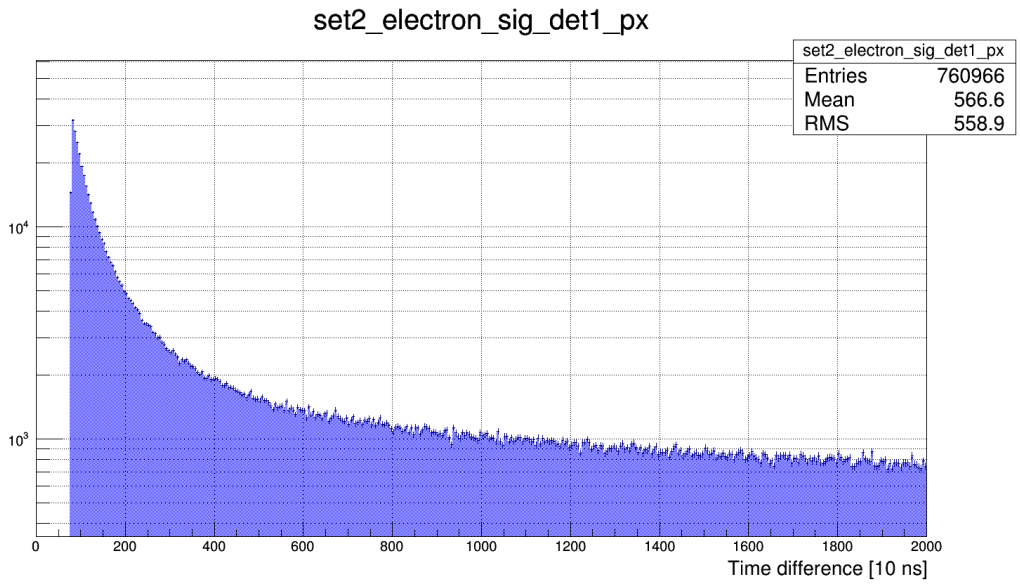

Figure B.2.: Delta time histogram (upstream Detector) from the `FULL850_BT` retardation and data group 2.

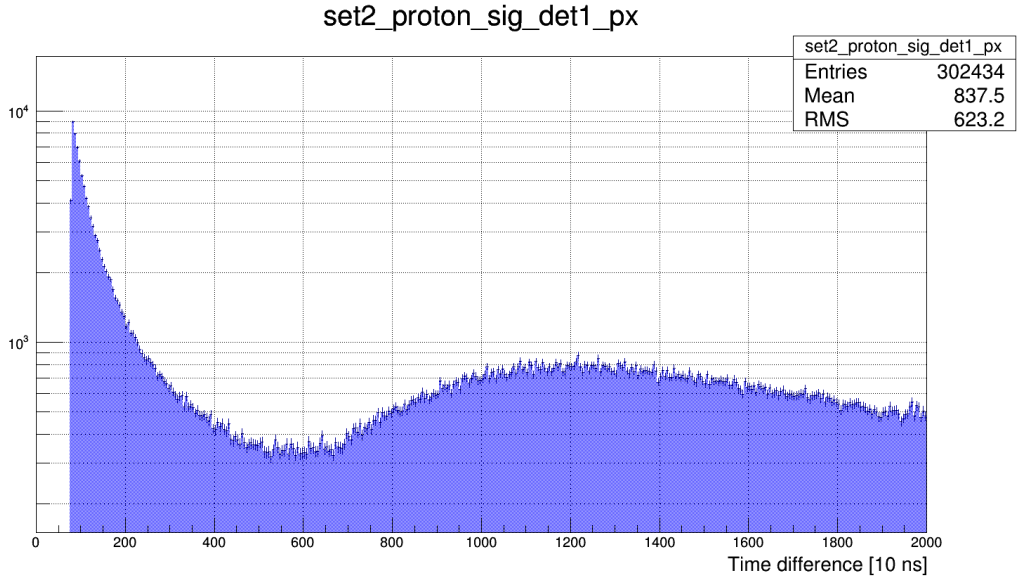

Figure B.3.: Delta time histogram (upstream Detector) from the `PROTONBLOCK10_BT` retardation and data group 2.

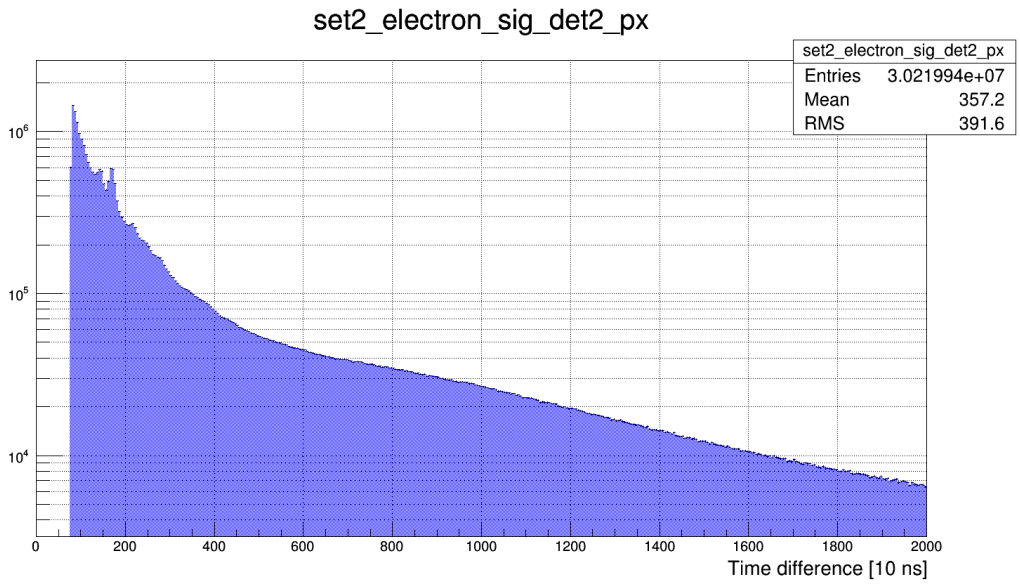

Figure B.4.: Delta time histogram (downstream Detector) from the `FULL850_BT` retardation and data group 2.

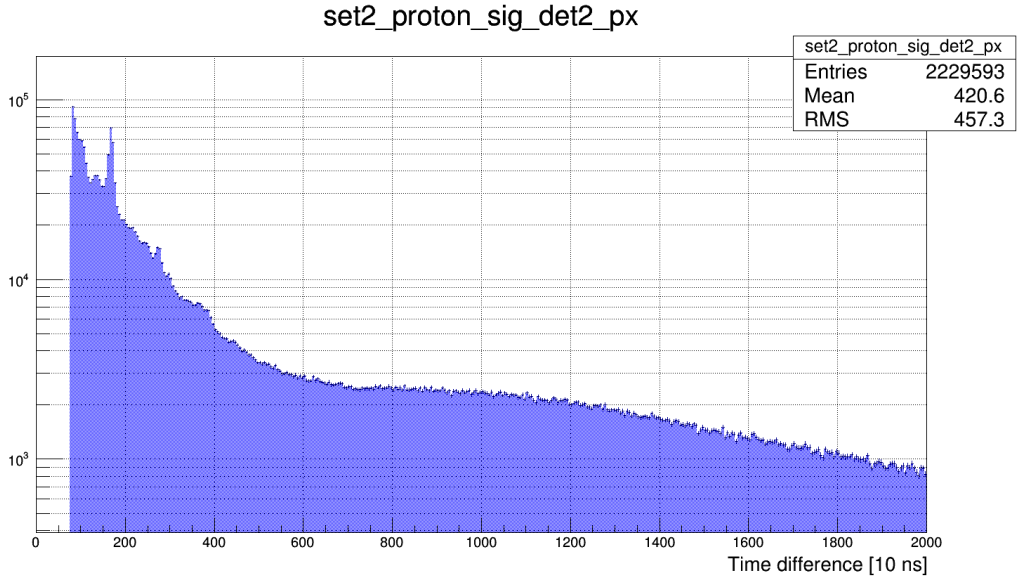

Figure B.5.: Delta time histogram (downstream Detector) from the `PROTONBLOCK10_BT` retardation and data group 2.

C. Mathematica Code for the Simple Baffle Calculations

```
In[248]:= thickEdge = ParallelTable[
            {edge
             , NIntegrate[Boole[
                 Max[Abs[r0[En] * Sin[θ] * (Cos[ϕ] + 1) ], Abs[r0[En] * Sin[θ] * (Cos[ϕ] - 1)]] < edge * rmax * 2 &&
                  Max[Abs[r0[En] * Sin[θ] * (Sin[ϕ] + 1) ], Abs[r0[En] * Sin[θ] * (Sin[ϕ] - 1)]] < edge * rmax * 2
                ] Sin[θ], {θ, 0, π / 2}, {ϕ, 0, 2 π}, PrecisionGoal → 4, AccuracyGoal → 4, Method → "AdaptiveMonteCarlo"
              ] / (2 π)}
            , {En, 0, E0, 0.1 E0}, {edge, 0, 1.2, 0.01}
           ];

          thickEnergy = ParallelTable[
            {kEn, NIntegrate[Boole[
                 Max[Abs[r0[kEn * E0] * Sin[θ] * (Cos[ϕ] + 1) ], Abs[r0[kEn * E0] * Sin[θ] * (Cos[ϕ] - 1)]] < edge * rmax * 2 &&
                  Max[Abs[r0[kEn * E0] * Sin[θ] * (Sin[ϕ] + 1) ], Abs[r0[kEn * E0] * Sin[θ] * (Sin[ϕ] - 1)]] < edge * rmax * 2
                ] Sin[θ], {θ, 0, π / 2}, {ϕ, 0, 2 π}, PrecisionGoal → 4, AccuracyGoal → 4, Method → "AdaptiveMonteCarlo"
              ] / (2 π)}
            , {edge, 0, 1, 0.1}, {kEn, 0, 1, 0.01}
           ];
```

Figure C.1.: Code for the thick baffle calculation

```
In[278]:= thinEdge = ParallelTable[
            {edge,
             NIntegrate[Boole[Abs[r0[En] * Sin[θ] * (1 - Cos[α]) Cos[ϕ] + r0[En] Sin[θ] Sin[α] Sin[ϕ]] < edge * rmax * 2 &&
                  Abs[-r0[En] * Sin[θ] * (1 - Cos[α]) Sin[ϕ] + r0[En] Sin[θ] Sin[α] Cos[ϕ]] < edge * rmax * 2] Sin[θ],
               {α, 0, 2 π}, {θ, 0, π / 2}, {ϕ, 0, 2 π}, PrecisionGoal → 3, AccuracyGoal → 2, Method → "AdaptiveMonteCarlo"] /
              (2 π * 2 π)}
            , {En, 0, E0, 0.1 E0}, {edge, 0, 1.2, 0.01}
           ];
          thinEnergy = ParallelTable[
            {kEn,
             NIntegrate[
               Boole[Abs[r0[kEn * E0] * Sin[θ] * (1 - Cos[α]) Cos[ϕ] + r0[kEn * E0] Sin[θ] Sin[α] Sin[ϕ]] < edge * rmax * 2 &&
                  Abs[-r0[kEn * E0] * Sin[θ] * (1 - Cos[α]) Sin[ϕ] + r0[kEn * E0] Sin[θ] Sin[α] Cos[ϕ]] < edge * rmax * 2] Sin[θ],
               {α, 0, 2 π}, {θ, 0, π / 2}, {ϕ, 0, 2 π}, PrecisionGoal → 3, AccuracyGoal → 2, Method → "AdaptiveMonteCarlo"] /
              (2 π * 2 π)}
            , {edge, 0, 1, 0.1}, {kEn, 0, 1, 0.01}
           ];
```

Figure C.2.: Code for the thin baffle calculation

```
In[380]:= ListLinePlot[thickEdge
 , GridLines → Automatic
 , PlotLabel → "thick baffle"
 , Frame → True
 , FrameLabel → {"baffle diameter [ 4 r_max(E_0) ]", "Transmission"}
 , BaseStyle → {FontSize → Larger, FontWeight → Bold, FontFamily → "Helvetica"}
 , ImageSize → 600
 ,
 PlotLegends ->
  Placed[LineLegend[Range[0, 100, 10], LabelStyle → {GrayLevel[0.3], Bold}, LegendLabel → "% of Emax",
    LegendLayout → {"Column", 2}], {1., 0.5}]
]

ListLinePlot[thickEnergy
 , GridLines → Automatic
 , PlotLabel → "thick baffle"
 , Frame → True
 , FrameLabel → {"Energy [E_0]", "Transmission"}
 , BaseStyle → {FontSize → Larger, FontWeight → Bold, FontFamily → "Helvetica"}
 , ImageSize → 600
 ,
 PlotLegends ->
  Placed[LineLegend[Range[0, 100, 10], LabelStyle → {GrayLevel[0.3], Bold}, LegendLabel → "% of Dmax",
    LegendLayout → {"Column", 2}], {1., 0.5}]
]
```

Figure C.3.: Code to plot the thick baffle data

D. Rates

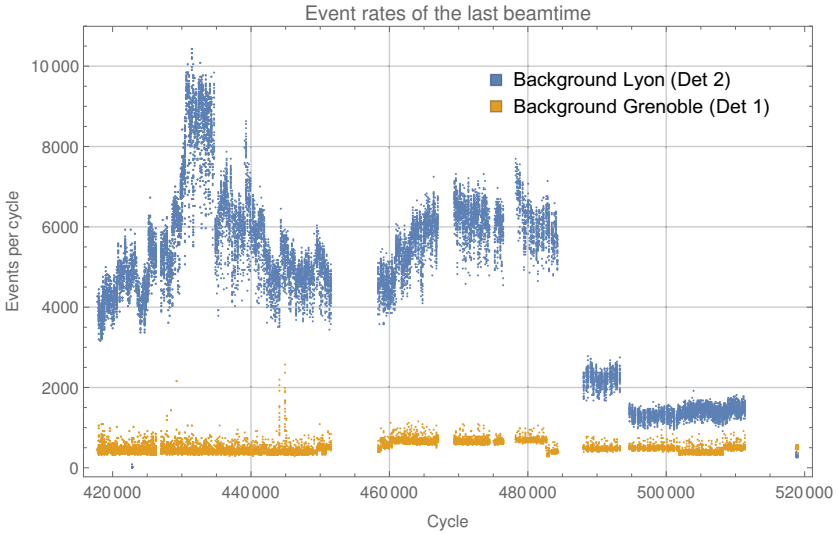

Figure D.1.: Background rates separated by the first triggered detector.

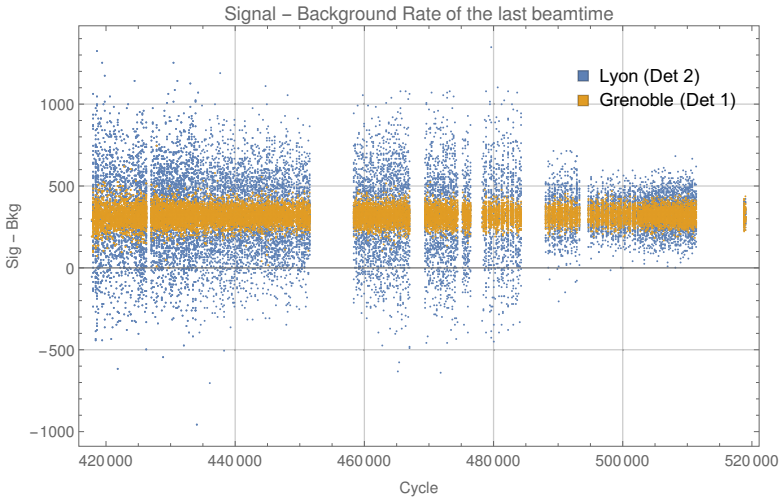

Figure D.2.: Signal - Background separated by the first triggered detector.

E. Histograms of correction factors

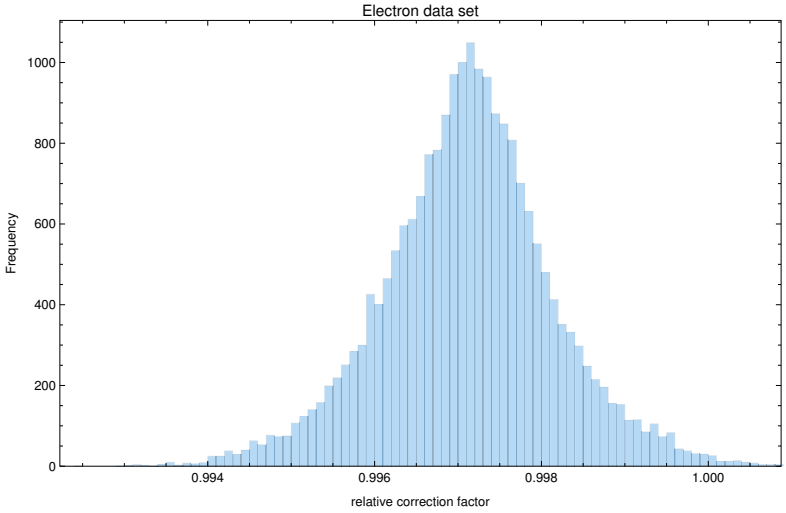

Figure E.1.: Histogram of relative correction factor dataset electrons

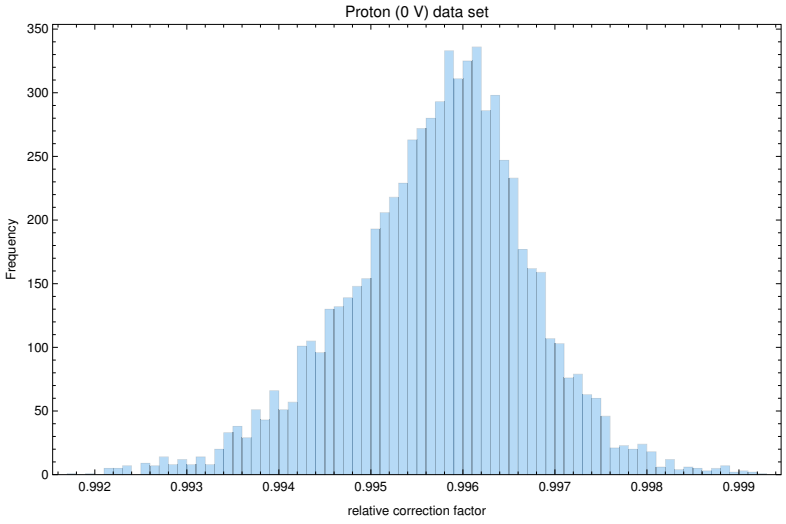

Figure E.2.: Histogram of relative correction factor dataset Proton (0 V)

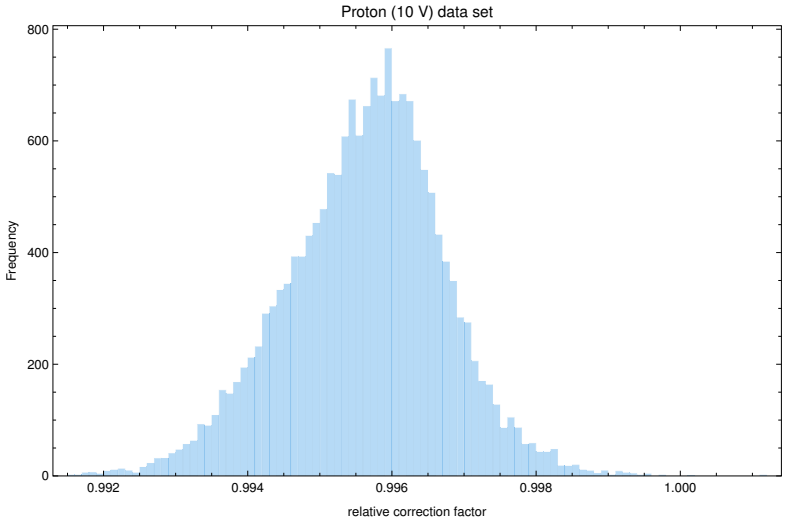

Figure E.3.: Histogram of relative correction factor dataset Proton (10 V)

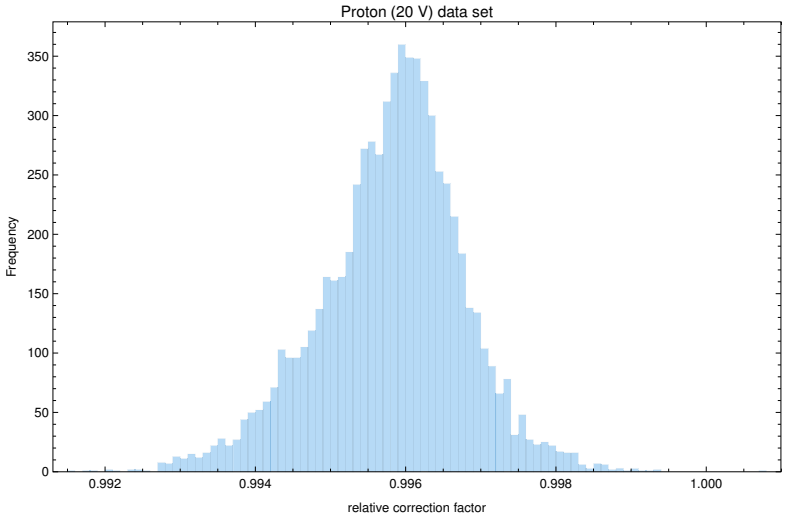

Figure E.4.: Histogram of relative correction factor dataset Proton (20 V)

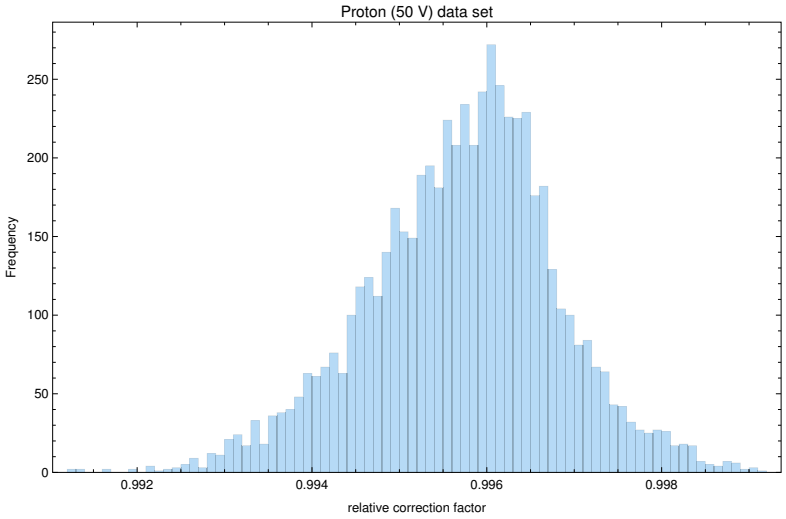

Figure E.5.: Histogram of relative correction factor dataset Proton (50 V)

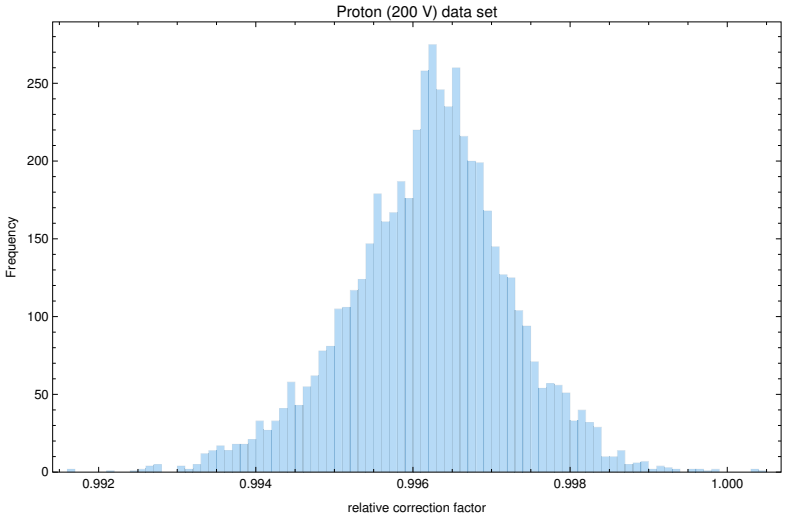

Figure E.6.: Histogram of relative correction Factor dataset Proton (200 V)

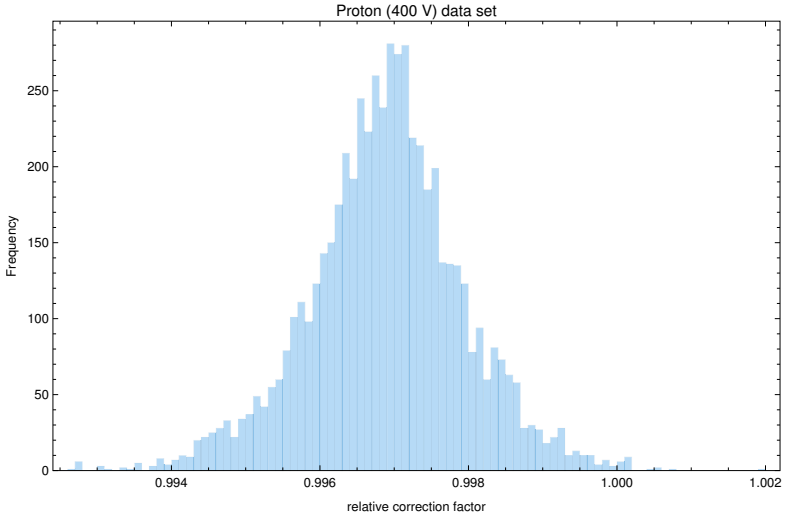

Figure E.7.: Histogram of relative correction factor dataset Proton (400 V)

List of Figures

List of Tables

Bibliography

[AAA+83] G. Arnison et al. "Experimental observation of isolated large transverse energy electrons with associated missing energy at s=540 GeV". In: *Physics Letters B* 122.1 (1983), pp. 103–116. DOI: http://dx.doi.org/10.1016/0370-2693(83)91177-2.

[ABM+12] S. S. Arzumanov, L. N. Bondarenko, V. I. Morozov, Yu. N. Panin, and S. M. Chernyavsky. "Analysis and correction of the measurement of the neutron lifetime". In: *JETP Letters* 95.5 (2012), pp. 224–228. DOI: 10.1134/S0021364012050025.

[ADH+06] H. Abele et al. "Characterization of a ballistic supermirror neutron guide". In: *Nuclear Instruments and Methods in Physics Research Section A: Accelerators, Spectrometers, Detectors and Associated Equipment* 562.1 (2006), pp. 407–417. DOI: http://dx.doi.org/10.1016/j.nima.2006.03.020.

[AFG+04] S. Ando, H.W. Fearing, V. Gudkov, K. Kubodera, F. Myhrer, S. Nakamura, and T. Sato. "Neutron beta-decay in effective field theory". In: *Physics Letters B* 595.1–4 (2004), pp. 250–259. DOI: http://dx.doi.org/10.1016/j.physletb.2004.06.037.

[Age89] Paul Ageron. "Cold neutron sources at ILL". In: *Nuclear Instruments and Methods in Physics Research Section A: Accelerators, Spectrometers, Detectors and Associated Equipment* 284.1 (1989), pp. 197–199. DOI: http://dx.doi.org/10.1016/0168-9002(89)90281-7.

[ATL12] G. Aad et al. "Observation of a new particle in the search for the Standard Model Higgs boson with the {ATLAS} detector at the {LHC}". In: *Physics Letters B* 716.1 (2012), pp. 1–29. DOI: http://dx.doi.org/10.1016/j.physletb.2012.08.020.

[Bac15] H. Backe. "Note: Precise radial distribution of charged particles in a magnetic guiding field". In: *Review of Scientific Instruments* 86.7, 076104 (2015). DOI: http://dx.doi.org/10.1063/1.4926565.

[Bac16a] H. Backe. "On magnetic guidance of charged particles". In: *Physics Letters B* 755 (2016), pp. 409–413. DOI: http://dx.doi.org/10.1016/j.physletb.2016.02.027.

[Bac16b] H. Backe. "Corrigendum to "On magnetic guidance of charged particles" [Phys. Lett. B 755 (2016) 409–413]". In: *Physics Letters B* 756 (2016), pp. 413–414. DOI: http://dx.doi.org/10.1016/j.physletb.2016.03.058.

[BBB+83] M. Banner et al. "Observation of single isolated electrons of high transverse momentum in events with missing transverse energy at the CERN pp collider". In: *Physics Letters B* 122.5 (1983), pp. 476–485. DOI: http://dx.doi.org/10.1016/0370-2693(83)91605-2.

[BBD+11] J. F. Bueno et al. "Precise measurement of parity violation in polarized muon decay". In: *Phys. Rev. D* 84 (3 Aug. 2011), p. 032005. DOI: 10.1103/PhysRevD.84.032005.

[BBM+77] M. A. B. Beg, R. V. Budny, Rabindra N. Mohapatra, and A. Sirlin. "Manifest Left-Right Symmetry and Its Experimental Consequences". In: *Phys. Rev. Lett.* 38 (1977). [Erratum: Phys. Rev. Lett.39,54(1977)], p. 1252. DOI: 10.1103/PhysRevLett.38.1252.

[BDG+02] J Byrne, P G Dawber, M G D van der Grinten, C G Habeck, F Shaikh, J A Spain, R D Scott, C A Baker, K Green, and O Zimmer. "Determination of the electron–antineutrino angular correlation coefficient a_0 and the parameter $|\lambda| = |G_A/G_V|$ in free neutron β-decay from measurements of the integrated energy spectrum of recoil protons stored in an ion trap". In: *Journal of Physics G: Nuclear and Particle Physics* 28.6 (2002), p. 1325.

[BDH+86] P. Bopp, D. Dubbers, L. Hornig, E. Klemt, J. Last, H. Schütze, S. J. Freedman, and O. Schärpf. "Beta-Decay Asymmetry of the Neutron and $\frac{g_A}{g_V}$". In: *Phys. Rev. Lett.* 56 (9 Mar. 1986), pp. 919–922. DOI: 10.1103/PhysRevLett.56.919.

[Ber16] Karina Bernert. "Detection of low energy protons". Bachelor's Thesis. TU Munich, 2016.

[BLP+93] A.N. Bazhenov, V.M. Lobashev, A.N. Pirozhkov, and V.N. Slusar. "An adiabatic resonance spin-flipper for thermal and cold neutrons". In: *Nuclear Instruments and Methods in Physics Research Section A: Accelerators, Spectrometers, Detectors and Associated Equipment* 332.3 (1993), pp. 534–536. DOI: http://dx.doi.org/10.1016/0168-9002(93)90311-5.

[BR97] Rene Brun and Fons Rademakers. "New Computing Techniques in Physics Research V ROOT — An object oriented data analysis framework". In: *Nuclear Instruments and Methods in Physics Research Section A: Accelerators, Spectrometers, Detectors and Associated Equipment* 389.1 (1997), pp. 81–86. DOI: http://dx.doi.org/10.1016/S0168-9002(97)00048-X.

[Bra00] Bernhard Brand. "Ein Detektor für die Messung der Neutrinoasymmetrie beim Zerfall freier Neutronen". Diploma Thesis. Ruprecht-Karls-Universität Heidelberg, 2000.

[Byr16] S. J. Byrnes. "Multilayer optical calculations". In: *ArXiv e-prints* (Mar. 2016). arXiv: 1603.02720 [physics.comp-ph].

[Cab63] Nicola Cabibbo. "Unitary Symmetry and Leptonic Decays". In: *Phys. Rev. Lett.* 10 (12 June 1963), pp. 531–533. DOI: 10.1103/PhysRevLett.10.531.

[CCC+12] T. E. Chupp et al. "Search for a T-odd, P-even triple correlation in neutron decay". In: *Phys. Rev. C* 86 (3 Sept. 2012), p. 035505. DOI: 10.1103/PhysRevC.86.035505.

[CDF95] F. Abe et al. "Observation of Top Quark Production in $\bar{p}p$ Collisions with the Collider Detector at Fermilab". In: *Phys. Rev. Lett.* 74 (14 Apr. 1995), pp. 2626–2631. DOI: 10.1103/PhysRevLett.74.2626.

[CDJ+13] Ruiyi Chen, Suprem R. Das, Changwook Jeong, Mohammad Ryyan Khan, David B. Janes, and Muhammad A. Alam. "Co-Percolating Graphene-Wrapped Silver Nanowire Network for High Performance, Highly Stable, Transparent Conducting Electrodes". In: *Advanced Functional Materials* 23.41 (2013), pp. 5150–5158. DOI: 10.1002/adfm.201300124.

[CGZ99] M. Czakon, J. Gluza, and M. Zralek. "Low-energy physics and left-right symmetry: Bounds on the model parameters". In: *Phys. Lett.* B458 (1999), pp. 355–360. DOI: 10.1016/S0370-2693(99)00567-5. arXiv: hep-ph/9904216 [hep-ph].

[CMS12] S. Chatrchyan et al. "Observation of a new boson at a mass of 125 GeV with the {CMS} experiment at the {LHC}". In: *Physics Letters B* 716.1 (2012), pp. 30–61. DOI: http://dx.doi.org/10.1016/j.physletb.2012.08.021.

[D095] S. Abachi et al. "Search for High Mass Top Quark Production in $p\bar{p}$ Collisions at $\sqrt{s} = 1.8$ TeV". In: *Phys. Rev. Lett.* 74 (13 Mar. 1995), pp. 2422–2426. DOI: 10.1103/PhysRevLett.74.2422.

[DAB+08] D. Dubbers, H. Abele, S. Baeßler, B. Märkisch, M. Schumann, T. Soldner, and O. Zimmer. "A clean, bright, and versatile source of neutron decay products". In: *Nuclear Instruments and Methods in Physics Research Section A: Accelerators, Spectrometers, Detectors and Associated Equipment* 596.2 (2008), pp. 238–247. DOI: http://dx.doi.org/10.1016/j.nima.2008.07.157.

[Dai] *Neutron Velocity Selector, Blade rotor developed by Dornier/GKSS/PTB*. Daimler-Benz Aerospace, Dornier Satellitensysteme GmbH.

[Día14] Jorge S. Díaz. "Tests of Lorentz symmetry in single beta decay". In: *Adv. High Energy Phys.* 2014 (2014), p. 305298. DOI: 10.1155/2014/305298. arXiv: 1408.5880 [hep-ph].

[DKL13] Jorge S. Díaz, V. Alan Kostelecký, and Ralf Lehnert. "Relativity violations and beta decay". In: *Phys. Rev. D* 88 (7 Oct. 2013), p. 071902. DOI: 10.1103/PhysRevD.88.071902.

[DRM+14] D. Dubbers, L. Raffelt, B. Märkisch, F. Friedl, and H. Abele. "The point spread function of electrons in a magnetic field, and the decay of the free neutron". In: *Nuclear Instruments and Methods in Physics Research Section A: Accelerators, Spectrometers, Detectors and Associated Equipment* 763 (2014), pp. 112–119. DOI: http://dx.doi.org/10.1016/j.nima.2014.06.020.

[DS11] Dirk Dubbers and Michael G. Schmidt. "The neutron and its role in cosmology and particle physics". In: *Rev. Mod. Phys.* 83.4 (4 Oct. 2011), pp. 1111–1171. DOI: 10.1103/RevModPhys.83.1111.

[Dub15] Dirk Dubbers. "Magnetic guidance of charged particles". In: *Physics Letters B* 748 (2015), pp. 306–310. DOI: http://dx.doi.org/10.1016/j.physletb.2015.07.004.

[FG58] R. P. Feynman and M. Gell-Mann. "Theory of the Fermi Interaction". In: *Phys. Rev.* 109 (1 Jan. 1958), pp. 193–198. DOI: 10.1103/PhysRev.109.193.

[FWW89] H. Friedrich, V. Wagner, and P. Wille. "A high-performance neutron velocity selector". In: *Physica B: Condensed Matter* 156 (1989), pp. 547–549. DOI: http://dx.doi.org/10.1016/0921-4526(89)90727-8.

[GGV+68] V. K. Grigoriev, A. P. Grishin, V. V. Vladimirsky, and E. S. Nikolaevsky. "Measurement of Angular $(e, \overline{\nu_e})$ Correlation at Free Neutron Decay". In: *Sov. J. Nucl. Phys.* 6 (1968), p. 239.

[GJL95] F. Glück, I. Joó, and J. Last. "Measurable parameters of neutron decay". In: *Nuclear Physics A* 593.2 (1995), pp. 125–150. DOI: http://dx.doi.org/10.1016/0375-9474(95)00354-4.

[Gla61] S. L. Glashow. "Partial Symmetries of Weak Interactions". In: *Nucl. Phys.* 22 (1961), pp. 579–588. DOI: 10.1016/0029-5582(61)90469-2.

[Glü96] F. Glück. "The proton asymmetry in neutron decay". In: *Physics Letters B* 376.1–3 (1996), pp. 25–28. DOI: http://dx.doi.org/10.1016/0370-2693(96)00290-0.

[Gud08] Vladimir P. Gudkov. "Asymmetry of recoil protons in neutron beta-decay". In: *Phys. Rev. C77* (2008), p. 045502. DOI: 10.1103/PhysRevC.77.045502. arXiv: 0801.4896 [hep-ph].

[HKF+02] H. Häse, A. Knöpfler, K. Fiederer, U. Schmidt, D. Dubbers, and W. Kaiser. "A long ballistic supermirror guide for cold neutrons at {ILL}". In: *Nuclear Instruments and Methods in Physics Research Section A: Accelerators, Spectrometers, Detectors and Associated Equipment* 485.3 (2002), pp. 453–457. DOI: http://dx.doi.org/10.1016/S0168-9002(01)02105-2.

[HKK+73] F.J. Hasert et al. "Observation of neutrino-like interactions without muon or electron in the gargamelle neutrino experiment". In: *Physics Letters B* 46.1 (1973), pp. 138–140. DOI: http://dx.doi.org/10.1016/0370-2693(73)90499-1.

[HT09] J. C. Hardy and I. S. Towner. "Superallowed $0^+ \to 0^+$ nuclear β decays: A new survey with precision tests of the conserved vector current hypothesis and the standard model". In: *Phys. Rev. C* 79 (5 May 2009), p. 055502. DOI: 10.1103/PhysRevC.79.055502.

[HYA+06] S. A. Hoedl, A. R. Young, H. Ade, and A. Lozano. "An electron transparent proton detector for neutron decay studies". In: *Journal of Applied Physics* 99.8, 084904 (2006). DOI: http://dx.doi.org/10.1063/1.2186970.

[Inz08] G. Inzelt. *Conducting Polymers: A New Era in Electrochemistry*. Monographs in Electrochemistry. Springer Berlin Heidelberg, 2008.

[Jac99] John David Jackson. *Classical electrodynamics*. eng. 3. ed. New York ; Weinheim [u.a.]: Wiley, 1999, XXI, 808 S.

[JTW57] J. D. Jackson, S. B. Treiman, and H. W. Wyld. "Possible Tests of Time Reversal Invariance in Beta Decay". In: *Phys. Rev.* 106 (3 May 1957), pp. 517–521. DOI: 10.1103/PhysRev.106.517.

[KAB+12] G Konrad et al. "Neutron Decay with PERC: a Progress Report". In: *Journal of Physics: Conference Series* 340.1 (2012), p. 012048.

[KBB+12] A. Kozela et al. "Measurement of the transverse polarization of electrons emitted in free neutron decay". In: *Phys. Rev. C* 85 (4 Apr. 2012), p. 045501. DOI: 10.1103/PhysRevC.85.045501.

[KHB+12] G. Konrad, W. Heil, S. Baeßler, D. Počanić, and F. Glück. "Impact of Neutron Decay Experiments on non-Standard Model Physics". In: *Physics Beyond the Standard Models of Particles, Cosmology and Astrophysics*. 2012, pp. 660–672. DOI: 10.1142/9789814340861_0061. eprint: http://www.worldscientific.com/doi/pdf/10.1142/9789814340861_0061.

[KHS+11] Andriy V Kyrylyuk, Marie Claire Hermant, Tanja Schilling, Bert Klumperman, Cor E Koning, and Paul Van der Schoot. "Controlling electrical percolation in multicomponent carbon nanotube dispersions". In: *Nature nanotechnology* 6.6 (2011), pp. 364–369.

[KLK+14] Tobias A. F. König, Petr A. Ledin, Justin Kerszulis, Mahmoud. A. Mahmoud, Mostafa A. El-Sayed, John R. Reynolds, and Vladimir V. Tsukruk. "Electrically Tunable Plasmonic Behavior of Nanocube–Polymer Nanomaterials Induced by a Redox-Active Electrochromic Polymer". In: *ACS Nano* 8.6 (2014). PMID: 24870253, pp. 6182–6192. DOI: 10.1021/nn501601e. eprint: http://dx.doi.org/10.1021/nn501601e.

[Klo15] Michael Klopf. *private communication*. 2015.

[Klo17] Michael Klopf. "unpublished". PhD thesis. TU Wien, 2017.

[KM73] Makoto Kobayashi and Toshihide Maskawa. “CP-Violation in the Renormalizable Theory of Weak Interaction”. In: *Progress of Theoretical Physics* 49.2 (1973), pp. 652–657. DOI: 10.1143/PTP.49.652. eprint: http://ptp.oxfordjournals.org/content/49/2/652.full.pdf+html.

[Kon15] Gertrud Konrad. *private communication*. 2015.

[Kre04] Michael Kreuz. “Messung von Winkelkorrelationen im Zerfall polarisierter Neutronen mit dem Spektrometer PERKEO II”. PhD thesis. Universität Heidelberg, 2004.

[KSB+05] M. Kreuz et al. “A measurement of the antineutrino asymmetry B in free neutron decay”. In: *Physics Letters B* 619.3–4 (2005), pp. 263–270. DOI: http://dx.doi.org/10.1016/j.physletb.2005.05.074.

[Len14] Peter Lennert. *Private communication*. 2014.

[Leo94] William R. Leo. *Techniques for nuclear and particle physics experiments. a how-to approach ; with 40 tables and numerous worked examples*. eng. 2., rev. ed. Berlin ; Heidelberg [u.a.]: Springer, 1994, XVIII, 378 S.

[LHA+00] L. J. Lising et al. “New limit on the $\boldsymbol{D}$ coefficient in polarized neutron decay”. In: *Phys. Rev. C* 62 (5 Sept. 2000), p. 055501. DOI: 10.1103/PhysRevC.62.055501.

[LSK+97] P. Liaud, K. Schreckenbach, R. Kossakowski, H. Nastoll, A. Bussière, J.P. Guillaud, and L. Beck. “The measurement of the beta asymmetry in the decay of polarized neutrons”. In: *Nuclear Physics A* 612.1 (1997), pp. 53–81. DOI: http://dx.doi.org/10.1016/S0375-9474(96)00325-9.

[LY11] Cai-Hong Liu and Xun Yu. “Silver nanowire-based transparent, flexible, and conductive thin film”. In: *Nanoscale Research Letters* 6.1 (2011), pp. 1–8. DOI: 10.1186/1556-276X-6-75.

[LY56] T. D. Lee and C. N. Yang. “Question of Parity Conservation in Weak Interactions”. In: *Phys. Rev.* 104 (1 Oct. 1956), pp. 254–258. DOI: 10.1103/PhysRev.104.254.

[MAD+09] B. Märkisch, H. Abele, D. Dubbers, F. Friedl, A. Kaplan, H. Mest, M. Schumann, T. Soldner, and D. Wilkin. “The new neutron decay spectrometer Perkeo {III}”. In: *Nuclear Instruments and Methods in Physics Research Section A: Accelerators, Spectrometers, Detectors and Associated Equipment* 611.2–3 (2009). Particle Physics with Slow Neutrons, pp. 216–218. DOI: http://dx.doi.org/10.1016/j.nima.2009.07.066.

[Mär06] Bastian Märkisch. “Das Spektrometer PERKEO III und der Zerfall des freien Neutrons”. PhD thesis. Universität Heidelberg, 2006. DOI: urn:nbn:de:bsz:16-opus-69278.

[Mär15] Bastian Märkisch. *private communication*. 2015.

[Math10] Wolfram Research Inc. *Wolfram Language Symbol Documentation Version 10.4*.

[Mes11] Holger Mest. “Measurement of the β-Asymmetry in the Decay of Free Polarized Neutrons with the Spectrometer Perkeo III”. PhD thesis. Universität Heidelberg, 2011.

[MMD+13] D. Mund, B. Märkisch, M. Deissenroth, J. Krempel, M. Schumann, H. Abele, A. Petoukhov, and T. Soldner. “Determination of the Weak Axial Vector Coupling $\lambda=g_A/g_V$ from a Measurement of the β-Asymmetry Parameter A in Neutron Beta Decay”. In: *Phys. Rev. Lett.* 110.17 (17 Apr. 2013), p. 172502. DOI: 10.1103/PhysRevLett.110.172502.

[Mos15] Daniel Moser. *Private communication*. 2015.

[MPB+13] M. P. Mendenhall et al. "Precision measurement of the neutron β-decay asymmetry". In: *Phys. Rev. C* 87 (3 Mar. 2013), p. 032501. DOI: 10.1103/PhysRevC.87.032501.

[Mun06] Daniela Mund. "Messung der Betaasymmetrie A im Neutronenzerfall". PhD thesis. Universität Heidelberg, 2006.

[NG13] Oscar Naviliat-Cuncic and Martín González-Alonso. "Prospects for precision measurements in nuclear β decay in the LHC era". In: *Annalen der Physik* 525.8-9 (2013), pp. 600–619. DOI: 10.1002/andp.201300072.

[pdg15] K. A. Olive et al. "Review of Particle Physics". In: *Chin. Phys.* C38 (2014), p. 090001. DOI: 10.1088/1674-1137/38/9/090001.

[Plo00] Christian Plonka. "Verbesserung der Lichtauskopplung zur Messung der Neuttrinoasymmetrie mit PERKEO-II". Diplomarbeit. Universität Heidelberg, 2000.

[Rav95] Carsten Raven. "Erste Messungen mit Perkeo II. Beta-Asymmetrie im Neutron Zerfall ; Vorbereitung und Test des Experiments". ger. Diploma Thesis. Universität Heidelberg, 1995, 60 S.

[RDE+98] Aleksandar D. Rakić, Aleksandra B. Djurišić, Jovan M. Elazar, and Marian L. Majewski. "Optical properties of metallic films for vertical-cavity optoelectronic devices". In: *Appl. Opt.* 37.22 (Aug. 1998), pp. 5271–5283. DOI: 10.1364/AO.37.005271.

[Reb14] Nataliya Rebrova. "Development of a non-depolarizing neutron guide for PERC". PhD thesis. Universität Heidelberg, 2014.

[Rei91] Robert Reiner. "Winkel-Korrelationshoeffizienten im Neutronen Zerfall". Diploma Thesis. Universität Heidelberg, 1991.

[Rei99] Jürgen C. Reich. "Winkelkorrelationen im Zerfall polarisierter Neutronen". PhD thesis. Universität Heidelberg, 1999.

[Roi12] Christoph Roick. "Untersuchungen zur Elektronendetektion in Neutronenzerfallsexperimenten". Master's Thesis. Universität Heidelberg, 2012.

[Roi15] Christoph Roick. *Private communication*. 2015.

[Roi17] Christoph Roick. "unpublished". PhD thesis. TU München, 2017.

[SA08] M. Schumann and H. Abele. "Unrecognized backscattering in low energy beta spectroscopy". In: *Nuclear Instruments and Methods in Physics Research Section A: Accelerators, Spectrometers, Detectors and Associated Equipment* 585.1–2 (2008), pp. 88–92. DOI: http://dx.doi.org/10.1016/j.nima.2007.11.016.

[Sai14] Saint-Gobain. *Premium Plastic Scintillators*. 2014.

[Sal68] Abdus Salam. "Weak and Electromagnetic Interactions". In: *Conf. Proc.* C680519 (1968), pp. 367–377.

[Sau16] Heiko Saul. "unpublished". PhD thesis. TU Wien, 2016.

[SBM+15] S. K. L. Sjue, L. J. Broussard, M. Makela, P. L. McGaughey, A. R. Young, and B. A. Zeck. "Radial distribution of charged particles in a magnetic field". In: *Review of Scientific Instruments* 86.2, 023102 (2015). DOI: http://dx.doi.org/10.1063/1.4906547.

[SBP+04] T Soldner, L Beck, C Plonka, K Schreckenbach, and O Zimmer. "New limit on T violation in neutron decay". In: *Physics Letters B* 581.1–2 (2004), pp. 49–55. DOI: http://dx.doi.org/10.1016/j.physletb.2003.12.004.

[Sch+06] S. Schael et al. "Precision electroweak measurements on the Z resonance". In: *Phys. Rept.* 427 (2006), pp. 257–454. DOI: 10.1016/j.physrep.2005.12.006. arXiv: hep-ex/0509008 [hep-ex].

[Sch07] Marc Schumann. "Measurement of Neutrino and Proton Asymmetry in the Decay of polarized Neutrons". Phd Thesis. Universität Heidelberg, 2007.

[Sch15] Ulrich Schmidt. *Private communication*. 2015.

[SDW78] Chr. Stratowa, R. Dobrozemsky, and P. Weinzierl. "Ratio $|\frac{g_A}{g_V}|$ derived from the proton spectrum in free-neutron decay". In: *Phys. Rev. D* 18 (11 Dec. 1978), pp. 3970–3979. DOI: 10.1103/PhysRevD.18.3970.

[SFS15] Jaber Saghaei, Ali Fallahzadeh, and Tayebeh Saghaei. "ITO-free organic solar cells using highly conductive phenol-treated PEDOT:PSS anodes". In: *Organic Electronics* 24 (2015), pp. 188–194. DOI: http://dx.doi.org/10.1016/j.orgel.2015.06.002.

[SKD+08] M. Schumann, M. Kreuz, M. Deissenroth, F. Glück, J. Krempel, B. Märkisch, D. Mund, A. Petoukhov, T. Soldner, and H. Abele. "Measurement of the Proton Asymmetry Parameter in Neutron Beta Decay". In: *Phys. Rev. Lett.* 100.15 (15 Apr. 2008), p. 151801. DOI: 10.1103/PhysRevLett.100.151801.

[SM58] E. C. G. Sudarshan and R. E. Marshak. "Chirality Invariance and the Universal Fermi Interaction". In: *Phys. Rev.* 109 (5 Mar. 1958), pp. 1860–1862. DOI: 10.1103/PhysRev.109.1860.2.

[SPK+12] A. Steyerl, J. M. Pendlebury, C. Kaufman, S. S. Malik, and A. M. Desai. "Quasielastic scattering in the interaction of ultracold neutrons with a liquid wall and application in a reanalysis of the Mambo I neutron-lifetime experiment". In: *Phys. Rev. C* 85 (6 June 2012), p. 065503. DOI: 10.1103/PhysRevC.85.065503.

[SS89] O. Schaerpf and N. Stuesser. "Recent progress in neutron polarizers". In: *Nuclear Instruments and Methods in Physics Research Section A: Accelerators, Spectrometers, Detectors and Associated Equipment* 284.1 (1989), pp. 208–211. DOI: http://dx.doi.org/10.1016/0168-9002(89)90283-0.

[SSD+07] M. Schumann, T. Soldner, M. Deissenroth, F. Glück, J. Krempel, M. Kreuz, B. Märkisch, D. Mund, A. Petoukhov, and H. Abele. "Measurement of the Neutrino Asymmetry Parameter B in Neutron Decay". In: *Phys. Rev. Lett.* 99 (19 Nov. 2007), p. 191803. DOI: 10.1103/PhysRevLett.99.191803.

[SVK+05] A. Serebrov et al. "Measurement of the neutron lifetime using a gravitational trap and a low-temperature Fomblin coating". In: *Physics Letters B* 605.1–2 (2005), pp. 72–78. DOI: http://dx.doi.org/10.1016/j.physletb.2004.11.013.

[Tre58] S. B. Treiman. "Recoil Effects in K Capture and β Decay". In: *Phys. Rev.* 110 (2 Apr. 1958), pp. 448–450. DOI: 10.1103/PhysRev.110.448.

[WAH+57] C. S. Wu, E. Ambler, R. W. Hayward, D. D. Hoppes, and R. P. Hudson. "Experimental Test of Parity Conservation in Beta Decay". In: *Phys. Rev.* 105 (4 Feb. 1957), pp. 1413–1415. DOI: 10.1103/PhysRev.105.1413.

[Wan13] Xiangzun Wang. "The Free Neutron β-Decay: A Powerful Tool for the Investigation in Particle Physics". PhD thesis. Technische Universität München, 2013.

[Wei67] Steven Weinberg. "A Model of Leptons". In: *Phys. Rev. Lett.* 19 (1967), pp. 1264–1266. DOI: 10.1103/PhysRevLett.19.1264.

[Wer09] Dominik Werder. "Development and Characterization of a Pulsed Beam for Neutron Decay Experiments". Diploma Thesis. Universität Heidelberg, 2009.

[WFW92] V. Wagner, H. Friedrich, and P. Wille. "Performance of a high-tech neutron velocity selector". In: *Physica B: Condensed Matter* 180 (1992), pp. 938–940. DOI: http://dx.doi.org/10.1016/0921-4526(92)90515-T.

[WFW95] V. Wagner, H. Friedrich, and P. Wille. "Higher-order suppression by a mechanical velocity selector". In: *Physica B: Condensed Matter* 213 (1995), pp. 963–965. DOI: http://dx.doi.org/10.1016/0921-4526(95)00336-8.

[WG11] Fred E. Wietfeldt and Geoffrey L. Greene. "*Colloquium* : The neutron lifetime". In: *Rev. Mod. Phys.* 83 (4 Nov. 2011), pp. 1173–1192. DOI: 10.1103/RevModPhys.83.1173.

[Wil07] Daniel Wilkin. "Aufbau eines Kollimationssystems und Entwicklung eines Scanners für das Spektrometer PERKEO III". ger. Diploma Thesis. Universität Heidelberg, 2007, 58 S.

[WTP+11] D. M. Webber et al. "Measurement of the Positive Muon Lifetime and Determination of the Fermi Constant to Part-per-Million Precision". In: *Phys. Rev. Lett.* 106 (4 Jan. 2011), p. 041803. DOI: 10.1103/PhysRevLett.106.041803.

[XSO12] Yijie Xia, Kuan Sun, and Jianyong Ouyang. "Solution-Processed Metallic Conducting Polymer Films as Transparent Electrode of Optoelectronic Devices". In: *Advanced Materials* 24.18 (2012), pp. 2436–2440. DOI: 10.1002/adma.201104795.

[YDG+13] A. T. Yue, M. S. Dewey, D. M. Gilliam, G. L. Greene, A. B. Laptev, J. S. Nico, W. M. Snow, and F. E. Wietfeldt. "Improved Determination of the Neutron Lifetime". In: *Phys. Rev. Lett.* 111 (22 Nov. 2013), p. 222501. DOI: 10.1103/PhysRevLett.111.222501.

[YKM+97] B. Yerozolimsky, I. Kuznetsov, Yu. Mostovoy, and I. Stepanenko. "Corrigendum: Corrected value of the beta-emission asymmetry in the decay of polarized neutrons measured in 1990". In: *Physics Letters B* 412.3 (1997), pp. 240–241. DOI: http://dx.doi.org/10.1016/S0370-2693(97)01004-6.

[Zie15] Carmen Ziener. "Das Spektrometer PERC zur Untersuchung des Neutron-Beta-Zerfalls". PhD thesis. Universität Heidelberg, 2015.

[ZZB10] James F. Ziegler, M.D. Ziegler, and J.P. Biersack. "{SRIM} – The stopping and range of ions in matter (2010)". In: *Nuclear Instruments and Methods in Physics Research Section B: Beam Interactions with Materials and Atoms* 268.11–12 (2010). 19th International Conference on Ion Beam Analysis, pp. 1818–1823. DOI: http://dx.doi.org/10.1016/j.nimb.2010.02.091.

Acknowledgements

I would like to thank ...

- ... Bastian Märkisch for bringing this diversified and challenging project to my attention, for accepting me into the group and for many inspiring conversations at the coffee-machine.
- ... Ulrich Schmidt for his feedback and the sharing of his huge amount of knowledge and experience.
- ... Torsten Soldner for all the coordination within the ILL and the huge experience with proton measurements.
- ... Gertrud Konrad for her efforts and overview during the beam times at the ILL.
- ... all people from the mechanics and construction workshop of the institute for their efforts in realizing the detector and for their patience with my requests.
- ... the colleagues from the experiment IN11 who borrowed us their 600 A power supply and had to schedule their measurements around our erratic magnetic field settings.
- ... my colleagues in the office for all the answers to the little questions in daily work.
- ... the whole team involved in the beam time including the interns, neighbours and friends.
- ... especially everyone involved in maximizing the fun in the few free moments in Grenoble.
- ... everyone involved in proofreading this thesis.
- ... Claudia for emotional support during the whole process of the thesis and for tolerating extension after extension.
- ... my parents for supporting me during my studies and the whole dissertation project.
- ... and finally Heiko, Christoph, Michi, Daniel and all the others: you made the time in Grenoble memorable.

Impressions

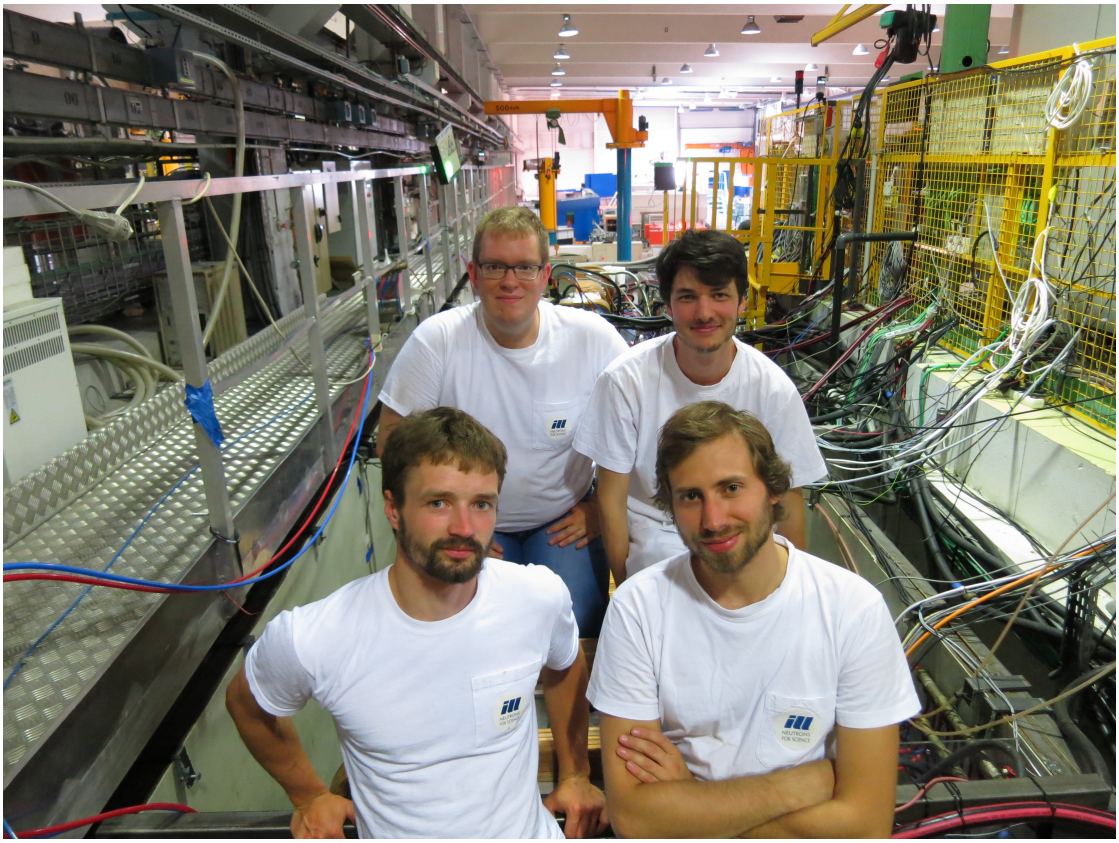

A part of the team of the 2015 part of the beamtime. From left to right and back to front: L. Raffelt, D. Moser, C. Roick, M. Klopf